

## ABSTRACT

FAN, YUQIAO. Counter Current Flow Studies Using Interface Capturing Simulations. (Under the direction of Dr. Igor A. Bolotnov).

Counter current two-phase flows (CCF) represent an important problem for both nuclear reactor operation and safety analysis. CCF limitation (CCFL) occurs when upward steam flow rate is sufficiently large such that the downflowing liquid coolant cannot penetrate the channel. CCFL can occur in the subchannels and larger piping systems of light water reactors, and at smaller scales CCFL can occur in the pores of debris bed and in the deposited crud on fuel cladding. Despite the significant progress achieved by experimental studies and analytical analysis on large scale CCFL, certain limitations exist for millimeter scale CCFL such as the difficulties in measurement and visualization. CCF in this dissertation is studied based on two topics: the controlled single bubble studies (note that phase directions are also considered counter current), and the counter current flow limitation in the reactor debris bed channel. To provide fundamental studies on CCFL at such small scales, level-set method (one of the interface capturing methods) in well-resolved transient three-dimensional simulations are used to produce high resolution data to evaluate this phenomenon. The major objectives of this work include: (1) strengthen the capability of evaluating the interfacial forces through controlled single bubble studies; (2) reveal the level-set method capability on solving CCF in debris bed channels; (3) develop a proportional-integral-derivative (PID) CCFL pressure gradient controller to demonstrate integration of control theories into CCFL analysis in debris bed channels. To address these objectives, bubble studies of interfacial force and topology are presented, as well as CCF simulations in the debris bed channel which is driven by gravity and steam generation rate. A PID pressure gradient controller is developed to accurately and efficiently control the flow rate and to achieve CCFL conditions. The performed foundational simulations are to ensure that the results from this most innovative PID pressure gradient controller

to achieve CCFL conditions are trustworthy. Finally, three computational geometries with some representative features of debris bed channels were selected to study two-phase mechanism at CCFL and the corresponding bed coolability. Based on those representative simulations, a pressure gradient correlation and a dimensionless number is proposed to predict CCFL occurrence. The PID pressure gradient controller is also shown to be robust even under very complex debris bed geometry and two-phase flow conditions. The presented studies contribute to fill the knowledge gaps on the closure law development of interfacial forces as well as the CCFL mechanisms in debris bed channels.

© Copyright 2022 by Yuqiao Fan

All Rights Reserved

Counter Current Flow Studies Using Interface Capturing Simulations

by  
Yuqiao Fan

A dissertation submitted to the Graduate Faculty of  
North Carolina State University  
in partial fulfillment of the  
requirements for the degree of  
Doctor of Philosophy

Nuclear Engineering

Raleigh, North Carolina  
2022

APPROVED BY:

---

Dr. Igor Bolotnov  
Committee Chair

---

Dr. Nam Dinh

---

Dr. Joseph Doster

---

Dr. Pramod Subbareddy  
Minor / GSR

---

Dr. William Pointer

---

Dr. Jun Fang  
External member

## **DEDICATION**

This dissertation is dedicated to my twenties and to families and friends who always love and support me.

## BIOGRAPHY

Yuqiao “Joy” Fan was born in Xi’an, a city with the histories of thirteen ancient dynasties, in China. While people worldwide are familiar with the Terra-Cotta Warriors near Xi’an, local people are more familiar with the middle/high school Joy attended, XiGongDa Fuzhong. All courses taught at the school, especially the math, physics, and chemistry classes, were equivalent to university freshman courses or higher level. The education Joy received there built a solid foundation for her to explore the world of science and engineering. Around that time, awareness of the harm of PM2.5/haze grew and emissions from the local coal power plant were discovered to have significant impacts on air pollution and human health. Therefore, Joy decided to choose Nuclear Engineering rather than what was her favorite, architecture, as her major in university. In addition, impacts of the Fukushima accident right before her college entrance examination, further supported her decision to pursue nuclear to create a safe and green future for her peers, her parents, and society.

During her four-year undergraduate period at Xi’an Jiaotong University (XJTU), Joy was exposed to a diverse range of research, especially experimental projects. Beginning in Joy’s sophomore year, she started her research by conducting small-scale experimental studies on flow instability. From there, she moved onto large-scale experiments, specifically the steam generator rod-bundle studies for her capstone project. XJTU also had opportunities for students to study abroad, providing Joy the chance to study at the Hong Kong University of Science and Technology (HKUST). During her internship at HKUST in the summer of 2014, her mentor, Prof. Huihe Qiu, provided her with an opportune experimental study environment in addition to moral support. The feeling of achievement in research and the day-to-day incremental progress in cutting edge development convinced Joy to pursue her Ph.D. and become a full researcher.

Joy started graduate school in August of 2015 in the United States. She finished her master's degree at the University of Michigan, Ann Arbor, and then joined Prof. Igor Bolotnov's research group at North Carolina State University (NCSU). The new position also implied that Joy would have to begin a new journey into the world of computational fluid dynamics (CFD). Although, her experience in interface tracking simulation or complex code development was little to none, it was Prof. Bolotnov strong encouragement that motivated Joy to continue. Her previous education and research experience was what made Prof. Bolotnov believe Joy would succeed. The CFD related courses at NCSU, regardless in Nuclear or Mechanic Engineering departments, were fantastic, which made CFD a new passion for Joy. Her favorite moments were when the code under development worked and produced beautiful flow figures, signifying the end to a long coding process. In the fall of 2019, she attended an internship at Oak Ridge National Laboratory (ORNL), where she realized the significance of her PhD research. This only furthered her passion for CFD and allowed her to gain the courage and knowledge to conquer the difficulties encountered during academic career.

Joy is grateful that her hard work over the past decade will finally come to a conclusion as Dr. Fan. After graduation, she will join ORNL to continue on the path of research in nuclear engineering and CFD.

## TABLE OF CONTENTS

DEDICATION .....	ii
BIOGRAPHY .....	iii
TABLE OF CONTENTS.....	v
LIST OF TABLES .....	viii
LIST OF FIGURES .....	x
Chapter 1. INTRODUCTION .....	1
1.1 Overview of the counter current flow limitation studies.....	3
1.1.1 Experimental CCFL studies.....	3
1.1.2 Computational fluid dynamics CCFL studies.....	7
1.1.3 Debris bed CCFL studies .....	8
1.1.4 Direct numerical simulation of CCFL .....	13
1.1.5 Knowledge gap .....	14
1.2 Overview of bubble studies.....	18
1.2.1 Bubble interfacial force studies .....	18
1.2.2 Complex bubble topology studies.....	21
1.2.3 Experimental controlled bubble studies.....	23
1.2.4 PID controlled bubble studies.....	24
1.2.5 Knowledge gap .....	28
1.3 Validation hierarchy.....	28
1.4 Major Research Objectives .....	31
Chapter 2. NUMERICAL TOOLS.....	34
2.1 Governing equations in PHASTA.....	35
2.2 Level-set method .....	36
Chapter 3. PID PRESSURE GRADIENT CONTROLLER .....	38
3.1 Introduction of PID pressure gradient controller .....	38
3.2 Development of PID pressure gradient controller.....	40
3.2.1 Code development of velocity integral .....	42
3.2.2 Verification of computed velocity integral .....	47
3.2.3 Integration of PID theory in pressure gradient control .....	51
3.3 Performance evaluation of PID pressure gradient controller .....	54
3.3.1 Tuning of PID pressure gradient controller .....	55
3.3.2 Verification of PID pressure gradient controller .....	65
3.3.3 Robustness of PID pressure gradient controller.....	68

3.3.4	Computational cost evaluation of the PID pressure gradient controller .....	70
3.4	Chapter Summary.....	72
Chapter 4.	RESULTS OF BUBBLE IN COUNTER CURRENT FLOW .....	74
4.1	PID bubble controller.....	74
4.2	Bubble interfacial force studies.....	78
4.2.1	Simulation setup.....	79
4.2.2	Domain study .....	80
4.2.3	Transverse force.....	82
4.3	Bubble interface topology studies .....	88
4.3.1	Simulation setup.....	88
4.3.2	Grid convergence study .....	90
4.3.3	Verification .....	93
4.3.4	Validation.....	95
4.4	Gravity control capability.....	98
4.5	Chapter summary .....	104
Chapter 5.	RESULTS OF COUNTER CURRENT FLOW LIMITATION.....	105
5.1	Counter-current flow studies without PID control.....	105
5.1.1	Counter current flow driven by gravity .....	105
5.1.2	Counter current flow driven by both gravity and steam generation rate .....	109
5.2	CCFL studies in cylindrical channels under PID control.....	115
5.2.1	Simulation setup.....	119
5.2.2	Separate effect tests.....	122
5.2.3	CCFL studies under varying void fractions .....	135
5.2.4	Comparison with CCFL experiments .....	138
5.2.5	Pressure gradient model development .....	140
5.2.6	Dimensionless number for pressure gradient under CCFL conditions.....	142
5.3	CCFL studies of complex debris bed channel under PID control.....	144
5.3.1	Debris bed channel with small obstacles .....	145
5.3.2	Debris bed channel with large obstacles.....	154
5.3.3	Effect of PID control on fluid dynamics in complex debris bed channels .....	165
5.4	Application range and parametric studies .....	171
5.4.1	Liquid density .....	171
5.4.2	Steam density .....	176
5.4.3	Surface tension.....	178

5.4.4	Channel porosity .....	182
5.4.5	Application of proposed models .....	185
5.5	Chapter summary .....	187
Chapter 6.	CONCLUSIONS & FUTURE WORK.....	189
6.1	Improvement on developed correlation and dimensionless number .....	190
6.2	PID pressure gradient control in more complex scenarios.....	191
6.3	Improved PID pressure gradient controller for complex geometry .....	192
6.4	Potential coupling of PID theory with boiling .....	193
REFERENCES	.....	194
APPENDICES	.....	201
A.	Scripts of probe area computation.....	202
B.	Scripts of subroutine <i>asigr</i> .....	203
C.	Scripts of subroutine <i>timeseries</i> and <i>modify_xyzts</i> .....	208
D.	Scripts of PID pressure gradient control in <i>itrdrv.f</i> .....	212
E.	Velocity field evolution of cylindrical debris bed channel .....	215
F.	Velocity field of debris bed channel with small obstacles .....	222
G.	Interface evolution of debris bed channel with large obstacles .....	230

## LIST OF TABLES

Table 3.1. Numerical error of computing xyzts probe area. ....	45
Table 3.2. Parameters used in tuning of PID pressure gradient controller. ....	56
Table 3.3. Control coefficients used in tuning tests of the PID pressure gradient controller. ....	56
Table 3.4. Recommended control coefficient sets in PID pressure gradient controller. ....	64
Table 3.5. <i>Nspeed</i> (number of core hours to compute 1 billion elements per time step) for 4 test cases. ....	71
Table 4.1. Parameters for simulation setup.....	81
Table 4.2. Variables in low shear flow studies ( $Sr = 3.8/s$ ). ....	83
Table 4.3. Summary of mesh resolution, mesh size and <i>GCI</i> computation. ....	92
Table 4.4. Difference between presented simulation and the reference research. ....	93
Table 4.5. Parameter design for verification.....	94
Table 4.6. Verification of bubble deformation. ....	94
Table 4.7. Comparison of temporal topology change.....	95
Table 4.8. Common parameter in each validation case. ....	95
Table 4.9. Comparison of bubble shape between classical experiments and simulations. The values in the last row are the liquid viscosity, $\mu_l$ ( $Pa \cdot s$ ), for each simulation.....	96
Table 4.10. Comparison of dimensionless number between classical experiments (exp.) and simulations (sim.).....	96
Table 4.11. Comparison of complex bubble deformation with a film formed at the wake side of the bubble.....	97
Table 4.12. Comparison of complex topology change during bubble break-up and the formation of satellite bubbles. ....	98
Table 4.13. Post-processed results under each relative velocity.....	102
Table 5.1. Fluid and system properties in preliminary study.....	106
Table 5.2. Simulation parameters. ....	110
Table 5.3. Simulation results for different steam superficial velocities. ....	111
Table 5.4. Parameters used in debris bed channel CCFL simulations.....	121
Table 5.5. Interfacial shear comparison between two steam viscosities.....	124
Table 5.6. Averaged variables in the quasi-steady state of two test cases under $\alpha = 30\%$ . ....	129
Table 5.7. CCFL definition sensitivity analysis (initial downflow of $-0.01m/s$ ). ....	130
Table 5.8. Mesh configuration statistics and the corresponding pressure gradients and coolant velocities at CCFL. ....	134
Table 5.9. Void fraction and the corresponding gas column radius in the case study.....	136
Table 5.10. Averaged variables in the quasi-steady state of each case.....	138

Table 5.11. Dimensional analysis of $dp/dx$ with regarding to key parameters.....	143
Table 5.12. Liquid density values in the parametric study. ....	172
Table 5.13. Pressure gradient model predictive capability when liquid density changes.....	174
Table 5.14. Liquid and steam velocities and the corresponding parameter with $dp/dx$ unit. ...	175
Table 5.15. Steam density values in the parametric study.....	177
Table 5.16. Pressure gradient model predictive capability when steam density changes.....	178
Table 5.17. Surface tension values in the parametric study.....	179
Table 5.18. Pressure gradient model predictive capability when surface tension changes. ....	180
Table 5.19. Liquid and steam velocities at CCFL. ....	181
Table 5.20. Porosity computation for three debris bed channels.....	182
Table 5.21. Summarization of CCFL results from different debris bed channels. ....	183

## LIST OF FIGURES

Figure 1.1. Illustration of liquid being carried beyond injector.....	16
Figure 1.2. Illustration of CCFL criterion when liquid velocity is zero ( $v_l = 0$ ).....	16
Figure 1.3. Illustration of the lift force change on the bubble with different deformation. The wall existence is neglected in (a) but considered in (b). The wall force is a constant when the $L/D$ remains unchanged. ....	20
Figure 1.4. Migration curve at $L/D = 1.0$ from Fig. 19 of Feng and Bolotnov’s publication (Feng and Bolotnov, 2017a). ....	26
Figure 1.5. Illustration of high shear domain setup compared to a turbulent channel.....	26
Figure 1.6. Validation hierarchy. ....	31
Figure 3.1. Illustration on gas flow rate driven counter current flows. ....	39
Figure 3.2. Illustration of the fluid domain.....	41
Figure 3.3. PID control scheme. ....	41
Figure 3.4. Probe distribution with each probe collecting flow field information. ....	42
Figure 3.5. xyzts probe area and the illustration on how to compute it.....	44
Figure 3.6. Parallel computation of velocity integral. ....	46
Figure 3.7. Mesh and xyzts probes used in verification test.....	48
Figure 3.8. Velocity integral single phase verification. ....	49
Figure 3.9. Velocity integral two phase verification.....	50
Figure 3.10. The control effect of historical average versus time window average. ....	53
Figure 3.11. Control scheme of using PID pressure gradient controller to obtain CCFL. ....	54
Figure 3.12. Illustration of an annular flow for tuning tests. ....	55
Figure 3.13. Tuning results of 12 combinations. ....	58
Figure 3.14. Tuning results of $KD = 1.0E10$ , $KP = -1.0E11 \sim -1.0E13$ .....	61
Figure 3.15. Tuning results of $KP = -1.0E12$ and $KD = 1E9 \sim 1E13$ .....	62
Figure 3.16. Tuning results of $KP = -1.0E11$ and $KD = 1E9 \sim 1E11$ .....	63
Figure 3.17. Verification test comparing two-phase velocity changes where PID control is deactivated (flow driven by a constant pressure gradient) and activated (flow driven by PID controller).....	66
Figure 3.18. Two-phase fluid dynamics comparison with and without PID control.....	67
Figure 3.19. Robustness test #1 result where initial $x$ pressure gradient is 0.0. ....	68
Figure 3.20. Turbulent flow regime and highly deformed interface in robustness test #2. ....	69
Figure 3.21. Robustness test #2 result where $x$ velocity goal in PID control is 0.5m/s.....	70
Figure 4.1. Illustration of coordinate system transform from realistic upflow conditions to PID controlled environment at steady state.....	75

Figure 4.2. Mesh comparison without and with PID bubble controller.....	78
Figure 4.3. Computation domain and mesh configuration. ....	80
Figure 4.4. Control forces acting on the bubble. The legends 1 time, 2 times, and 3 times denote 18mm, 36mm, 54mm wall distances respectively. ....	82
Figure 4.5. Illustration of $L/D$ . ....	83
Figure 4.6. Quasi-steady state achieved under each surface tension coefficient. ....	84
Figure 4.7. Transverse direction distribution with $Re_b$ , $We$ , and $L/D$ . ....	85
Figure 4.8. Computation domain and cylindrical mesh refinement zones. ....	89
Figure 4.9. Comparison among uniformly refined meshes from (a) to (e) on $x - y$ plane and zoomed-in mesh in $y - z$ plane (f). ....	91
Figure 4.10. Comparison of film sizes among refined meshes and $GCI$ varying with mesh configurations. ....	92
Figure 4.11. Flow diagram of the gravity control capability. ....	100
Figure 4.12. Automatic adjustment of $u_r$ and the corresponding response of $F_D$ . ....	101
Figure 4.13. Bubble wake formation and wake change with $u_r$ . ....	103
Figure 4.14. Bubble shape comparison. ....	104
Figure 5.1. Mesh configuration and interface initialization. ....	107
Figure 5.2. Interface topology (white surface) changes with time. ....	107
Figure 5.3. Mesh configuration and interface initialization. ....	108
Figure 5.4. Interface topology (white surface) changes with time. ....	108
Figure 5.5. Counter current flow case setup. ....	110
Figure 5.6. Interface initialization in a cylindrical channel of the debris bed. ....	111
Figure 5.7. Progression of CCFL event, magenta line represents liquid gas interface. ....	112
Figure 5.8. Semi-transparent 3D interface showing the process of generating Rayleigh-Taylor instability inside the channel. Cross sections of 2D interface are provided in (b) and (c) to better illustrate the interface topology. ....	113
Figure 5.9. The process of achieving a force balance in the channel. ....	114
Figure 5.10. Comparison of velocity fields and interfaces driven by three different contact angle values. ....	115
Figure 5.11. Debris bed channel domain and a counter current flow configuration inside. ....	120
Figure 5.12. Debris bed channel mesh configuration and xyzts probe used. ....	122
Figure 5.13. Liquid phase velocity growth with original steam viscosity and high viscosity. ....	123
Figure 5.14. Domain length effect simulation setup with void fraction of 60%. ....	125
Figure 5.15. Domain length effect comparison. ....	126
Figure 5.16. Influence of initial liquid velocity on PID controlled CCFL. ....	128
Figure 5.17. PID controlled CCFL under different definition. ....	131

Figure 5.18. Desired terminal liquid velocity compared with actual simulation results. ....	132
Figure 5.19. Mesh configurations with different elements across channel diameter (#/D).....	133
Figure 5.20. Grid convergence index vs. the mesh configuration. ....	135
Figure 5.21. Pressure gradient and velocities of liquid and gas phase to achieve CCFL conditions under varying void fractions. ....	137
Figure 5.22. Pressure gradient obtained from PID control compared with experimental data (Rashid et al., 2012). ....	139
Figure 5.23. Illustration of possible channel configuration in the debris bed experiment (Rashid et al., 2012). ....	140
Figure 5.24. Pressure gradient correlations fitted in linear or exponential trends. ....	140
Figure 5.25. Pressure gradient correlations with regard to the void fraction.....	142
Figure 5.26. Performance of the dimensionless analysis where $SU$ is the slope for the trendline. The trendline does not across the origin because it includes the gravity and wall shear into consideration. ....	144
Figure 5.27. Debris bed channel with small obstacles.....	146
Figure 5.28. Two phase debris bed channel with small obstacles and $\alpha = 30\%$ .....	147
Figure 5.29. PID control on debris bed channel with small obstacles ( $\alpha = 30\%$ ). ....	148
Figure 5.30. Two-phase velocity vector fields under CCFL at the same time. ....	148
Figure 5.31. Velocity comparison between two debris bed channels.....	151
Figure 5.32. Two phase debris bed channel with small obstacles and $\alpha = 20\%$ .....	153
Figure 5.33. Velocity field distribution at $t = 9.436E - 3s$ (gravity direction: $-x$ ). ....	153
Figure 5.34. Debris bed channel with large obstacles. ....	154
Figure 5.35. Velocity change in single-phase simulation under $dp/dx = 1.01\rho_l g$ . The corresponding computation time at 10000 <sup>th</sup> time step is $t = 4.057s$ . ....	155
Figure 5.36. Single-phase flow in the debris bed channel with large obstacles. ....	156
Figure 5.37. Velocity change with pressure gradient. A steady state is achieved with $dp/dx = \rho_l g$ after 10349 <sup>th</sup> time step or $t = 10.88s$ . ....	159
Figure 5.38. Net zero liquid velocity in debris bed channel with large obstacles. ....	160
Figure 5.39. Interface initialization in the channel with a steam volume fraction of 30%. ....	161
Figure 5.40. The phase distribution (red: steam; blue: coolant) and the 3D interface of formed steam film around the middle two obstacles.....	162
Figure 5.41. Velocity distribution under CCFL in the debris bed channel when large obstacles exist. ....	163
Figure 5.42. PID control on debris bed channel with large obstacles ( $\alpha = 30\%$ ). ....	165
Figure 5.43. Comparison of coolant velocity integral changes where PID control is deactivated (flow driven by a constant pressure gradient) and activated (flow driven by PID controller) for debris bed channel with small obstacles. ....	166

Figure 5.44. Comparison of phase and velocity distributions at CCFL in small obstacle debris bed channel with or without PID control. - $x$ indicates the gravity direction. ....	167
Figure 5.45. Comparison of coolant velocity integral changes where PID control is deactivated (flow driven by a constant pressure gradient) and activated (flow driven by PID controller) for debris bed channel with large obstacles.....	169
Figure 5.46. Comparison of phase and velocity distributions at CCFL in large obstacle debris bed channel with or without PID control. - $x$ indicates the gravity direction. ....	170
Figure 5.47. PID controlled CCFL in liquid density parametric study.....	172
Figure 5.48. Performance of the dimensionless analysis when liquid density varies.....	176
Figure 5.49. PID controlled CCFL in steam density parametric study.....	177
Figure 5.50. PID controlled CCFL in surface tension parametric study. ....	179
Figure 5.51. Two-phase velocity distributions in surface tension parametric study. ....	181
Figure 5.52. Pressure gradient obtained from PID control in three different debris bed channels, compared with experimental data (Rashid et al., 2012).....	184
Figure 6.1. Illustration of debris bed flow channel with steam generated in the heated channel. The channel geometry is more realistic than the simplified cylindrical channel, but it still needs the debris to be simplified into overlapping spheres. ....	192

## Chapter 1. INTRODUCTION

In recent years, there has been significant investment interest towards clean and safe energy. The need and drive for an energy sustainable future is one of the most prominent challenges required by our society. Nuclear energy has been one of the most developed and proven technologies both as a strategic resource but also as a large sustainable base load generator of emission-free power. However, critics against nuclear energy are concerned about the safety of nuclear technology citing historical cases of catastrophic accident scenarios to justify their conclusion. Three Mile Island, Chernobyl, and Fukushima are the most well-known examples of severe accident scenarios. In each case, one of the most significant concerns is the decay heat removal from the reactor to prevent reactor melt down. One of the major two-phase flow phenomenon which might prevent the effective heat removal from intact or melted core is the counter current flow limitation.

Counter current two-phase flows are complex flow phenomena in which vapor and liquid phases have opposite flow rate directions. Counter current flow limitation (CCFL) corresponds to one phase having a large enough velocity to inhibit the counter flow of the other phase. In nuclear thermal-hydraulic (TH) studies, CCFL typically refers to steam rising at a fast rate such that it prevents coolant from draining down within a confined channel. CCFL is a crucial issue in safety analysis due to its possibility to occur at different locations in the reactor during severe accidents. At the decimeter scale, CCFL can happen in the downcomer, when the downflow of emergency core cooling water is injected and encounters steam flowing upward. When the residual heat in fuel rods is still generating steam, CCFL can also occur in the reactor core subchannels (centimeter scale). Even at the millimeter scale, CCFL can happen in the deposited crud on fuel cladding.

CCFL can also exist in the debris bed, formed in the lower plenum of reactor pressure vessel, and dramatically deteriorate the coolability of the molten core.

In most of the TH studies, the experimental approach used to determine the occurrence of CCFL are often through tried-and-true methods, which typically include increasing the steam rate until coolant stops draining down (Vierow, 2008). Such manually controlled process is also accommodated in numerical CCFL studies. However, if a control theory is integrated, the occurrence can be found more efficiently and accurately. One successful integration is the proportional-integral-derivative (PID) bubble controller in PHASTA code to evaluate the interfacial forces (Thomas et al., 2015; Feng and Bolotnov, 2016). Instead of computing the interfacial forces after a rising bubble achieves a uniform motion, the PID controller is adjusting the forces to fix the bubble at the same location. The steady-state force balance is then used to determine the interfacial forces which are balanced by the applied control forces. Similarly, experiments of controlled single bubble studies were also conducted where the liquid was injected downward towards the rising bubble, restrained the bubble movement upward (Salibindla et al., 2020). Such control of a bubble in liquid is another type of counter current two-phase flow.

With the successful application of the PID control theory in interfacial force evaluation for single bubble, CCFL studies can also be carried out in a controlled manner. The target zero coolant velocity is selected for input (similar to fixing bubble location) and the corresponding output is the pressure gradient (relative to the bubble interfacial force) which produces CCFL occurrence. Such PID control will greatly facilitate numerical studies, but its accuracy and reliability need to be proved through a series of verification and validation (V&V) efforts. CCFL involves complex flow characteristics such as interfacial forces and topologies. It is very challenging to conduct a comprehensive V&V for CCFL, not to mention the addition of PID control. However, V&V of

PID controlled CCFL simulation can be decomposed into benchmark problems, such as interfacial forces and topology, CCFL without PID control, etc. Among them, using bubble studies to ensure the correct assessment of interfacial forces and complex topology evolution is trustworthy considering adequate references from experimental studies. The following sections present the comprehensive literature review, the CCFL studies followed by the published single bubble studies on interfacial force and topology evolution. The knowledge gaps and validation hierarchy are identified afterwards, and the research objectives are formulated to tackle each challenge.

## **1.1 Overview of the counter current flow limitation studies**

Counter current flow is driven by interfacial shear resulted from the relative motion between vapor and liquid phases. CCFL occurs due to the high interfacial shear generated by large value of vapor velocities, so liquid is inhibited from draining down even under gravity (Wallis, 1969). Besides interfacial shear and gravity, channel dimension is also crucial in the hydrodynamics of CCFL. The flow regimes of CCFL under different channel sizes are distinct and mechanisms have not been well studied to establish trustworthy predictive capabilities. Even CCFL occurrence itself has been difficult to determine in many conditions (Hewitt and Wallis, 1963). The following section reviews the experimental and numerical efforts in CCFL and more specific CCFL studies in the debris bed.

### **1.1.1 Experimental CCFL studies**

There are numerous CCFL experimental studies at large scales. One of the most well-recognized experimental correlations to evaluate the occurrence of CCFL is the Wallis correlation based on dimensionless liquid and vapor superficial velocities (Wallis, 1969).

$$J_g^{*0.5} + mJ_l^{*0.5} = C \quad (1)$$

Here,  $J_g^*$  and  $J_l^*$  are dimensionless Wallis numbers for gas and liquid phase defined below,  $m$  and  $C$  are two empirical constants which change with the geometry and fluid properties. This correlation shows that the dimensionless liquid and gas Wallis numbers under CCFL are aligned on a straight line.

$$J_l^* = j_l \sqrt{\frac{\rho_l}{(\rho_l - \rho_g)Dg}} \quad (2)$$

$$J_g^* = j_g \sqrt{\frac{\rho_g}{(\rho_l - \rho_g)Dg}} \quad (3)$$

$$j_l = \alpha_j v_j \quad (4)$$

$$j_g = \alpha_g v_g \quad (5)$$

In the definitions,  $J_l^*$  and  $J_g^*$  are dimensionless Wallis numbers.  $\rho_l$  and  $\rho_g$  are densities for liquid and gas phase.  $D$  is the pipe diameter.  $g$  is the earth gravity.  $j_l$  and  $j_g$  are superficial velocities for liquid and gas phase respectively.  $\alpha_j$  and  $\alpha_g$  are the void fraction of each phase, where  $\alpha_j + \alpha_g = 1$ .  $v_j$  and  $v_g$  are the phase velocities.

This correlation includes the inertial and gravitational effects on CCFL occurrence, which has been widely used as a validation resource for later experimental and numerical studies (Zapke and Kröger, 1996; Vierow, 2008; Murase et al., 2012; Murase et al., 2017). The original data was obtained from air-water pipe flows with diameters of 17 mm and 30 mm, which are considered to be small diameters. Another researcher also pointed out that channel size indeed affected CCFL conditions (Jayanti et al., 1996). It was acknowledged that interfacial shear or drag on the interface governs the condition of counter current flow, which highly depends on channel diameter. Therefore, the gas velocity required to transport interface upwards increases with the channel diameter.

The dimensionless channel diameter is proposed by Kutateladze (Kutateladze, 1972):

$$D^* = D \sqrt{\frac{g(\rho_l - \rho_g)}{\sigma}} \quad (6)$$

Here  $D^*$  is the dimensionless pipe diameter and  $\sigma$  is the surface tension coefficient. The dimensionless pipe diameter connects Wallis number with Kutateladze number.

$$Ku_l^* = D^{*0.5} J_l^* \quad (7)$$

$$Ku_g^* = D^{*0.5} J_g^* \quad (8)$$

Note that dimensionless liquid and gas Kutateladze numbers under CCFL are aligned on a straight line as well. The criterion to choose between Wallis and Kutateladze numbers to represent CCFL is through  $D^*$ . When  $D^*$  is smaller than 24.5, Wallis correlation predicts CCFL better. Kutateladze numbers have a better performance when  $D^* > 24.5$ .

Later, the experimentalists found that the entrance geometry (sharp or curved) and the inclination of the pipe also affects the onset of CCFL (Zapke and Kröger, 1996). Therefore, they added new dimensionless numbers to describe these new variables in the correlation, but the mathematically still similar to Wallis's form (Zapke and Kröger, 1996). Besides the geometry effect, there is also another hysteresis effect that exists which changes the onset of CCFL (Hewitt and Wallis, 1963). Numerous researchers observed that for the CCFL occurrence obtained from increasing the gas velocity (from pre CCFL to CCFL) and decreasing the gas velocity (from post CCFL to CCFL), the required gas velocity for the latter condition is lower (Al Issa and Macian, 2011).

Aside from studying the influential factors on CCFL and improving the correlation, researchers also worked on establishing a flow regime map for characteristics of CCFL. Bankoff and Lee studied the liquid film motion under different pressure gradients and gas flow rates and sketched

a map with falling climbing film zones (Bankoff and Lee, 1983). Recent experiments explored comprehensive flow patterns through a “one-dimensional (1D)” test section (rectangular cross section), but the counter current flow is horizontally stratified, which has distinct behavior different from the one observed in cylindrical channels (Gallego, 2004). In 2012, a review on reactor hot leg CCFL studies was published (Höhne et al., 2012). The authors point out that the existing experimental correlations have a relatively narrow range for application, and the mechanistic models are limited for CCFL (Höhne et al., 2012).

CCFL experiments at the millimeter scale have rarely been published. Two relevant studies were found including the CCFL experiments at the millimeter scale gap and two-phase flow regime studies in capillary tubes (Fukano and Kariyasaki, 1993; Rapolu and Son, 2007; Jeong, 2008). Jeong conducted CCFL experiments at the millimeter scale gap between two concentric pipes with large diameters. The gap sizes are of 1, 2, 3, and 5 *mm*, but the outer diameter of the annular channel is 0.5 *m*, which yields CCFL occurrence more comparable with parallel plates, but completely different compared with conduit flows (e.g. such as in pipes or square ducts) (Jeong, 2008). For small channels (less than several millimeters in hydraulics diameter), no matter they are cylindrical or square channels, due to the size limitation, CCFL occurs globally. However, in the narrow annular gap of Jeong’s experiment, partial CCFL can happen locally while other regions still have liquid draining. The local CCFL will expand when air flow rate increases before the global CCFL can be achieved (Jeong, 2008). When global CCFL happens, the liquid across the entire annular gap all moves upwards. Other relevant small-scale experiments focus on two-phase flow regimes rather than CCFL in mini channels or capillary tubes. Specifically, where varying air and water flow rates are used to produce certain two-phase configurations (Fukano and Kariyasaki, 1993; Rapolu and Son, 2007).

### 1.1.2 Computational fluid dynamics CCFL studies

The majority of computational fluid dynamics (CFD) CCFL studies in nuclear engineering applications are still for large scales, like the hot leg or the pressurizer surge line of the nuclear reactor (Murase et al., 2012; Murase et al., 2017). Since the diameters of the hot leg and the pressurizer surge line are  $750\text{ mm}$  and  $300\text{ mm}$ , the superficial liquid and steam velocities at CCFL obtained from these numerical simulations can be normalized with the definitions in Eq. (2) and (3) (Murase et al., 2012; Murase et al., 2017), and CCFL model can be correspondingly developed in the form of Wallis correlation as well. The study on reactor hot leg indeed suggests one special condition for nuclear reactor CCFL compared with CCFL under normal condition. When the system is pressurized ( $1.5\text{ MPa}$ ), the CCFL characteristics are slightly different than those under atmospheric condition. In addition, the liquid viscosity under pressurized condition is more influential for determining CCFL occurrence (Murase et al., 2012).

For the above large scale CCFL simulations, the volume of fluid (VOF) method has been widely used due to the successful implementation in commercial CFD software (Murase et al., 2012; Murase et al., 2017). However, in most simulations, the spatial resolution was not fine enough to well resolve the interface motion even in 2D scenarios. For instance, Lu et al (2016) performed a series of parameter studies on counter current flow behaviors under different gas and liquid flow rate in a 2D channel, but the interface could not be well resolved. Although surface tension effect is included, the transient CCFL could not be achieved (Lu et al., 2016). In order to obtain CCFL occurrence with relatively low computation cost, CFD researchers also implement liquid film flow model into the commercial software to couple with the VOF method (Watanabe et al., 2017). This liquid film model evaluates the thickness of virtual liquid film with an annular flow assumption so does not require the VOF simulation to resolve the film. With such virtual

liquid film, the mesh spatial resolution can be quite coarse, and the CCFL could be obtained practically in a 2D simulation, however, due to the model simplifications, the results of the CCFL conditions are questionable.

Rarely 3D direct numerical simulation (DNS) using interface capturing methods is performed to model the CCFL phenomena. The most relevant simulation is a 3D quasi-DNS conducted annular flow study using coupled hybrid method of front-tracking and level set method (Shin et al., 2018). However, the annular flow was aimed to demonstrate the scalability of their code in large-scale simulation. Some researchers attempt to conduct 3D high resolution CCFL simulation, but they cannot afford grid convergence study due to very high computational costs (Deendarlianto et al., 2010). It is understandable that the computational cost of DNS was more of a concern for some researchers, thus a less computationally expensive approach, two-fluid models involving turbulence models, was preferably used in CCFL/churn flow/severe accident-related studies (Tekavčić et al., 2016).

### **1.1.3 Debris bed CCFL studies**

CCFL is a dominant two-phase flow phenomenon in the drying-out of the debris bed. Debris bed forms from relocated corium in the nuclear reactor pressure vessel (RPV) during severe accidents. Famous examples of the debris bed are in the Three-Mile Island unit-2 accident, and the Fukushima Daiichi Unit-3 accident. Ideally, with the residual coolant in the lower plenum of the RPV, the decay heat produced by the debris bed can be removed. However, with the increasing bed height, the steam velocity is higher. At a certain height of the debris bed, the steam velocity is high enough which prohibits coolant from draining, i.e. CCFL occurrence, therefore the upper debris bed is the CCFL dominant region (Abe and Adachi, 1994; Rashid et al., 2012). The heat transfer deterioration due to inadequate coolant greatly increases the local temperature in the debris

bed. Corium with sufficient temperature can melt concrete, which can cause severe radiation leakage and environmental pollution. A criterion has been generally accepted that dry-out should not occur locally for successful long-term cooling in debris bed. Therefore, it is necessary to better understand the coolability of the debris bed through debris bed CCFL studies. These studies can inform the nuclear community on how to better design the reactor structures / operating regimes and to help prevent melt-through accidents from happening.

The debris bed formation was already experimentally investigated in the DEFOR test facility (Karbojian et al., 2009). In the experiment, simulant melt material was poured onto water. High temperature liquid melt was delivered into the coolant tank, and the debris bed was formed after mixing (Karbojian et al., 2009). The formed debris bed has very complicated structure which can be described as mixture of particles in rough shapes, with particles contacting and not contacting. Each flow channel formed among particles is around the *mm* scale, but has very rough shape and can be partially blocked by bed structures as well. Moreover, the flow channels are also connected with each other. This brings lots of challenges in the measurement of flow parameters. On one hand, only temperature, coolant volume, size etc can be obtained, which do not require devices to intrude the formed bed (thermocouples were pre-set before the debris bed was formed). However, flow rate and pressure gradient in the formed debris bed cannot be measured and thus CCFL studies in debris bed cannot be conducted in the same way as other CCFL experiments. On the other hand, a geometry duplicating the real debris bed shape is almost impossible to draw because none of the flow channels can be described as a regular shape, even not a cross section. Lastly, with enough pressure in the vapor such that can overcome the suppression from the coolant pool above the bed, the top side of debris bed particles can also be pushed aside by the vapor (Lipinski, 1984). Under such scenario, the debris bed study is complicated from a two-phase problem of steam-coolant

counter current flow into a three-phase problem of steam, coolant, and solid particles all with movements.

The debris bed geometry challenge cannot be resolved, and approximations are necessary in domain design to study the CCFL and dry-out mechanisms. For instance, the experiments for the debris bed CCFL are mainly conducted in a mock debris bed packed by small particles in a mocked pressure vessel (for instance a cylindrical tank) with sensors distributing around the tank (Abe and Adachi, 1994; Abe and Sudo, 2006; Rashid et al., 2012; Repetto et al., 2013). The particles are of a character length 1 – 5 mm or similar sizes (Fichot et al., 2006) and usually more obtainable materials, such as glass, stainless steel, or alumina, are used for particles to replace relocated corium in the reactor debris bed (Abe and Adachi, 1994; Rashid et al., 2012). In these experiments, global and local flow parameters can be measured or indirectly computed, such as the overall pressure gradient, void fraction, vapor superficial velocity etc, for model improvement purpose. One major effort is on the friction law development. Some researchers measure the pressure gradient at CCFL condition which can inform friction law in system code development (Rashid et al., 2012). Other researchers proposed friction factor correlations (Abe and Sudo, 2006), which then was validated by their experimental data. In Rashid's experiment, pressure gradient at CCFL appears to reduce with the vapor superficial velocity when  $j_g < 0.2m/s$  under system pressures of 1-5 bar. They also found that under most of the CCFL condition, dynamic pressure gradient ( $dp/dz$ ) is less than the hydrostatic pressure gradient of coolant ( $\rho_l g$ ) (Rashid et al., 2012).

It is worthwhile to mention that the CCFL definitions in debris bed experimental studies are also different based on if boiling exists. If water and air are used as working fluids, CCFL determination is similar to that in the classical CCFL studies discussed in Section 1.1.1 (Abe and Sudo, 2006). However, if the mock debris bed is heated up, the onset CCFL cannot be measured

due to the lack of two-phase dynamics information in the bed. Instead, dry-out is used as a criterion and determined when an appreciable fast temperature increase happens in the bed (Rashid et al., 2012). Since local debris bed surface becomes dry when nearby coolant is completely evaporated, from a progression perspective, dry-out happens slightly later than CCFL occurrence (Lipinski, 1984).

In order to develop usable model with unknown two-phase flow dynamics inside the debris bed channel without the two-phase fluid dynamics information, one research effort was the approximation of an individual debris bed channel. An annular flow model was previously developed for debris bed channel estimates of the velocity profile and radial shear stress at CCFL, which treated the debris bed channel as a pipe (Abe, 1995). For debris bed particles larger than 3 mm, the overall behavior of CCFL in the debris bed can be estimated by the annular flow model. The validity of the simplified annular flow model is also experimentally proved by validating the interfacial and wall shear stresses derived from it (Abe and Sudo, 2006). Another model development effort was treating the debris bed as a one-dimensional (1D) porous medium (Lipinski, 1984). With this premise, the mass, energy, and momentum conservation equations can be combined with models which were applicable for spherical porous media, such as capillary force, friction loss, and evaporation models. Then, the combination yields a first-order differential equation, which can be numerically solved to analyze the debris bed coolability along the elevation (Lipinski, 1984).

Other research on debris bed caters to the need to Fukushima accident, which focuses on the seawater coolability on the debris bed (Franken et al., 2019; Ahmed et al., 2019). The debris bed is also approximated by packed solid particles, and Lipinski's 1D model was used to complete the scaling analysis (Ahmed et al., 2019). The major difference between seawater and regular coolant

water in the debris bed cooling is the solubility of the liquid. In seawater, mass diffusion is slower than thermal diffusion, also the salts in sea water decreases contact angle on the heated debris bed surface, therefore the bubble departure diameter is reduced, which affects the boiling behavior significantly. The pressure drop is also lower due to the smaller bubble sizes, which yields the two-phase flow a more homogenous mixture (Franken et al., 2019). However, those bubble-seawater dynamics cannot be observed in the debris bed, and the conclusions were drawn from a high resolution experiment on a heater immersed in the sea water to inspire the boiling behavior in the debris bed when cooled by the sea water (Franken et al., 2019).

The CFD topics on debris bed studies include the pressure drop across the debris bed (Azam et al., 2018), the debris bed particle sedimentation (Hwang et al., 2019; Li, C. et al., 2021), and heat transfer performance in severe accidents (Dutt et al., 2020), etc. However, CCFL was not studied most likely restricted by computational cost. Simplifications in CFD studies were often used for more affordable simulations, i.e. the porous media and the cluster cell treatments (Azam et al., 2018; Chakravarty et al., 2019; Hwang et al., 2019; Li, C. et al., 2021). For instance, the study which involves the pressure drop across the debris bed treats the bed as a porous media (Azam et al., 2018), but it does not resolve the debris bed channel. The cluster cell conception is similar to porous media, but the simplification is splitting the debris bed into cluster cells (Hwang et al., 2019; Li, C. et al., 2021). Each cluster cell includes multiple particles, therefore, the spatial discretization does not need to be smaller than the particle size, instead just need to resolve the cluster cell. Only a couple of mesh elements across each cluster cell was used, which greatly saves the computational cost (Li, C. et al., 2021). With the cluster cell approximation, even the particle sedimentation for a whole debris bed can be affordable (Hwang et al., 2019). For CFD simulations which resolves the debris, only heat transfer is investigated for suspended debris (exposed fuel

channels) in a pure steam environment (Dutt et al., 2020), rather than the debris bed formed by relocated corium. Researchers found that with only 1% decay heat, the suspended debris will not melt down (Dutt et al., 2020).

In conclusion, no researchers have explored the micro-scale two-phase flow phenomena inside the debris bed in depth. Additional issues including the inability to experimentally study the flow behaviors due to the complex flow geometries, as well as high temperature environments. CCFL in the debris bed was not studied with the CFD approach either. Therefore, the details of counter-current flow in micro flow channels/gaps of the debris bed need to be revealed. No existing published result show the flow regime or evaluate the coolability inside the gap of the debris bed. High resolution interface capturing simulations can be an ideal tool to study the CCFL phenomenon inside the debris bed.

#### **1.1.4 Direct numerical simulation of CCFL**

DNS is a first-principle based simulation approach, which directly solves Navier-Stokes equations with adequate spatial and temporal resolutions to capture all flow scales of interest. DNS approach is the best approximation for experiments among all other types of simulation scales for single and two-phase flows. DNS results have, in previous instances, consistently agreed well with the experimental data, which often can be treated as the virtual experiment (Rodriguez et al., 2013; Behafarid et al., 2015; Zimmer, Matthew D. and Bolotnov, 2019; Zimmer, Matthew Daly, 2020). Though the computation cost of DNS is very high, the recent development of high-performance computing capabilities provides sufficient resources to conduct DNS in wider range of conditions. Therefore, it is more affordable and desirable to use DNS for research purposes to gain better understanding of the physical phenomena and use it (in addition to available experimental data) to develop and calibrate models for system-level codes. Utilizing DNS in studying the CCFL has

three major advantages compared to the multiphase computational fluid dynamics (M-CFD) models. DNS has the ability to extensively reveal and visualize the flow regime in the flow channel even at the Kolmogorov scale (the smallest turbulence scale). In addition, DNS can also build a high-resolution database for M-CFD and system-scale codes on CCFL, meaningfully reducing the prediction uncertainty in those simulations.

#### **1.1.5 Knowledge gap**

Despite the significant progress achieved by experimental studies and analytical analysis on large scale CCFL, the correlations cannot be directly utilized in small scale studies. This includes the equations developed by Wallis (Wallis, 1969) as well as by Zapke and Kroger (Zapke and Kröger, 1996), which are based on centimeter-scale CCFL experiments. As for the two-phase configurations categorized into the CCFL flow regime map, the experimental mechanisms were still studied under the large scales (Dukler and Smith, 1977). Even for modern experiments conducted after 2000 (Gallego, 2004; Vierow, 2008), decimeter-scale facility were still dominantly used. Currently, there are only a handful of publications of CCFL experiments at the millimeter scale. For the published work investigating millimeter two-phase counter current flow, the information does not adequately inform on the debris bed channel CCFL phenomenon (Fukano and Kariyasaki, 1993; Rapolu and Son, 2007; Jeong, 2008). Apart from lacking experimental studies, the two-phase flow interaction and its physics of CCFL at a small scale has also not received adequate attention.

Even if small scale CCFL experiments can be conducted, certain limitations also exist for millimeter scale CCFL experiments such as the difficulties in measurement and visualization. The experimental data collected for flow rates and pressure drop in small scales are often with higher uncertainties compared with large scales (Rapolu and Son, 2007). Capturing subtle interface

topology changes is already a challenge, but if the channel wall is heated, transparent material is typically changed to stainless steel thus visualization is impossible (Vierow, 2008). Last but not the least, the surface tension effect becomes more significant as channel size decreases. However, any small amounts of impurities act as a surfactant can change the effective surface tension which in turn affects the interfacial forces and topology in CCFL (Wesselingh and Bollen, 1999).

Last but not the least, the occurrence of CCFL is not universally well defined among different studies; some of the definitions are even contradictory to each other. For instance, Hewitt and Wallis define that gas phase velocity at CCFL is a value which carries liquid upwards beyond the liquid injector consistently (Figure 1.1), rather than when flow reversal happens (Hewitt and Wallis, 1963). However, Govan et. al. did not have this requirement for liquid carried beyond the injector consistently. In their definition, liquid may partially flow downwards (Govan et al., 1991). Also contradictory to Hewitt and Wallis, Gallego defines CCFL occurrence to be when flow reversal happens (Gallego, 2004). Aside from those definitions, significant variation in pressure gradient with gas phase velocity is also an indicator for CCFL to happen (Vijayan et al., 2001; Vierow, 2008). It is understandable that under different experimental facility setup and device measurement restrictions, researchers have had to propose criterion on CCFL based on their specific experimental conditions. However, the corresponding application ranges are indeed narrow due to specific experimental conditions (Höhne et al., 2012). Moreover, the lack of universal definitions results in incoherent understanding of the physics of CCFL and brings additional difficulty for the validation of CCFL simulations.

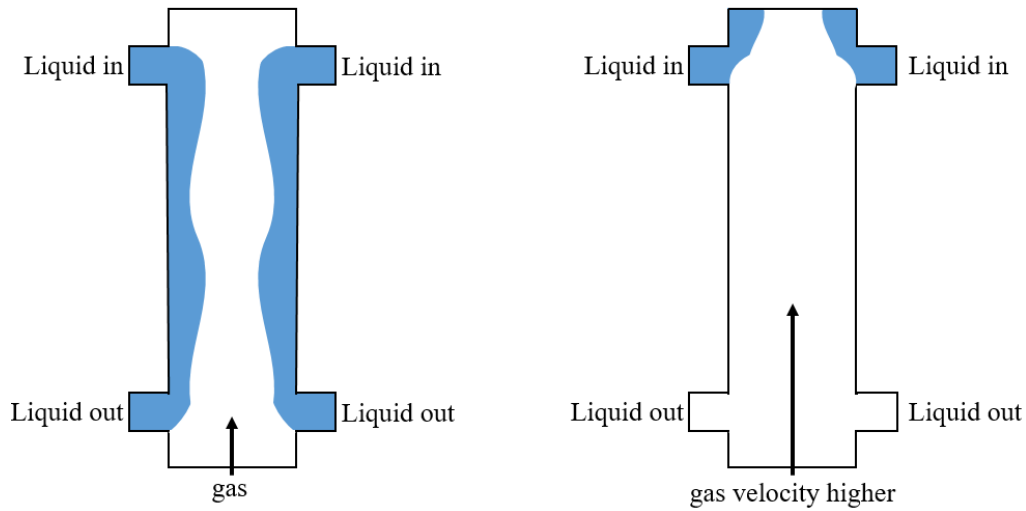


Figure 1.1. Illustration of liquid being carried beyond injector.

DNS coupled with interface capturing method is capable to address the above challenges. Numerically, the onset of CCFL can be defined as zero flow rate of either phase, which will be consistent even for different flow conditions. Specifically, for nuclear reactor application, CCFL occurrence corresponds to zero flow rate of the liquid phase. This definition is proposed to describe the critical condition and illustrated in Figure 1.2. If steam velocity is slightly lower, then the coolant is still draining down (pre CCFL); if steam velocity is slightly higher, then CCFL already happened and coolant is moving upwards (post CCFL). Only in the middle of those two conditions, steam is still moving up but liquid velocity is zero, which corresponds to the CCFL occurrence.

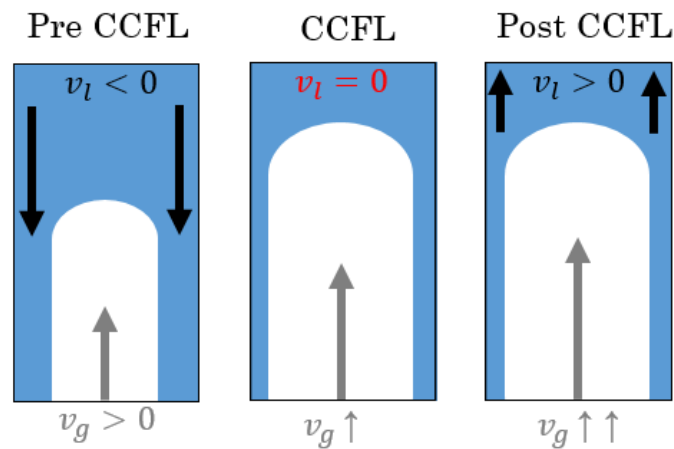


Figure 1.2. Illustration of CCFL criterion when liquid velocity is zero ( $v_l = 0$ ).

Besides applying a universal CCFL criterion in DNS studies (zero coolant velocity), there are other advantages of study CCFL using DNS coupled with interface capturing method. With an adequate spatial discretization, accurate measurement and high-resolution visualization can be obtained, including but not limited to, in-situ velocities of liquid or gas phase, pressure, and the interface topology. Although simulations naturally have specific sources of uncertainties compared with experiments, for instance, discretization error, the parameters can be accurately assigned. Therefore, the uncertainties on pressure drop, phase velocity, and surface tension in experiments can be eliminated by specifying appropriate values in boundary conditions and material properties in simulations. With PID control theory integrated into CCFL studies, it is more efficient to determine the occurrence of CCFL, and thus influential factors can be well-studied such as channel sizes, vapor/liquid densities, surface tensions, and interface topologies. Specifically, the pressure gradient obtained from PID control can be very accurate under zero liquid flow rate. Pressure gradients has been a key parameter measured in experiments to predict CCFL occurrence which strongly connects to dry-out in debris bed. Similar to steam velocity increasing with debris bed height, pressure gradient also follows this trend. Pressure gradient is also a significant parameter to determine the two-phase flow pattern in the flow channel (Abe and Adachi, 1994). However, there was no appropriate model developed for predicting pressure gradients (Park et al., 2016). The obtained pressure gradient can be beneficial as an accurate verification resource for future model developments.

The trustworthiness of PID controlled CCFL simulations depends on the accuracy in the interfacial forces and topology, and the reliability of PID control. PID related concerns can be addressed by the verification, accuracy and robustness tests of the developed PID controller. Other concerns can be addressed by validated and verified unit problems though single bubble studies.

## 1.2 Overview of bubble studies

The bubble interfacial force and topology evolution studies are foundational for the V&V of CCFL interface capturing simulations. This section introduces the bubble studies under natural conditions and under control. Specifically, the bubble studies under PID control are presented which was an inspiration for integrating PID theory into CCFL studies.

### 1.2.1 Bubble interfacial force studies

Interfacial forces play a pivotal role in the two-phase phenomena in nuclear reactor systems. There are typically identified five interfacial forces (drag, lift, wall, virtual mass, and turbulent dispersion forces (Ishii, Mamoru, 1990)). Among them, drag force is generally considered one of the most important as it governs the bubble's terminal velocity and hence the gas-liquid momentum transfer. Lift force has significant impacts on determining the void fraction distribution in reactor subchannels and affects predictions of the departure from nucleate boiling (DNB) in reactor thermal-hydraulic analysis. Wall force is the most influential if the bubble is near wall and the net sum of the wall and lift forces dominates the bubble migration direction. The following introduction illustrates the interfacial forces in more detail.

#### 1.2.1.1 Lift force

Lift force for a single bubble in shear flow can be modeled (Tomiyama, Akio et al., 2002) as:

$$F_L = -C_L V_b u_r \frac{du_l}{dy} \rho_l \quad (9)$$

In the definition,  $C_L$  is the lift coefficient,  $V_b$  is the bubble volume, and  $Sr = du_l/dy$  is the liquid velocity gradient or shear rate. The sign of  $C_L$  is deterministic of the bubble migration direction. In initial lift force models, the lift coefficient  $C_L$  was assumed to be a constant (Moujaes and Dougall, 1985). In subsequent models,  $C_L$  was treated as a variable to explain the effect of lift

force on bubble migration behavior. Corresponding models were proposed in both numerical (Legendre and Magnaudet, 1998) and experimental (Tomiyama, Akio et al., 2002) studies. Tomiyama's study revealed the strong effect of bubble deformation on the migration direction. However, it is difficult to evaluate the effect of shape distortion for each individual bubble in the bubbly flow model. In recent lift force model proposed by Shaver and Podowski, the bubbles were still assumed to be spherical even for deformable bubbles with diameter of 2.5 mm (Shaver and Podowski, 2015). Although  $C_L$  was modified to vary with the distance to the wall, this model still under-predicted the void fraction compared to existing experimental data (Wang K. et al., 1987). While multiphase flow is a very complex and non-linear phenomenon, we believe the improvement of the lift force model by considering bubble deformation may significantly help to improve the predictive capabilities of CFD scale models.

#### **1.2.1.2 Wall force**

In a two-phase upflow conditions, spherical bubbles tend to migrate towards a channel wall under the effect of lift force. Meanwhile, the wall force keeps the bubble at some distance away from the wall (Antal et al., 1991). Therefore, void fraction profiles demonstrate a peak near the wall, but zero at the wall. The wall force is reduced to zero at large distances from the wall due to the decreasing wall effect experienced by the bubble. In Antal's analysis, the expression of the wall force was combined with the lift force equation and was used to predict void fraction distribution. The resulting void fraction distribution achieved a good agreement with the previous experimental data. However, existing models on lift and wall forces still need to be improved for the near wall region. The recent models yielded good transverse void fraction distribution in the bulk of the flow channel, but resulted in peaking and flattening void fraction profiles near the wall for adiabatic flows (Shaver and Podowski, 2015; Sugrue et al., 2017). Such distribution was due

to the lack of wall repellent effect in the vicinity of the wall, which needs improvement to eliminate the disparity with the realistic void fraction distribution.

### 1.2.1.3 Transverse force

It is well recognized that  $C_L$  for a spherical bubble is positive, however it can be negative for deformable bubbles (Tomiyama, Akio et al., 2002). Figure 1.3 illustrates the lift force change on bubble depending on deformability, where  $x$  and  $y$  denote streamwise and transverse directions, respectively. If the wall existence is neglected,  $F_L$  obtained by Eq. (9) directs to the positive  $y$  direction as Figure 1.3 (a) depicts. As the bubble becomes more deformable,  $C_L$  and the corresponding  $F_L$  will change the sign. Adding the wall causes the interfacial forces on the bubble to be more complex (Figure 1.3 (b)). Both the bubble deformation and the wall existence will induce the net lift force,  $\vec{F}_L + \vec{F}_W$ , to change direction.

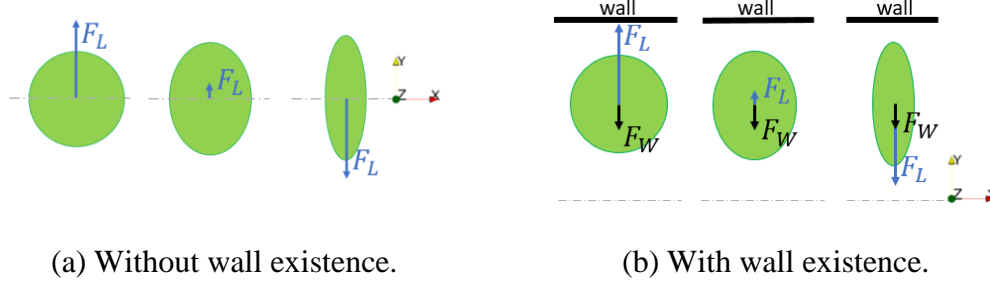


Figure 1.3. Illustration of the lift force change on the bubble with different deformation. The wall existence is neglected in (a) but considered in (b). The wall force is a constant when the  $L/D$  remains unchanged.

Since lift force and wall force act on the bubble in transverse directions, the net force can be a representation of migration behavior. Analogous to the lift coefficient  $C_L$ , a transverse coefficient  $C_T$  can also be used to demonstrate the effects of fluid motion, bubble deformability, wall distance, and shear rate on interfacial forces. The sign of  $C_T$  determines the direction of  $F_T$ , thus the bubble migration direction.

$$F_T = |\vec{F}_L + \vec{F}_W| = -C_T V_b u_r \frac{du_l}{dy} \rho_l \quad (10)$$

### 1.2.2 Complex bubble topology studies

Complex bubble topology studies were reviewed in a published journal paper (Fan et al., 2021). Bubble deformation is a ubiquitous phenomenon in gas-liquid two-phase flow and has significant impacts on various interface related flow physics. For example, bubble induced turbulence has distinct characteristics from particle induced turbulence. Given specific bubble deformability, the existence of bubbles can either augment or suppress local liquid turbulence (Gore and Crowe, 1989); in other words, the turbulent intensity change depends on the bubble distortion level (Feng and Bolotnov, 2017b). In addition, the bubble deformation also plays an important role in determining bubble interfacial forces, such as drag force, lift force, and virtual mass force (Bhaga and Weber, 1981). Severe deformation may result in bubble break-up, which leads to more complex flow regimes. One such example is the slug bubble during the slug-to-church flow regime transition (Zimmer, Matthew D. and Bolotnov, 2019). As the gas flow rate increases, satellite bubbles are teared off from the slug bubble which contribute to the interface instability and eventually trigger the transition. Fundamental studies on bubble topology evolution could help reveal the underneath mechanisms and produce improved predictive models. This in turn will lead to optimized engineering designs (e.g. nuclear, thermal, and chemical reactors) and industrial processes (e.g. purification of polluted water, and the charging of plasma bubbles) where bubble topology evolution play a pivotal role (Guillen et al., 2018; Yamatake et al., 2007).

A considerable amount of literature has been published on the experimental studies concerning bubble deformation (Bhaga and Weber, 1981; Sharaf et al., 2017). Bhaga and Weber injected the air bubble in aqueous sugar solution and the various liquid viscosities were obtained by solutions of different concentrations (Bhaga and Weber, 1981). The photos of bubble deformation and the

streamline in the wake region have become classical references for two-phase flow model development and validation (Sussman, Mark et al., 2007; Tripathi et al., 2015). As an extension of the numerical study conducted by Tripathi et al. (2015), Sharaf et al. (2017) performed an experimental investigation with high-speed camera and a satisfying agreement was reported between experiments and the corresponding simulations. Despite the significant progress achieved by experiments, certain limitations persist. Examples include the availability of working fluid properties, fine control of experimental conditions as well as measurement uncertainties.

Although Bhaga and Weber's experiments covered an adequate range of flow conditions (e.g. Eotvos number, Morton number and Reynolds number) to produce a bubble deformation map, the parametric exploration is primarily achieved by altering the liquid viscosity with varying concentration of the solutions. With almost unchanged surface tension, liquid density and gas parameters, they were not able to capture the bubble break-up phenomenon which is more sensitive to surface tension (Bhaga and Weber, 1981). The experimental conditions are hard to control at constant values in two-phase studies. To simplify the measurement of fluids, all of the aforementioned experiments require liquid to be stagnant when bubble rises up, which limits the research scope into purely gravity-driven. However, it is rarely the case in engineering applications. As bubbles and liquid are moving together, the inertia of bubble could be sometimes more dominant than gravity (Ishii, M. et al., 2004). Although experimental data remains the major knowledge source on two-phase flow physics, the uncertainty quantification (UQ) of measurements is still challenging and the UQ analysis is often lacked (especially in legacy experimental studies). Bubble columns are usually built with fixed height, thus for fast-rising bubbles it is hard to determine if bubbles reached steady state at the observation section.

Consequently, the measured bubble terminal velocity generally has higher uncertainty than other experimental parameters.

Meanwhile, numerical simulations have grown into an attractive investigation approach to compensate the shortcomings of experiments. Any working fluid and physical condition could be readily represented by changing material properties and initial/boundary conditions. In particular, 3D interface resolved simulations can provide all the quantities of interest in bubble dynamics studies, such as bubble topology changes, velocity and pressure distributions, flow field streamlines, etc. Sussman et al. (2007) reproduced nearly identical deformable bubbles in the experiments with a high-order interface capturing method. Tripathi et al. (2015) computationally investigated bubble deformation and break-up with wide-ranging fluid properties. Their simulations revealed that bubble topology is not only affected by fluid properties, but also strongly dependent on bubble sizes.

### **1.2.3 Experimental controlled bubble studies**

Bubble terminal velocity ( $u_t$ ) is a significant parameter in both interfacial force and interface topology studies. Traditionally,  $u_t$  was measured when a rising bubble in the liquid eventually achieved a uniform motion. This approach was straight-forward but the uncertainty quantification was challenging and lacked in many legacy experimental studies. It also required the experimental bubble column or the computational domain to be adequately tall for bubbles to achieve  $u_t$ .

In recent years researchers have been using a new approach to study bubble-liquid interactions by reversing the movements of the bubble and the liquid (Dueñas, 2019; Salibindla et al., 2020). Instead of letting the bubble rise freely in the stagnant liquid, they inject the liquid downward towards the bubble, so the bubble rising movement is restricted. Considering the liquid and bubble velocities are opposite, this is also one of the counter current two-phase flow phenomena.

With such new approach, Dueñas at Oregon State University (OSU) utilized particle image velocimetry (PIV) to track the velocity of rising ellipsoidal bubbles and developed improved drag coefficient ( $C_D$ ) models (Dueñas, 2019). OSU researchers also explored the complex bubble topology inspired by the DNS studies of Tripathi et al. (2015). Salibindla et al. covered a large range of the bubble diameter from 0.5 mm to 10 mm and provided corresponding bubble rise velocity, liquid injection velocity, and lift coefficient (Salibindla et al., 2020). They also studied drag behavior under bubble Reynolds number ( $Re_b$ ) from 10 to 5000 and demonstrated that as  $Re_b$  exceeds 400, the large bubble shows systematically lower  $C_D$  in intense turbulence.

The control methodology in the experimental studies has many advantages. To begin with, if the liquid injection rate is appropriately adjusted to be the expected bubble terminal velocity, the bubble mass center can be stagnant in the test section. With such approach, the uncertainty quantification (UQ) of  $u_t$  becomes the UQ of liquid injection rate and setting up the experimental facility is easier. Also, the test section does not need to be fabricated very tall. Lastly, the camera can be installed at a fixed position focusing on the bubble behavior and the liquid motion in the vicinity.

#### **1.2.4 PID controlled bubble studies**

PID bubble controller was previously implemented in PHASTA code to control the bubble at a proposed position (Thomas et al., 2015; Feng and Bolotnov, 2017c). Similar to the experiments (Dueñas, 2019; Salibindla et al., 2020), liquid is also injected from the inlet plane towards the bubble. Therefore, it is also representing a counter current two-phase flow. This reverse process is equivalent to switching the reference frame from the container to the bubble. The two reference frames, the mass, momentum, and energy are invariant (McComb, 1999), so interfacial forces and topologies should not change either.

PID bubble controller has been used for bubble interfacial force studies in uniform flow and shear flows. For small size bubbles (diameter  $D = 1mm$ ), the drag coefficients obtained from the PID bubble controller achieved nearly identical magnitudes with the experimental  $C_D$  correlations varied with  $Re_b$  in uniform flows (Thomas et al., 2015). As for medium size bubbles ( $D = 3.52mm$ ), the lift and drag coefficients in viscous shear flows and turbulent flows agree well with previous experimental studies (Feng and Bolotnov, 2017c).

The wall effect is difficult for most experimental and numerical studies because the distance from the bubble and wall is a variable. PID bubble controller removes such challenge by fixing the bubble at a specific distance to the wall. The transverse force at wall distance equal to bubble size was validated and verified for viscous shear flows (Feng and Bolotnov, 2017a). The correlation of  $C_T$  was established with regard to  $Re_b$  and Weber number ( $We$ ) at a wall distance equal to bubble diameter ( $L/D = 1$ ) (Feng and Bolotnov, 2017a):

$$\begin{cases} C_T > 0, \text{ if } Re_b - \left[ 30 + 0.6 \exp\left(\frac{4}{3}We\right) \right] < 0 \\ C_T < 0, \text{ if } Re_b - \left[ 30 + 0.6 \exp\left(\frac{4}{3}We\right) \right] > 0 \\ C_T = 0, \text{ if } Re_b - \left[ 30 + 0.6 \exp\left(\frac{4}{3}We\right) \right] = 0 \end{cases} \quad (11)$$

This correlation is based on the bubble simulation with a diameter of  $1.76mm$  in a viscous shear flow with shear rate of  $3.8s^{-1}$ . The sign of  $C_T$  corresponds to the bubble migration direction. A migration curve at the same  $L/D$  was then proposed which separates the opposite directions of the transverse force, which is also the mathematical expression for  $C_T = 0$  in Eq. (11). The curve is replotted in Figure 1.4, where red triangles denote transverse force pointing to the wall, reflecting bubble migrating to the wall; blue triangles are opposite where the transverse force points to the center of the channel, indicating that more deformable bubble tends to be repelled from the wall.

$$Re_b = 30 + 0.6 \exp\left(\frac{4}{3}We\right) \quad (12)$$

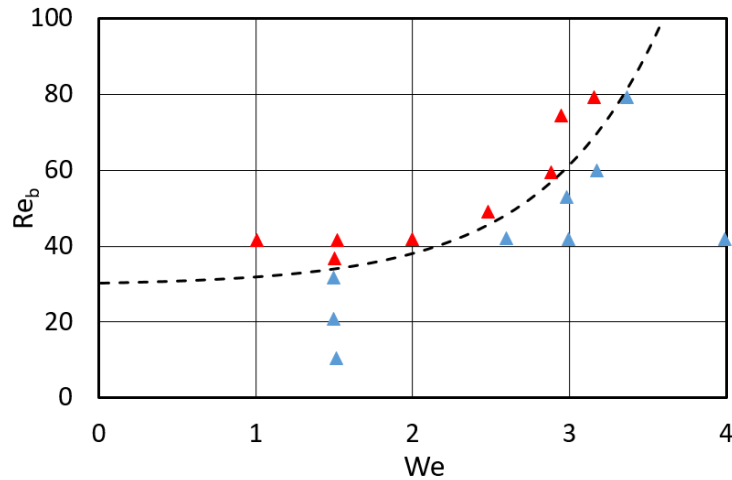


Figure 1.4. Migration curve at  $L/D = 1.0$  from Fig. 19 of Feng and Bolotnov’s publication (Feng and Bolotnov, 2017a).

The challenge of bubble in high shear is the non-identifiability of the interfacial forces under effects of both shear and shear-generated turbulence. In traditional studies, if a laminar high-shear velocity field is applied to the inlet of a flow channel, the transition to turbulence regime will affect the bubble motion as well (Figure 1.5). With the leverage of PID bubble controller, a laminar high-shear flow can be applied in a streamwise short domain (red box in Figure 1.5 which is equivalent to the inlet segment of a turbulent channel). Therefore, the sole effect of high-shear on the bubble can be investigated without the disturbance of turbulence.

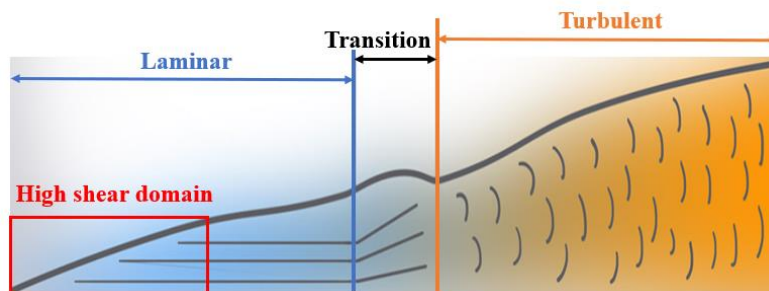


Figure 1.5. Illustration of high shear domain setup compared to a turbulent channel.

Such simulation was conducted using the PID bubble controller for a small bubble ( $D = 1 \text{ mm}$ ) and it revealed that drag increases by shear rate ( $Sr$ ) but lift decreases when  $Sr$  exceeds  $75/s$  (Thomas et al., 2015).

As for the investigation of bubble topology evolution, PID bubble controller with the support of unstructured meshes are particularly suitable. It is reported by previous DNS and experimental studies that some bubbles with severe deformation also have complicated travel trajectories (Tripathi et al., 2015; Sharaf et al., 2017). The trajectories vary with fluid conditions thus determining the size of computation domain and the mesh resolution is a process of trial-and-error. A more common practice is to refine all the regions where bubbles could possibly travel, which may lead to exceedingly large computational costs. However, with the PID bubble controller, bubbles would only vibrate initially in the vicinity of and eventually settle down at the prescribed control location, which significantly reduces the size of mesh refinement zone and thus the computational costs. Moreover, due to the bubble movement, a conventional investigation would have to realign the bubble center before comparing the relative interface topology change at different time stages (Tripathi et al., 2015; Sharaf et al., 2017). With the PID bubble controller, this burdensome task can be totally avoided because the bubble has a fixed steady-state location. With the support of unstructured mesh, an optimized computational mesh can be easily created with additional mesh refinement only around the bubble control location. Furthermore, accurate three-dimensional (3D) bubble shape are extremely difficult to obtain in experiments. Cameras could only take two-dimensional (2D) photos, thus most studies have to assume bubbles to be axisymmetric which is only applicable for simply deformed bubbles (Dueñas, 2019). Even with tomography technique to reconstruct the 3D bubble shape, the accuracy still depends on the

rotation speed of camera, the strength of received signal from the sensors, and the selection of back projection algorithms (Utomo et al., 2001).

### **1.2.5 Knowledge gap**

Despite the progress in bubble interfacial force and topology evolution studies, there still remains the wall effect as well as complex deformation to be further investigated. PID bubble controller tackles lots of involved challenges such as fixing the wall distance, applying a laminar shear flow, and fully resolving bubble topology by pre-designed mesh. Therefore, many knowledge gaps can be filled through PID controlled bubble studies.

Current wall affected transverse force study only has one specified wall distance completed (Feng and Bolotnov, 2017a). Further investigation is needed to include more distances from the bubble to the wall to comprehensively establish effect on the transverse force. The bubble topology obtained from PID bubble controller are all slightly deformed (Thomas et al., 2015; Feng and Bolotnov, 2017c), therefore complex topology evolution needs to be further verified and validated. Lastly, since single bubble in liquid is also a counter current flow, mesh study for the bubble is also required to provide references for spatial resolution to well resolve the CCFL interfacial shear and interface topology.

The above fundamental bubble studies will build confidence that CCFL is driven by the correct interfacial forces and that the interface topology is also correct. The work also improves the closure laws of interfacial forces and contributes to the development of M-CFD closure models.

## **1.3 Validation hierarchy**

Counter current flow in this dissertation is studied based on two topics; CCFL in the debris bed and the PID-controlled single bubble studies. Specifically, the controlled bubble simulations, are fundamental for studying more complex CCFL flow characteristics in the debris bed channel.

First, the interfacial forces for CCFL and bubble are connected. Interfacial shear on the interface governs the condition of counter current flow. In essence, interfacial shear is the drag between liquid and gas phases and CCFL is achieved when wall shear, interfacial shear, and gravity are balanced. Similarly, drag force is also one of the most important interfacial forces for the bubble liquid flow, and in the vertical direction a bubble reaches steady state when the drag forces and gravity are balanced. Besides from the force balance, the drag force on bubble is essentially integrated interfacial shear, and thus correct drag prediction capability is an essential condition for correct interfacial shear prediction. The second similarity between controlled bubble and debris bed CCFL is that the velocity scales are very similar. CCFL in the reactor pressurizer surge line or hot leg can happen under turbulent conditions, but in the debris bed the coolant flow is expected to be laminar. Even though the secondary flow can form around the complex geometry in the debris bed channel, integrated coolant flow approaches zero velocity when CCFL occurs. As for steam, generally the average steam velocity can be lower than  $1\text{ m/s}$  which is very similar to the single bubble velocities. If compared in dimensionless number, the Reynolds number of a pure steam debris channel is approximately 6.0~60.0; the bubble Reynolds number in single bubble studies is in a similar range of 5.0~80.0. Lastly, aside from the similarity in velocity scale, debris bed CCFL can also form the interface topology as the single bubble flow. Given the diameter of debris bed is in millimeter scale, steam bubble can form especially when the void fraction is low. Here, the surface tension is under approximately 3 atm during the debris bed formation so the Weber number for the formed steam bubble is approximately 6.0, which is a typical value in deformed single bubble studies as well. Therefore, for each steam bubble formed in the debris bed channel, it can be investigated using a similar methodology as to single bubble flow studies.

Validation hierarchy in Figure 1.6 illustrates that bubble simulations as fundamentals for more complex CCFL flow characteristics, especially in the scale of the debris bed channel. For all the interface involved numerical features (i.e. interfacial force and interface topology), preliminary single bubble simulations provide foundational evidence for debris bed CCFL as well as validation, verification, and uncertainty quantification. Specifically, these supportive studies help to ensure that the debris bed CCFL results from the most innovative PID pressure gradient controller are trustworthy. To begin, bubble interfacial force studies are necessary to demonstrate that the interface is well-resolved (Section 4.2). It is necessary to include shear flow conditions in the bubble study to illustrate the relationship between bubble interfacial forces and interfacial shear to support CCFL flow characteristics. Furthermore, verified and validated complex bubble deformations under PID-bubble controller supports the more complicated topology change in CCFL under the PID control (Section 4.3). Finally, accurately controlled annular flows are necessary to verify the PID pressure gradient control to generate the desire flow rate (Section 3.3). The presented research is conducted under adiabatic conditions. While heat transfer is not solved, the results determined for CCFL condition are still acceptable. Previous investigation revealed that under both adiabatic (air-water) and boiling (steam-water) conditions CCFL occurs at similar velocities (Vierow, 2008).

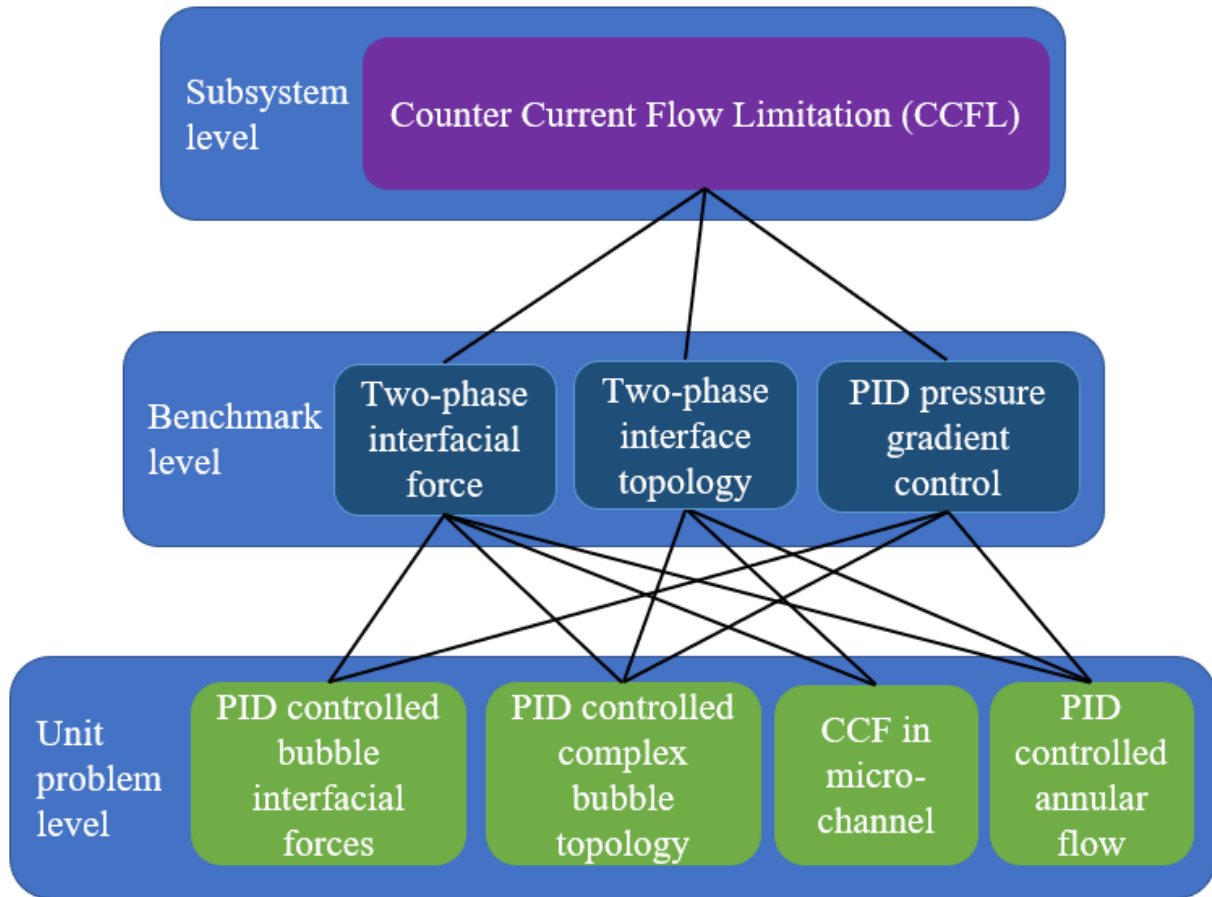


Figure 1.6. Validation hierarchy.

#### 1.4 Major Research Objectives

The presented research aims to inform the knowledge base of CCFL in small scales (debris bed channels) with the integration of control theories. Before 3D DNS on CCFL using level-set method is conducted, the fundamental mechanics behind CCFL requires investigation. This procedure is based on verified and validated studies on two-phase interfacial forces, interface topology, and reliability of PID control. The key research objectives are listed below:

1. **Strengthen the capability of evaluating the interfacial forces through controlled single bubble studies.**

Based on previous interfacial force studies in (Feng and Bolotnov 2018) and (Thomas et al 2015), transverse force needs to be investigated at different distances to the wall to demonstrate the capability of PID bubble controller in computing the interfacial forces.

Previous studies conducted by PHASTA were for minor deformations with PID (Feng and Bolotnov 2017) and complex deformation without PID (Guillen et al 2019). Therefore, complex bubble deformation with PID needs to be studied to demonstrate the capability of resolving interface topology under controlled condition.

PID gravity control capability will be developed for bubble studies to automatically generate earth gravity for lightly or heavily deformed bubbles rising in liquids. The control on gravity is essential in bubble shape validation and will provide reference for further pressure gradient in PID control.

## **2. Verify and Demonstrate the level-set method capability of solving CCFL in micro channels.**

Debris bed channel is selected as the geometry to conduct CCFL study without PID control. The capability of level-set method on two-phase flow behavior will be demonstrated in previously unanalyzed micro-scale structures. The effect of interface topology initialization, gravity driven/steam velocity driven, and contact angle on CCFL are investigated. This is a fundamental study before implementing the PID control into CCFL studies.

## **3. Develop PID pressure gradient controller to demonstrate integration of control theories into CCFL analysis in debris bed channels.**

The occurrence of CCFL will be defined as the volume liquid phase velocity equal to zero. With such definition, the PID controller can be developed to automatically change the pressure

gradient until the onset of CCFL is achieved. With PID theory integrated into flow rate control, the CCFL occurrence can be obtained more efficiently and accurately.

The following chapters are structured to address the stated objectives: the numerical methods are introduced in Chapter 2 including the basics of PHASTA code and the level-set method; Chapter 3 presents the development of PID pressure gradient controller to achieve CCFL conditions in an accurate and efficient manner. Chapter 4 consists of the bubble studies of interfacial force and topology to address Objective 1; Section 5.1 presents the CCFL study in a micro-channel to complete Objective 2; Section 5.2~5.4 includes the PID controlled CCFL flow regimes in debris bed channel to fulfill Objective 3. The presented studies contribute to fill the knowledge gaps on the closure law development of interfacial forces as well as the CCFL mechanisms in the debris bed channels.

## Chapter 2. NUMERICAL TOOLS

Direct numerical simulation (DNS) has become more affordable with the advancement of high-performance computing (HPC). Interface capturing methods coupled with DNS is a powerful tool to study counter current flow by solving interface evolution with reasonable accuracy. Fluid flow solver PHASTA (Parallel, Hierarchic, higher-order accurate, Adaptive, Stabilized, finite element method Transient Analysis) is utilized for conducting interface capturing studies in the presented research (Jansen, Kenneth E., 1999; Jansen, K. E., 1993). Specifically, the incompressible flow solver in PHASTA has been selected in this work. PHASTA uses the level-set method coupled with the finite element based Navier-Stokes flow solver, which allows to achieve accurate single- and two-phase solutions in simple and complex geometries (Feng and Bolotnov, 2015; Fang et al., 2017). PHASTA has been verified and validated for multiple scenarios, some of them are summarized next.

For large scale simulations, the adaptive refinement mesh capabilities used in PHASTA were verified to successfully capture the waving interface structures of the annular steam/water flow, and to save the computation cost (Rodriguez et al., 2013). As for non-adapted mesh, the two-phase flow-regime transition from slug to churn-turbulent flows agreed well with the existing experimental and analytical results (Zimmer, Matthew D. and Bolotnov, 2019). The nose of the Taylor bubble was well resolved by uniform mesh and can accurately determine the beginning of the flow regime transition. In smaller scale simulations, the large bubble motion in vertical and inclined channels (Behafarid et al., 2015) achieved almost identical results compared to the experimental study (Maneri, 1970). The code-to-code verification between PHASTA and Star-CCM+ (utilizing volume of fluid approach) was also carried out for highly deformed bubble simulation (Guillen et al., 2018). As for the interfacial force estimation for small spherical bubble

(1 mm diameter) under varying shear rates (Thomas et al., 2015), it was validated by experiment-based correlation for the drag coefficient (Tomiyama, Akio et al., 1998), and were verified by simulation results of lift coefficient (Legendre and Magnaudet, 1998).

This Chapter will introduce the governing equations, the level-set method, and the PID bubble controller implemented in PHASTA.

## 2.1 Governing equations in PHASTA

The presented two-phase studies use the incompressible flow solver of PHASTA for the adiabatic conditions (no energy equation is solved in the presented simulations). The governing equations are the incompressible Navier-Stokes equations for mass and momentum conservation. In gas-liquid simulations, the “one-fluid” approach is typically used to describe the two-phase flow fields (Prosperetti and Tryggvason, 2007):

$$\nabla \cdot \mathbf{u} = 0 \quad (13)$$

$$\rho \frac{\partial \mathbf{u}}{\partial t} + \rho \nabla \cdot (\mathbf{u} \times \mathbf{u}) = -\nabla p + \nabla \cdot \mu (\nabla \mathbf{u} + (\nabla \mathbf{u})^T) + \mathbf{f} + \gamma \kappa \delta(\mathbf{x}) \mathbf{n} \quad (14)$$

Here,  $\mathbf{u}$ ,  $\rho$ ,  $p$ , and  $\mu$  are the velocity, density, pressure, and viscosity of either liquid or gas.  $\nabla p$  is the pressure gradient;  $\nabla \cdot \mu (\nabla \mathbf{u} + (\nabla \mathbf{u})^T)$  represents the viscous stress tensor;  $\mathbf{f}$  represents the body force and it is normally gravity force  $\rho \mathbf{g}$ . A finite interface thickness is assumed and the surface tension force  $\gamma \kappa \delta(\mathbf{x}) \mathbf{n}$  is added in the interface region as an additional body force. In the surface tension term,  $\gamma$  is the surface tension coefficient,  $\kappa$  is the curvature.  $\delta(\mathbf{x})$  is the Dirac delta function ( $\delta$ -function), which equal to zero everywhere except for zero and whose integral over the entire real line is equal to one.  $\mathbf{x}$  in  $\delta(\mathbf{x})$  is the interface location, and  $\mathbf{n}$  is the unit normal vector at the interface.

A step Heaviside function  $H$  is typically used to identify different phases.  $H$  is 1 for liquid and 0 for gas. Therefore, the densities and viscosities of the two phases can be described by the step Heaviside function.

$$\rho(\mathbf{x}) = \rho_l H(\mathbf{x}) + \rho_g (1 - H(\mathbf{x})) \quad (15)$$

$$\mu(\mathbf{x}) = \mu_l H(\mathbf{x}) + \mu_g (1 - H(\mathbf{x})) \quad (16)$$

Here,  $\rho_l$ ,  $\rho_g$ ,  $\mu_l$ , and  $\mu_g$  are the densities and viscosities for liquid and gas phases, respectively. In addition, the interface  $\delta(\mathbf{x})\mathbf{n}$  in the surface tension term can be represented by the gradient of the step Heaviside function.

$$\delta(\mathbf{x})\mathbf{n} = \nabla H(\mathbf{x}) \quad (17)$$

It is numerically difficult to compute derivative of the discontinuous Heaviside function  $H(\mathbf{x})$ , thus PHASTA uses the level-set method to replace step Heaviside function  $H$  by smoothed Heaviside function  $f$ , which is easy to implement and increases numerical robustness.

## 2.2 Level-set method

The level-set method is a well-known interface capturing approach (Sussman, Mark et al., 1994; Sussman, Mark et al., 1998; Sussman, M. and Fatemi, 1999), and was implemented in PHASTA for two-phase computations (Nagrath et al., 2005; Nagrath et al., 2006). The level-set function  $\phi$  has negative and positive values in the gas and liquid phases, respectively. The magnitude of  $\phi$  gives the distance to the nearest interface. The interface location thus corresponds to the zero level-set,  $\phi = 0$ . To improve the numerical robustness, the transition of fluid density and viscosity across the interface is described by a smoothed Heaviside function  $f(\phi)$ .

$$f(\phi) = \begin{cases} 0, & \text{if } \phi < -Mh \\ \frac{1}{2} \left( 1 + \frac{\phi}{Mh} + \frac{1}{\pi} \sin \left( \pi \frac{\phi}{Mh} \right) \right), & \text{if } |\phi| \leq Mh \\ 1, & \text{if } \phi > Mh \end{cases} \quad (18)$$

$$\rho(\phi) = \rho_l f(\phi) + \rho_g(1 - f(\phi)) \quad (19)$$

$$\mu(\phi) = \mu_l f(\phi) + \mu_g(1 - f(\phi)) \quad (20)$$

The  $\delta$ -function in the surface tension force ( $\gamma\kappa\delta\mathbf{n}$ ) can therefore be represented by the gradient of the smoothed Heaviside function. The interface normal  $\mathbf{n}$  and the curvature  $\kappa$  are also conveniently computed by the normal vector in the level-set method. The surface tension force is applied as a continuous, three-dimensional effect across the interface rather than being a boundary condition on the interface (Brackbill et al., 1992).

$$\delta = \frac{df(\phi)}{d(\phi)} \quad (21)$$

$$\mathbf{n} = \frac{\nabla\phi}{|\nabla\phi|} \quad (22)$$

$$\kappa = \nabla \cdot \mathbf{n} \quad (23)$$

At each time step the level-set function  $\phi$  is advected with the local velocity  $\mathbf{u}$  calculated from the Navier-Stokes equations followed by a redistancing process (Sussman, Mark et al., 1998). The main advantages of level-set method are: (1) the interface is always determined by the location of  $\phi = 0$ , thus level-set method can naturally capture the change in interface topology during bubble break-up and coalescence events and even the CCFL interface under high interfacial shear; (2) the algorithms are easy to implement, and the normal and curvature of the interface can be calculated accurately based on the gradient of  $\phi$ ; (3) coupling the level-set method with finite element analysis and unstructured meshes is advantageous in complex geometries and 3D simulations. There is one major disadvantage of the level set method, that the advection of  $\phi$  is not mass conserved. Increasing the spatial discretization can reduce the mass loss. As PHASTA simulations typically involve very fine meshes, the mass conservation issue can be efficiently mitigated.

The counter current flow limitation (CCFL) condition was traditionally obtained by trial and error, specifically in experimental studies. Researchers would change the flow rate by adjusting gate valves located after the pump in order to obtain the desired flow characteristics (Vierow, 2008). In numerical studies, where changing flow rates can be done through adjustments of the simulation input parameters, researchers still need to test a combination of liquid and gas velocities to investigate the characteristics and mechanisms of counter current two-phase flows (Lu et al., 2016). In order to achieve CCFL, many attempts are typically needed regardless of simulation or experiment. This is not only inefficient, but also can become costly for experimental time and computational resources. Therefore, the capability to automatically adjust the flow rate to produce CCFL occurrence efficiently would be a significant improvement to simulation framework. This chapter introduces the development work of integrating proportional–integral–derivative (PID) control theory into the flow rate control, referenced as the PID pressure gradient controller. The benefits of the PID pressure gradient controller are more than just simplifying the workflow to obtain CCFL and are further elaborated in this chapter.

### **3.1 Introduction of PID pressure gradient controller**

Normally there are two ways to generate CCFL, either by adjusting system pressure or gas flow rate (Gallego, 2004; Vierow, 2008). For the pressure driven approach, the liquid flow is accelerated or decelerated by the pressure gradient and statistically steady state flow conditions can be achieved by balancing the pressure gradient, wall and interfacial shears, as well as gravity or other body forces. In the gas flow rate driven scenario, gas is injected and increased gas flow rates will prevent liquid from flowing towards gas. As Figure 3.2 shows, the gas may even reverse the liquid flow direction in certain high gas flow rate cases. Regardless of pressure or gas rate

driven, the liquid flow rate rarely is exactly zero as the CCFL occurrence is transient in nature. In the majority of scenarios, either CCFL has yet to be achieved, or has already occurred in which case the liquid flow is reversed (Figure 3.2).

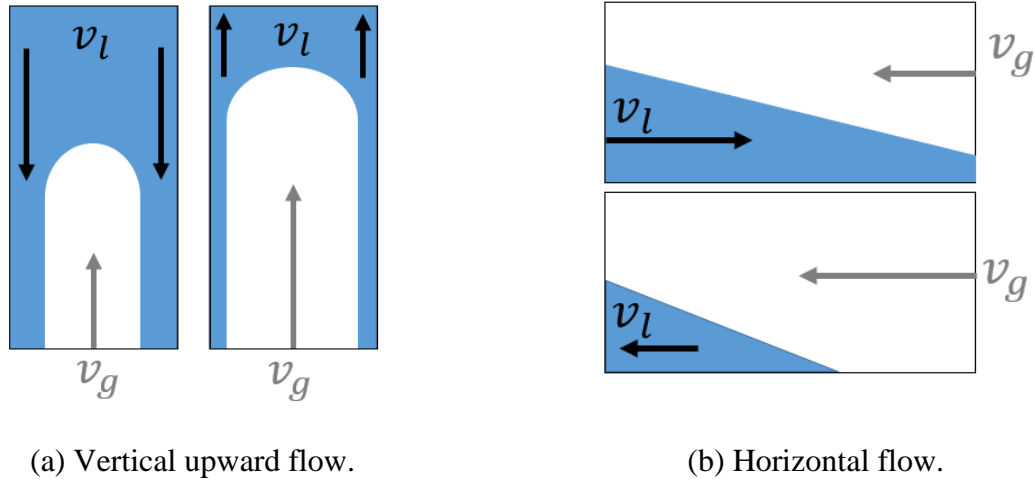


Figure 3.1. Illustration on gas flow rate driven counter current flows.

To study the physical phenomena happening in the CCFL transition, numerical studies, with good control of pressure gradient, can help explore how the transition happens as experimentally the high resolution details of two phase flow are difficult to measure. With the PID theory integrated in the two-phase flow simulations, the flow rate can be accurately and efficiently controlled. Considering the pressure gradient in a flow channel will change both the liquid and gas flow rates, it can be adjusted to converge to a zero liquid flow rate. For upward vertical flows, gas always moves faster than liquid due to buoyancy. Therefore, when the liquid velocity is zero, gas will still be moving upward, which corresponds to CCFL occurrence that gas has a large enough velocity which prevents liquid from draining down. Liquid flow rate being exactly zero is a strict-criterion of CCFL, but it is also a critical condition which is difficult to be achieved. Considering the accurate automatic control capability of PID controller and its successful application in a single bubble control (Thomas et al., 2015), a PID pressure gradient controller is designed and developed

to achieve CCFL conditions efficiently. Such approach of integrating control theory to produce CCFL occurrence has never been demonstrated before.

One of the major applications of the PID pressure gradient controller is to obtain CCFL in the nuclear debris bed channels, although a wider application range will be also demonstrated in this Chapter. For the flow features inside the debris bed, traditionally it is hard to observe or measure in experiments (Karbojian et al., 2009). Debris bed simulations also do not have the capability to explore flow structures in small channels (Ma and Dinh, 2010). It is therefore impossible to determine when CCFL can happen in such small channels without proper understanding of the two-phase flow regimes inside. Therefore, an advance interface capturing simulation and in-situ data analysis is used to better understand the flow phenomena. Through the application of this PID pressure gradient controller into debris bed CCFL studies, it can shed light onto the underlying physics of the critical condition for CCFL to occur and the corresponding fluid mechanics and flow regimes.

This chapter first presents an overview of virtual data probes used for flow data collection, the code development for in-situ computing of the velocity integral, and the verification of computed velocity integral. Next, the development of PID pressure gradient controller will be explained, specifically the integration of PID control theory into flow rate control. The performance of the PID pressure gradient controller will be evaluated on the response time, accuracy, robustness, and penalty on parallel code performance. Finally, the potential capabilities of PID pressure gradient controller will be introduced.

### **3.2 Development of PID pressure gradient controller**

A cylindrical domain with periodical boundary conditions is set up to demonstrate the PID pressure gradient controller tests (Figure 3.2). The gas and liquid will be driven by a pressure

gradient assigned to the channel and adjusted by the PID control. Since the flow is incompressible, zero volumetric liquid velocity in the channel enforces zero cross sectional liquid velocity. Therefore, any cross section on the  $y - z$  plane of the channel can be selected to collect the velocity. The PID pressure gradient controller will compute the liquid velocity integral, and then use it to adjust the pressure gradient value in order to eventually achieve the desired statistically steady state liquid flow rate (zero for CCFL problems).

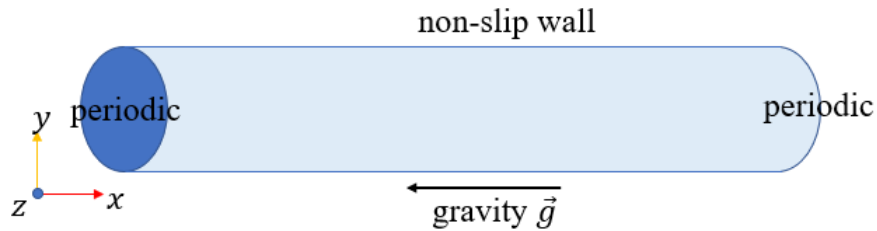


Figure 3.2. Illustration of the fluid domain.

The scheme of the PID pressure gradient control is illustrated in Figure 3.3. At each time step, velocity integral  $\int u dS$  on a  $y - z$  cross section is evaluated and used to adjust the pressure gradient ( $\frac{dp}{dx}$ ) in the domain, until  $\frac{dp}{dx}$  yields  $\int u dS = 0$ , i.e. CCFL occurrence. The first step of the capability development is to accurately compute the velocity integral to be used as the input of the controller.

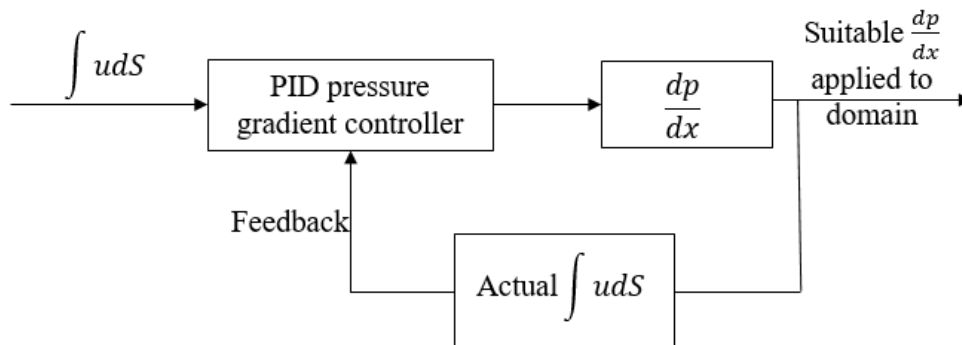
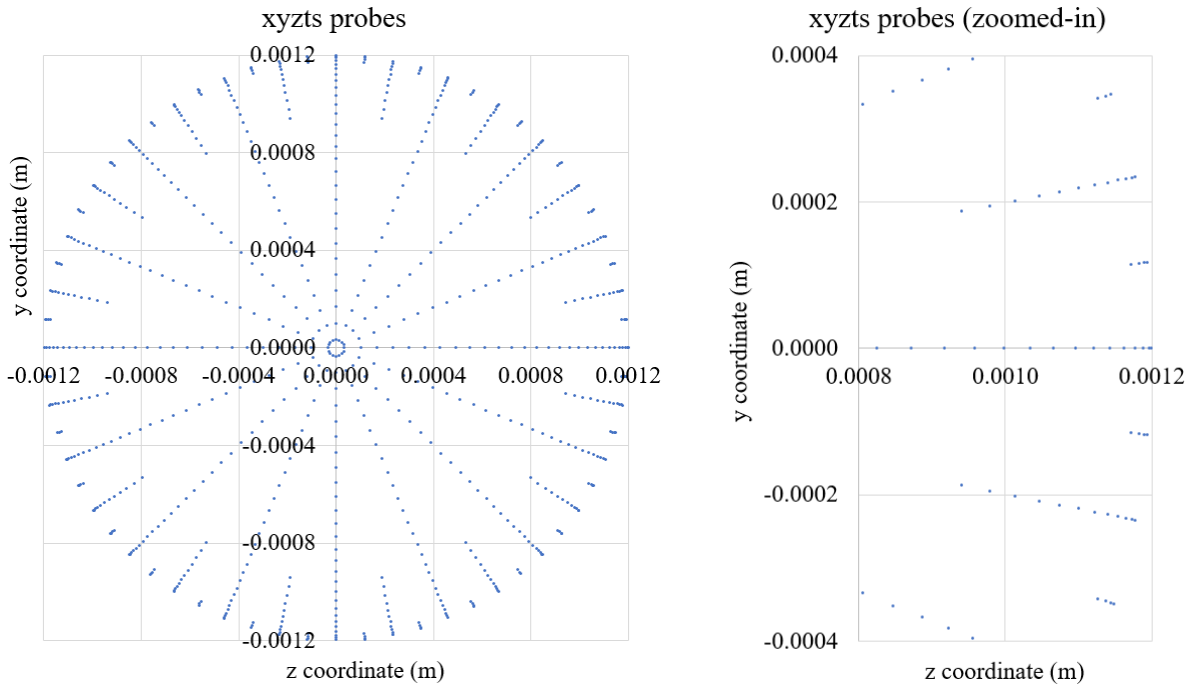


Figure 3.3. PID control scheme.

### 3.2.1 Code development of velocity integral

PHASTA can utilize static virtual probes (namely xyzts probes) on any cross section to collect flow field information at the location of each probe, including pressure, temperature, velocities, level-set values, etc (Bolotnov, 2013). The capability range of xyzts probes were expanded with newly developed velocity integral option and in the future more integrated variables can be implemented in a similar way.

Figure 3.4 (a) depicts the distribution of 768 xyzts probes on a cylindrical channel cross section with a radius of 1.2 mm. Near wall probes are depicted in the zoomed-in figure (Figure 3.4 (b)). From the wall to the center of the channel, the growth rate between each two probes in the radial direction is 1.2.



(a) xyzts probe distribution on a  $y - z$  plane.

(b) Zoomed-in distribution.

Figure 3.4. Probe distribution with each probe collecting flow field information.

The velocity integral  $\int u dS$  in the numerical simulation is a weighted summation over  $N$  probes.

$$\int udS = \begin{cases} \sum_{i=1}^N u_i S_i, \phi_i > 0 \\ 0, \phi_i \leq 0 \end{cases} \quad (24)$$

Here,  $u_i$  and  $\phi_i$  are the velocity and level-set values at probe  $i$ , which will be collected by xyzts probes.  $S_i$  is the area around each probe (Figure 3.5 (a) and (b)), used as the weight of the velocity to compute the numerical integral or weighted summation.  $\phi_i > 0$  implies that only the probes currently occupied by liquid phase will contribute to the velocity integral. Through this condition, liquid flow rate control can be achieved. Previously, xyzts probes only store three values, the  $x$ ,  $y$ , and  $z$  coordinates of each probe. However, the probe areas were not included. Therefore, in order to compute the velocity integral, which will then be used in PID control, the area of each probe should be determined first.

As Figure 3.5 (a) and (b) depicts,  $S_i$  is the area of the ring cell region around each probe. The radius of the ring cell increases as the probe is closer to the wall. For any ring cells as Figure 3.5 (c) shows, the radius of each ring shape,  $R_i (i = 1, 2, 3)$ , are all known. Those radii along with the central angle  $\theta$ , are used in xyzts generation script to determine the coordinates of each probe.  $\theta$  is determined by number of probes in homogenous direction ( $N_{homo}$ ) specified along the peripheral direction. As  $N_{homo}$  increases, the total number of probes,  $N$ , increase proportionally.  $N_{homo} = 64$  for the probe distribution in Figure 3.5 (a) and (b) where the corresponding  $N = 768$ .

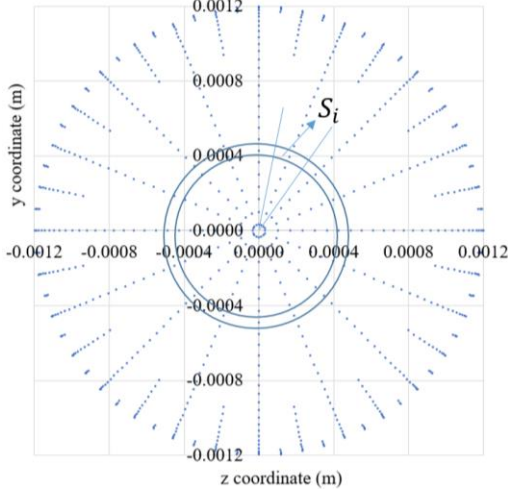
$$\theta = \frac{2\pi}{N_{homo}} \quad (25)$$

For any three neighboring ring cells in Figure 3.5 (c), the area of cell 2 is computed as:

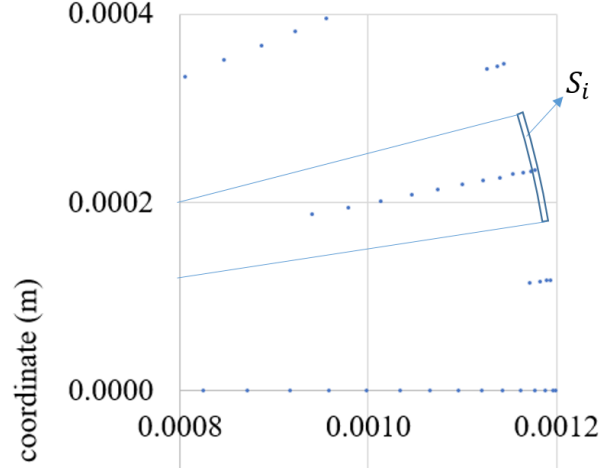
$$S_2 = (R_2\theta) \cdot \Delta R \approx (R_2\theta) \cdot \frac{R_3 - R_1}{2} \quad (26)$$

However, the wall probe needs special treatments (Figure 3.5 (d)), where the pipe radius ( $R_{pipe}$ ) is used:

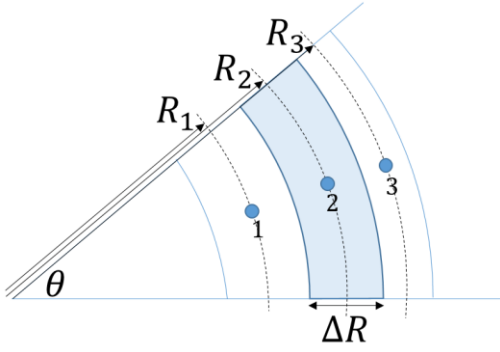
$$S_2 = (R_2\theta) \cdot \Delta R \approx (R_2\theta) \cdot [(R_{pipe} - R_2) + \frac{R_2 - R_1}{2}] \quad (27)$$



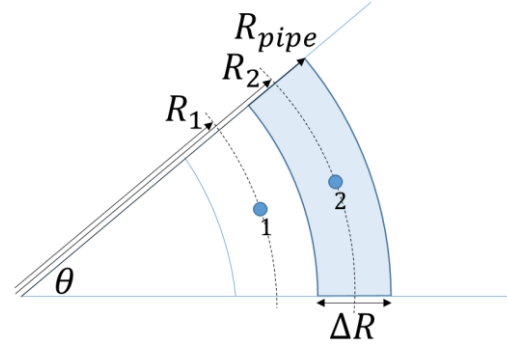
(a) Probe area in the bulk region.



(b) Probe area in the wall region.



(c) Bulk probe area computation.



(d) Wall probe area computation.

Figure 3.5. xyzts probe area and the illustration on how to compute it.

The uncertainty of using approximated  $\Delta R$  is evaluated under different  $N_{homo}$  and  $N$ . Table 3.1 summarizes the relative error between the computed summation of probe areas (numerical pipe cross section area) with the analytical value ( $\pi R_{pipe}^2$ ). The relative errors are all below 0.1% so can be considered negligible. With area of each probe computed accurately, it can be used as the input of each xyzts probe to compute instantaneous velocity integral in the simulation. The xyzts probe generation script including newly developed probe area computation is included in Appendix.

Table 3.1. Numerical error of computing xyzts probe area.

$N_{homo}$	$N$	Numerical pipe area ( $m^2$ )	Analytical pipe area ( $m^2$ )	Relative difference
16	192	4.52746E-06	4.52389E-06	0.079%
32	384	4.52746E-06	4.52389E-06	0.079%
64	768	4.52746E-06	4.52389E-06	0.079%
128	1536	4.52746E-06	4.52389E-06	0.079%
256	3072	4.52746E-06	4.52389E-06	0.079%

PHASTA is a paralleled code, so the development of velocity integral also needs to be parallelized. The schematic of the parallel computation is illustrated in Figure 3.6. The computation domain is usually split into large number of mesh partitions to be processed by parallel computing cores, therefore the xyzts probes should be divided accordingly (Saini, 2020). The number of xyzts probes ( $N_{proc}$ ) on each processor depends on how the domain was split during the mesh partition process and the probes' locations. Usually  $N_{proc}$  are different on all the processors, but the computation on those processors are processed simultaneously. On each processor, velocity integral is simply a summation of the product of velocity  $u_i$  and areas  $S_i$  over  $N_{proc}$  xyzts probes. For the processor which does not have xyzts probe ( $N_{proc} = 0$ ), the velocity integral is correspondingly 0. Message Passing Interface (MPI) is used to pass all the velocity integral values together. Specifically, MPI\_ALLREDUCE is utilized to sum up velocity integrals from all the processors so the expected velocity integral is obtained. This velocity integral value will then be distributed to all processes as an input into the PID pressure gradient controller. It is worth mentioning that  $u_i$  and  $\phi_i$  are in-situ data collected by xyzts probes, but only  $S_i$  needs to be read into the code in the beginning of the simulation. This process does not need extra computation of  $S_i$  during the simulation.

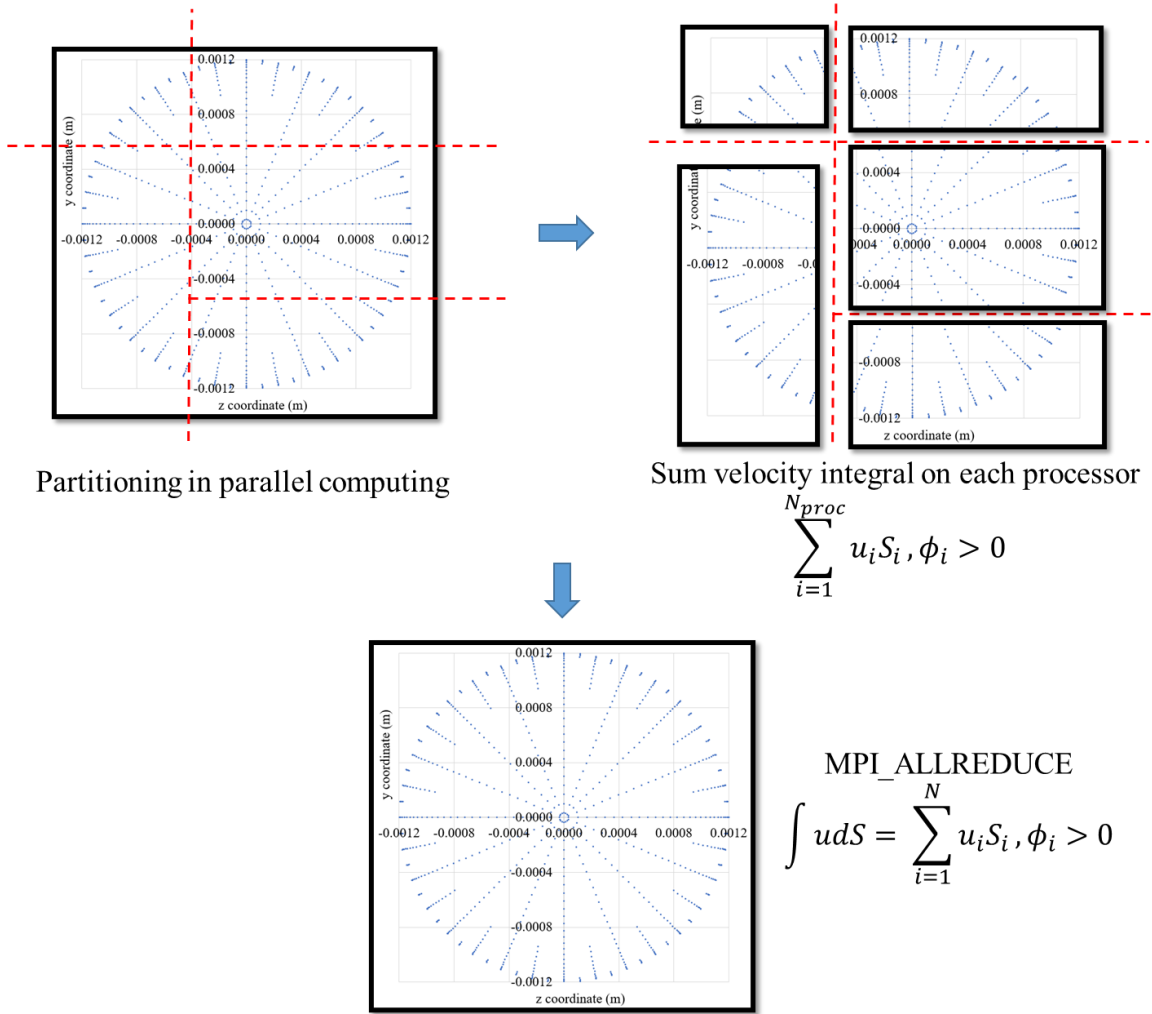


Figure 3.6. Parallel computation of velocity integral.

More detailed steps for computing velocity integral are listed below, including some representative subroutines, and variables. The corresponding scripts are included in the Appendix.

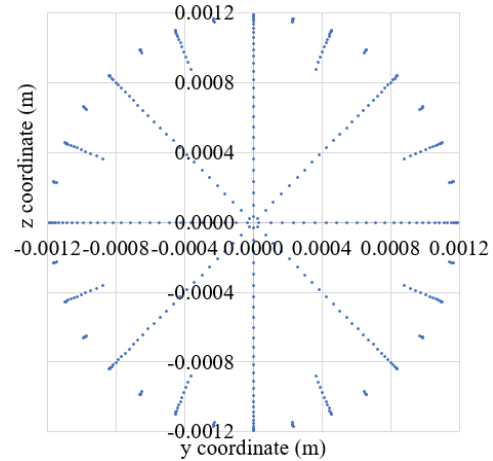
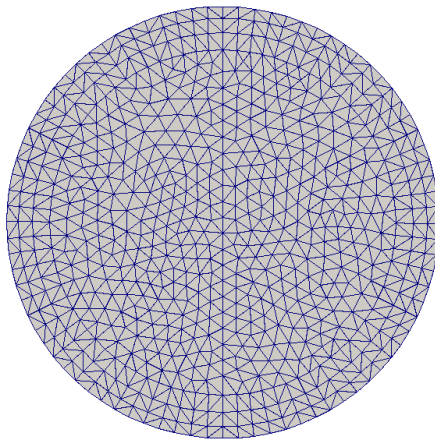
1. The  $x$ ,  $y$ ,  $z$  coordinates and probe area of each xyzts probe is read into an array *ptts*. The 2<sup>nd</sup> dimension of *ptts* was expanded from 3 to 4 to store the newly added probe area.
2. A record code of 7 is added in *asigmr.f* to specially collect velocity and level-set in-situ data for velocity integral computation. During the data collection process, *timeseries* will be called to collect those two values and store them in *varts* array.

3. The MPI process of velocity integral happens in *itrdrv.f* through *varts*. In *varts(i, j)* array, dimension *i* corresponds to each xyzts probe. Dimension *j* includes recorded or read data, in which *varts(i, 2)* and *varts(i, 6)* are  $u_i$  and  $\phi_i$  respectively; and *varts(i, 7 – 10)* are the *x*, *y*, and *z* coordinates and  $S_i$  of each xyzts probe. In each processor, a summation loop is coded for  $varts(i, 2) \cdot varts(i, 10)$  if  $varts(i, 6) > 0$ . Then MPI\_ALLREDUCE computed the desired velocity integral,  $\int u dS = \sum_{i=1}^N u_i S_i, \phi_i > 0$ , by adding the contribution from each processor.

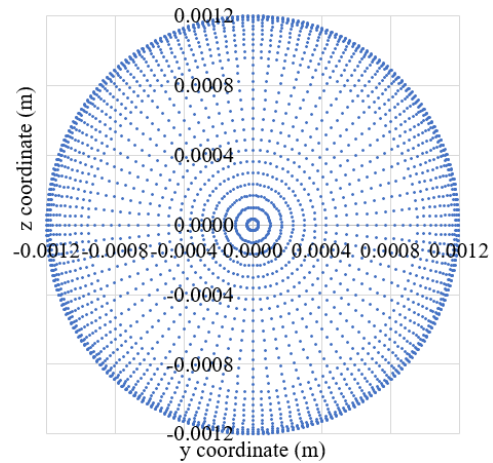
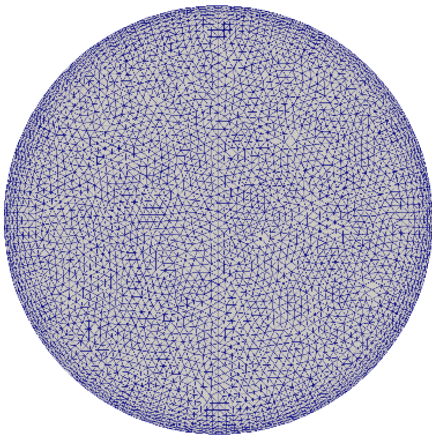
### 3.2.2 Verification of computed velocity integral

In order to test the correctness and reliability of velocity integral computation, a verification test is required. The verification of velocity integral is carried out in both single- and two-phase flows with support from Paraview, a post-processing tool. Paraview can conduct variable integration based on the value of each mesh element, including velocity integral. The computation of velocity integral in code development is dependent on the number of xyzts probes, so different probe counts are included in this verification test.

In single-phase flow verification, two conditions were selected according to the actual engineering needs: (1) coarse mesh with coarse probes (Figure 3.7 (a)) for low-resolution simulations; (2) fine mesh with fine probes (Figure 3.7 (b)) for high-resolution simulations. The geometry is the same, a cylinder with a radius of 1.2 mm, but the number of elements across the diameter is doubled in the fine mesh set up. The prism boundary layer mesh elements are tetrahedralized to avoid xyzts probe overlapping, which will prevent probe deletion during mesh partitioning process.



(a) Coarse mesh (25 elements across diameter) with 384 probes.



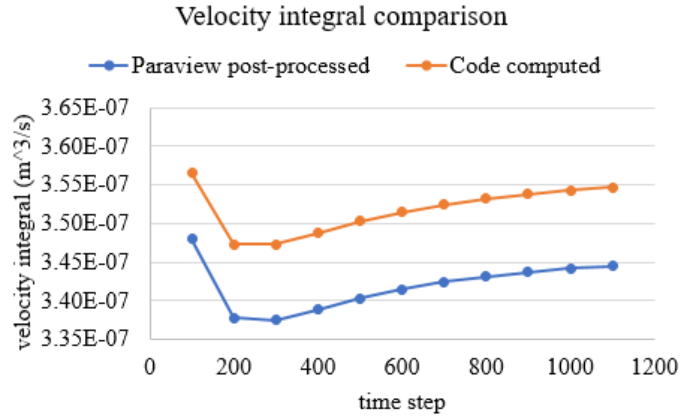
(b) Fine mesh (50 elements across diameter) with 3072 probes.

Figure 3.7. Mesh and xyzts probes used in verification test.

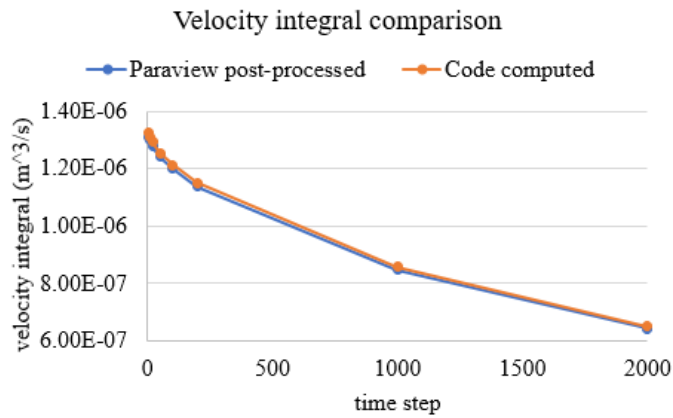
For coarse mesh, an initial velocity of  $(0.1, 0, 0)$   $m/s$  is assigned in the domain. From Figure 3.8 (a), the velocity integral change with time step has a systematic difference between the code output and Paraview post-processed values, which should come from lack of probes in the near wall region where velocity gradient is high. However, the relative differences are all below 3%, which is acceptable for a coarse mesh setup.

For the fine mesh setup, an initial velocity of  $(0.3, 0, 0)$   $m/s$  is assigned into the domain and deceleration of the flow is observed due to wall shear. The velocity integral obtained from

Paraview and code computation are overlapped in Figure 3.8 (b). The relative errors are all below 1.5%, with the majority of errors below 1.0%, which signifies sufficient accuracy.



(a) Coarse mesh and coarse probes.

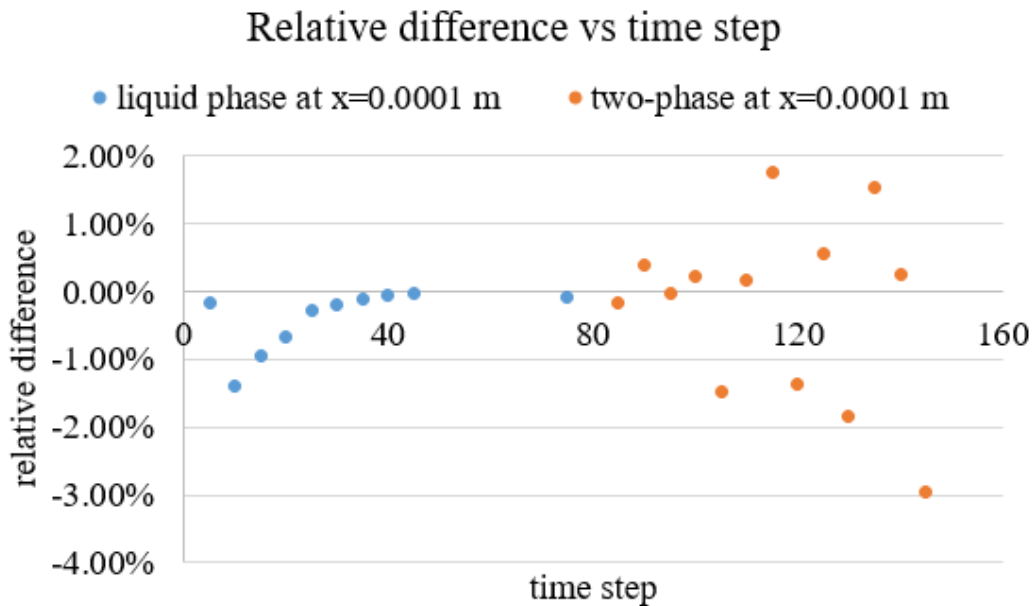
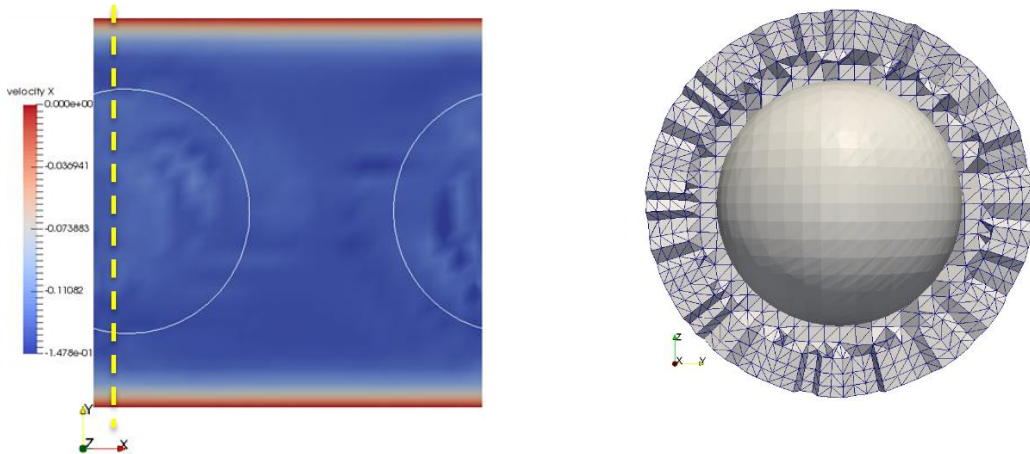


(b) Fine mesh and fine probes.

Figure 3.8. Velocity integral single phase verification.

In the two-phase verification test, a single bubble is initialized in a liquid domain as Figure 3.9 (a) and (b) show. The velocity integral computation is more challenging than the single phase since the bubble will cross the xyzts probe plane so the liquid phase area changes with time. The xyzts probe plane is located at  $x = 0.00001 \text{ m}$ , marked by the yellow dash line in Figure 3.9 (a). There are 768 probes (Figure 3.4 (a)) on this cross section, and the coarse mesh used is the same as Figure 3.7 (a). In the beginning of the simulation, the single bubble is in the center of the cylindrical channel, so the flow around xyzts probe plane is liquid phase only. As Figure 3.9 (c) plots, the

relative errors (blue dots) between Paraview post-processed and code computed velocity integrals are all below 1.5%. Starting from the 85<sup>th</sup> time step, the bubble begins to cross the xyzts probe plane and it leaves the plane after the 145<sup>th</sup> time step. As the orange dots in Figure 3.9 (c) depict, except for the last data point when the bubble is touching the xyzts probe plane (relative error is the maximum,  $-2.95\%$ ), all other relative errors are below 1.5%.



(c) Relative error between Paraview post-processed and code computed velocity integrals.

Figure 3.9. Velocity integral two phase verification.

With the above verification test for both single- and two-phase flows, the velocity integral computation is proved to be accurate enough regardless of mesh coarseness or xyzts probe counts. The developed code has a very low uncertainty for parallelized velocity integral computation (below 3% even with coarse mesh and coarse probes) so obtained velocity integrals can be used as an accurate and reliable input for the PID pressure gradient controller.

### 3.2.3 Integration of PID theory in pressure gradient control

This section introduces the integration of PID theory into the design and implementation of the pressure gradient controller. PID control will continuously calculate the error between the actual velocity integral and the desired value in each time step, which is used to determine a correction-based pressure gradient. Eq. (28) illustrates the equation of how pressure gradient ( $\nabla p$ ) changes with time based on proportional ( $P(t)$ ), integral ( $I(t)$ ), and derivative components ( $D(t)$ ) in the PID control. The coefficients in front of each component ( $K_P$ ,  $K_I$ , and  $K_D$ ) determines the control effect of each term. Since there is always a streamwise direction in a channel flow, the pressure gradient here uses the most dominant  $\frac{dp}{dx}$  to drive the flow. The control terms will use  $x$  direction velocity integral accordingly ( $\int u dS$ ) as the input to adjust the pressure gradient. Therefore, in all the simulation setups, the streamwise direction should align with the  $x$  axis in order to use PID pressure gradient control. The rest of the section will introduce each term in Eq. (28).

$$\nabla p(t) = K_P P(t) + K_I I(t) + K_D D(t) \quad (28)$$

First, the proportional term  $K_P P(t)$  in Eq. (28) determines the adjustment size of the PID controller when there is an error between desired velocity integral ( $\int u_{desire} dS$ ) and the actual velocity integral at  $n^{th}$  time step ( $\int u dS^{(n)}$ ):

$$K_P P(t) = K_P P^{(n)} = K_P \cdot \Delta \int u dS^{(n)} = K_P \left( \int u dS^{(n)} - \int u_{desire} dS \right) \quad (29)$$

Next, integral term  $K_I I(t)$  in Eq. (28) accounts for the historical change of pressure gradient and integrate all instantaneous values over time. For stability consideration, this integral term is designed to be the averaged pressure gradient within a past time window.

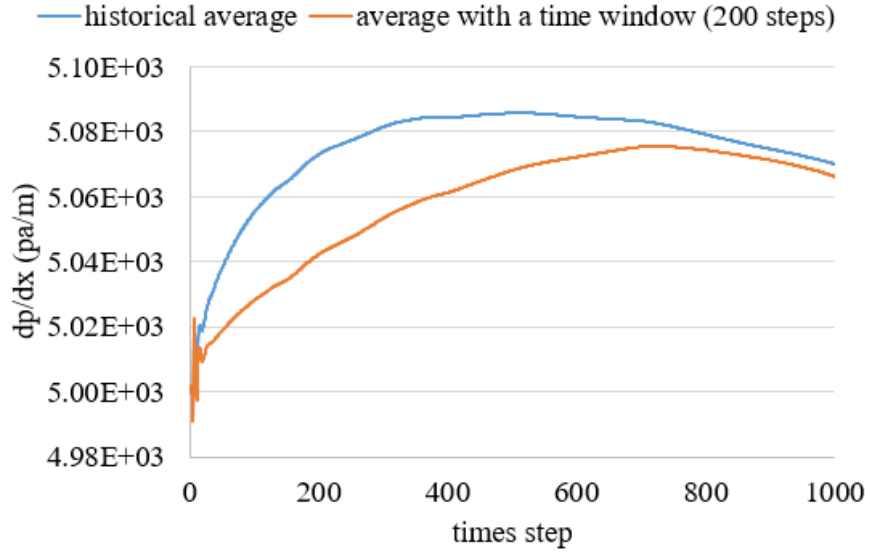
$$K_I I(t) = K_I I^{(n)} = K_I \cdot \overline{\left(\frac{dp}{dx}\right)}^{(n)} = K_I \left( \frac{1}{T} \sum_{k=n-T}^n \left(\frac{dp}{dx}\right)^{(k)} \right) \quad (30)$$

Here,  $k$  is an index when computing the time average of past pressure gradients at each time step  $k$ . The time window is selected to be  $T = 200$  time steps, and Figure 3.9 shows the pressure gradient and velocity integral under historical average  $\left(\frac{1}{n} \sum_{k=1}^n \left(\frac{dp}{dx}\right)^{(k)}\right)$  versus under time window average. The control effects after 800<sup>th</sup> time step almost converge under those two average approaches, but the peak value of pressure gradient is lower with a time window. In addition, time window average can exclude the influence from old time values, which increases the stability of the numerical simulation. In future applications, users can also select any other time window length based on the numerical stability of the simulation.

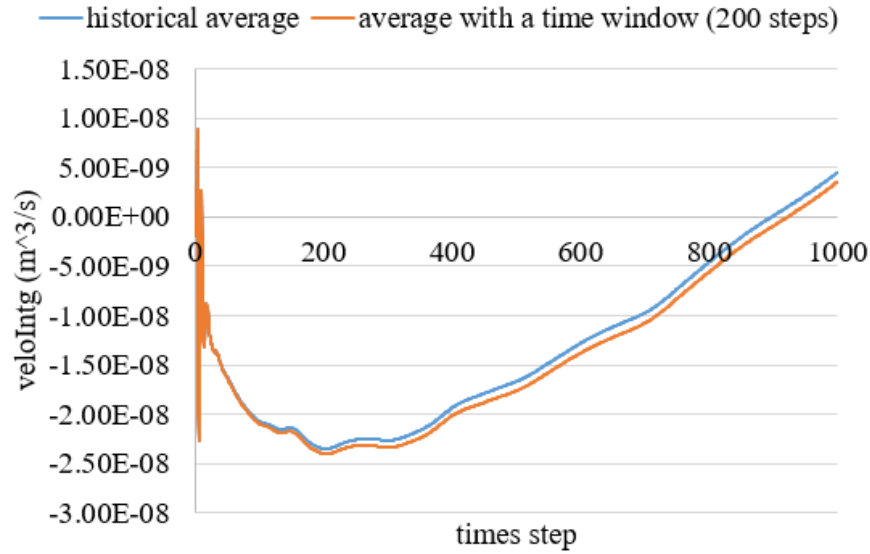
In the code development process, this time average is implemented using a time relaxation approach.

$$K_I I(t) = K_I I^{(n)} = K_I \cdot \overline{\left(\frac{dp}{dx}\right)}^{(n)} = K_I \left[ \left(1 - \frac{1}{T}\right) \cdot \overline{\left(\frac{dp}{dx}\right)}^{(n-1)} + \frac{1}{T} \left(\frac{dp}{dx}\right)^n \right] \quad (31)$$

Here  $\frac{1}{T}$  is used as a relaxation factor to add the contribution of the most recent pressure gradient into the averaged pressure gradient. Compared with allocating an array for  $\frac{dp}{dx}$  and then averaging across a certain time interval of this array, the relaxation approach saves memory and guarantees a faster computation of PID control.



(a) Pressure gradient comparison.



(b) Velocity integral comparison.

Figure 3.10. The control effect of historical average versus time window average.

At last, the derivative term  $K_D D(t)$  in Eq. (28) is responsible for damping the fluctuation of the controlled variable. The more rapid the velocity integral change is, the stronger the control effect will be.

$$K_D D(t) = K_D D^{(n)} = K_D d \int u dS^{(n)} = K_D \left( \int u dS^{(n)} - \int u dS^{(n-1)} \right) \quad (32)$$

In this term, a more exact form of the derivative should be divided by the time step size  $\Delta t$ , however since  $\Delta t$  are slightly varying constant values and almost do not change during the steady state, there is no specific need to add it in the derivative term. The magnitude of  $K_D$  can be tuned to include the effect of dividing the time step size.

With the design of the P, I, and D control terms explained, the updated PID control schematic is presented in Figure 3.11. For CCFL application, the desired velocity integral is zero. As long as the actual velocity integral achieves zero, the proportional term will be 0. If velocity integral can be stabilized, the derivative term will be zero. If such steady state can be maintained, pressure gradient average will not change any further, so averaged pressure gradient is the steady state pressure gradient itself. With the above scenario achieved, there is no need to correct the pressure gradient further, and the output from the PID control is the averaged pressure gradient, which is also the desired value to produce CCFL occurrence.

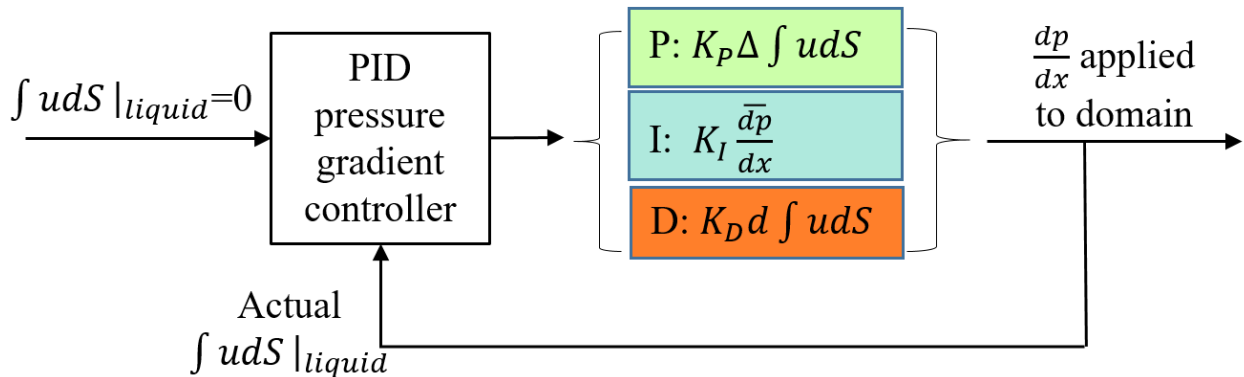


Figure 3.11. Control scheme of using PID pressure gradient controller to obtain CCFL.

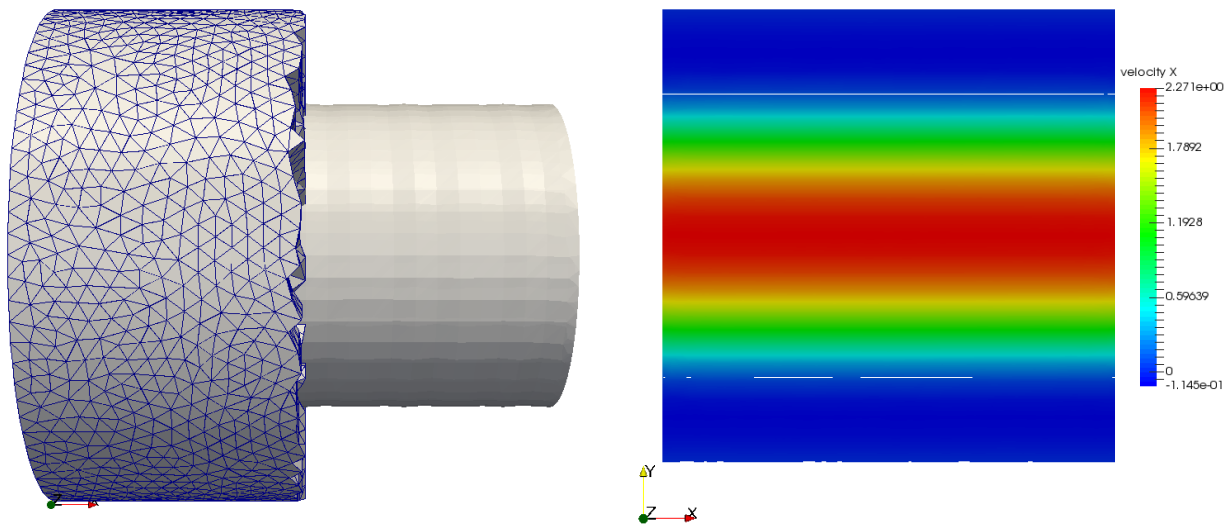
### 3.3 Performance evaluation of PID pressure gradient controller

This section will demonstrate the accuracy, fast response, and robustness of the PID pressure gradient controller. The accuracy and fast response of PID pressure gradient controller will be conducted in a series of tuning tests, where the most efficient control coefficients will be obtained. The robustness tests will be carried out for different initial conditions and control goals. A penalty

test will also be conducted to evaluate how new capabilities affect the parallel computation, through evaluating the number of core hours to compute one billion elements per time step.

### 3.3.1 Tuning of PID pressure gradient controller

Tuning is always required for PID controllers during the application process. When control systems are different or when the PID terms in the controller change, the coefficients in front of each PID components needs to be tuned to produce the most efficient controller. The tuning simulations are carried out in a cylindrical channel with a diameter and length of  $2.4\text{mm}$  initialized with annular flow (Figure 3.12). A coarse mesh is designed (Figure 3.12 (a)) to expedite the tuning process, which is still adequate to resolve a laminar annular flow (Figure 3.12 (b)). The number of elements in the computational mesh is 113,005, and 16 processors is used on a local cluster *Insight* to conduct the tuning simulations. The key parameters used in the simulation are selected as water and steam properties in boiling water reactors (Table 3.2). The viscosities of the water and the steam are higher than the original values to increase the numerical stability of the two-phase simulations.



(a) Configuration of mesh and initial interface.

(b) Transient velocity distribution.

Figure 3.12. Illustration of an annular flow for tuning tests.

Table 3.2. Parameters used in tuning of PID pressure gradient controller.

	Liquid	Gas
Density ( $kg/m^3$ )	758.15	30.83
Viscosity ( $Pa \cdot s$ )	8.5439E-04	2.858E-04
Surface tension coefficient ( $N/m$ )	0.071	
Earth gravity ( $m/s^3$ )	(-9.8, 0, 0)	
Initial pressure gradient ( $Pa/m$ )	(5000.0, 0, 0)	
Initial velocity ( $m/s$ )	(0, 0, 0)	
$x$ velocity goal in PID control ( $m/s$ )	0.0	

According to the design of the PID pressure gradient controller, when steady state is achieved, averaged pressure gradient should be equal to the steady state pressure gradient itself, therefore  $K_I = 1.0$  is the best value for numerical stability and does not need tuning. The values of  $K_P$  and  $K_D$  in Table 3.3 are combined in tuning sets, involving 17 test cases. It is worth mentioning that  $K_P$  uses negative values because of the physics of pressure driven flows. When velocity is lower than the desired value,  $\left( \int u dS^{(n)} - \int u_{desire} dS \right)$  is negative in the proportional term of Eq. (29). Therefore, the pressure gradient needs to increase to accelerate the flow, thus  $K_P$  must be negative to produce a positive proportional term.

Table 3.3. Control coefficients used in tuning tests of the PID pressure gradient controller.

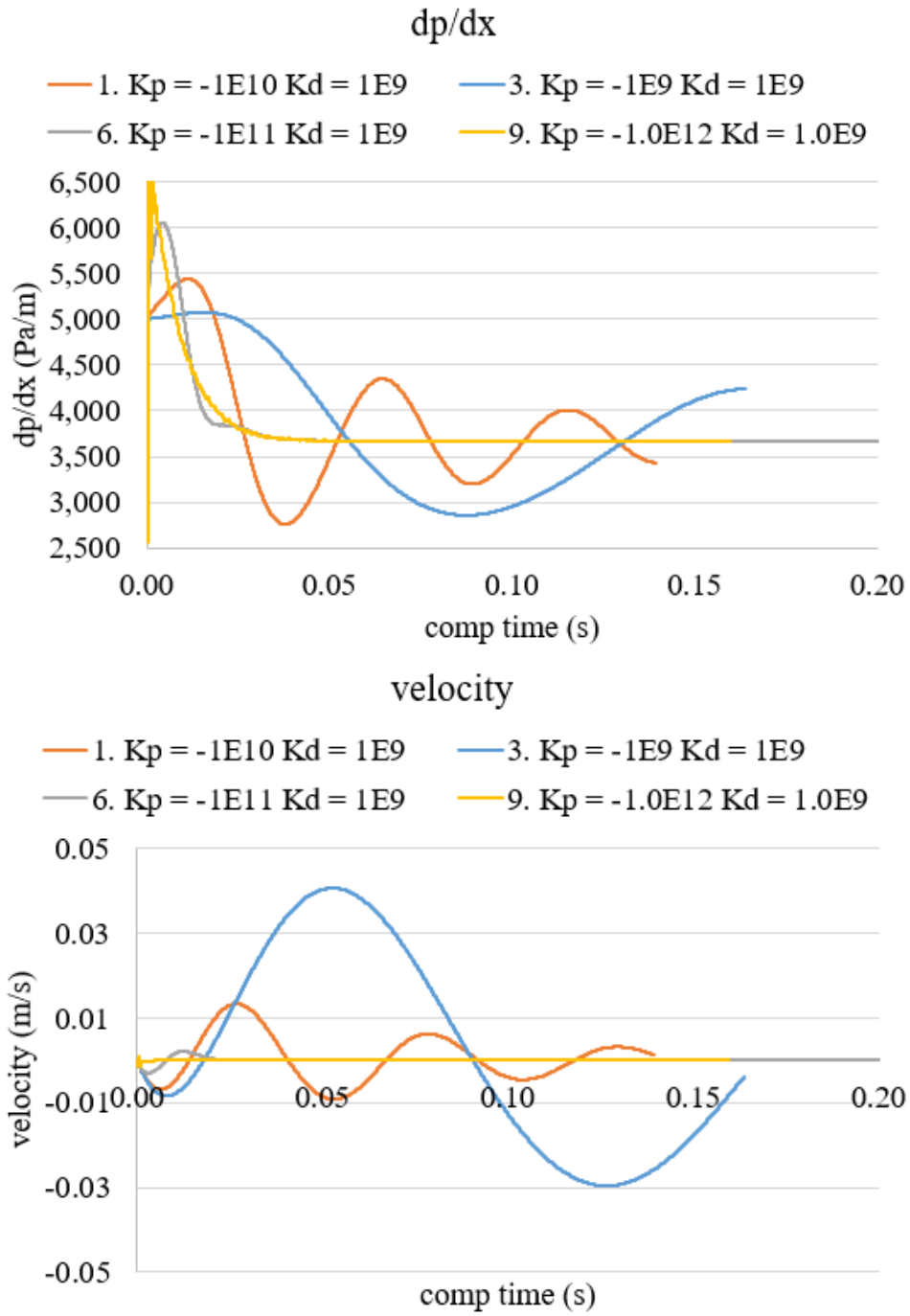
$K_P$	-1.0E9, -1E10, -1.0E11, -1.0E12, -1.0E13
$K_I$	1.0
$K_D$	1.0E9, 1E10, 1.0E11, 1.0E12, 1.0E13

Since the proportional term contributes majorly to changes in the PID controller, an appropriate  $K_P$  value will be identified first before tuning  $K_D$ . To begin, the pair-wise test cases of

combinations between  $K_p = -1.0E9, -1E10, -1.0E11, -1.0E12$  and  $K_D = 1.0E9, 1E10, 1.0E11$  are conducted. There are 12 cases in total, numbered from 0 to 11 as Figure 3.13 shows. Figure 3.13 plots velocity rather than velocity integral. Since velocity integral involves the multiplication of liquid cross-section area, which is a very small number, resulting in the velocity integral magnitude in the test cases to be extremely small as well. After dividing by liquid cross-sectional area, the magnitude in the plot is more understandable.

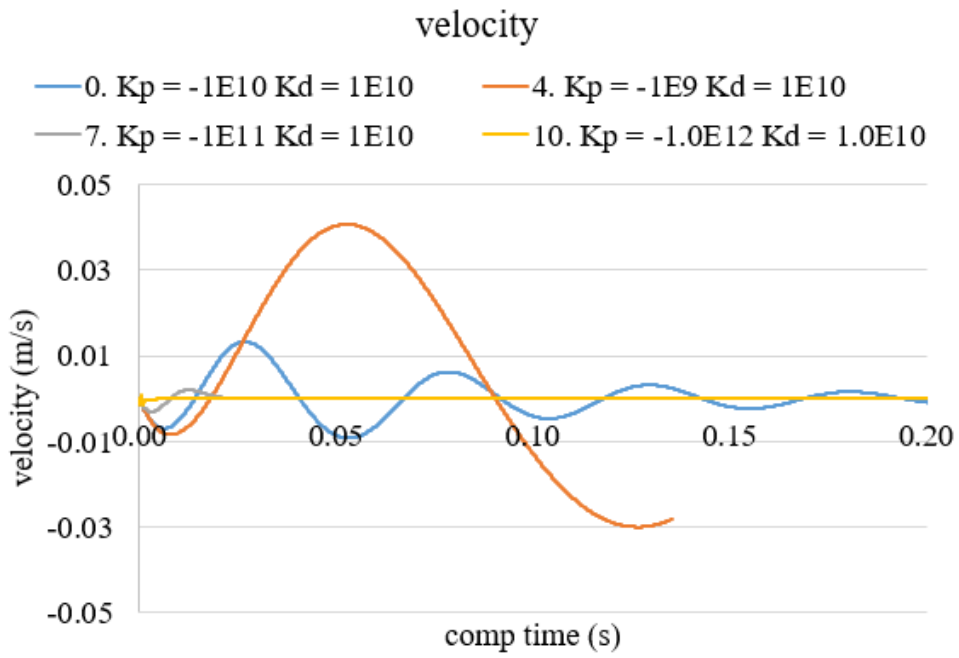
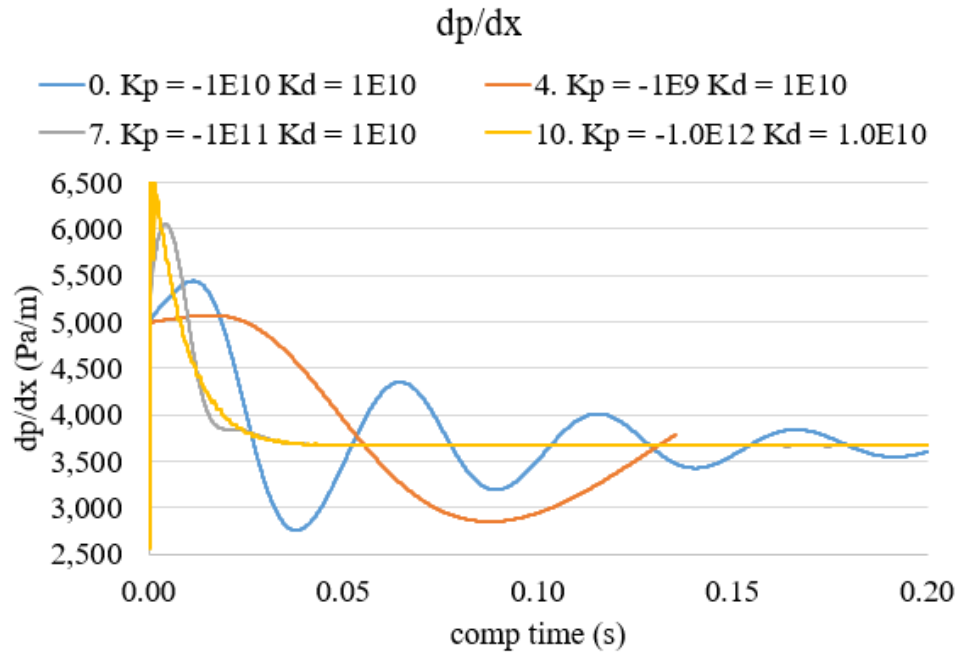
From Figure 3.13, it is clear that  $K_p = -1.0E9$  and  $-1.0E10$  (blue and orange curves) are too small so the PID control is insensitive. The control action of small  $K_p$  is not responsive enough for actual velocity integral to reach zero. An opposite condition appears in Figure 3.14 where  $K_p = -1.0E13$  so the PID control is over-sensitive. Large  $K_p$  yields a large fluctuation on both pressure gradient and velocity. Among the 4 tested proportional coefficients,  $K_p = -1.0E11$  and  $-1.0E12$  (yellow and grey plots) have the best performance in the control process. Whenever velocity integral overshoots or undershoots zero, the controller can always immediately adjust the pressure gradient to yield velocity integral closer to the desired value. The fluctuation of velocity and pressure gradient are minimal as well, which produces stable simulations.

Figure 3.13. Tuning results of 12 combinations.



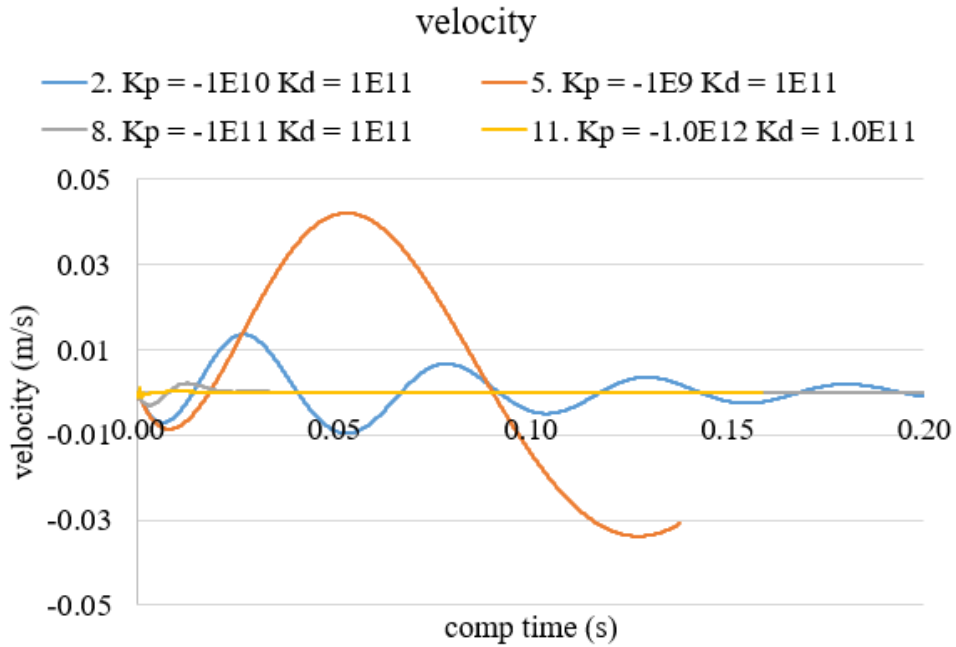
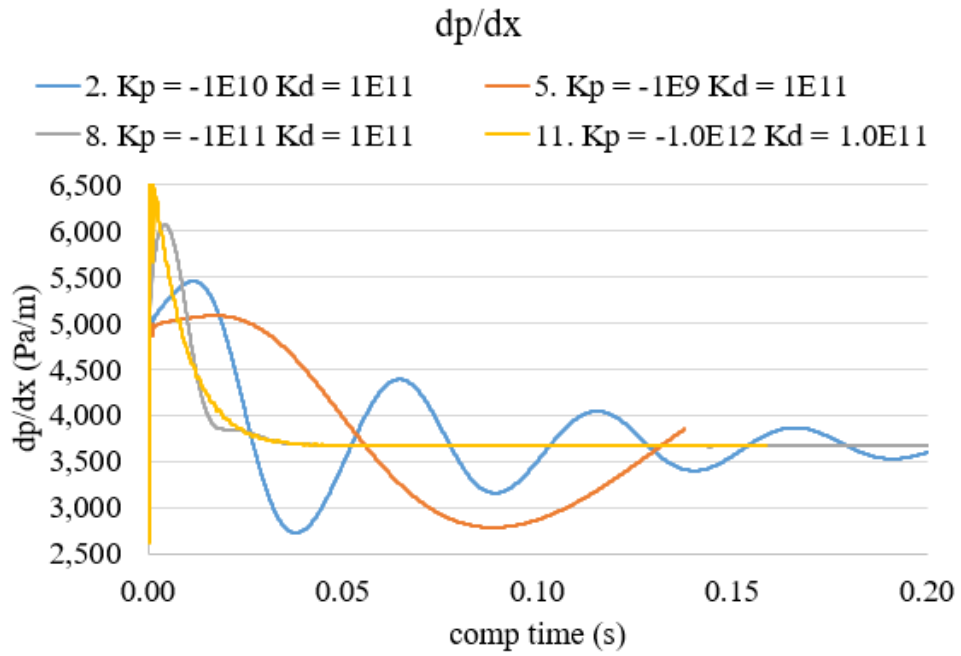
(a)  $K_D = 1.0E9$ ,  $K_P = -1.0E9 \sim -1.0E12$ .

Figure 3.13. (continued)

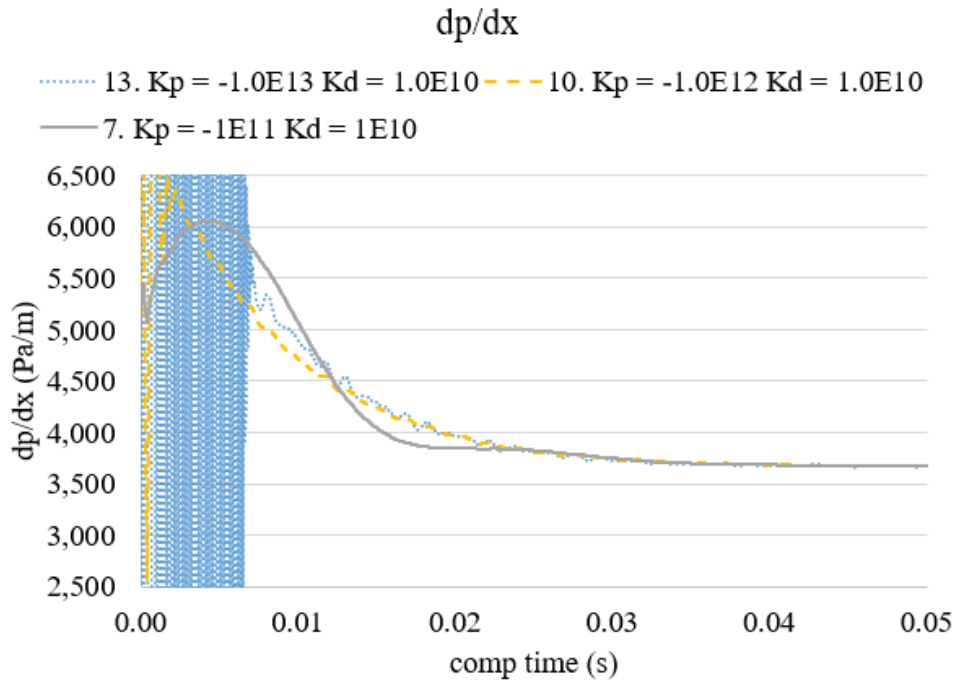


(b)  $K_D = 1.0E10$ ,  $K_P = -1.0E9 \sim -1.0E12$ .

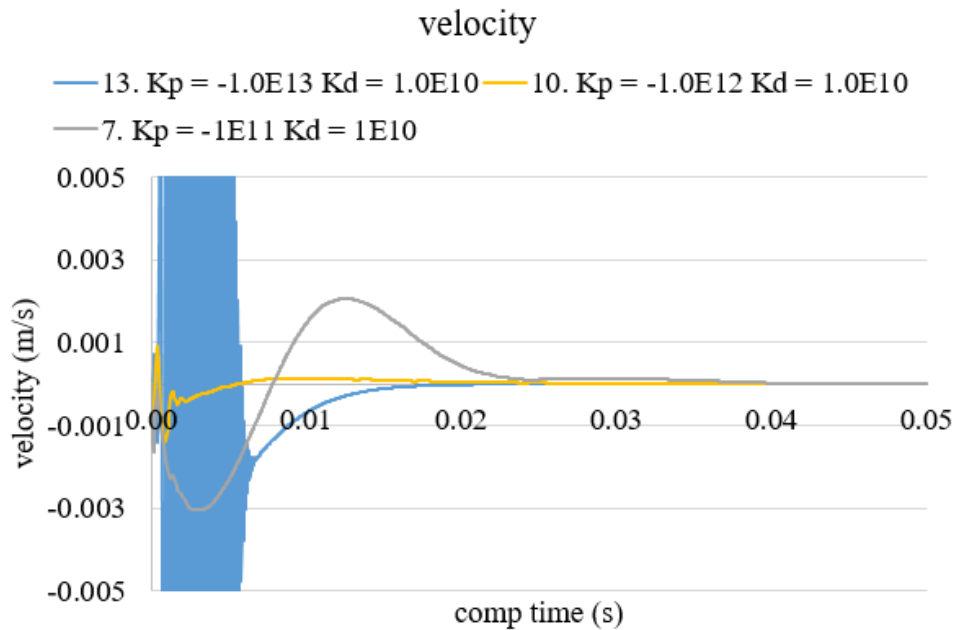
Figure 3.13. (continued)



(c)  $K_D = 1.0E11$ ,  $K_P = -1.0E9 \sim -1.0E12$ .



(a) Pressure gradient.

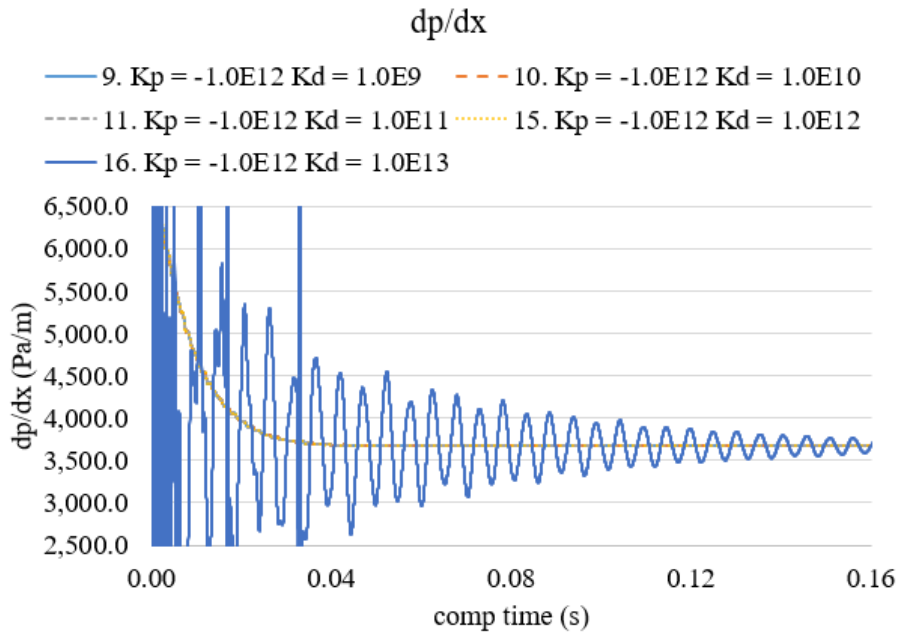


(b) Velocity.

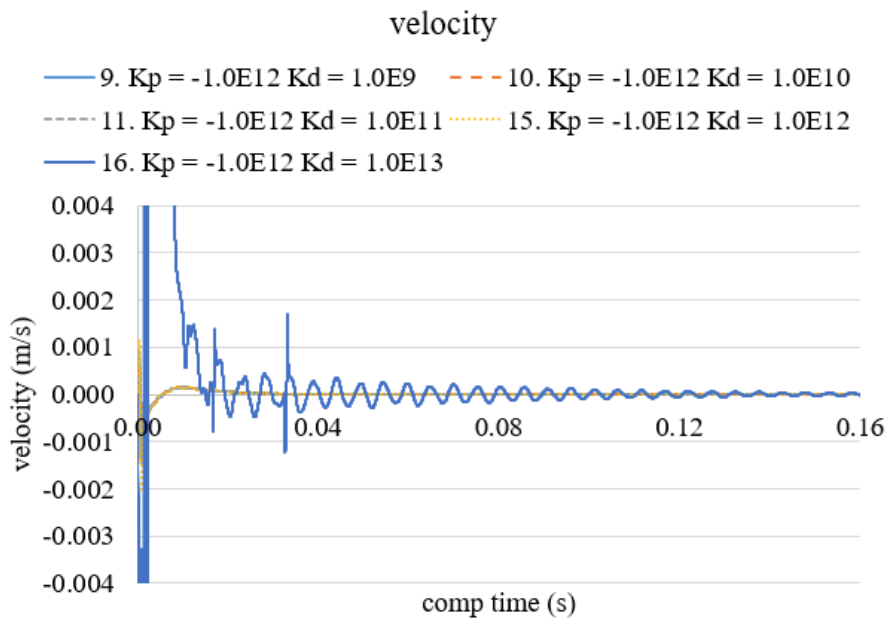
Figure 3.14. Tuning results of  $K_D = 1.0E10$ ,  $K_P = -1.0E11 \sim -1.0E13$ .

With  $K_P = -1.0E11$  and  $-1.0E12$  selected to be the most efficient proportional coefficients, a further tuning of  $K_D$  is carried out. First, 5 comprehensive tests with  $K_P = -1.0E12$  and  $K_D =$

1E9 to 1E13 are carried out with results presented in Figure 3.15. Aside from  $K_D = 1E13$ , all other  $K_D$  parameters produce overlapped results. Too large  $K_D$  yields a controller too sensitive to velocity change, and as a result the pressure gradient fluctuates significantly as well.



(a) Pressure gradient change with time. Plots of  $K_D = 1E9 \sim 1E12$  overlap.

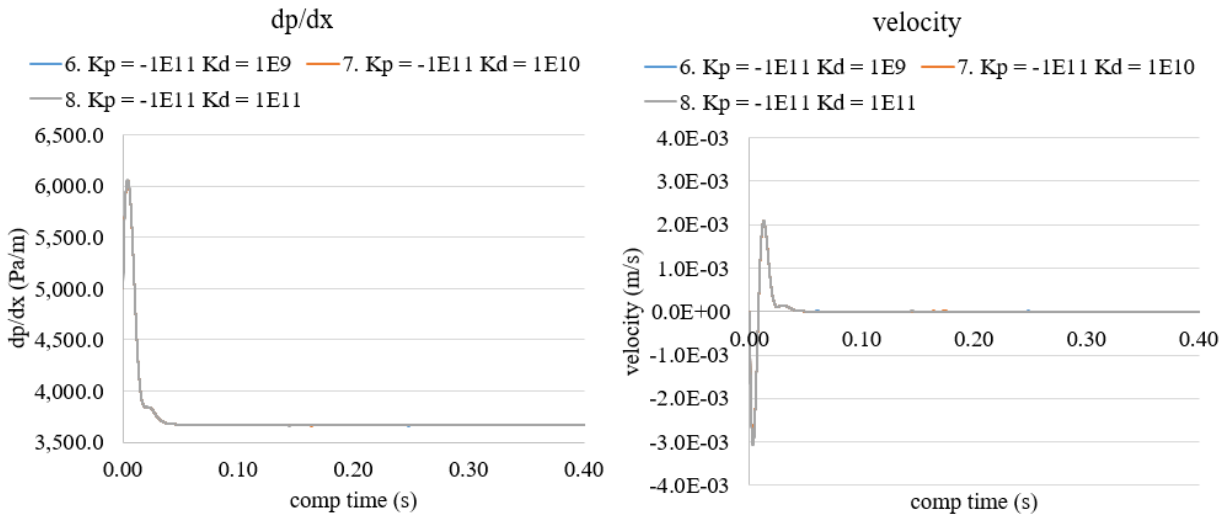


(b) Velocity change with time. Plots of  $K_D = 1E9 \sim 1E12$  overlap.

Figure 3.15. Tuning results of  $K_P = -1.0E12$  and  $K_D = 1E9 \sim 1E13$ .

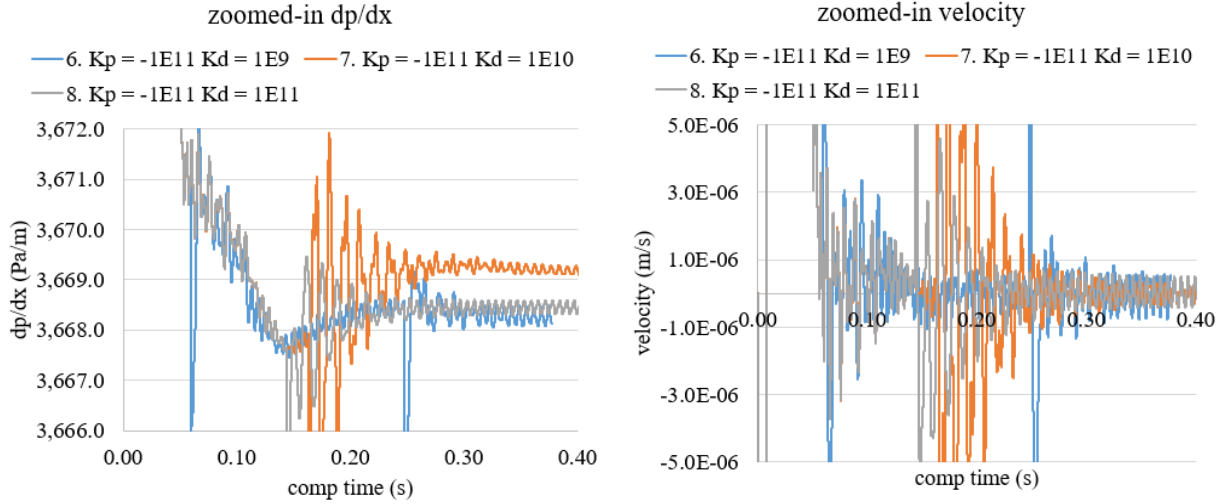
Since  $K_D$  should not be more dominant than  $K_P$ , in the tuning tests of  $K_P = -1.0E11$ , only  $K_D = 1E9$  to  $1E11$  are selected and the results are depicted in Figure 3.16 (a). The difference under three  $K_P$  parameters are not observable, therefore the plots are zoomed-in in Figure 3.16 (b), from which  $K_D = 1E10$  (orange plots) has the minimal fluctuation. However, the other two  $K_D$  values still produce zero velocity integrals eventually. Aside from that, the eventual pressure gradient in Figure 3.16 (b) are all approximately  $3669 \text{ Pa/m}$ , and the relative differences among them are all below 0.05%. Therefore, the three  $K_D$  values in this tuning test can all be used in PID control. This is expected since in traditional PID controller, the derivative component always has the smallest effect on control compared with proportional and integral terms.

Figure 3.16. Tuning results of  $K_P = -1.0E11$  and  $K_D = 1E9 \sim 1E11$ .



(a) Overall plots.

Figure 3.16. (continued)



(b) Zoomed-in plots.

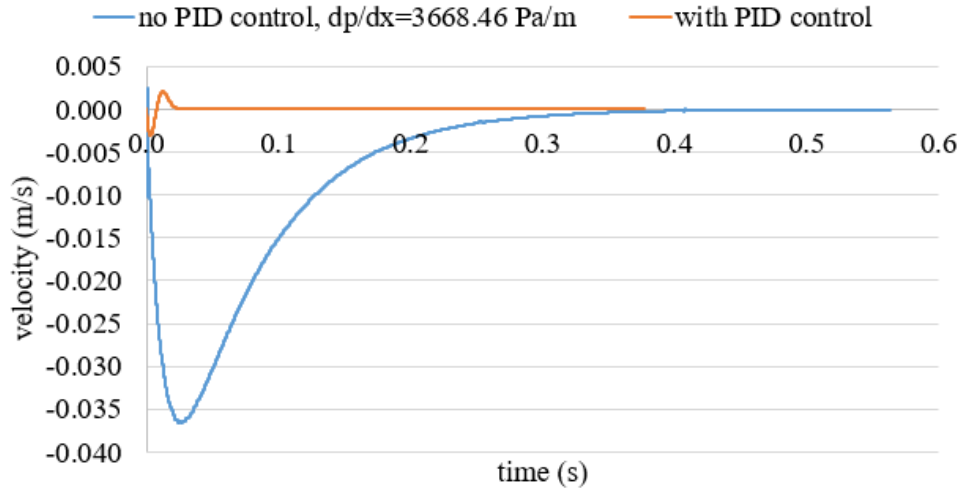
The tuning tests identified the best combination of control coefficients for producing accurate and responsive CCFL control. The proportional, integral, and derivative effects are balanced well together, which produces the optimal control effect. The eventual velocities obtained from all turning cases are all within  $\pm 1E - 6$  m/s which is accurate enough to meet the strict criterion of CCFL occurrence that is liquid velocity is zero. The recommended control coefficients are summarized in Table 3.4 and the best  $K_D$  should be one magnitude smaller than  $K_P$ . Limited tests using different geometry sizes find out that the recommended control coefficients can be used in cylindrical channels with diameters from 0.75mm to 4.0mm. However, if most of the material properties of the working fluids are 10 times different than the values used in Table 3.2, a further tuning test is recommended.

Table 3.4. Recommended control coefficient sets in PID pressure gradient controller.

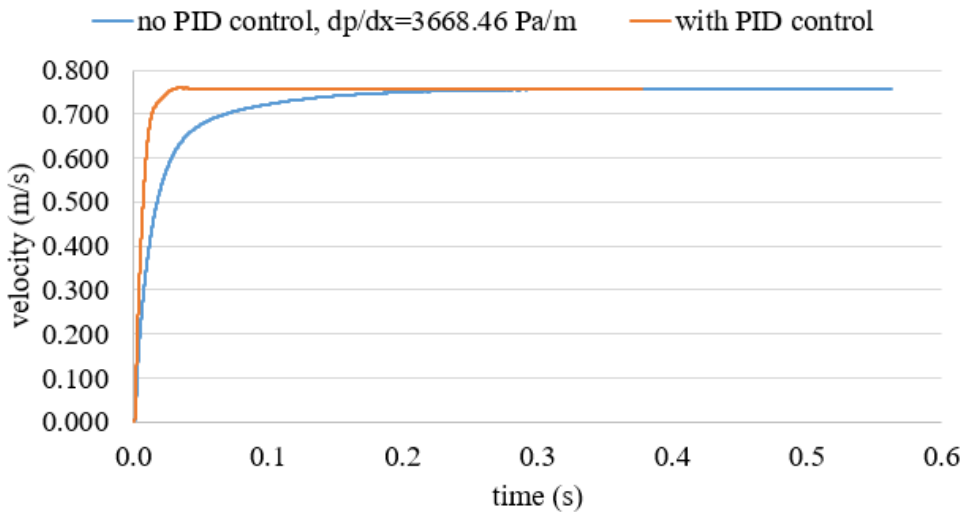
$K_P$	-1.0E11	-1.0E12
$K_I$	1.0	1.0
$K_D$	1.0E9, 1E10, 1.0E11	1.0E9, 1E10, 1.0E11, 1.0E12

### 3.3.2 Verification of PID pressure gradient controller

A verification test is conducted after the tuning tests has revealed the pressure gradient for obtaining a zero liquid flow rate, or CCFL. At the quasi-steady state, the average pressure gradient is  $3668.46 \text{ Pa/m}$ . This value is used in this verification test as the input to confirm if CCFL can be achieved without PID controller. The parameters in this verification test are still the same as those in Table 3.2, but the only change is that the PID pressure gradient control is deactivated. Figure 3.17 (a) shows how the velocity change under a constant pressure gradient  $3668.46 \text{ Pa/m}$  is compared with PID controlled flow behavior. It is clear that eventually the average liquid velocity on the xyzts probe plane achieves zero. Quantitatively averaging the velocity at steady state obtains  $-5.57E - 05 \text{ m/s}$  which confirms the observation as well. Therefore, although PID control is dependent on the cross-sectional liquid velocity integral rather than the volumetric liquid velocity integral, the pressure gradient obtained from the controller can still produce a zero liquid phase velocity. In addition, the gas phase averaged velocity obtained from bubble tracking data is plotted (Fang, 2016). As Figure 3.17 (b) shows, the gas phase also achieves a steady state and reaches the same gas velocity when PID is activated. This test further confirms the accuracy of the PID pressure gradient controller. Moreover, with the PID control, the flow rate actually achieves zero faster than without it. Comparing the velocity changes in Figure 3.16 (a), CCFL is achieved within  $0.2s$  under PID control, which is only one third of the time without PID control. This is because when there is a constant pressure gradient, the two-phase flow requires a longer time to develop when the gas moves upwards and liquid drains down, until interfacial shear, wall shear, and gravity achieves a balance so that the liquid flow rate can be zero. This process is very similar to the condition in experimental studies that a constant pressure drop is applied into the facility loop and the two phase develops accordingly.



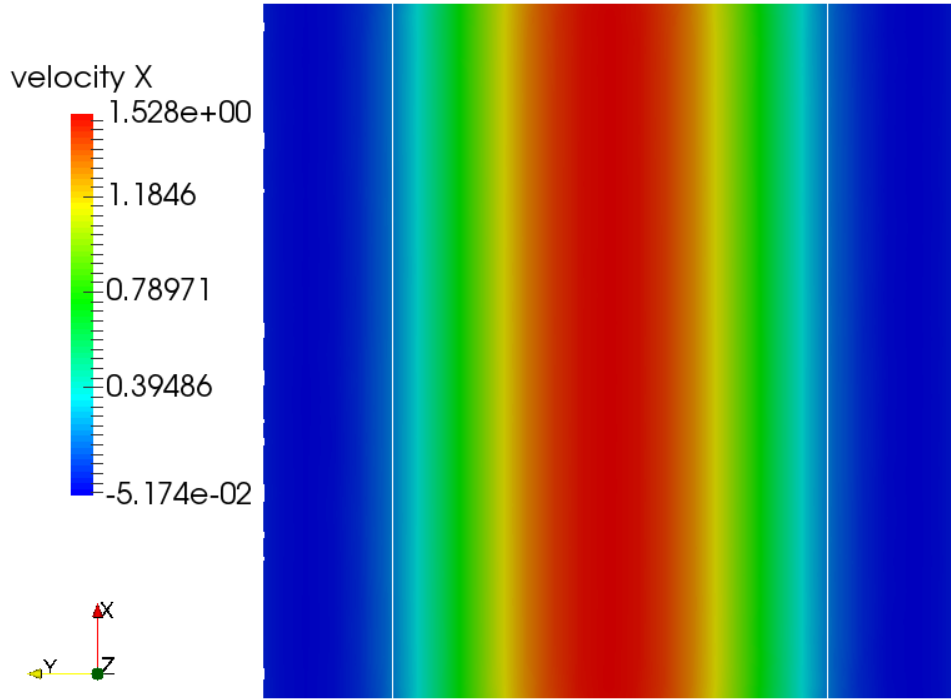
(a) Liquid cross-sectional averaged velocity.



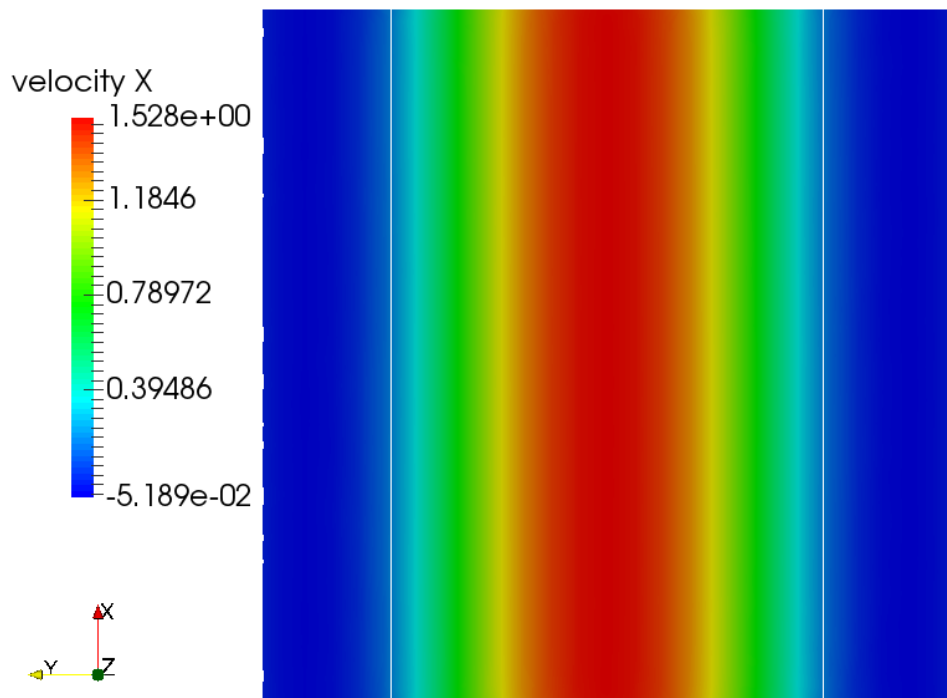
(b) Gas volumetric averaged velocity.

Figure 3.17. Verification test comparing two-phase velocity changes where PID control is deactivated (flow driven by a constant pressure gradient) and activated (flow driven by PID controller).

The two-phase velocity distributions with and without PID control are depicted and compared in Figure 3.18. The color bars in Figure 3.18 indicate the minimum and maximum  $x$  velocities. The maximum velocities are exactly the same and the minimum velocities only have a relative difference of 0.3%. The annular flow distributions are almost identical. It is clear that with PID control, the two-phase fluid dynamics can still be properly captured.



(a) With PID control.



(b) Without PID control.

Figure 3.18. Two-phase fluid dynamics comparison with and without PID control.

### 3.3.3 Robustness of PID pressure gradient controller

The robustness tests are conducted based on different initial condition (test #1) and different velocity goal (test #2) in the PID pressure gradient controller simulations. Compared with the parameters used in Table 3.2, test #1 changes the initial  $x$  pressure gradient from 5000.0 to 0.0. Since the eventual pressure gradient to achieve zero velocity integral is 3669  $Pa/m$  (Figure 3.16 (b)) initial pressure gradient in test #1 is farther from the expected pressure gradient, which is more difficult for the controller to achieve the target value.

The result of test #1 is plotted in Figure 3.19. Due to initial pressure gradient being zero, the effect of gravity is dominant in driving the liquid flowing towards the  $-x$  direction, which yields a severe back flow. However, PID pressure gradient controller is still robust enough to bring the velocity integral back to positive and eventually zero. The quasi-steady state pressure gradient is 3668.65  $Pa/m$  which is almost identical with the reference value 3669  $Pa/m$ . This test also verifies the reliability of the PID pressure gradient controller and that the results do not depend on initial flow condition.

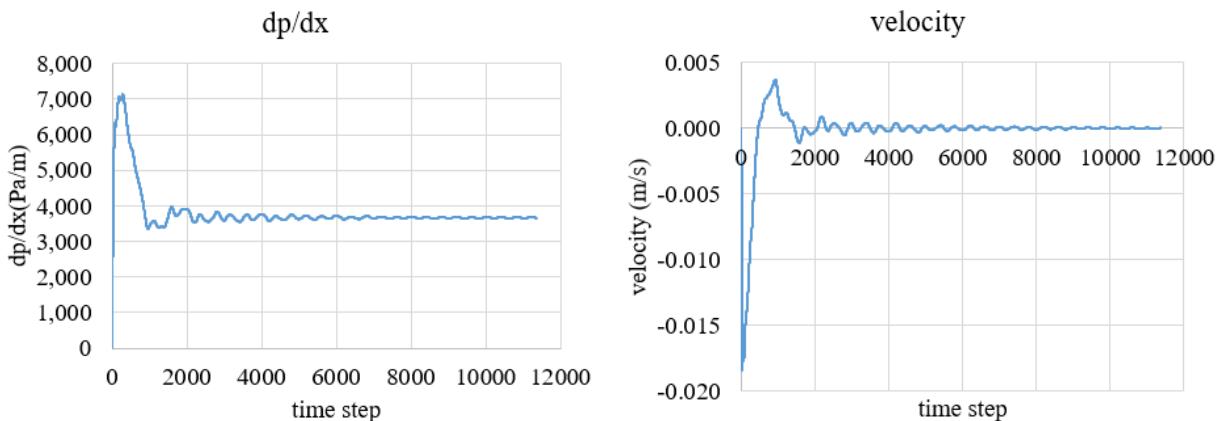


Figure 3.19. Robustness test #1 result where initial  $x$  pressure gradient is 0.0.

Compared with the parameters used in Table 3.2, robustness test #2 change the  $x$  velocity goal in PID control from 0.0 to be 0.5  $m/s$ . This condition is not for generating CCFL, but for a more

general test of the PID pressure gradient controller performance. With a significant increase of liquid velocity, the gas core velocity increases greatly, and the two-phase flow becomes turbulent. As Figure 3.20 depicts, the flow is not annular anymore, and the interface is highly distorted, even generating droplets entrained by the gas column. In addition, compared with the maximum velocity magnitude in Figure 3.16 ( $2.0E - 3 \text{ m/s}$ ) and Figure 3.19 ( $4.0E - 3 \text{ m/s}$ ), the maximum velocity magnitude in this test is  $1.1 \text{ m/s}$ , which is 250 to 500 times higher, so it is very challenging for the numerical solver. However, the PID pressure gradient controller is still robust enough to handle such condition and achieves a quasi-steady state eventually.

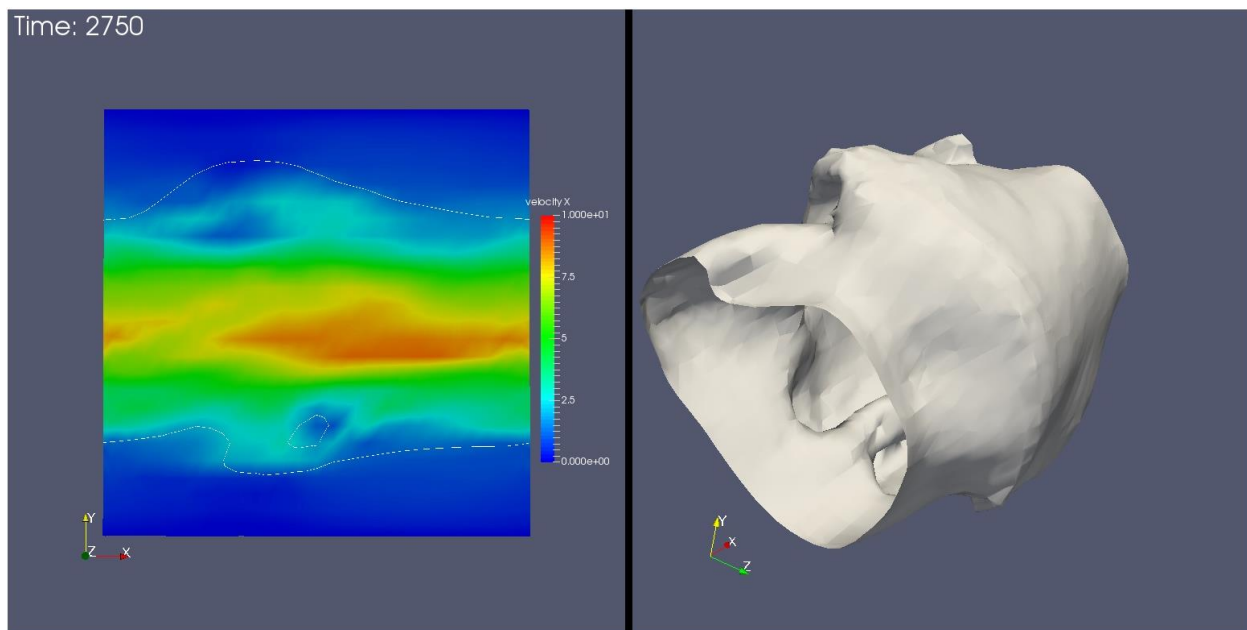


Figure 3.20. Turbulent flow regime and highly deformed interface in robustness test #2.

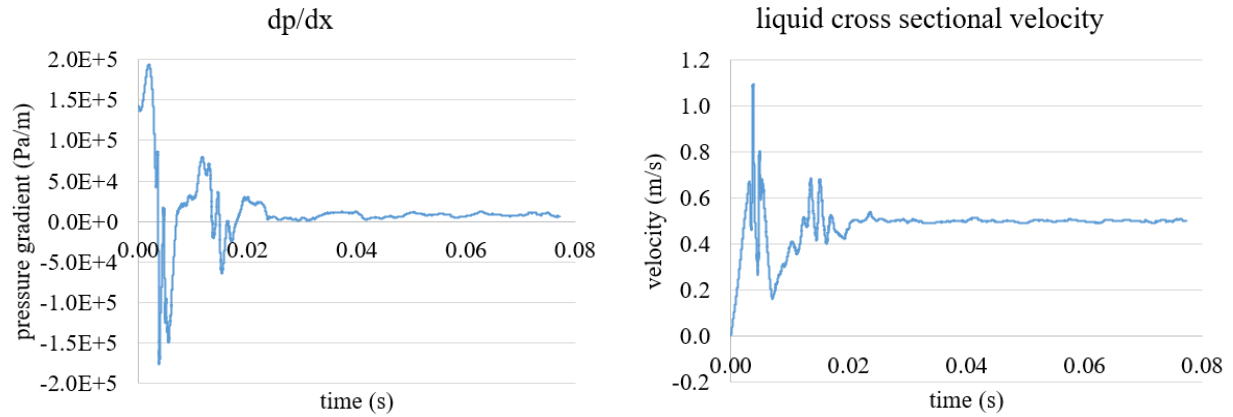


Figure 3.21. Robustness test #2 result where  $x$  velocity goal in PID control is  $0.5\text{m/s}$ .

### 3.3.4 Computational cost evaluation of the PID pressure gradient controller

The speed test compares running time of the code by gradually adding new developed capabilities. The speed is normalized to be the number of core hours required to compute 1 billion elements for one time step ( $N_{speed}$ ). The lower the  $N_{speed}$  is, the better the scaling performance and the quicker the code executes. An empirical reference value of  $N_{speed}$  is 100-200 is provided, which comes from speed tests on the supercomputer *Mira* (Jansen, Kenneth E. et al., 2017). The following are four cases running on the local cluster *Insight* and the speed of each test is evaluated using 64 processors:

1. A regular single-phase flow using liquid properties in Table 3.2 as the working fluid.
2. Addition of PID pressure gradient control capability in case #1.
3. A regular two-phase annular flow (properties from Table 3.2).
4. Addition of PID pressure gradient control capability in case #3.

The above four cases were meshed with a fine mesh totaling 725,058 elements, and 11,329 elements per core. The wall clock time collection does not include the beginning of the simulation when probe information was read into the solver. Table 3.5 summarizes  $N_{speed}$  for those test cases.

Table 3.5.  $N_{speed}$  (number of core hours to compute 1 billion elements per time step) for 4 test cases.

Case number	Simulation description	$N_{speed}$
1	Regular single-phase flow	146
2	Single-phase + PID pressure gradient controller	109
3	Regular two-phase annular flow	335
4	Two-phase + PID pressure gradient controller	195

When PID pressure gradient controller is activated either in the single-phase or in the two-phase runs,  $N_{speed}$  is even better than the original code version. It is because adding PID control changes the velocities in the simulation. As Figure 3.17(a) shows, the velocity magnitude under PID control is much lower than that without PID control. Therefore, the redistancing process takes less iterations to converge, which reduces the wall clock time for each time step. Even though the flow condition in each comparison set (Case 1&2, Case 3&4) are not identical,  $N_{speed}$  of the single-phase tests as well as the two-phase test with PID control (Cases 1, 2, and 4) are all in the reference range of *Mira* (100-200), which indicates that the parallel computation with newly added capability does not cause noticeable penalty. Since the velocity integral parallelization was reasonably implemented and there is no additional array acclaimed in PID pressure gradient controller, the speed should not be slow. Even for flow rate control, using xyzts probes to compute cross-sectional velocity integral is cheaper than computing the volumetric velocity integral in a three-dimensional domain. Therefore, the design and implementation of the entire PID pressure gradient controller is very efficient in the perspective of computation cost.

### 3.4 Chapter Summary

This chapter introduced the development, verification, and performance evaluation of the PID pressure gradient controller. The main goal of developing this controller is to efficiently adjust pressure gradient to accurately control the liquid velocity. One of the major applications is to produce counter current flow limitation in flow channels when the desired velocity integral is zero.

Compared with the existing PID bubble controller in PHASTA code, PID pressure gradient controller is more challenging in the perspective of robustness. In two-phase flow simulations, the inertia of liquid is much stronger than gas due to the higher density. PID bubble controller can have a fine control on the bubble since, compared with liquid, bubble inertia in two-phase flow is almost negligible even in an acceleration process. However, variations in liquid flow rate, especially the acceleration and deceleration across the whole domain, can easily destabilize due to high liquid inertia. Traditionally, in order to decelerate a laminar flow to stagnant, thousands of time steps are required to gradually stop the flow, however with the current PID pressure gradient controller, this process may happen within hundreds of time step. Even in turbulent two-phase flows, PID pressure gradient controller can still achieve a stable velocity integral. The robustness of this controller on changing liquid fields and maintaining stability significantly expands the capability range even in challenging flow conditions.

In CCFL studies, the transient phenomenon cannot be captured in experiments or simulations as the transition occurs too quickly. The recorded flow conditions are, for the majority of the time, post-CCFL without an accurate control on the liquid flow rate. PID pressure gradient controller can shed light onto the transient flow regimes when CCFL happens, which is irreplaceable by any traditional approaches. The evaluation of the flow regime of CCFL and the collection of high

resolution in-situ data will greatly benefit the development of Multiphase CFD (M-CFD) and thermal hydraulic models.

Aside from producing zero liquid velocity for studying counter current flow limitation, this controller was able to achieve other liquid velocities successfully as well. In addition, PID control on gas phase velocity can be easily achieved by changing  $\phi_i > 0$  to  $\phi_i < 0$  in Eq. (24), so researchers can obtain much richer dataset of flow field previously unavailable. The PID control methodology can also be utilized in other scenarios, such as controlling the heat flux to automatically generate the departure of nucleate boiling.

## Chapter 4. RESULTS OF BUBBLE IN COUNTER CURRENT FLOW

Foundational counter-current flow simulations for supporting more complex CCFL studies are presented in this Chapter. The major goal of this Chapter is to demonstrate the predictive capability of CCFL phenomenon using interfacial-capturing approach. The validation hierarchy of counter current flow limitation (CCFL) provides the connections of all supportive studies, including single bubble interfacial forces, single bubble topology changes, single-phase heat transfer, and contact angle model. This research tackles the challenges in the thermal-hydraulics field of nuclear engineering on the closure law development of interfacial forces as well as the understanding of the CCFL mechanisms in the debris bed in the nuclear reactor.

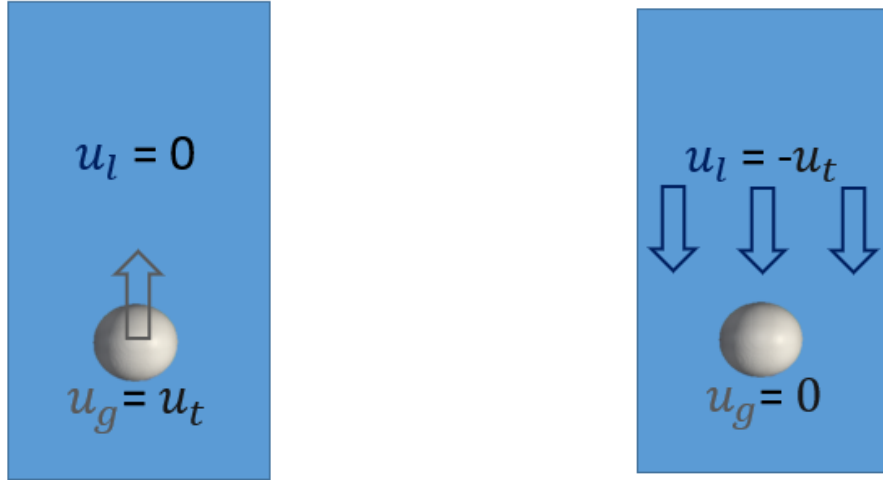
### 4.1 PID bubble controller

The proportional-integral-derivative (PID) bubble controller was previously developed and implemented in PHASTA to control the bubble at a proposed position (Thomas et al., 2015). In recently published experimental bubble studies, the experimental method resembles the PID bubble controller methodology (Dueñas, 2019; Salibindla et al., 2020), where liquid is injected from the inlet plane towards the bubble and the flow rate is controlled such that the bubble rises extremely slowly. This experimental method further validates our PID approach in bubble control simulations.

In both the experiments and simulations, the reverse process is equivalent to switching the reference frame from the container to the bubble. In the container-based frame, the bubble terminal velocity is  $u_g = u_t$  and the stagnant liquid has a velocity of  $u_l = 0$ . In the bubble-based frame,  $u_g = 0$  and  $u_l = -u_t$  where the negative sign denotes downward movement of the liquid. Therefore, the relative velocity ( $u_r$ ) in both frames are equal to  $u_t$ .

$$\text{Container-based: } u_r = u_g - u_l = u_t - 0 = u_t \quad (33)$$

$$\text{Bubble-based: } u_r = u_g - u_l = 0 - (-u_t) = u_t \quad (34)$$



(a) Realistic condition (reference system: container-based).

(b) PID controlled condition (reference system: bubble-based).

Figure 4.1. Illustration of coordinate system transform from realistic upflow conditions to PID controlled environment at steady state.

According to Galilean transformation theory, with identical  $u_r$  in the two reference frames, the mass, momentum, and energy are invariant (McComb, 1999), so interfacial forces will not change either. Such invariance is also valid in shear flows, where relative velocity is defined as the difference of the bubble velocity and the liquid velocity at the bubble center.

Using a steady state balance on the bubble, the net force on the bubble should be zero. Therefore, PID bubble controller allows the interfacial forces to be extracted as the opposite of the control forces:

$$F_D \equiv -\frac{1}{2}C_D\rho_l A_b u_r^2 = F_{cx} \quad (35)$$

$$F_T = |\vec{F}_L + \vec{F}_W| = F_{cy} \quad (36)$$

On the left hand sides,  $F_D$  is the drag force,  $F_T$  is the transverse force normal to the flow direction, which can be decomposed into the lift force  $F_L$  and the wall force  $F_W$ . On the right hand sides,  $F_{cx}$  and  $F_{cy}$  are the control force in the  $x$  and the  $y$  directions. In the drag force definition,  $C_D$

is the drag coefficient, and  $A_b$  is the bubble cross sectional area. The relative velocity  $u_r$  between the bubble and the liquid is a major input parameter of the PID bubble controller. It is worth to mention that under PID bubble controller, gravity field is deactivated so  $F_{cx}$  is equal to buoyancy force at the steady state.

$$F_B \equiv (\rho_l - \rho_g)gV_g = F_D = F_{cx} \quad (37)$$

If the bubble is at the centerline of the domain, wall forces from the two walls cancel each other thus only the lift force remains in the lateral direction. This condition is also valid when the bubble is sufficiently far from the wall.

$$F_T = F_L \equiv -C_L\rho_l V_b u_r \frac{du_l}{dy} = F_{cx} \quad (38)$$

In the lift force definition,  $C_L$  is the lift coefficient,  $V_b$  is the bubble volume, and  $Sr = du_l/dy$  is the liquid velocity gradient or the shear rate.

The PID control model has three components: the proportional, integral, and derivative terms, respectively. In the bubble control scenario, the proportional component takes into consideration the bubble location changes with respect to the initial location. Next, the integral component averages the time-history of control forces. Finally, the derivative component will conduct derivatives on the bubble location and bubble velocity, which are velocity and acceleration respectively. The PID bubble controller was previously implemented in PHASTA with the following control force equations (Thomas et al., 2015):

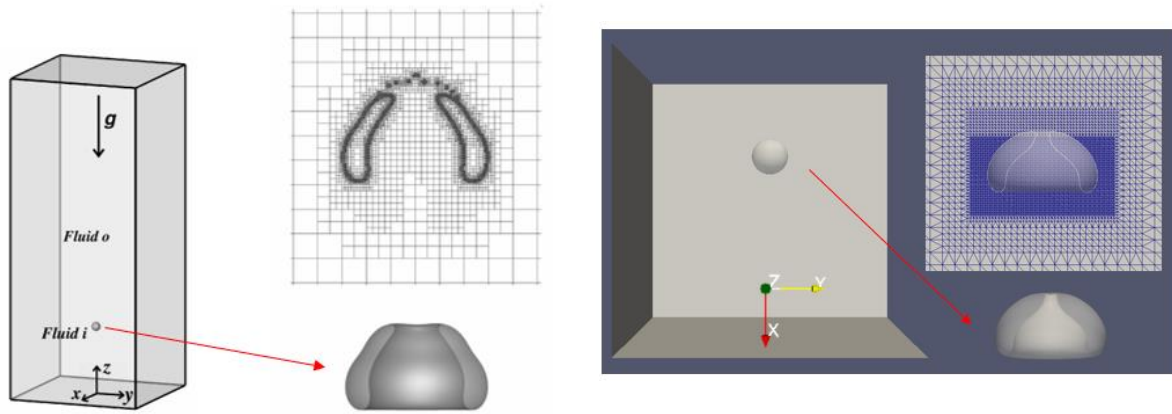
$$F_{ci}^{(n+1)} = c_1 \bar{F}_{ci}^{(n)} + c_2 \left[ F_{ci}^{(n)} + c_3 dx_i^{(n)} + c_4 v_i^{(n)} + c_5 dv_i^{(n)} \right] \quad (39)$$

Above,  $F_{ci}^{(n+1)}$  is the control force at the new time step (all terms with  $(n)$  are older time steps) and  $F_{ci}$  is the control force along the  $i$  direction. In the presented studies, control forces are enabled in all 3 directions ( $i = x, y, z$ ).  $c_j$  for each  $j \in \{1, 2 \dots 5\}$  is the constant coefficient for

each proportional ( $dx_i$ ), integral ( $\bar{F}_{ci}^{(n)}$ ), and derivative ( $v_i$  and  $dv_i$ ) component. Among them,  $\bar{F}_{ci}^{(n)}$  is the summation of historical control forces at each time step  $n$ .

$$\bar{F}_{ci}^{(n)} = \sum_{k=1}^{n-1} F_{ci}^{(k)} \quad (40)$$

PID bubble controller is beneficial for both interfacial force and interface topology studies. From the perspective of interfacial force evaluation, PID bubble controller can study individual interfacial forces. In traditional studies of a bubble in the shear flow, the distance from the bubble to the wall is constantly changing as the bubble moves. PID bubble controller avoids the change in the wall distance thereby separates the wall effect with shear-induced lift on the bubble. PID bubble controller coupled with unstructured mesh provides significant advantages in bubble topology studies. Since the bubble's location is fixed, the locally refined unstructured mesh around the interface is sufficient to resolve the deformation, eliminating the need for adaptive meshes (Figure 4.2). Also, a relatively small computation domain can be utilized for all deformation and break-up regimes for each bubble size. In addition, postprocessing the bubble topology evolution does not require additional procedures in experiments or other DNS to align bubble centers from different trajectories. With the mass center of bubble maintained at one location using PID controller, the bubble deformation relative to the initial shape can be observed and compared directly.



(a) Adaptive refinement (Tripathi et al., 2015) without PID bubble controller. (b) Pre-designed local refined mesh With PID bubble controller.

Figure 4.2. Mesh comparison without and with PID bubble controller.

Validation and verification of accurate estimation of lift and drag forces by the PID bubble controller has been achieved for small bubbles in the water-air condition (Thomas et al., 2015). The drag coefficients varied with  $Re_b$  and obtained from the PID bubble controller achieved nearly identical magnitudes with the experimental correlations (Tomiyama, Akio et al., 1998). As for medium size bubbles, the lift and drag coefficients in viscous shear flows and turbulent flows agree well with previous experimental studies (Feng and Bolotnov, 2017c). The transverse force at wall distance equal to bubble size was also validated and verified for viscous shear flows (Feng and Bolotnov, 2017a).

#### 4.2 Bubble interfacial force studies

With the bubble interfacial force studies, the confidence of the interface being well-resolved by the unstructured mesh and PID bubble controller can be built. Specifically, as CCFL is driven by interfacial shear, the bubble interfacial force studies in shear flows serve as fundamental research for CCFL condition.

This study aims to verify the transverse force (the net sum of the lift force and the wall force) obtained from PID bubble controller in shear flows to support the interfacial force in CCFL studies,

especially under the PID controller. The transverse force is examined based on the effects of wall distance, bubble deformation, and relative velocity between the bubble and the liquid. This section presents a comprehensive expanded study of Feng and Bolotnov's work (Feng and Bolotnov, 2017a) in which they only studied the single distance to the wall location:  $L/D = 1$ . A domain size study is also conducted as a supplementary work.

#### 4.2.1 Simulation setup

Single bubble two-phase simulations are set up in a cuboid computation domain. Figure 4.3 depicts the cross section of the domain with three edges to be  $L_x = 18mm$ ,  $L_y = 54mm$ , and  $L_z = 18mm$  in streamwise ( $x$ ), lateral ( $y$ ), and spanwise ( $z$ ) directions, respectively. A bubble of with a diameter of  $D = 3.52mm$  is located at  $(L_x/3, L_y/2, L_z/2)$  mm on the centerline of the domain. The bubble diameter maintain the value used in the previous work, which was verified by experimental bubble studies (Feng and Bolotnov, 2017a). The tetrahedral unstructured mesh is selected to allow for different refinement zones in the computation domain. The vicinity of bubble is resolved with the finest mesh (26 elements across the diameter) to obtain an accurate estimation of interfacial forces. With PID bubble controller activated, the bubble velocity is 0 and the liquid velocity is assigned as the velocity inlet boundary condition at  $x = 0$ .  $u_l$  is represented by the shear rate ( $Sr$ ) and the  $y$  coordinates.

$$u_l = Sr(y - y_c) + u_r \quad (41)$$

Here,  $y_c$  is the coordinate at the bubble center, and  $u_r$  is the relative velocity between the bubble and the liquid at  $y_c$ . This correlation is also applied on the top wall ( $y = L_y$ ) and the bottom wall ( $y = 0$ ). Symmetrical boundary conditions are assigned to the remaining domain faces normal to the  $z$  direction.

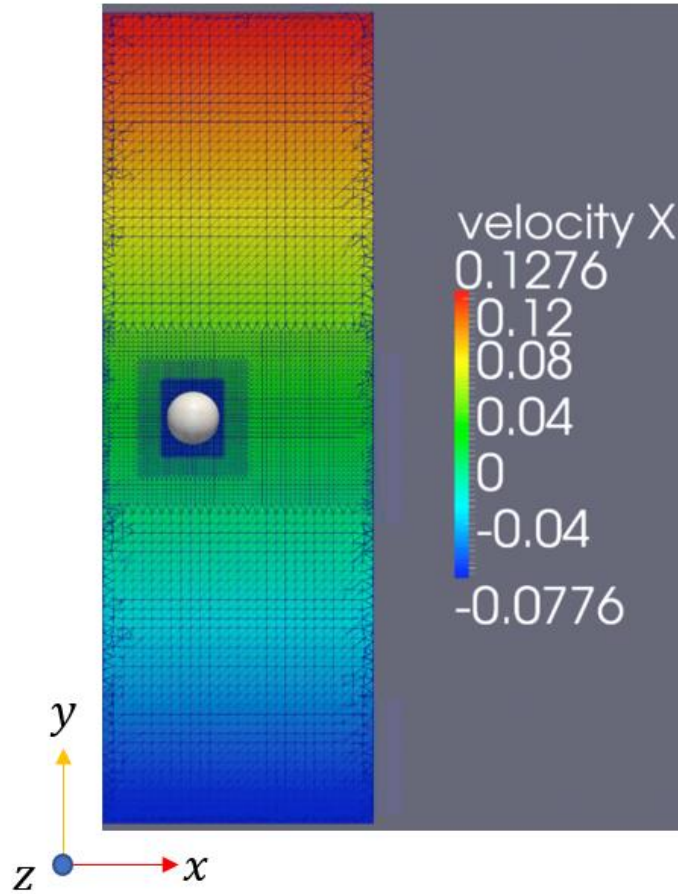


Figure 4.3. Computation domain and mesh configuration.

#### 4.2.2 Domain study

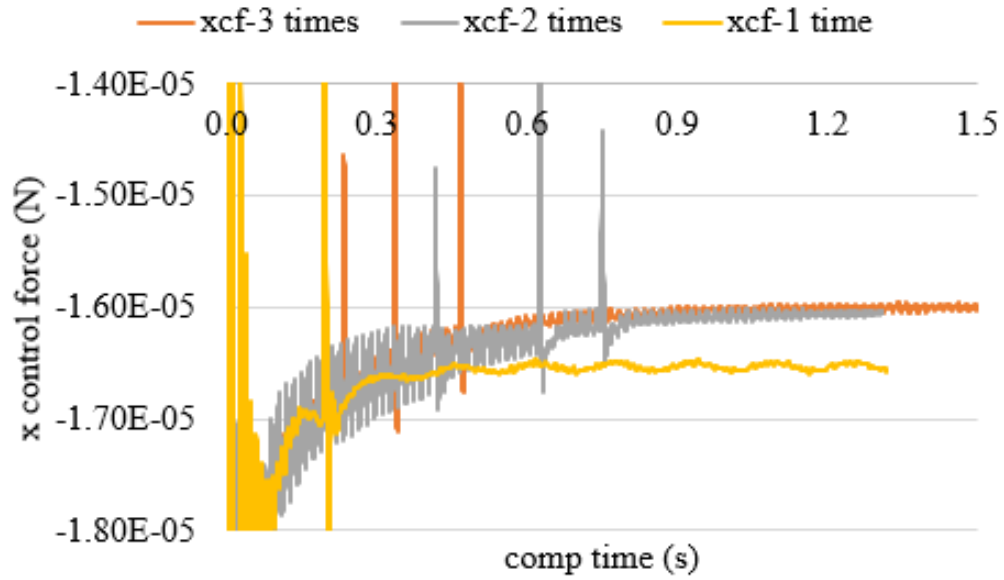
When the bubble is near to the wall, bubble-wall interaction will push the bubble away from the wall. Besides, the wall shear effect will accelerate the re-circulation of gas inside the bubble, potentially affecting the lift force as well. Another mechanism especially for lift force is that the non-symmetry of the wake of the bubble could lift the bubble. Therefore, if the domain is not wide enough in the  $y$  direction, the flows around the two walls may both affect the bubble in between, which cancels out the walls effect on the bubble. Small domain size in  $y$  direction also affects the bubble wake, which will change the local shear rate around the bubble interface, and then affect the magnitude of the lift force.

To quantify the effects of the wall on the interfacial forces acting on the bubble, three distances between two walls ( $L_y$ ) are selected as 18mm, 36mm, and 54mm. The simulation parameters are listed in Table 4.1.

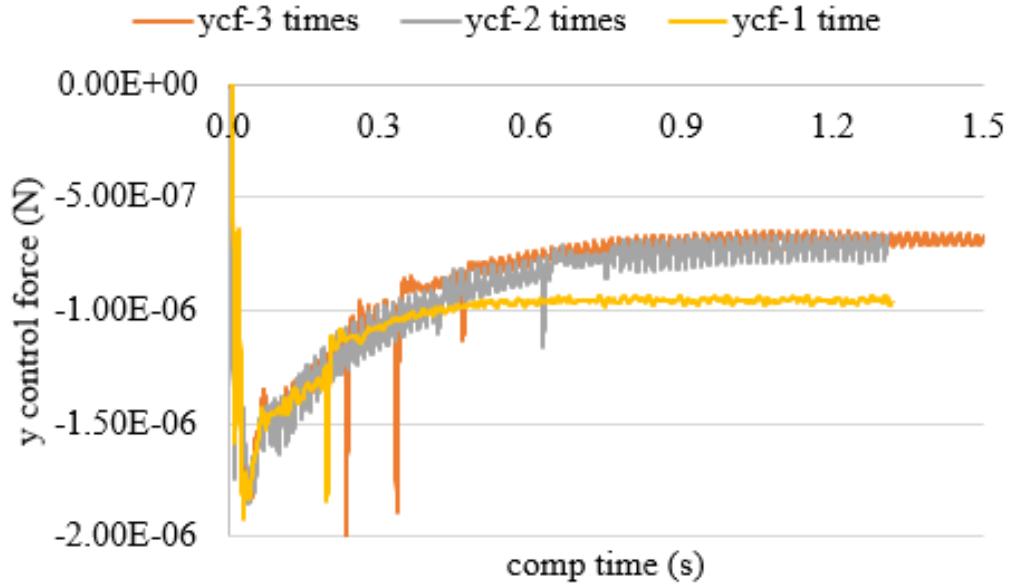
Table 4.1. Parameters for simulation setup.

Parameter	Magnitudes
Liquid density, $\rho_l$	$1154 \text{ kg} \cdot \text{m}^{-3}$
Vapor density, $\rho_g$	$1.161 \text{ kg} \cdot \text{m}^{-3}$
Dynamic viscosity, $\mu_l$	$0.019 \text{ Pa} \cdot \text{s}$
Bubble diameter, $D$	$3.52 \text{ mm}$
Shear rate, $Sr$	$3.8 / \text{s}$
Relative velocity, $u_r$	$0.025 \text{ m/s}$

Since the bubble is at the centerline of the domain, wall forces from the two walls negate each other, thus the only interfacial force on lateral direction is the lift force. The  $x$  control force and  $y$  control force on the bubble are plotted in Figure 4.4 (a) and (b) as the counter forces of the drag force and the lift force, respectively. It is clear that at the steady state, the interfacial forces of 2-times ( $L_y = 36\text{mm}$ ) and 3-times ( $L_y = 54\text{mm}$ ) domains almost overlap with each other. The relative differences are only 0.50% for  $x$  control force and 2.5% for  $y$  control force thus using any domain size between 36mm and 54mm should be reasonable so  $L_y = 54\text{mm}$  is selected.



(a) Streamwise direction control force.



(b) Lateral direction control force.

Figure 4.4. Control forces acting on the bubble. The legends 1 time, 2 times, and 3 times denote 18mm, 36mm, 54mm wall distances respectively.

### 4.2.3 Transverse force

The majority of the studies in this section were previously presented in published literature (Fan et al., 2018). The wall distance is described by  $L/D$ , where  $L$  is the distance from the bubble

center to the nearest wall (Figure 4.5) and  $D$  is the diameter of the bubble. The bubble deformation is described by the Weber number,  $We$  and the relative motion between two-phase is represented by the bubble Reynolds number,  $Re_b$ . The ranges of those three dimensionless numbers are provided in Table 4.2. The six  $L/D$  values covers the potential bubble locations across the flow channel along with the previous  $L/D = 1.0$  (Feng and Bolotnov, 2017a).

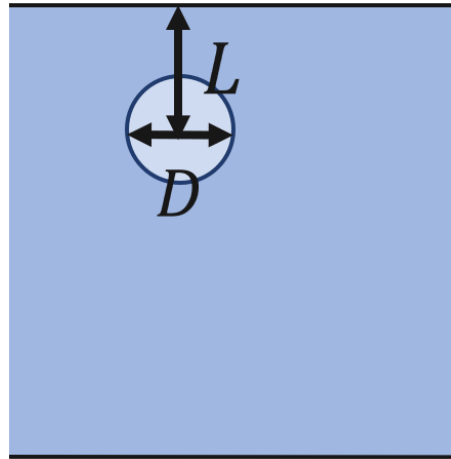


Figure 4.5. Illustration of  $L/D$ .

Table 4.2. Variables in low shear flow studies ( $Sr = 3.8/s$ ).

Parameter	Magnitudes
Dimensionless wall distance, $L/D$	1.25, 1.5, 1.75, 2.0, 2.25, 2.56
Weber number, $We$	0 – 6.0
Bubble Reynolds number, $Re_b$	5.34, 10.69, 21.38, 42.33, 59.86, 79.10

All the combinations of  $L/D$  and  $Re_b$  are carried out in the simulations. In each simulation,  $L/D$  and  $Re_b$  are fixed, and  $We$  is adjusted through changing the surface tension coefficient  $\sigma$  until  $y$  control force flips the sign. The simulation run achieves a quasi-steady state for each  $We$  before proceeding to another value of  $\sigma$  as Figure 4.6 illustrates. The transverse force is computed by averaging the  $y$  control force at each quasi-steady state condition.

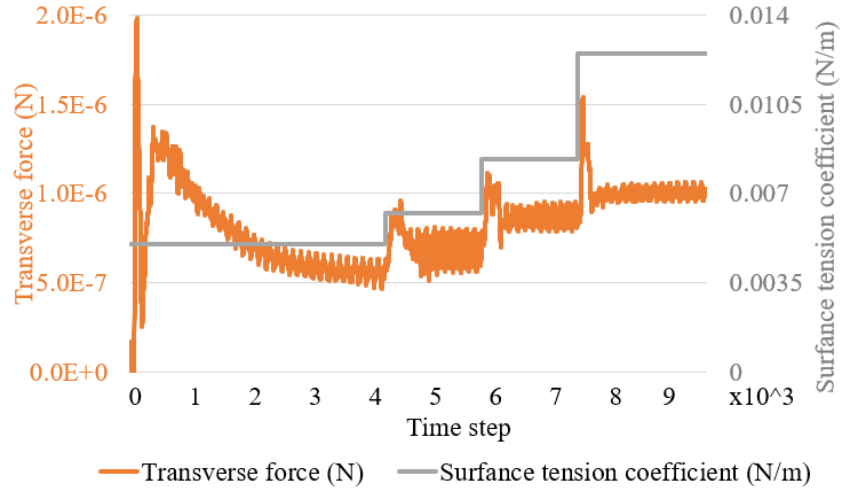
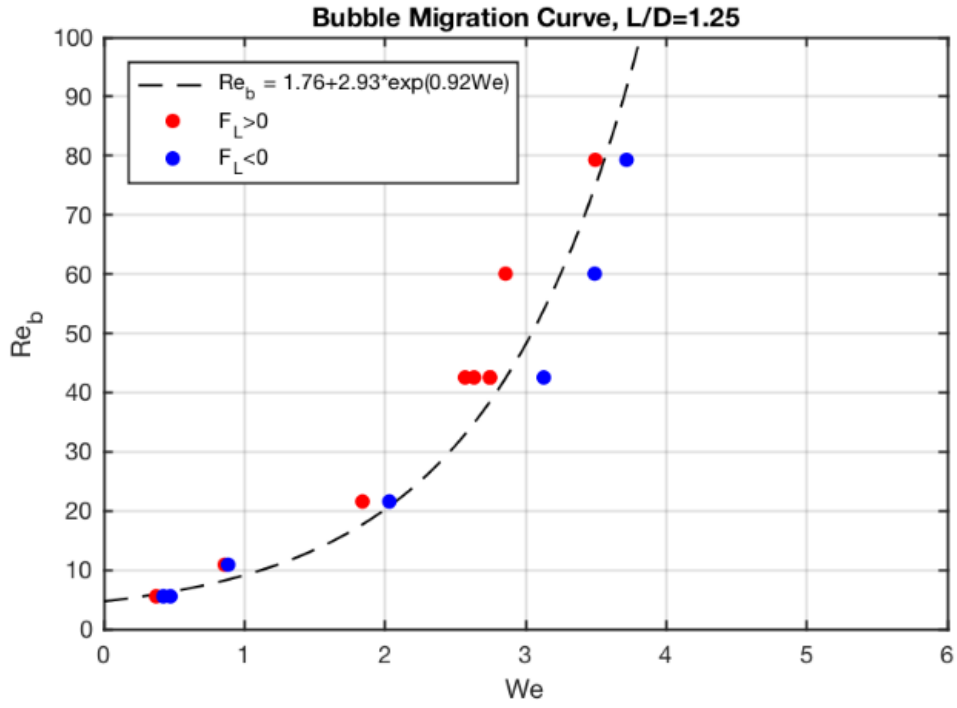


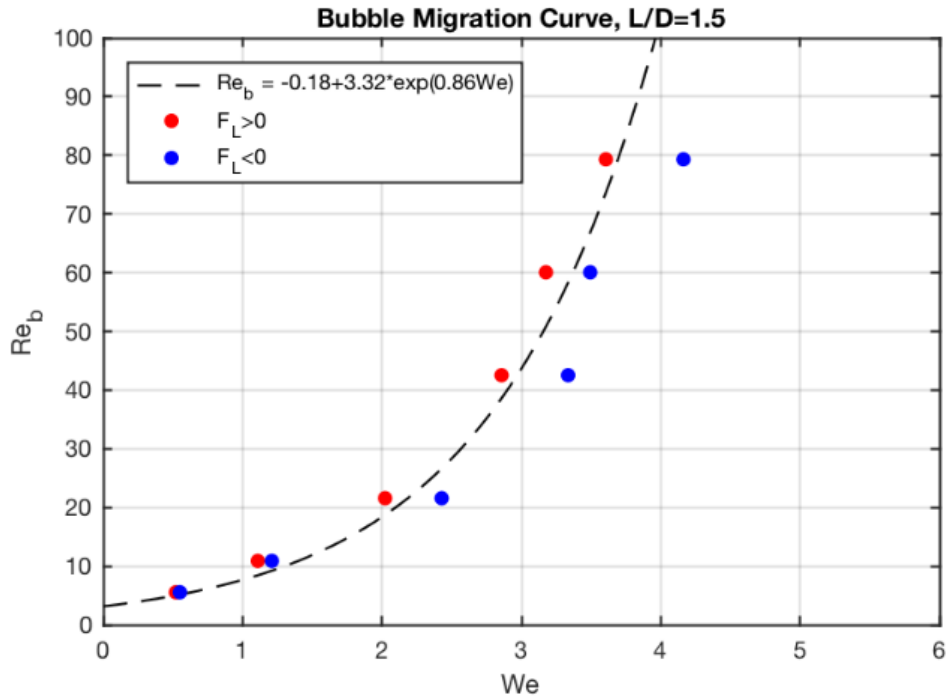
Figure 4.6. Quasi-steady state achieved under each surface tension coefficient.

The plots of  $Re_b$  vs  $We$  at each wall distance are shown in Figure 4.7 from  $L/D = 1.25$  to  $L/D = 2.56$ , where red dots denote transverse force pointing to the wall, reflecting bubble migrating to the wall; blue dots is opposite where the transverse force points to the center of the channel, indicating that more deformable bubble tends to be repelled from the wall. Comparing from (a) to (f), the data cluster moves towards higher  $We$ . In other words, as the bubble approaches the centerline of the domain, the wall-induced force is smaller, therefore, it requires the bubble to be more deformable to yield the transverse force to flip the sign. These observations are verified by the findings in (Tomiya, A. et al., 1995; Ervin and Tryggvason, 1997) and (Feng and Bolotnov, 2017a).

Figure 4.7. Transverse direction distribution with  $Re_b$ ,  $We$ , and  $L/D$ .

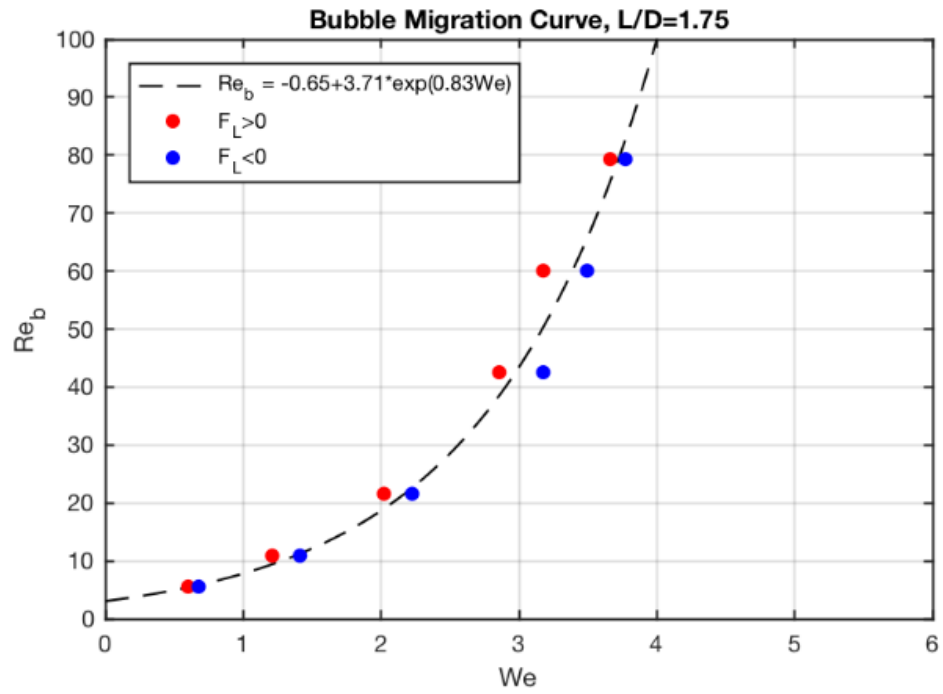


(a)  $L/D = 1.25$ .

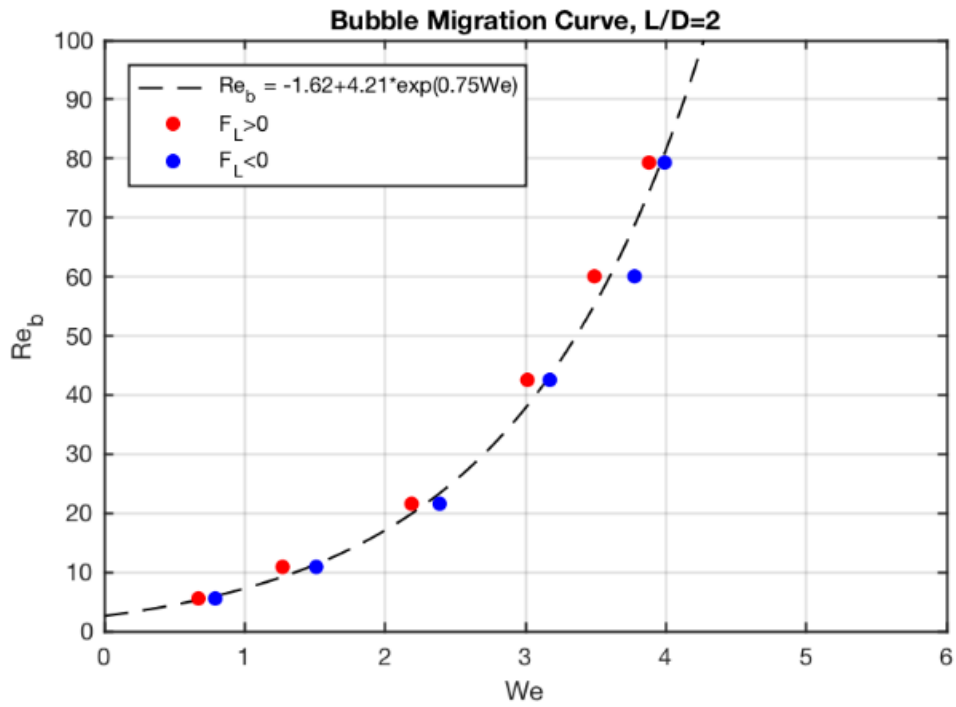


(b)  $L/D = 1.50$ .

Figure 4.7. (continued)

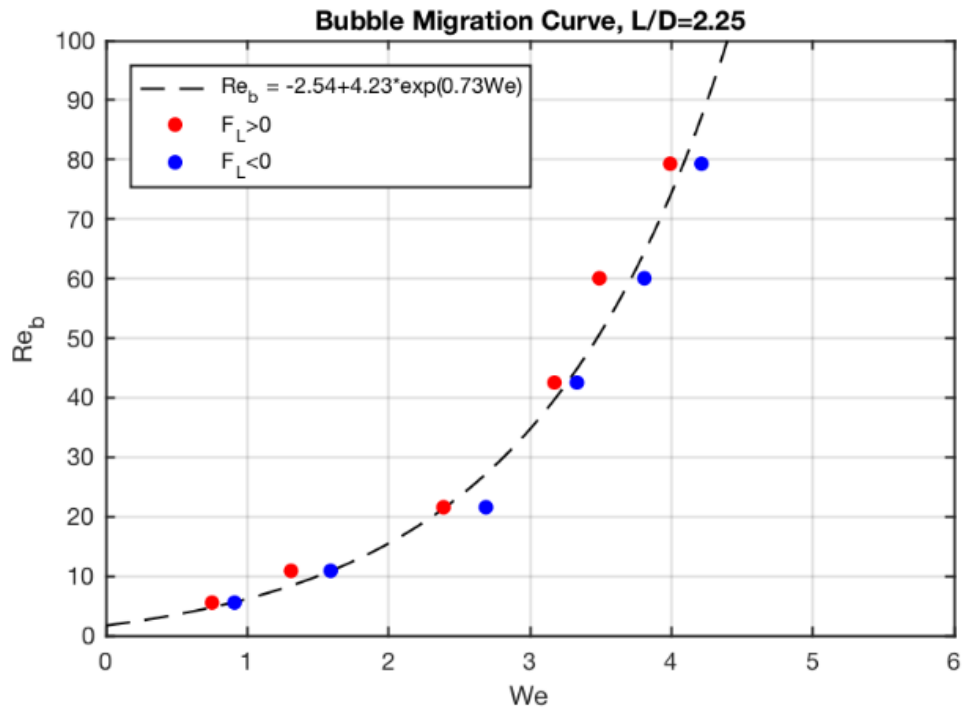


(c)  $L/D = 1.75$ .

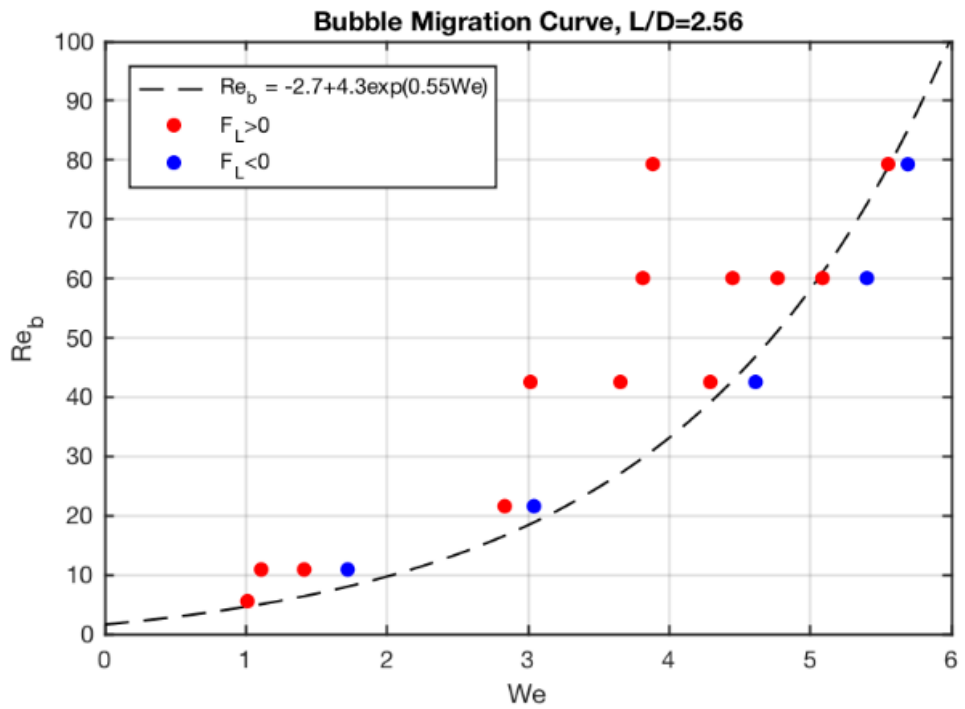


(d)  $L/D = 2.00$ .

Figure 4.7. (continued)



(e)  $L/D = 2.25$ .



(f)  $L/D = 2.56$ .

### 4.3 Bubble interface topology studies

In CCFL studies, PID control is integrated into two-phase simulation to produce the occurrence of CCFL, which typically involves complex interface topology change. To demonstrate that interface topology evolution under both PID control and natural conditions are invariant, this section compares single bubble interface topology evolution under PID-control and with a bubble simply rising in a liquid under buoyancy conditions. This is done through verification and validation (V&V) of the approach using published results. Ultimately, the capability and precision of the PID bubble controllers are assessed in revealing complex topology change. The majority of the studies in this section were previously presented in published literature (Fan et al., 2021).

#### 4.3.1 Simulation setup

As Section 4.1 illustrates, the PID bubble controller switches the reference frame from the container to the bubble. For rising bubbles in stagnant liquids driven by buoyancy, it corresponds to PID controlled bubbles in uniform liquid flow. The computational fluid domain is illustrated in Figure 4.8. The inlet plane and two moving walls have the velocity boundary condition all set to be  $u_l$ , thus the liquid has a uniform inflow velocity distribution towards the bubble in the controlled environment. The outlet plane has a pressure outlet boundary condition, and the remaining two domain faces are assigned with symmetry boundary conditions.

In Figure 4.8,  $x$  axis is the streamwise direction,  $y$  axis is the lateral direction, and  $z$  axis is the spanwise direction. The edge of the cube-shaped computation domain has a length of  $10R$  and the bubble is located at  $x = 3.3R$ ,  $y = z = 5R$  in all the simulations. The bubble size selections are based on published DNS and experimental studies (Bhaga and Weber, 1981; Tripathi et al., 2015; Sharaf et al., 2017). In studies where bubble sizes are implicitly contained in dimensionless numbers (Tripathi et al., 2015; Sharaf et al., 2017), the bubble sizes are selected to accommodate

the range of the dimensionless numbers. For studies with bubble size explicitly given (Bhaga and Weber, 1981), the bubble size is identical in the PID controlled simulation. Since the bubble is fixed, the domain size being  $10R$  is adequate for the bubble to deform and the bubble wake to form. Therefore, no matter how the bubble size varies, computation domain size and the distance from bubble center to the top inlet plane is always proportional to the initial bubble radius  $R$ .

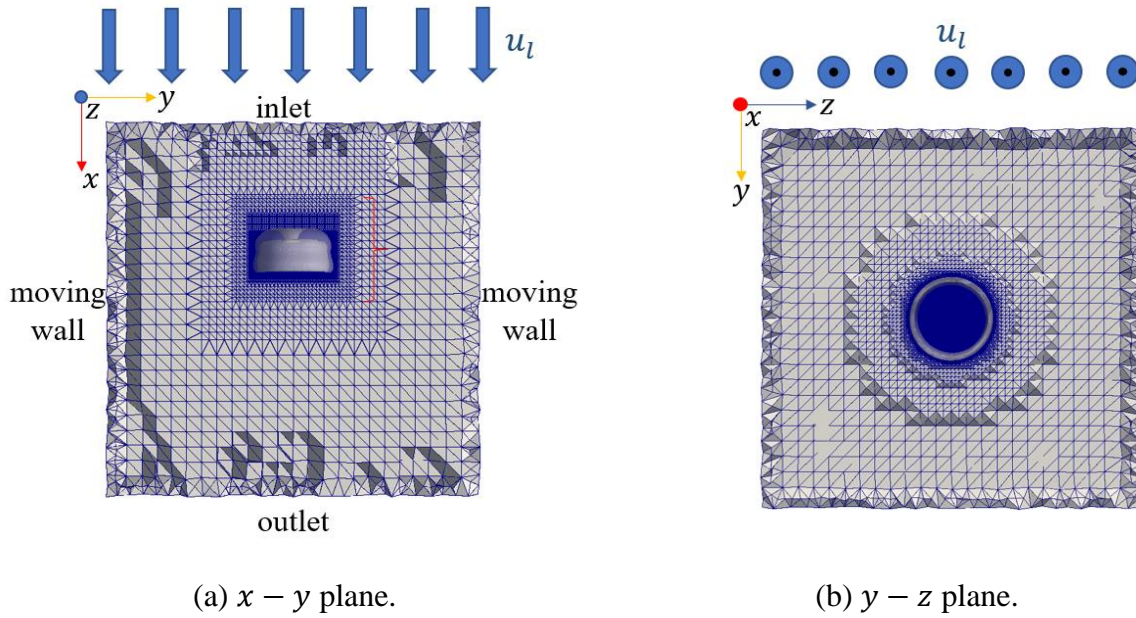


Figure 4.8. Computation domain and cylindrical mesh refinement zones.

Figure 4.8 also illustrates the spatial discretization with unstructured mesh for the deformed bubble. From the surrounding liquid to the bubble, the mesh is gradually refined. Since the bubble shape will most likely expand against the inflow, refinement regions are wider on lateral and spanwise directions ( $y - z$  plane) than the streamwise direction ( $x$  axis). Four different refinement zones are designed to better capture the interface distortion. Cylindrical refinement approach is utilized over box refinement as it better approximates bubble shape while also reducing computational cost. The near bubble wake region has the finest resolution due to the potential of forming thin film (Figure 4.8 (b)) and satellite bubbles after complex deformation and break-up.

### 4.3.2 Grid convergence study

A grid convergence study is performed to quantify the uncertainty from the computational mesh discretization (Roache, 1998). As Figure 4.8 (b) illustrates, the film of the deformed bubble is very thin which requires adequate spatial discretization to capture its topology. Therefore, the film sizes under different spatial discretization are measured and compared to support the choice of mesh configuration. This study also provides a reference of the mesh size selection for CCFL studies to well resolve the thin film formed under high interfacial shear.

Five mesh configurations depicted in Figure 4.9 (a)-(e) are selected to conduct the grid convergence study. The number of elements across initial bubble diameter are 34, 39, 45, 52, and 60 in each configuration, with a refinement ratio of  $r = 1.2$ . The bubble has a radius of  $R = 20 \text{ mm}$  and the relative velocity between the bubble and liquid is  $u_r = 0.8 \text{ m/s}$ . Severe deformation will happen at  $\sigma = 0.2 \text{ Nm}^{-1}$ ,  $\rho_l = 1403 \text{ kg} \cdot \text{m}^{-3}$ ,  $\mu_l = 1.0 \text{ Pa} \cdot \text{s}$ ,  $\rho_l : \rho_g = 1000$  and  $\mu_l : \mu_g = 100$ , and the wake side of the bubble will form a thin film (Figure 4.8 and Figure 4.9 (f)). It has traditionally been a challenge for simulations to resolve thin films but by utilizing level-set method in PHASTA it is possible to capture such severe interface distortions.

A grid convergence study can be used to estimate the uncertainty of spatial discretization via the well-developed approach of computing the grid convergence index (GCI) (Roache, 1998). As GCI reduces to 0, the numerical result theoretically approaches to the exact solution. For a group of meshes with a uniform refinement ratio  $r$ , GCI can be computed using a factor of safety ( $F_s$ ), the results from each mesh ( $f_i$ ), and the order of convergence ( $p$ ).

$$GCI = \frac{F_s |f_{i+1} - f_i|}{f_i (r^p - 1)} \quad (42)$$

Here, the factor of safety depends on the number of mesh configurations in the GCI study.  $F_s = 1.25$  when more than three meshes were involved (Roache, 1998).  $f_i$  and  $f_{i+1}$  are the results from finer and coarser grid resolutions.

The peripheral size of the thin film is a crucial parameter to describe deformability. The film has a ring shape on  $y - z$  plane (Figure 4.9 (f)) which corresponds to the same deformed bubble in Figure 4.8. The larger the ring, the more severe the bubble deformation is with respect to the initial state. Therefore, the outer radius of the film at the same  $x$  location is selected as the *GCI* metric in the grid convergence study and is computed with different elements across the initial bubble diameter ( $\#/D$ ).

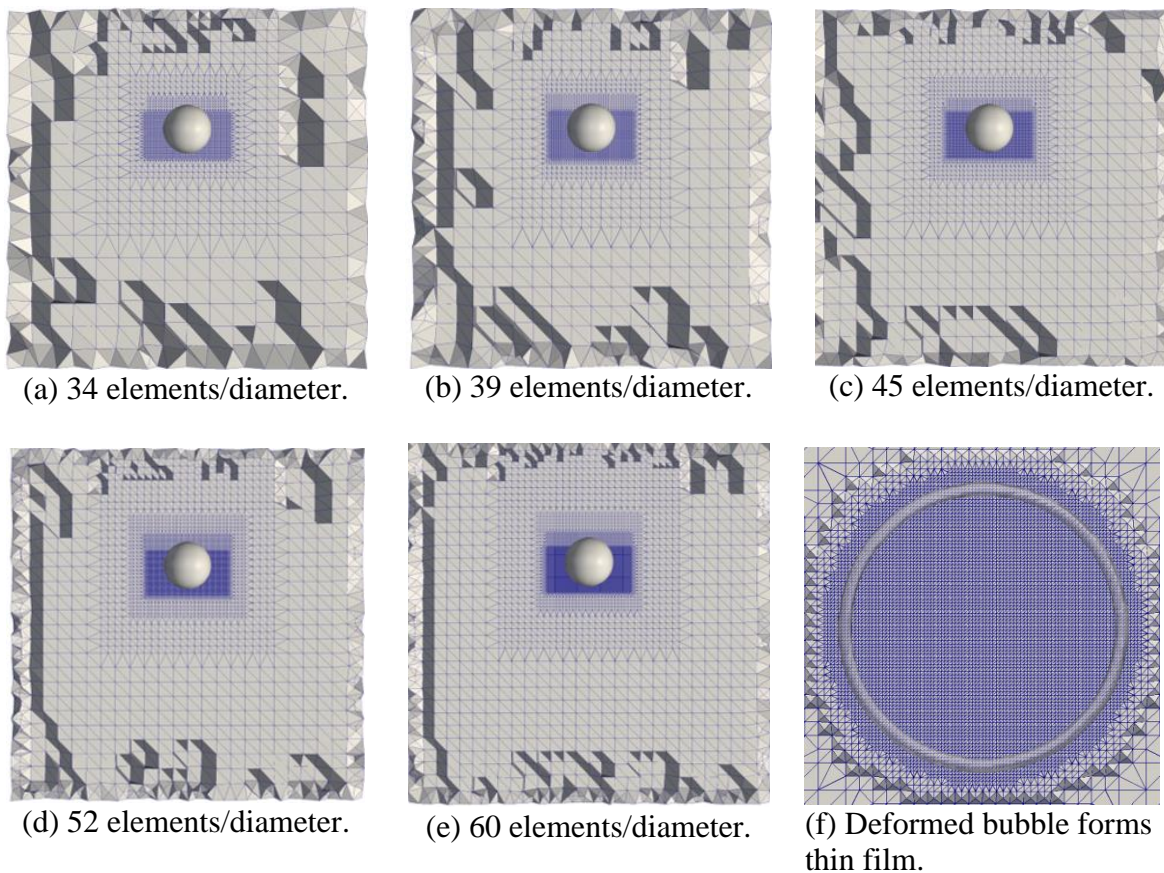
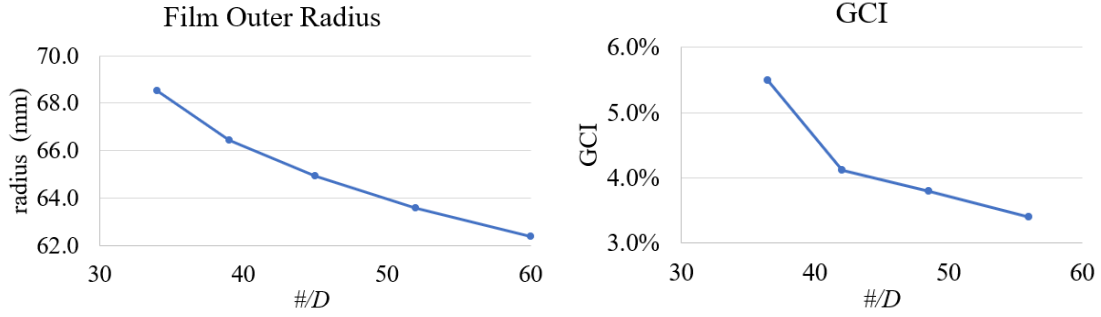


Figure 4.9. Comparison among uniformly refined meshes from (a) to (e) on  $x - y$  plane and zoomed-in mesh in  $y - z$  plane (f).



(a) Film outer radius.

(b) GCI reduced as the mesh is refined.

Figure 4.10. Comparison of film sizes among refined meshes and *GCI* varying with mesh configurations.

Table 4.3. Summary of mesh resolution, mesh size and *GCI* computation.

#/D	Mesh size	Film Outer Radius ( <i>mm</i> )	GCI
34	754,725	6.850E+01	-
39	1,164,089	6.645E+01	5.5%
45	1,752,438	6.494E+01	4.1%
52	2,649,215	6.358E+01	3.8%
60	3,807,249	6.239E+01	3.4%

From Figure 4.10, *GCI* curve is asymptotic to 0, which indicates that the numerical solution gradually approaches to the exact solution. The deformation will be the most accurate if using 60 #/D. However, Table 4.3 shows that the difference in *GCI* of 52 #/D and 60 #/D is only 0.4%, while 60 #/D requires an increase in mesh size of 43.7%. The minor gain in solution accuracy comes at the price of much larger computational cost, therefore 52 #/D is selected to conduct all the deformation studies as it is a more affordable mesh without significantly deteriorating the result accuracy. As a reference to CCFL studies in a cylindrical channel, in order to well resolve the formed thin film, there should be at least 52 elements across the cylinder diameter.

### 4.3.3 Verification

Simulation results of PHASTA are compared with published bubble deformation DNS studies (Tripathi et al., 2015). The differences between the presented simulation and Tripathi’s research are summarized in Table 4.4.

Table 4.4. Difference between presented simulation and the reference research.

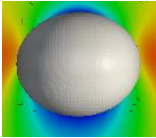
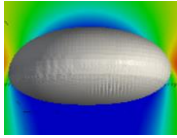
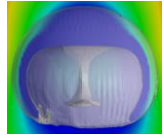
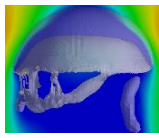
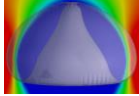
	(Tripathi et al., 2015)	Simulations in this paper
DNS code	Popinet’s DNS code (Popinet, 2003)	PHASTA code
Interface capturing method	Volume-of-fluid	Level-set
Reference system	Container-based (Figure 4.2 (a))	Bubble-based (under PID control, Figure 4.2 (b))
Domain size	(30R, 30R, 120R)	(10R, 10R, 10R)
Mesh type	Structured mesh	Unstructured mesh
Mesh refinement type	Adaptive	Pre-designed with multiple-level local refinements

The reference study provides rough ranges of Eotvos number ( $Eo$ ) and Galilei number ( $Ga$ ) and a representative bubble shape (Table 4.6) for different deformation dynamics (Tripathi et al., 2015). The simulation parameters in Table 4.5 were designed to accommodate the given ranges of  $Eo$  and  $Ga$  for each representative bubble, and the corresponding simulations reproduce the bubble topology (Table 4.6).

Table 4.5. Parameter design for verification.

Bubble radius, $R$ (mm)	2.0	2.0	20.0	2.0	20.0
Liquid density, $\rho_l$ ( $kg \cdot m^{-3}$ )	1154	1154	1800	1154	1403
Vapor density, $\rho_g$ ( $kg \cdot m^{-3}$ )	1.154	1.154	1.8	1.154	1.403
Dynamic viscosity, $\mu_l$ ( $Pa \cdot s$ )	0.025	0.019	10.0	0.05	1.0
Surface tension, $\sigma$ ( $Nm^{-1}$ )	0.2	0.025	0.067	0.0059	0.2
Relative velocity, $u_r$ ( $ms^{-1}$ )	0.275	0.198	0.8	0.198	0.8
Dimensionless numbers	$Eo = 0.89$ $Ga = 36.3$	$Eo = 7.23$ $Ga = 48.1$	$Eo = 432$ $Ga = 4.55$	$Eo = 97.4$ $Ga = 32.5$	$Eo = 112$ $Ga = 35.5$

Table 4.6. Verification of bubble deformation.

	$Eo \in (0, 30)$ $Ga \in (0, 40)$	$Eo \in (0, 20)$ $Ga \in (40, 500)$	$Eo \in (30, 500)$ $Ga \in (0, 50)$	$Eo \in (1, 500)$ $Ga \in (10, 500)$	$Eo \in (1, 500)$ $Ga \in (5, 500)$
(Tripathi et al., 2015)					
PHASTA with PID bubble controller					

The first four bubble deformation patterns (column 2- 5 in Table 4.6) can achieve a quasi-steady state, but the fifth bubble (last column) corresponds to an early stage deformation which will develop into an unsteady break-up, classified as a central break-up (Tripathi et al., 2015). The temporal topology change is also considered in the verification. Table 4.7 compares the predicted bubble deformations under identical normalized computation time ( $\tau$ ). Regardless of the bubble topology change or time varying shape change, from dimpled ellipsoid to uneven toroid, the generated results from the PHASTA PID controller exhibit high concurrency with those of Tripathi et al., further testifying its accuracy and versatility.

Table 4.7. Comparison of temporal topology change.

Normalized computation time	$\tau = 1$	$\tau = 2$	$\tau = 4$	$\tau = 5$
(Tripathi et al., 2015)				
PHASTA with PID bubble controller				

#### 4.3.4 Validation

To further gain confidence on the accuracy of interface topology under PID control, two experiments were selected as validation references, Bhaga and Weber's classical experiments on bubble deformation in viscous liquids, and Sharaf's experiment which was motivated by previously published DNS studies (Bhaga and Weber, 1981; Sharaf et al., 2017).

##### 4.3.4.1 Validation by classical experiment

Bhaga and Weber utilized aqueous sugar solutions with different concentrations to conduct air bubble deformation studies in stagnant liquids. They conducted a series of experiments on  $9.3 \text{ cm}^3$  bubbles aiming to understand the effect of viscosity on bubble deformation. Table 4.8 lists the unchanged parameters in each simulation case, and Table 4.9 compares bubble shapes in the experiments and simulations with viscosity monotonically decreased from bubble (a) to bubble (f). Table 4.10 summarized the corresponding dimensionless numbers  $Eo$ ,  $Mo$ , and  $Re_b$ .

Table 4.8. Common parameter in each validation case.

Item	$R \text{ (mm)}$	$\rho_l \text{ (kg} \cdot \text{m}^{-3}\text{)}$	$\rho_g \text{ (kg} \cdot \text{m}^{-3}\text{)}$	$\sigma \text{ (Nm}^{-1}\text{)}$	$\mu_g \text{ (Pa} \cdot \text{s)}$
Magnitude	13.0	1362.68	1.2047	0.07845	1.8205E-5

Table 4.9. Comparison of bubble shape between classical experiments and simulations. The values in the last row are the liquid viscosity,  $\mu_l$  ( $Pa \cdot s$ ), for each simulation.

	Bubble (a)	Bubble (b)	Bubble (c)	Bubble (d)	Bubble (e)	Bubble (f)
Experiment (Bhaga and Weber, 1981)						
Simulation with PID bubble controller						
	2.746	2.055	1.289	0.780	0.544	0.288

Table 4.10. Comparison of dimensionless number between classical experiments (exp.) and simulations (sim.).

	Bubble (a)		Bubble (b)		Bubble (c)		Bubble (d)		Bubble (e)		Bubble (f)	
	Exp.	Sim.	Exp.	Sim.								
$Eo$	116	121	116	107	116	110	116	112	116	117	116	107
$Mo$	848	882	266	246	41.1	39.1	5.51	5.33	1.31	1.32	0.103	0.095
$Re_b$	2.47	2.07	3.57	3.01	7.16	6.03	13.3	11.2	20.4	17.18	42.2	33.04

From Table 4.9, the aspect ratios of numerical bubbles are found to slightly deviate from the experiments. Since the experiment only provides a range for densities and surface tensions as clues, the material properties tentatively assigned in simulations may not be consistent with the selections of Bhaga and Weber. Comparing the dimensionless numbers in Table 4.10, numerical  $Eo$  and  $Mo$  are close to the experimental data, with relative differences between  $\pm 1\%$  and  $\pm 8\%$ . However, the discrepancy of  $Re_b$  can be observed to grow with bubble deformation level. As experimental measurements on bubble terminal velocity generally have higher uncertainty than other parameters, it is expected that  $Re_b$  (proportional to relative velocity  $u_r$ ) will consequently

have larger discrepancies. In conclusion, the trends of bubbles flattening can be easily observed in both results, and the experimental and numerical  $Eo$  and  $Mo$  match well, therefore the PID controlled bubble deformation is validated by the classical experiments.

It is worthwhile to mention that due to visualization from the simulation, the existence of a cavity inside the bubble was confirmed. The experimental figures are either too dark and opaque to demonstrate the interface or are poorly clarified by streamlines to depict the cavity. Although Bhaga and Weber used “oblate ellipsoidal cap” to describe the bubble shape, the “cap” was only confirmed with half-transparent numerical results.

#### 4.3.4.2 Validation by simulation-motivated experiment

This section validates complex bubble topologies in simulations carried out by PID bubble controller using parallel experiments and simulations in more recent studies (Tripathi et al., 2015; Sharaf et al., 2017). Table 4.11 compares the bubble deformation with a thin film forming at the wake side of the bubble, which satisfies  $Eo \in (30, 500)$  and  $Ga \in (0, 50)$ . Table 4.12 demonstrates the bubble break-up process with satellite bubbles shedding away from the leading bubble, which satisfies  $Eo \in (1, 500)$  and  $Ga \in (10, 500)$ .

Table 4.11. Comparison of complex bubble deformation with a film formed at the wake side of the bubble.

Experiment (Sharaf et al., 2017)					
DNS simulation (Sharaf et al., 2017)					
PHASTA with PID bubble controller					

Table 4.12. Comparison of complex topology change during bubble break-up and the formation of satellite bubbles.

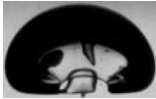
	Cavity forms	Thin film forms	Satellite bubbles form
Experiment (Sharaf et al., 2017)			
DNS simulation (Tripathi et al., 2015)			
PHASTA with PID bubble controller			

Table 4.11 describes the deformation process for a helmet-shape bubble. Compared with the cavity shape and film thickness in the reference simulation, PHASTA results match with the experiment better. The numerical satellite bubbles in Table 4.12 are not identical with the experimental findings, and the satellite bubbles produced by PHASTA are with different distributions compared with the existing simulations. It is worth to mention that the thin film and satellite bubble formation in Table 4.12 is a recurring dynamic process so it is almost not possible to reproduce the identical satellite bubbles as the ones in the experiment or in the published simulations. However, the thin film formation and interface topology change in the break-up process agree with the existing findings. Both Table 4.11 and Table 4.12 confirm the accuracy of PHASTA code and reinforce the precision of PID bubble controller to simulate complex interface distortions.

#### 4.4 Gravity control capability

The above bubble topology studies justify the reliability of complicated interface distortions under PID controller. To produce the same topology as the bubble rising in liquid under gravity, it is very important to match the numerical gravity derived from PID bubble controller with the earth

gravity. The majority of the studies in this section were previously presented in published literature (Fan and Bolotnov, 2020).

As Eq. (35) illustrates,  $u_r$  input into the PID bubble controller dominantly determines  $F_{cfx}$  due to the  $u_r^2$  term. However,  $u_r$  from experimental data always have higher uncertainties. Since gravity is always the most accurate data, i.e. the earth gravity, researchers can manually adjust  $u_r$  until the numerical gravity  $g$  computed by buoyancy force approaches the earth gravity (Feng and Bolotnov, 2017c). The above studies also involve such manual adaptations.

$$g = \frac{F_D}{(\rho_l - \rho_g)V_g} = \frac{F_{cx}}{(\rho_l - \rho_g)V_g} \quad (43)$$

From an experiment validation perspective, producing correct gravity is more important than  $u_r$ , and thus the interfacial forces can be more accurately evaluated. Such manual adjustment is time-consuming as each simulation with different  $u_r$  needs to start from scratch and takes time to achieve statistically steady state conditions which involve getting proper bubble deformation and resolving the fluid flow around the bubble. A tool to automatically change  $u_r$  during the simulation is highly desired to greatly simplify the process of such numerical experiments.

As an extension of the existing PID bubble controller, gravity control capability is developed to adjust  $u_r$  step by step until the numerical gravity ( $g$ ) approaches the earth gravity ( $g_{earth}$ ). The gravity control capability is expected to reduce the computation time and simplify the workflow because only one simulation is needed, and  $u_r$  is adjusted during the simulation after the bubble wake is already developed. Even though the bubble wake will change in response to the new  $u_r$ , it is still less time-consuming than developing a wake from the bubble in a brand-new simulation.

Under each  $u_r$ ,  $F_{cfx}$  is recorded and hence the numerical gravity can be obtained by Eq. (43) at a quasi-steady state. The new  $u_r$  at the center of the bubble is determined based on the relative

error ( $E_g$ ) between  $g$  and  $g_{earth}$  as Eq. (44) and (45). The closer of  $u_{r_{new}}$  to  $u_{r_{old}}$ , the smoother the bubble wake transition is, and the more stable the simulation is. However, the velocity adjusting should not be too subtle to extend the simulation time. Therefore,  $|E_g|$  is limited up to 7% when  $u_r$  is changed by Eq. (45), where the 7% is tested to be optimal to yield both numerical stability and an acceptable overall computation time.

$$E_g = \frac{g - g_{earth}}{g_{earth}} \quad (44)$$

$$u_{r_{new}} = \begin{cases} u_{r_{old}}(1 - E_g), & \text{if } E_g \geq 7\% \\ u_{r_{old}} \frac{\sqrt{g_{earth}}}{\sqrt{g}}, & \text{if } 2\% \leq E_g < 7\% \end{cases} \quad (45)$$

Once  $u_r$  is adjusted to yield  $g \cong g_{earth}$ , or  $|E_g| < 2\%$ ,  $u_r$  is close enough to the expected bubble terminal velocity, so the interfacial forces are correspondingly accurate. Figure 4.11 illustrates the flow diagram of the gravity control mechanism. The adjustment of  $u_r$  is achieved by utilizing the parallel Boundary Condition Transient (BCT) capability (Saini, 2020). It is also the first time to combine PID bubble controller and BCT capabilities.

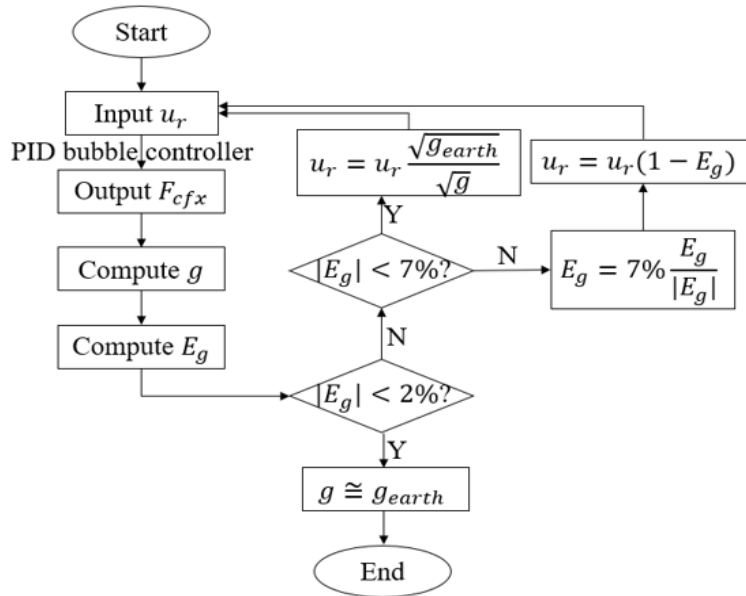


Figure 4.11. Flow diagram of the gravity control capability.

The bubble (a) in Section 4.3.4.1 is selected to test the gravity control capability. Before gravity control capability was developed, the liquid velocity (equal to  $-u_r$  considering bubble velocity is 0) was manually adjusted to  $0.16 \text{ m/s}$  to yield a correct gravity. It is expected that the gravity control capability will yield a final liquid velocity the same to  $0.16 \text{ m/s}$ . To test it, only the initial liquid velocity is  $0.19 \text{ m/s}$ , and all other simulation setups are all identical with the conditions of the bubble (a) in Section 4.3.4.1.

The relative velocity and the drag force ( $F_D$ , counter force of  $F_{cfx}$ ) varied with computation time are plotted in Figure 4.12.  $u_r$  is adjusted every  $0.4\text{s}$  and  $F_D$  changes correspondingly.  $F_D$  oscillates due to the mechanism of the PID bubble controller, but it will be averaged at each quasi-steady state to mitigate the influence of oscillations. Table 4.13 summarizes the averaged drag force ( $\overline{F_D}$ ) over a time interval  $0.1\text{s}$  before each  $u_r$  adjustment.  $\overline{F_D}$  is used to compute the numerical gravity and hence to determine the relative error between  $g$  and  $g_{earth}$  ( $9.8 \text{ m/s}^2$ ).

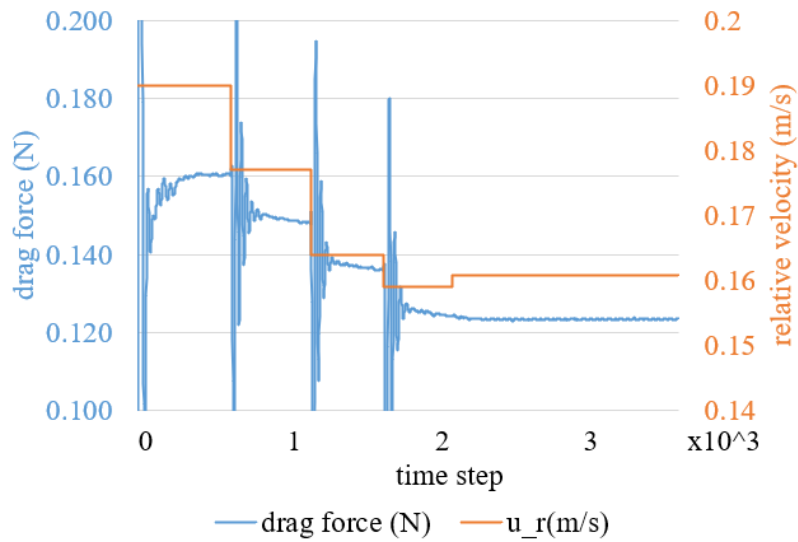


Figure 4.12. Automatic adjustment of  $u_r$  and the corresponding response of  $F_D$ .

Table 4.13. Post-processed results under each relative velocity.

Time $t$ (s)	$u_r$ (m/s)	$u_r$ adjusting	$\overline{F_D}$ (N)	$g$	$E_g$
0-0.4	0.1900	$u_{r_{old}}(1 - 7\%)$	0.161	12.66	29.2%
0.4-0.8	0.1767	$u_{r_{old}}(1 - 7\%)$	0.148	11.47	17.0%
0.8-1.2	0.1643	$u_{r_{old}} \frac{\sqrt{g_{earth}}}{\sqrt{g}}$	0.137	10.46	6.7%
1.2-1.6	0.1590	$u_{r_{old}} \frac{\sqrt{g_{earth}}}{\sqrt{g}}$	0.123	9.59	-2.1%
1.6-2.0	0.1608	-	0.123	9.62	-1.8%

In Figure 4.12, the  $F_D$  plot is truncated between 0.1 N and 0.2 N, but the  $F_D$  spikes in the beginning of the simulation is actually greater. It is because the bubble wake is formed from the initial uniform flow (Figure 4.13 (a) and (b)), and the abrupt change of the velocity field results in drag force spikes. Figure 4.13 (b) and (c) depict distinct wake development under  $u_r = 0.19m/s$ . However, the wake change is milder from Figure 4.13 (b) to (c) when  $u_r$  is adjusted in between. Consequently in Figure 4.12, the subsequent drag force spikes are much smaller since  $u_r$  is adjusted by 5% or lower, and the quasi-steady state is achieved faster. The magnitude of the spike is proportional to the change of  $u_r$ . As for the last adjustment from 0.1590 m/s to 0.1608 m/s,  $u_r$  is only changed by  $-1.098\%$ , so the drag force change is negligible.

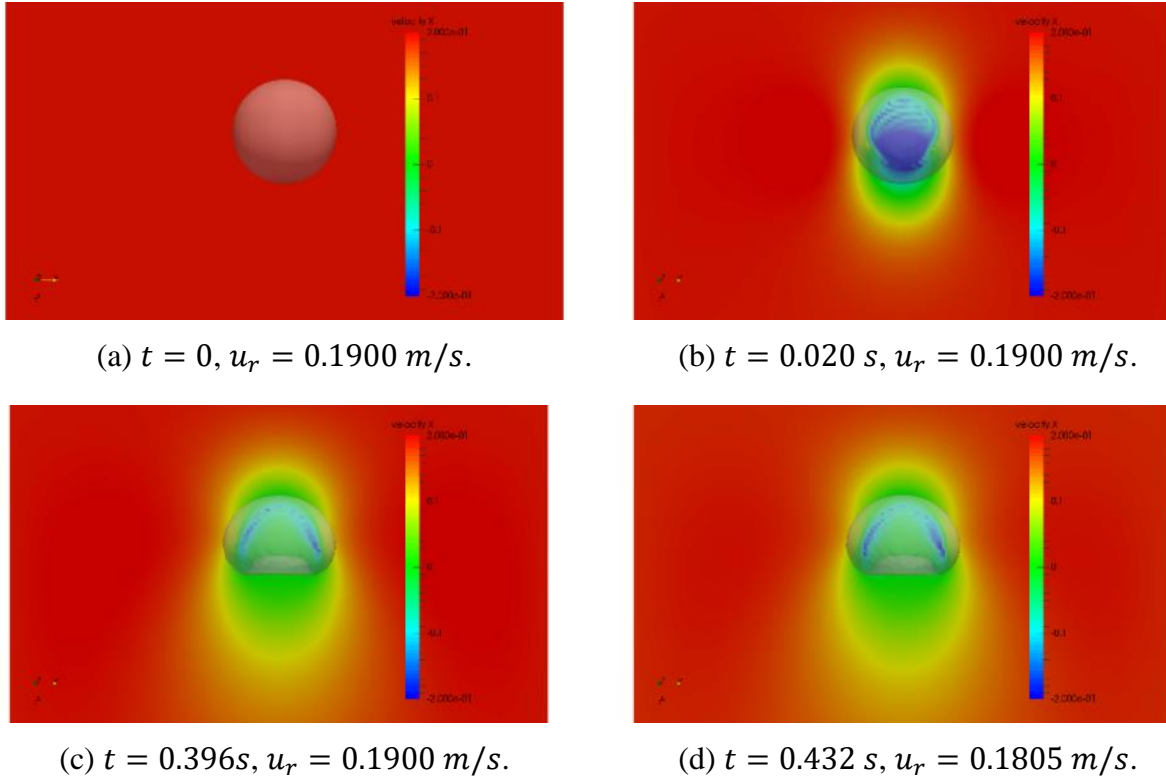
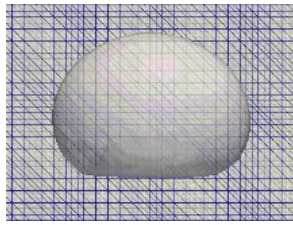


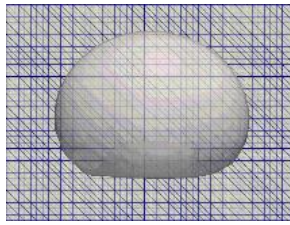
Figure 4.13. Bubble wake formation and wake change with  $u_r$ .

Table 4.13 and Figure 4.12 both demonstrate the gravity control mechanism illustrated in Figure 4.11. Before  $t = 1.2 \text{ s}$ , although  $E_g$  is greater than 7%,  $u_r$  is always reduced by only 7%. Afterwards  $u_r$  is adjusted by the gravity square root ratio. Eventually, the numerical gravity approaches the earth gravity with a very small  $E_g$  of  $-1.8\%$ . The eventual relative velocity in Table 4.13 is  $0.1608 \text{ m/s}$  which is close enough to the expected  $u_r$  ( $0.16 \text{ m/s}$ ) of the bubble (a) in Section 4.3.4.1. The bubble shapes under the initial and eventual  $u_r$  are compared in Figure 4.14. The shape in Figure 4.14 (b) is slightly taller and rounder than that in Figure 4.14 (a), which is more close to the bubble shape of the experiment (Bhaga and Weber, 1981). Although the shape change is subtle,  $u_r$  has a relative difference of  $(0.19 - 0.1608)/0.1608 = 18.16\%$ . Such large error partially reflects the uncertainty of measured relative velocity in the experiment (Bhaga and Weber, 1981). In addition, the relative difference of the initial  $\overline{F_D}$  compared with the eventual  $\overline{F_D}$

is 30.89%, which demonstrates the necessity of generating the accurate gravity to obtain the accurate interfacial forces.



(a)  $u_r = 0.1900 \text{ m/s}$ .



(b)  $u_r = 0.1564 \text{ m/s}$ .



(c) Experimental bubble shape  
(Bhaga and Weber, 1981).

Figure 4.14. Bubble shape comparison.

#### 4.5 Chapter summary

This chapter studied single bubble under PID control (also counter current flow) as fundamental investigations for debris bed CCFL studies. PID bubble controller is verified and validated in more broad studies, including wall-affected transverse forces and complex bubble topology evolutions. The capability and precision of the PID bubble controllers are assessed in revealing complex topology change, which is foundational for CCFL studies. The mesh studies of single bubbles provide reference on spatial discretization for more complex CCFL simulations as well. A new gravity control capability is added into the PID bubble controller which helps the validation of bubble dynamics. The control on gravity also provides reference for the development of PID pressure gradient controller.

## 5.1 Counter-current flow studies without PID control

The phenomena in the reactor debris bed is typically counter-current two-phase flow. Debris bed channel is selected as the smallest channel in the nuclear reactor that the presented research covers. This section reveals the flow behavior in the micro-scale structure that has not been previously analyzed by high resolution simulation approach in the debris bed. All simulations are adiabatic, but still can reveal the coolability of the debris bed through the contact area between coolant and the channel wall. The studies in this section provide a demonstration of the development of high-resolution database for M-CFD and system-scale codes on multiphase-flow in the debris bed.

### 5.1.1 Counter current flow driven by gravity

The debris-bed counter-current flow study involves complicated interface topology change and varying flow regimes. Before successfully dealing with both above challenges, the interface topology driven by gravity is first studied with different initial conditions.

The computation channel in gravity-driven studies are cylinders with radius of 0.5 *mm*. No inflow or outflow boundary conditions are specified so the domain is isolated. The channel height varies in different tests and are introduced individually. In all simulations, the coolant is initialized above the steam. The density difference is the only initiation for the flow instability where coolant and steam densities are assigned based on fluid properties at 1 atm and 100 degrees Celsius. The simulation parameters of the fluid and the system are listed in Table 5.1. Very small surface tension coefficient is used, thus gravity/density difference is adequate to drive the interface to move. The gravity-driven simulation is also a fundamental study for PID controlled CCFL simulation. The

latter uses pressure gradient in a periodical domain to drive the counter-current flow, which resembles the former approach.

Table 5.1. Fluid and system properties in preliminary study.

	Coolant	steam
Density ( $kg/m^3$ )	958.0	0.598
Viscosity ( $Pa \cdot s$ )	2.818E-04	1.227E-05
Surface tension coefficient ( $N/m$ )	1.1E-04	
Earth gravity ( $m/s^3$ )	9.8	
Cylindrical channel radius ( $mm$ )	0.5	

#### 5.1.1.1 Initial interface: horizontal flat surface

In this case, one gap in the debris bed was modeled into a cylindrical flow-channel with a diameter of 1 mm and depth of 20 mm. Figure 5.1 depicts the interface initialized horizontally at the centerline of the channel and the spatial discretization. The unstructured computational mesh (tetrahedral element) is used to design different refinement zones. The mesh is set finer in the lower side of the centerline to resolve the region where coolant flows through and coarser in areas unaffected. The results clearly demonstrate the Rayleigh-Taylor instability developing in this channel. The steam rises (forms into a bubble and detaches) and the coolant drains down. Here, the interface resolved very well by local refined meshes even with coarse meshes elsewhere. Assume the adiabatic phenomenon can reflect the steam and coolant behavior in the gap of the debris bed. The coolant will fall into the debris gap to cool the debris-bed down. At the same time, steam will form rising bubbles that leave the channel opening which will give way to the falling coolant. In reality, as the bubble rises in the coolant, it will cool and condense, however as long as the bubble does not lose significant mass and still continues to rise, the coolant is still able to drain down to cool the debris bed.

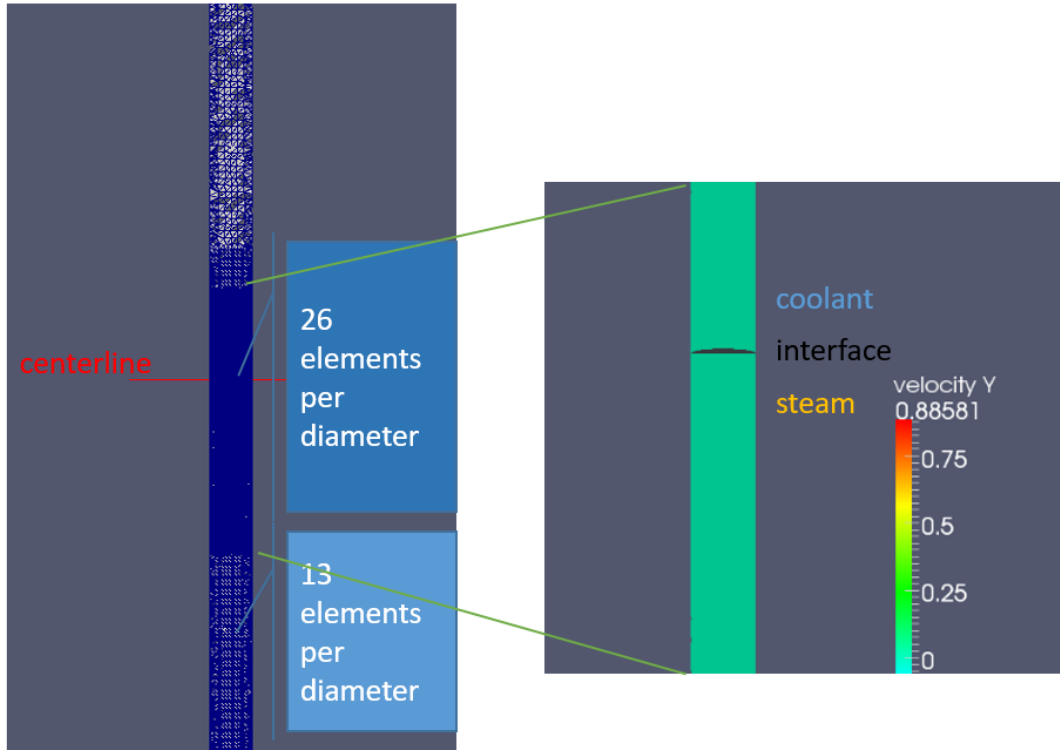


Figure 5.1. Mesh configuration and interface initialization.

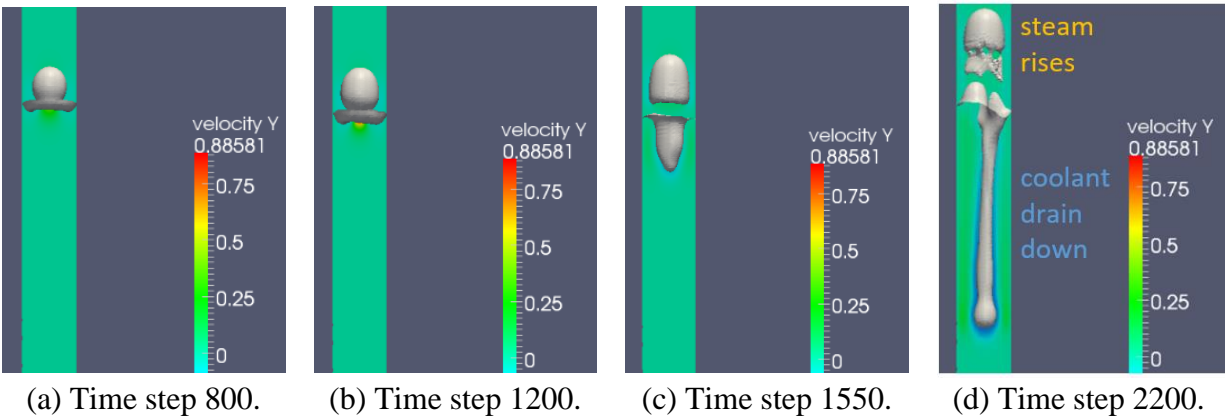


Figure 5.2. Interface topology (white surface) changes with time.

### 5.1.1.2 Initial interface: vertical film

In this case, one gap in the debris bed was modeled into a cylindrical flow-channel with a diameter of 1 mm and depth of 5 mm. On the top and bottom of the channel, two tanks are added and filled with coolant and steam to observe the interface topology change outside the cylindrical channel. The interface is initialized vertically, which models a coolant film occupying 1/3 of the

right side of the channel (Figure 5.3). Besides the tetrahedral mesh in the bulk region, boundary layer mesh (hexahedral element) is used to resolve the vertical film.

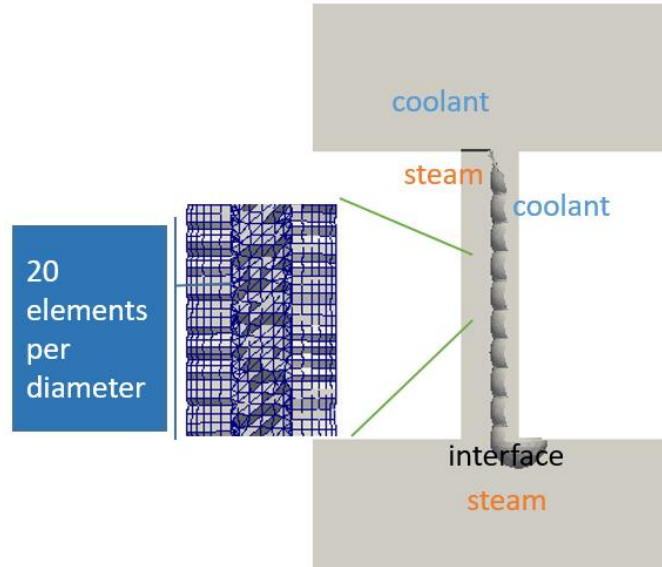
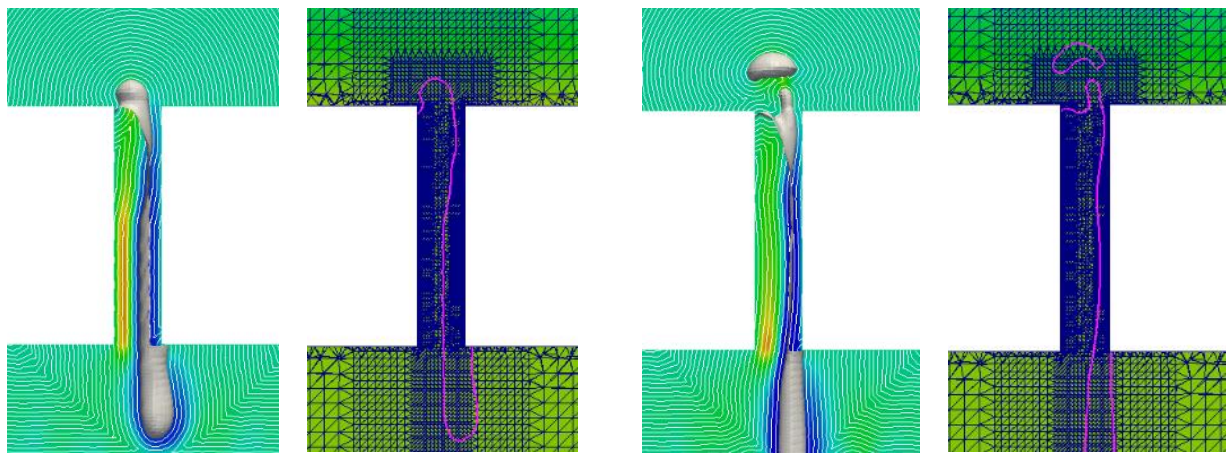


Figure 5.3. Mesh configuration and interface initialization.

Similarly, Rayleigh-Taylor instability was observed in this result, where steams rises and forms a bubble and detaches, allowing coolant to drain into the bottom. This case revealed the importance of the wettability of the debris bed. As long as a coolant film partially covers the flow channel, the coolant is able to drain down and significantly cool down the debris bed.



(a) Time step 850.

(b) Time step 2500.

Figure 5.4. Interface topology (white surface) changes with time.

### **5.1.1.3 Summary of the gravity-driven-only cases**

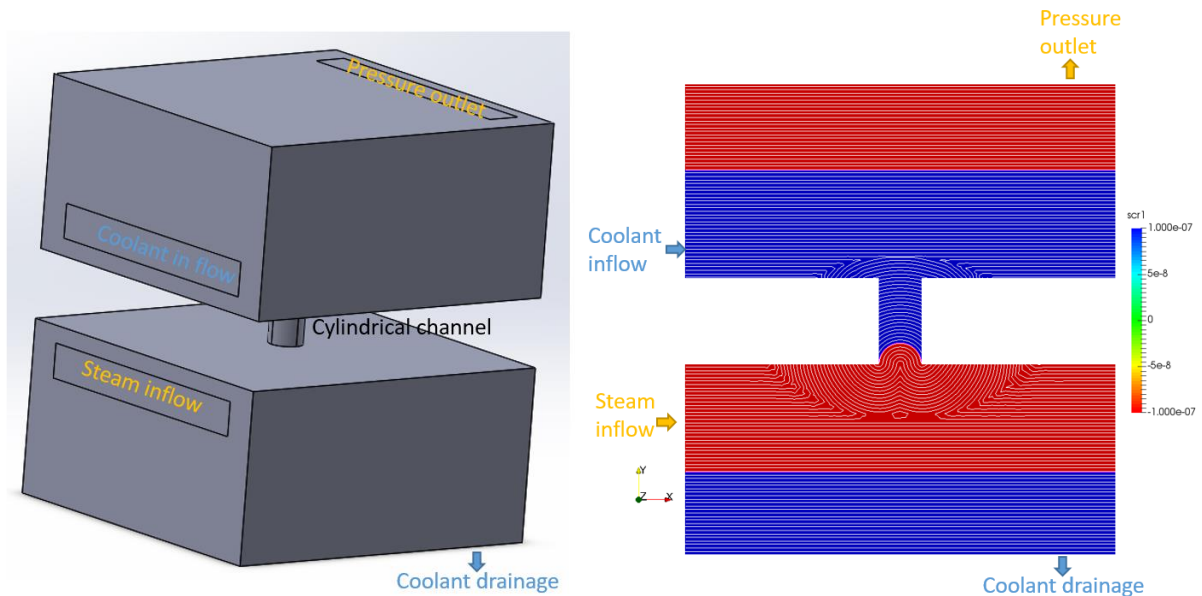
With only density difference/gravity yielding the Rayleigh-Taylor instability, the capability is demonstrated on resolving the complicated interface topology change of two-phase flow in the debris-bed channel. As long as counter-current flow can happen, the debris bed can be cooled by down flowing coolant. Otherwise, if a coolant film partially covers the debris bed flow channel, the coolant is able to drain down. This study reveals the significance of the wettability of the debris bed on increasing coolability.

### **5.1.2 Counter current flow driven by both gravity and steam generation rate**

With interface topology change driven by only gravity successfully carried out in Section 5.1.1, the effect of heat generation rate on coolability is considered to reveal the phenomenon when dry-out happens in the debris bed. Contact angle/wettability control is also implemented onto the cylindrical surface. Different contact angles were selected to decide its effect on coolability.

#### **5.1.2.1 Simulation setup**

The typical setups can be found in Figure 5.5. The debris gap, a cylindrical channel, is in the middle. The diameter is 1 mm and the height is 2 mm. The coolant is set on the upper side of the steam. Steam and coolant are specified with both inflow and outflow boundary conditions respectively. Steam is supplied from the bottom tank and coolant flow in from the top tank. Steam inflow rate is calculated by heat generation rate and the latent heat when coolant is heated into steam. Coolant flow rate is determined by steam flow rate and their density ratios to guarantee the mass conservation between two fluids during the phase change. The simulation parameters are listed in Table 5.2. In addition to physical properties of coolant and steam at 1 atm gauge and 100 Celsius degrees (the same with Table 5.1), natural surface tension is used, thus both steam inflow and gravity drive the interface to move.



(a) Geometry with steam and coolant inflow and outflow.

(b) Initial steam and coolant distribution (red-steam; blue- coolant; legend scr1- level-set).

Figure 5.5. Counter current flow case setup.

Table 5.2. Simulation parameters.

	Coolant	steam
Density ( $kg/m^3$ )	958	0.598
Viscosity ( $Pa \cdot s$ )	2.818E-04	1.227E-05
Surface tension coefficient ( $N/m$ )	0.0588	
Earth gravity ( $m/s^3$ )	9.8	
Cylindrical channel radius ( $mm$ )	0.5	
Cylindrical channel height ( $mm$ )	2	

### 5.1.2.2 Steam generation rate effects on counter current flow

Three cases start with interface on the bottom of the channel Figure 5.6 and are ran with contact angle control algorithm set for  $40^\circ$ , using the contact angle sub-grid model developed in PHASTA (Li, M. et al., 2019). The steam generation rates (in adiabatic simulations presented) are assumed

to be constant in each scenario, which is represented by steam superficial velocity in the cylindrical channel, 2.465 m/s, 0.493 m/s, and 0.2465 m/s. Those values are set as the inflow velocity boundary condition for the steam zone in Figure 5.5.

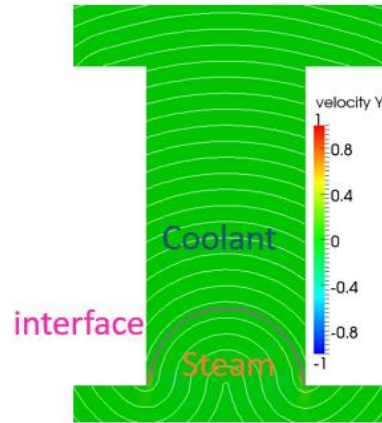


Figure 5.6. Interface initialization in a cylindrical channel of the debris bed.

The results under different steam superficial velocities are summarized in Table 5.3 and elaborated afterwards.

Table 5.3. Simulation results for different steam superficial velocities.

	Steam generation rate	Flow regime
High	2.465 m/s	CCFL / dry-out
Medium	0.493m/s	R-T instability
Low	0.2465 m/s	Balance between two phases

The steam superficial velocity of 2.465 m/s corresponds to the dry-out of the debris bed. Since the generated steam is too fast to allow liquid to drain down, gradually the entire cylindrical channel will be occupied by steam. Figure 5.7 illustrates how steam gradually blocks the entire channel. Even though the upward steam detaches from the top of the channel and is suspended in the coolant, the counter current flow limitation still exists and the liquid is unable to drain downwards. Although in Figure 5.7 (b) there is still some liquid film covering the upper wall, the

contact line (interface contacting wall surface) is still moving upward. The choking will continue and with little cooling happening in the channel, the debris bed will eventually dry-out.

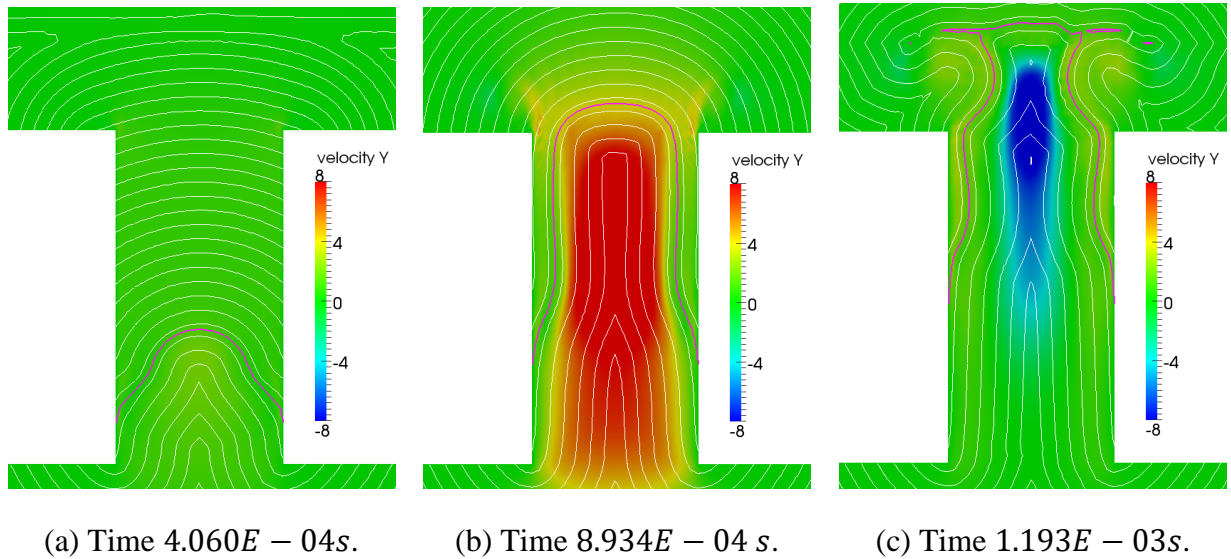


Figure 5.7. Progression of CCFL event, magenta line represents liquid gas interface.

When steam generation rate is not high enough to result in a complete dry-out ( $0.493m/s$ ), the Rayleigh-Taylor instability is the dominant flow regime in the debris-bed flow channel. The heavier coolant is displaced downward with an equal volume of steam displaced upward (Figure 5.8 (a)). The steam column will branch into 2 sub-columns as the interface is rising, after which each sub-column will continue to branch again (Figure 5.8 (b)). In the end, as the upper coolant push the interface down, the sub-columns are merged, but the interface topology stays complex.

The coolability of debris bed is affected by two factors in this case. Even though there is coolant dripping down in the center, it may not reach the debris bed. On the other hand, the contact line will not progress any further and the steam will only rise to the top of the channel. The remaining coolant film covering the wall will not be replaced by steam, thus the heat transfer can still occur. Should the majority of the water flowing down the channel be along the peripheral (i.e. along the

sides) rather than the center, there will be improved cooling of the debris bed as the coolant contact has a better heat release rate than along the center.

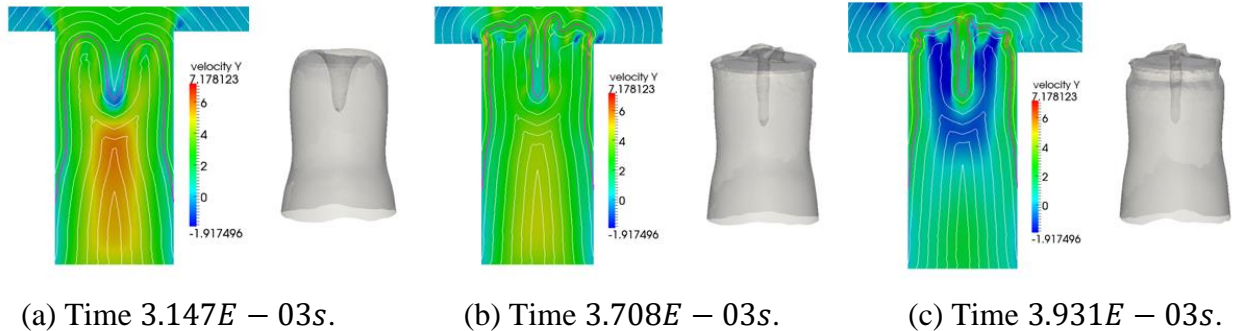
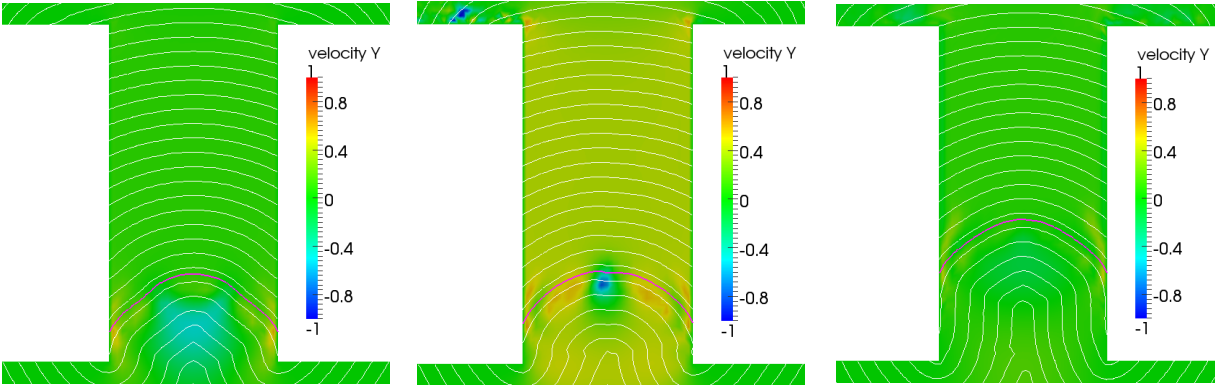


Figure 5.8. Semi-transparent 3D interface showing the process of generating Rayleigh-Taylor instability inside the channel. Cross sections of 2D interface are provided in (b) and (c) to better illustrate the interface topology.

When the steam generation rate is low, the density difference is not strong enough for R-T instability to happen ( $0.2465 \text{ m/s}$ ). Though the top of the interface begins to sink (Figure 5.9 (a)), liquid drainage still does not happen. With the current steam superficial velocity, a force balance can be established (Figure 5.9 (c)), where the interface almost comes to a balance. In the current situation, since the steam only occupies a small portion of the channel, the coolability is sufficient. It is worth mentioning that the force balance is established based on opposing gravity and buoyancy force, surface tension, contact angle force, and pressure difference. Any change in those factors will affect coolability. If steam generation rate decreases any further or the surface tension reduces, liquid drainage will happen and significantly increase the coolability.

In conclusion, this study demonstrates the mechanism of two-phase flow phenomenon in the gap of the debris bed (using adiabatic flow assumption). At high steam generation rate, the counter current flow limitation (CCFL) or the choking phenomenon occurs and the debris bed will dry out. With reduced steam generation rate, steam upwards into the coolant (R-T instability) forms. There might still be coolant to cool the debris bed. Under low steam generation rate, a balance between the coolant and steam can be established.



(a) Time  $3.898E - 04s$ .

(b) Time  $6.450E - 04s$ .

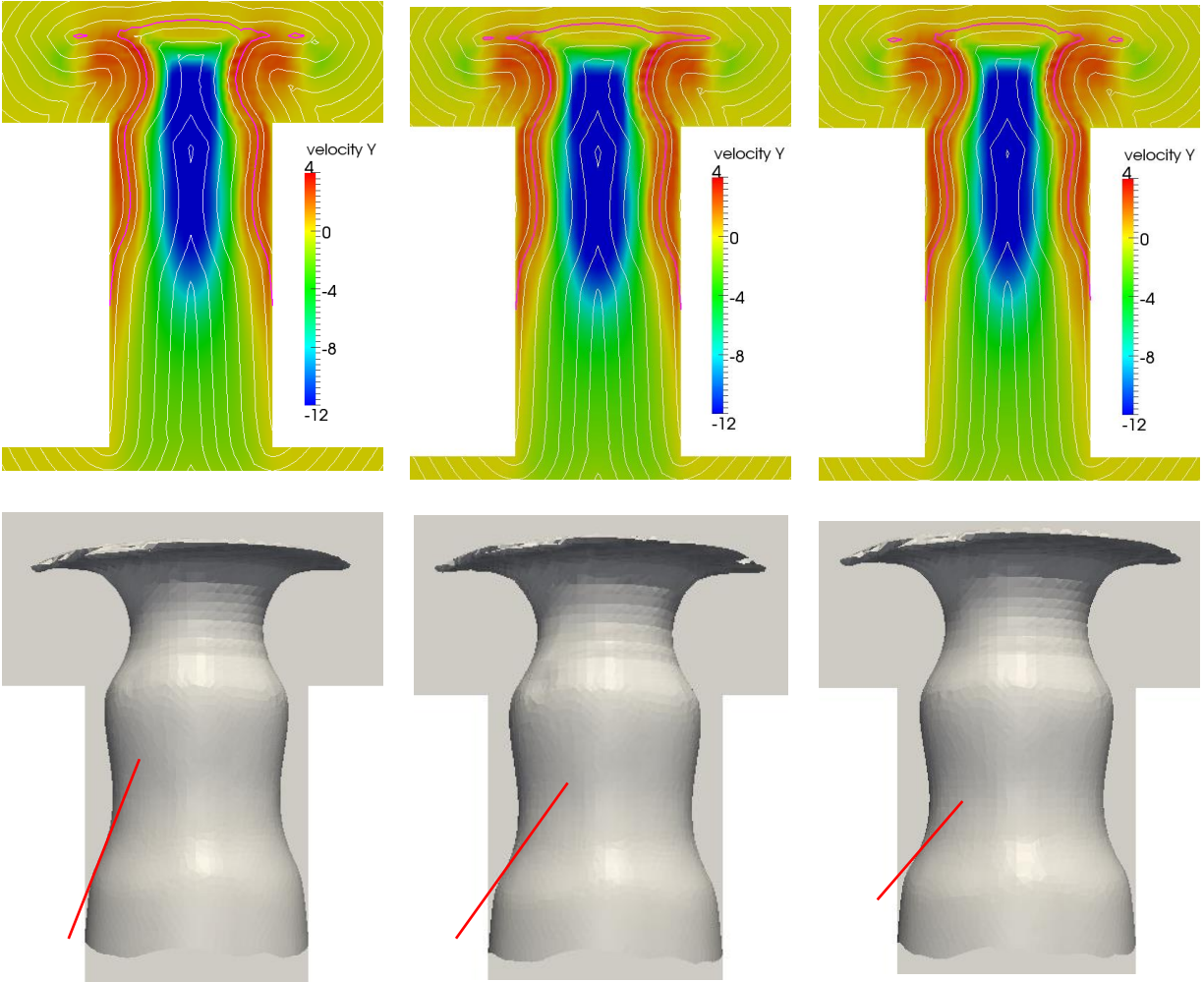
(c) Time  $1.774E - 03s$ .

Figure 5.9. The process of achieving a force balance in the channel.

### 5.1.2.3 Flow regime comparison with different contact angles

The contact angle/wettability is significant on heat transfer performance. When the steam generation rate is not dominant, factors like contact angle and counter current flow are significant variables when it comes to debris bed coolability. As long as the counter current flow limitation is not achieved, and there is a coolant film partially covering the debris bed flow channel, the debris bed can be cooled down. When the steam generation rate is high, the simulation shows that under dry-out condition, different contact angles/wettability does not make a significant difference in the two-phase flow regime.

The following three cases are with the same initial conditions and boundary conditions, only contact angle assigned on the channel wall varies. The steam inflow rate is evaluated by the dry-out heat flux in Table 5.3. The flow regime in the debris bed channel are compared in Figure 5.10. No matter the interface topology or the velocity field, these three cases are very similar to each other. The differences in contact angle can still be recognized by comparing the interfaces touching the wall. Physically, CCFL has already happened, resulting in the debris bed dry-out. In this scenario, no matter how the surface wettability change, the dry-out result are not affected.



(a) Contact angle =  $20^\circ$ .      (b) Contact angle =  $40^\circ$ .      (c) Contact angle =  $60^\circ$ .

Figure 5.10. Comparison of velocity fields and interfaces driven by three different contact angle values.

**5.2 CCFL studies in cylindrical channels under PID control**

The CCFL in debris bed was conducted in a cylindrical channel initialized with annular flow. The domain shape and annular flow selection has a fundamental base from published CCFL model in the debris bed (Abe, 1995). The real shape of debris bed channels can be very complex therefore, geometry selection is challenging. Of the regular shaped channel (cylindrical, square, triangle, etc), cylindrical channels do not have corners which are unlikely to appear in the debris bed channel. This shape can also be used to simplify the flow channel. In order to study the CCFL mechanism

in this channel, the coolant should still remain attached to the wall. If there is no liquid covering the wall, the heat transfer rate deteriorates and studying CCFL under such conditions is not useful. Therefore, researchers have proposed an annular flow model to explain the two-phase behaviors in the debris bed channel, which has inspired the simulation setup in this section. The simulation aims to obtain the accurate CCFL flow data based on high-resolution interface tracking simulations in cylindrical channels, and to shed light onto the physics behind the CCFL phenomena.

The assumptions of the debris bed CCFL studies in Section 5.2, 5.3, and 5.4 are listed in below:

**1. Statistically steady state condition exists at CCFL occurrence (i.e. zero liquid velocity).**

As described in Chapter 3, the liquid phase velocity was not used as the volumetric velocity integral, but the cross-sectional velocity integral to save the computational cost for in-situ integral evaluation. Since the flow is incompressible, the zero cross-sectional velocity integral can be shown to be equivalent to zero volumetric velocity integral. However, this statement is true when the steam phase achieves a steady state so it does not disturb the liquid cross-sectional velocity integral. Liquid should also reach a steady state with a zero velocity to prove CCFL obtained. In a conclusion, a steady state must exist for CCFL simulations so zero cross-sectional velocity integral can be used as a CCFL criterion. Simulations in Chapter 3 and the upcoming results all prove that a statistically steady state indeed exists for both liquid and gas phases.

**2. The adiabatic simulations can still represent CCFL under heat transfer condition.**

The presented research is conducted under adiabatic conditions. While heat transfer is not resolved, the results determined for CCFL condition are still considered acceptable. According to previous investigations, under both adiabatic (air-water) and boiling (steam-water) conditions CCFL occurs at similar velocities (Vierow, 2008). This conclusion is assumed to be applicable in debris bed channels as well.

### **3. Partial CCFL does not exist at the millimeter scale channels.**

As discussed in the literature review, partial CCFL can exist in millimeter size channel, for instance a large annular gap channel, which will turn into global CCFL as gas phase velocity further increases (Jeong, 2008). However, the coolant and steam in debris bed channels are conduit flows and the scale is too small to distinguish between local and global. Therefore, this assumption should not change the CCFL results.

### **4. The CCFL hysteresis effect does not exist or affect millimeter scale channel CCFL.**

Literature review in Section 1.1.1 includes the hysteresis effect that the gas velocities at the onset of CCFL are different when increasing it (from pre CCFL to CCFL) and decreasing it (from post CCFL to CCFL). In contrast, the PID controller yields fluctuation around the pressure gradient at CCFL at a quasi-steady state, which is equivalent to continuous trivial transitions among pre CCFL, CCFL and post CCFL, which conflicts with the hysteresis effect. However, the gas velocity under PID control always shows a monotonic increasing trend until steady state is achieved, which does not conflict with the hysteresis effect. Moreover, the hysteresis effect was observed only in large scale CCFL experiments. It is very possible that this effect is connected with the global and partial CCFLs, which should only exist in large scales. Therefore, it is reasonable to assume that hysteresis effect does not exist or affect millimeter scale channel CCFL.

One of the inferences from this assumption is that different initial conditions of the PID controlled CCFL simulations will not change the eventual results. As will be seen later (Section 5.2.2.3), this inference is proved.

### **5. The periodic boundary condition does not affect the occurrence of CCFL.**

The debris bed counter current flow simulations in Section 5.1 do not need to use periodic boundary conditions (B.C.) at the inlet and outlet of the debris bed channel. Two tanks were

arranged to hold the inflow and outflow fluids. However, the domain without the two tanks under PID control must use periodic B.C. on its inlet and outlet in the following debris bed studies. The error of periodic B.C. instead of freestream condition is estimated to be approximately 10 times of the spatial discretization error (Karniadakis, 1995), which will be included in the uncertainty quantification and the error bar computation in later sections (Section 5.2.4 and 5.4.4). For DNS simulations with very fine mesh and low spatial discretization error, the periodic B.C. can be considered not to affect the occurrence of CCFL.

#### **6. PID control on pressure gradient does not change the two-phase flow regime at CCFL.**

With PID pressure gradient controller applied in the simulation, the whole domain is affected when PID is activated, including the two-phase fluid dynamics. The flow rate is controlled by collecting velocity integral at one cross sectional plane which determines the pressure gradient input in the simulation. However, such capability does not unknowingly add body force, and it should not change the simulation outcome. It is assumed that PID control can still properly capture the two-phase flow regime. In other words, with or without PID, the two-phase flow regime at CCFL are the same. This assumption is later proved by comparing the phase distribution under PID pressure gradient controller and driven by a fixed pressure gradient (Section 5.3.3).

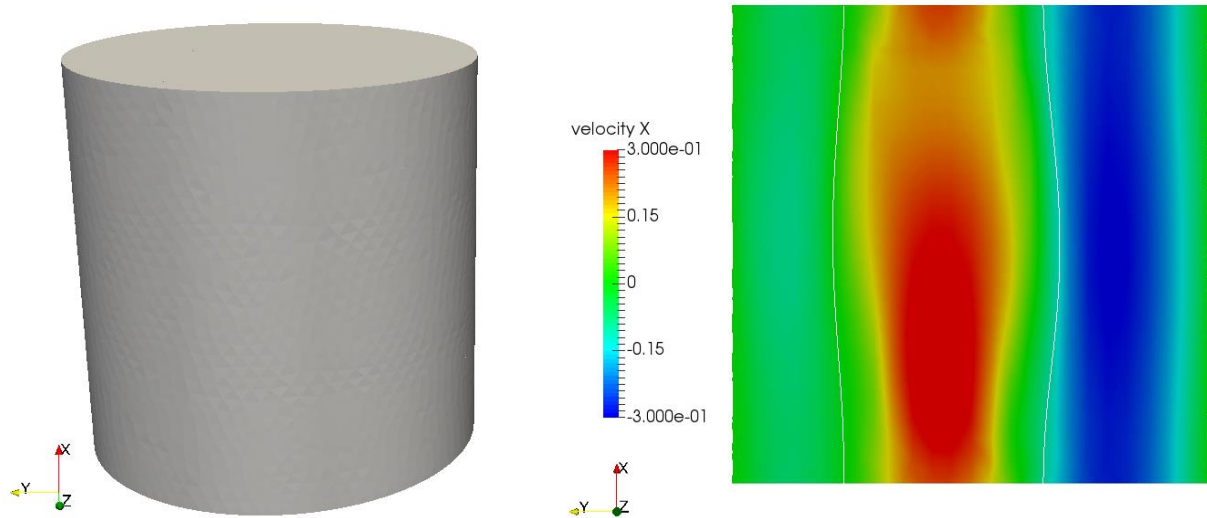
With the above assumptions, CCFL studies under PID control will be presented and then discussed. This section is structured as follows. First, the simulation case set-up including the mesh configuration is explained. Afterwards, the selection of simulation parameters is justified by separate effect tests. A grid convergence study is performed to justify the selection of the spatial discretization and to quantify the uncertainty of the numerical results. The results of the CCFL simulations in the debris bed channel with different void fractions are presented. The obtained pressure gradient is also qualitatively compared with existing debris bed experiments. Moreover,

a quantitative analysis is provided to inform CCFL debris bed channel model development. At last, the connection between CCFL phenomena in the debris channel and dynamics of bubble in mm size is developed.

### 5.2.1 Simulation setup

Debris bed flow channels have very complex shape and directions. Although a cylindrical shape is selected, the length and direction of the channel still needs to be determined. The travel path for two-phase flow inside the debris bed can be upward, horizontal, or inclined and depends on the local structure. Therefore, this study selected a small portion to represent a local channel in the debris bed, specifically a vertical cylindrical segment with  $D = 1 \text{ mm}$  and  $L = 1 \text{ mm}$ . The value for  $D = 1 \text{ mm}$  was selected based on the characteristic length scale of debris bed particles which is usually between  $1 - 5 \text{ mm}$  (Fichot et al., 2006). With smaller particles, the flow channel is therefore smaller, and the likelihood for dry out to happen is higher (Repetto et al., 2013). Therefore, the channel diameter is determined to be equal to the smallest particle size for providing more understanding of CCFL in dry out. The length selection is further justified in Section 5.2.2.2.

The domain setup is provided in Figure 5.11(a), where the earth gravity is along the  $-x$  direction. Figure 5.11 (b) is an example of an instantaneous counter current flow in the channel, where steam is moving upward in the middle and coolant is draining downward around steam. Periodic boundary conditions are applied on the top and bottom of this vertical cylinder so the CCFL pressure gradient controller can be utilized to drive the two-phase flow until the liquid flow rate is zero.



(a) Simulation domain.

(b) Steam moves upward and the surrounding coolant drains downward.

Figure 5.11. Debris bed channel domain and a counter current flow configuration inside.

During severe accident, the debris bed is formed in the bottom of the pressure vessel and the pressure level is determined by the containment condition. The design pressure of the nuclear reactor containment is 52 *psig* (approximately 3.5 atm) (Hessheimer and Dameron, 2006), therefore 3 atm is chosen as the simulation pressure environment as it does not exceed the design limit. The simulation parameters are summarized in Table 5.4. Among the material parameters, all values come from the saturated water and steam properties under 3 atm. Note that the steam viscosity is set to be 10 times higher than the original value. This choice is justified by studying the liquid flow rate and interfacial shear under original and high steam viscosities in separate effects tests (Section 5.2.2.1). With the liquid and steam properties in Table 5.4, the dimensionless diameter  $D^*$  of the debris bed channel computed by Eq. (14) is only 0.42, therefore it is far below the criteria of using Kutateladze or Wallis correlations ( $D^*$  close to 24.5).

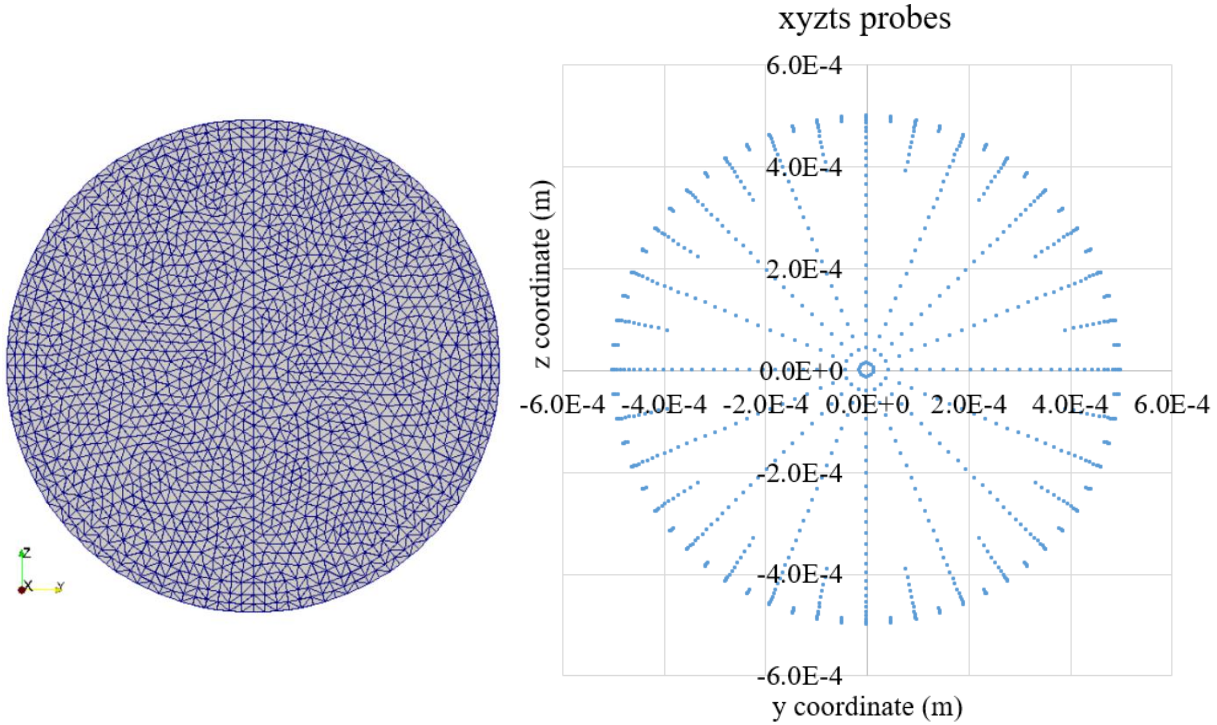
Table 5.4. Parameters used in debris bed channel CCFL simulations.

	Liquid	Steam
Density ( $kg/m^3$ )	931.430	1.67133
Viscosity ( $Pa \cdot s$ )	2.06097E-04	1.34384E-04
Surface tension coefficient ( $N/m$ )	0.0516	
Earth gravity ( $m/s^3$ )	(-9.8, 0, 0)	
Initial pressure gradient ( $Pa/m$ )	(5000.0, 0, 0)	
Initial velocity ( $m/s$ )	(0, 0, 0)	
$x$ velocity goal in PID control ( $m/s$ )	0	

The mesh configuration depends on the Reynolds number in each phase and the interfacial shear. Since liquid phase velocity is eventually controlled to be zero, the liquid flow is strictly laminar. Even if the velocity is not exactly zero, the maximum liquid velocity determined in Section 3.3.3 before CCFL was achieved was only  $0.003 \text{ m/s}$ . The steam velocity magnitude was also determined to be miniscule. In Section 3.2, a representative gas velocity to achieve CCFL condition is  $0.757 \text{ m/s}$  (Figure 3.17 (b)). The tests conducted in Section 3.2 use  $D = 2.4 \text{ mm}$  channel, so in this section with  $D = 1 \text{ mm}$  the gas velocity should be even lower. Considering a high steam viscosity is also used in steam, the gas phase is guaranteed to be laminar flow.

Besides resolving a laminar flow, the mesh element size selection also needs to consider the interfacial shear. A reference value of 18 elements or above across the gas phase diameter in high shear two-phase flows is used (Zimmer, Matthew Daly, 2020). Since the steam is surrounded by annular coolant in the debris bed channel, 40-element across the channel diameter is selected which is adequate to resolve the interfacial shear and to achieve CCFL conditions. The mesh configuration is depicted in Figure 5.12 (a), and the corresponding xyzts probes are plotted in

Figure 5.12 (b). The smallest mesh elements are in the closest-to-the-wall boundary layer region with a thickness of  $1.649E - 05$  m. There are 4 xyzts probes in this element, so the xyzts probe distribution is fine enough to capture the velocity field, especially in the liquid phase.



(a) Mesh configuration.

(b) xyzts probe distribution.

Figure 5.12. Debris bed channel mesh configuration and xyzts probe used.

## 5.2.2 Separate effect tests

In order to justify the selection of simulation parameters, this section discusses the effects in the CCFL simulations from the perspective of fluid parameters and domain length, the sensitivity of the CCFL criteria and the potential influence from the initial conditions, as well as the spatial discretization.

### 5.2.2.1 Steam viscosity

In order to study how steam viscosity affects the two-phase flow in the debris bed channel, two simulations without PID pressure gradient control are conducted under constant  $\frac{dp}{dx} =$

13000.0 Pa/m with different steam viscosities. The void fraction of the steam is 60%. From Figure 5.13, the liquid average velocities collected by xyzts probes grow with time under both viscosities. In the beginning, from  $t = 0$  to  $1.0E - 3$  s), the two liquid velocity plots overlap considerably. After  $t = 1.0E - 3$  s, the flow with the original viscosity begins to fluctuate. However, with 10 times steam viscosity, the liquid is smoothly accelerated. Since liquid flow rate equal to zero is the critical criterion of CCFL condition, a flow field with stabilized liquid flow rate is essential to accurately determine if CCFL is achieved. Even though the discrepancy of liquid velocity between original and 10-time viscosities exists, the overall liquid magnitudes are still very similar. Therefore, even with steam using 10 times of the original viscosity, the liquid flow rate is still trustworthy.

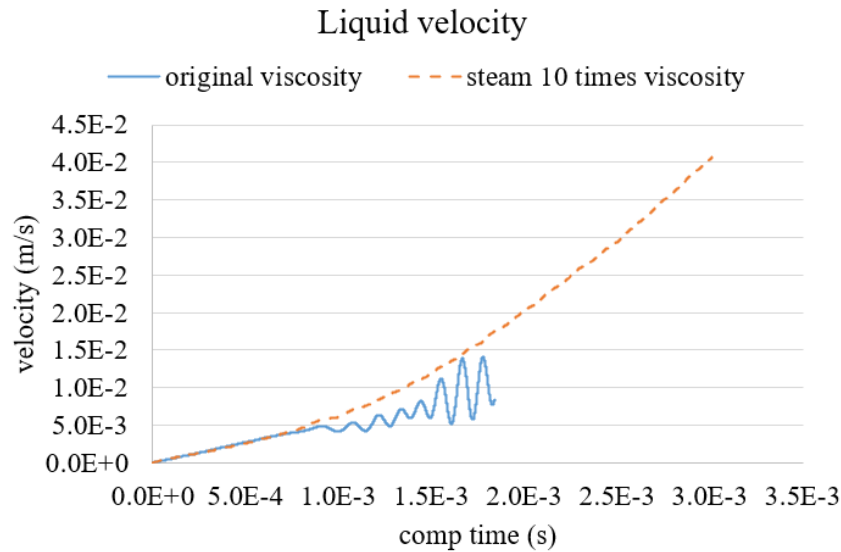


Figure 5.13. Liquid phase velocity growth with original steam viscosity and high viscosity.

A further analysis is done through evaluating the interfacial shear under the two viscosities, which is computed as the velocity gradient near the interface multiplied by the dynamics viscosity.

$$\tau_i = \mu \frac{u_{1\varepsilon} - u_{1.33\varepsilon}}{0.33\varepsilon} \quad (46)$$

In this definition,  $\tau_i$  is the interfacial shear,  $\mu$  is the viscosity, and  $\varepsilon$  is the interface half thickness.  $u_{1\varepsilon}$  and  $u_{1.33\varepsilon}$  are the velocities parallel to the interface at distances of  $1\varepsilon$  and  $1.33\varepsilon$  respectively. In this simulation,  $\varepsilon = 5E - 05m$ . The velocities,  $u_{1\varepsilon}$  and  $u_{1.33\varepsilon}$ , can be obtained from the post-processing tool Paraview (Zimmer, Matthew Daly, 2020). Table 5.5 summarizes the velocity value and computed interfacial shear under two steam viscosities. Before  $t = 1.0E - 3 s$ , not only are the liquid flow rates the same, the interfacial shear is also identical. As flow develops and after the deviation between velocities shows up, the interfacial shears in Table 5.5 are still comparable.

Last but not the least, researchers have demonstrated that when the system is pressurized, the liquid viscosity under pressurized condition is more influential on determine CCFL occurrence (Murase et al., 2012). Since liquid viscosity is not changed and with the justification from liquid phase flow rate and interfacial shear in this test, the 10 times steam viscosity effect on CCFL is concluded to be minimal.

Table 5.5. Interfacial shear comparison between two steam viscosities.

	Viscosity	$\mu_g (Pa \cdot s)$	$u_{1\varepsilon} (m/s)$	$u_{1.33\varepsilon} (m/s)$	$\tau_i (N/m^2)$
$t = 9.2E - 4 s$	Original	1.34384E-05	0.00771	0.00730	0.0102
	10 times	1.34384E-04	0.00864	0.00823	0.0102
$t = 1.75E - 03 s$	Original	1.34384E-05	0.01323	0.01095	0.05696
	10 times	1.34384E-04	0.01576	0.01422	0.03847

### 5.2.2.2 Domain length

Since the two-phase flow setup in the debris bed channel is annular flow, the domain length may not affect the CCFL condition. To confirm this assumption, two domains with lengths of 1mm and 2mm are selected to conduct the domain length effect study. Figure 5.14 compares the

discretized domains with the interfaces initialized for annular flows under different domain lengths. A void fraction of 60% is used for both cases and the base mesh resolutions are the same. The control coefficients in the PID pressure gradient controller are selected from the recommended value in Table 3.4 being  $K_P = -1.0E11$ ,  $K_I = 1.0$ , and  $K_D = -1.0E10$ .

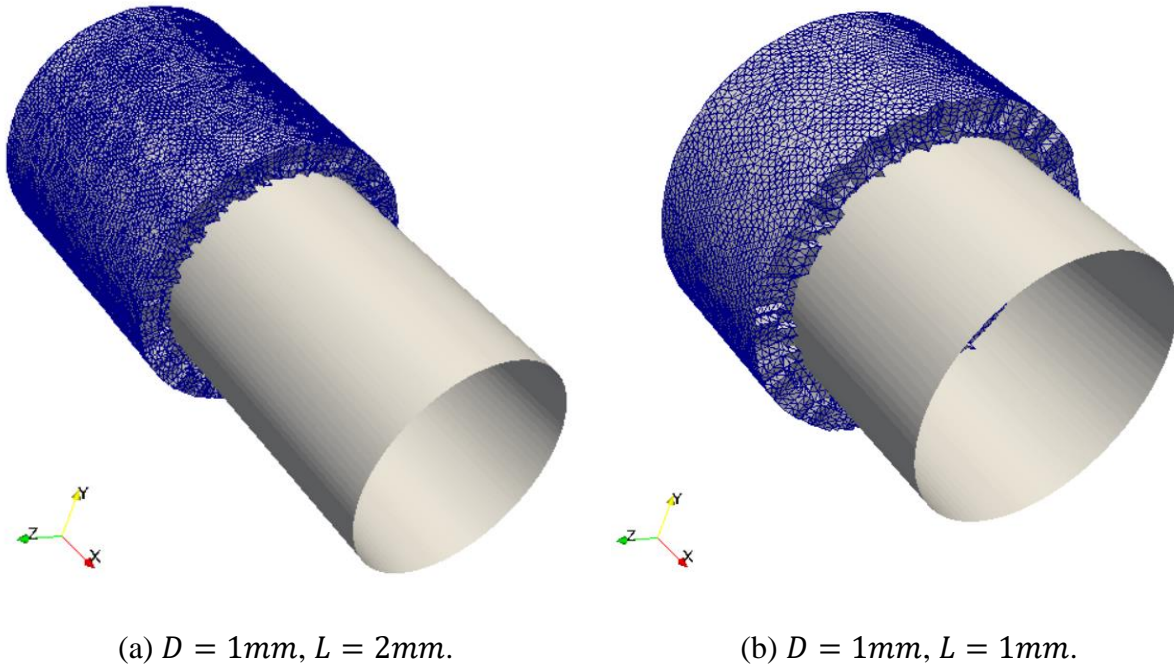


Figure 5.14. Domain length effect simulation setup with void fraction of 60%.

The results of PID pressure gradient controller are plotted in Figure 5.15. Although the control coefficients are the same, the  $L = 2mm$  domain actually achieves a quasi-steady state slightly faster than the  $L = 1mm$  domain. However, since the number of elements for  $L = 2mm$  is twice of  $L = 1mm$ , the wall clock time is much higher. The averaged eventual pressure gradients are  $2765 Pa/m$  and  $2786 Pa/m$ , with a relative difference of only 0.76%. Therefore, using  $L = 1mm$  domain has negligible influence on the CCFL conditions, but greatly conserves computational resources. Therefore, the following CCFL parameter studies are all conducted with the  $L = 1mm$  domain.

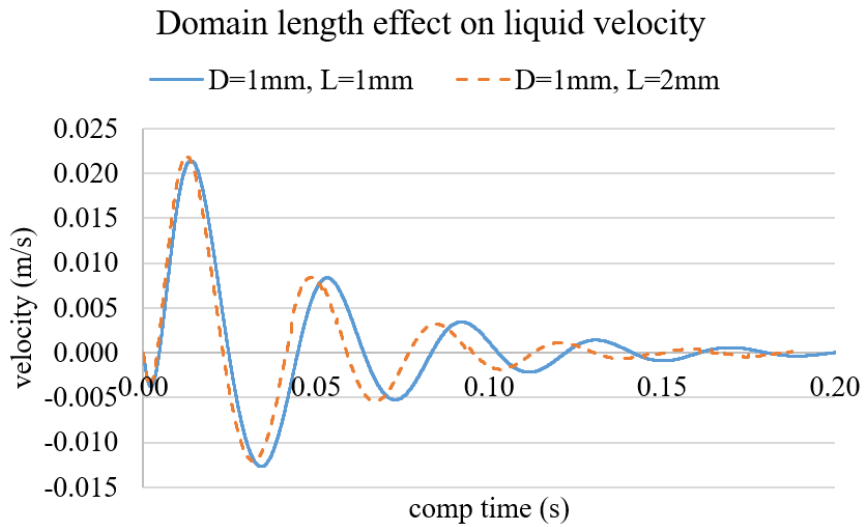
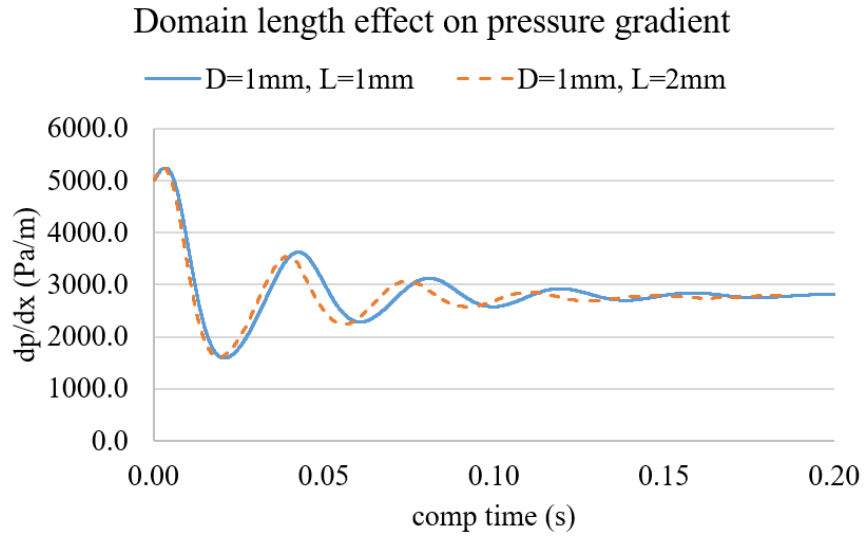


Figure 5.15. Domain length effect comparison.

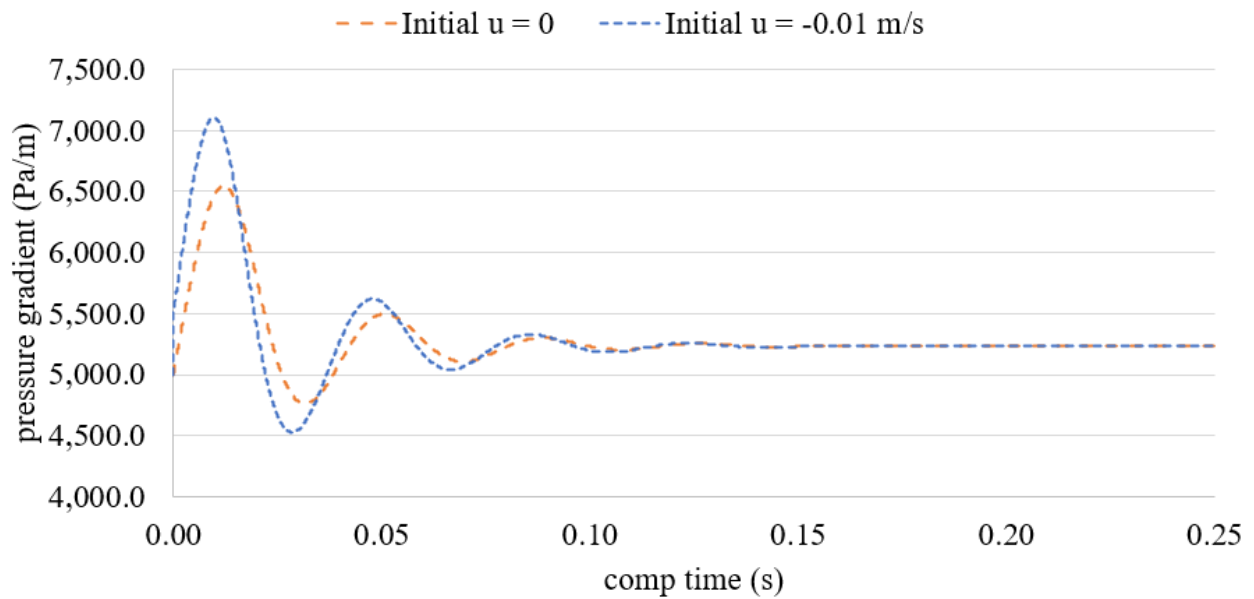
### 5.2.2.3 Initial conditions

Robustness test #1 in Section 3.3.3 already proves that the eventual flow rate control is not affected by the initial pressure gradient in the flow channel. The test in this section will explore the effects of varying initial liquid velocity on the CCFL. The initial velocity field in liquid indicates the coolant flow direction before CCFL occurs.

The assumption for the PID pressure gradient controller is that the eventual flow rate control should not vary with initial liquid velocity given all other parameters unchanged. In order to verify this assumption, the simulation of steam volume fraction  $\alpha = 30\%$  is selected with two different initial liquid flow directions, one of (0.0, 0.0, 0.0) which is a stagnant flow, the other of  $(-0.01, 0.0, 0.0) m/s$  indicating a downflow (as the  $x$  direction is stream-wise in the up direction). Aside from the difference in initial liquid velocity, other simulation parameters are duplicated from Table 5.4.

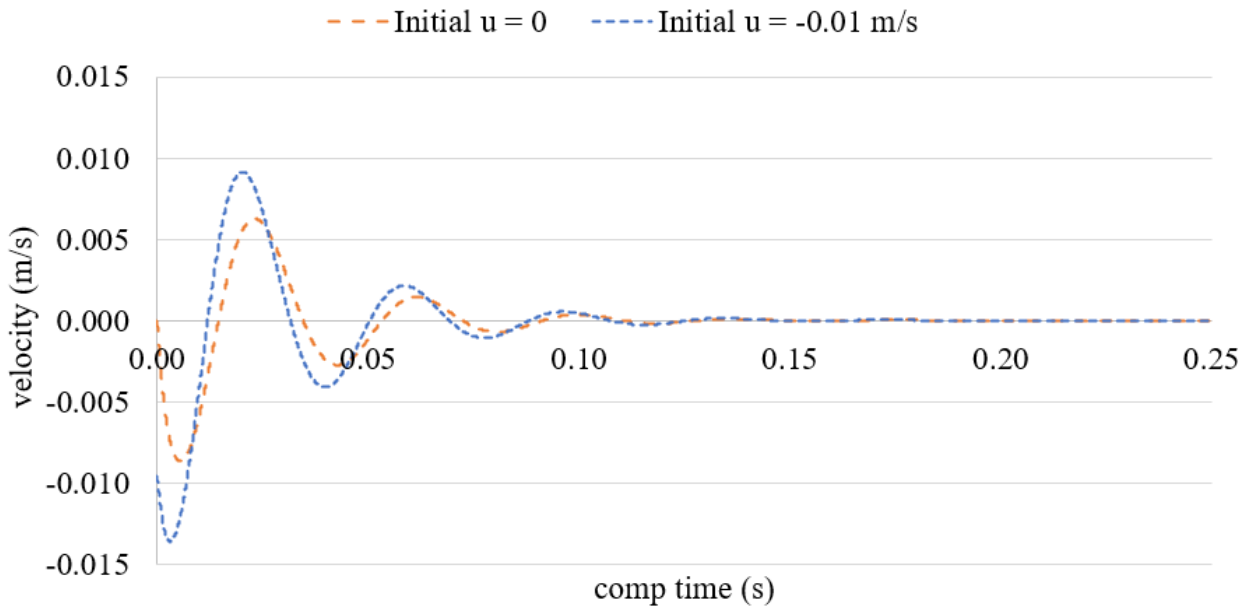
The results of the PID control of the above two tests are plotted in Figure 5.16. In Figure 5.16(a), there is a pressure gradient jump in the beginning of the simulation for initial condition of the downflow. This jump is resulted from the proportional component of the PID controller. At the first time step, integral and derivative components are zero, so the input to PID control is only the proportional component,  $K_P(\int udS^{(0)} - \int u_{desire}dS)$ . Since the desired liquid velocity is zero, the initial proportional component is equal to  $\int udS^{(0)}$ . Compared to initial stagnant flow, the downflow has much larger proportional component which causes PID controller to react immediately, therefore a jump is observed at the beginning. Although such jump causes greater fluctuation of the PID control curve, eventually the two tests will still reach CCFL occurrence almost simultaneously (Figure 5.16 (a)). Similarly, liquid velocity also achieves zero together in Figure 5.16 (b). The time-averaged final pressure gradients and velocities are very close to each other (Table 5.6). The relative difference between pressure gradients is only 0.06%, which verifies the assumption that initial velocity field does not affect the condition for CCFL to occur, regardless of stagnant flow (used in the majority of simulations) or down flow (used in the next section for sensitivity analysis of CCFL criteria).

Pressure gradient under different initial liquid velocity ( $\alpha=30\%$ )



(a) Pressure gradient.

Liquid velocity under different initial liquid velocity ( $\alpha=30\%$ )



(b) Cross-sectional averaged liquid velocity.

Figure 5.16. Influence of initial liquid velocity on PID controlled CCFL.

Table 5.6. Averaged variables in the quasi-steady state of two test cases under  $\alpha = 30\%$ .

Initial velocity field	Pressure gradient (Pa/m)	Liquid cross-sectional averaged velocity (m/s)	Steam volumetric averaged velocity (m/s)
(0.0, 0.0, 0.0)	5235.76	7.44E-07	4.61E-01
(-0.01, 0.0, 0.0) m/s	5232.42	1.17E-06	4.61E-01

#### 5.2.2.4 CCFL criteria

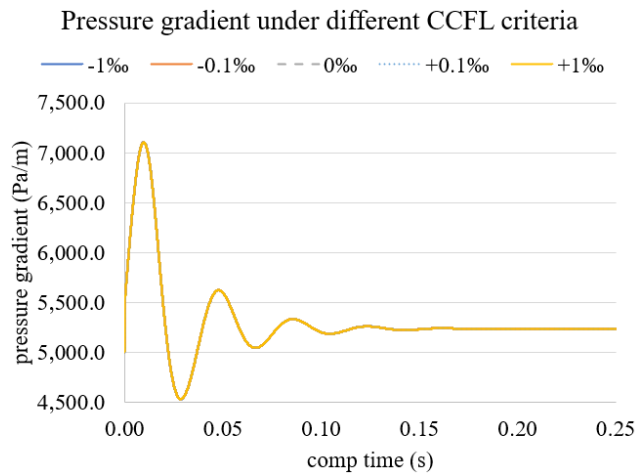
The CCFL criterion proposed in this dissertation is very specific, i.e., liquid cross-sectional velocity integral or cross-sectional averaged liquid velocity is equal to 0. However, there are indeed other potential criteria which can be chosen for describing the zero liquid flow rate at CCFL. For instance, volumetric liquid velocity integral or volumetric averaged liquid velocity. For incompressible flows where steam does not change volume, cross-sectional averaged liquid velocity equal to 0 is adequate to determine if CCFL occurs and it is also more computational efficient. However, if boiling is involved or the steam volume changes, a volumetric averaged liquid velocity equal to zero can be more appropriate.

Apart from the quantity to integrate, if the definition of zero velocity is relaxed, the effect on the pressure gradient to determine CCFL can be unknown. In this section, different definitions of liquid velocities are incorporated into the controller to examine the sensitivity of the results to the definition. The initial velocity field is the same with the test case as in Section 5.2.2.3, also under  $\alpha = 30\%$ . A relative velocity is used here as the CCFL criterion to quantify how the eventual liquid velocity compares to the initial velocity field,  $\frac{u_t}{u_0}$ . In order to generate a liquid velocity small enough relative to the initial velocity field, 5 values of  $\frac{u_t}{u_0}$  are chosen, which are  $-1\%$ ,  $-0.1\%$ ,  $0\%$ ,  $+0.1\%$ , and  $+1\%$ . The case with  $\frac{u_t}{u_0} = 0\%$  is identical with the proposed CCFL criterion

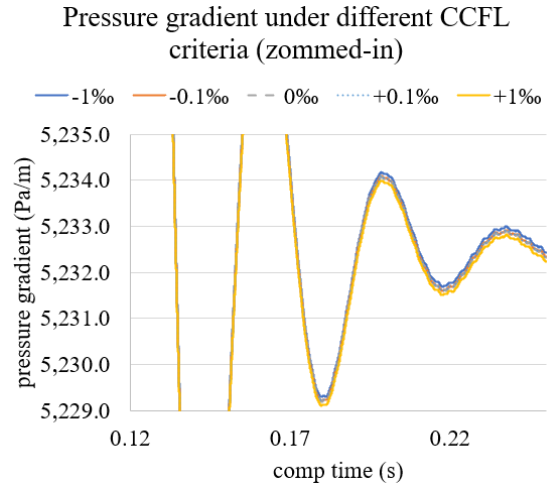
that the eventual liquid cross-sectional averaged velocity is equal to 0. The test values are summarized in Table 5.10, along with the simulation results averaged at the quasi-steady state in Figure 5.21. In Figure 5.21, the simulation results for  $\frac{u_t}{u_0} = -0.1\text{‰}, 0\text{‰}$  and  $+0.1\text{‰}$  almost overlap with each other even in the zoomed-in plots; only the plots of  $\frac{u_t}{u_0} = -1\text{‰}$  and  $+1\text{‰}$  have an observable difference with the middle three curves. Before a computation time of 0.12 s, all the control curves nearly overlap since the dominant control is still proportional component. After a computation time of 0.12 s, all simulations are convergent to the desired velocities ( $1.0E - 5$  m/s versus  $1.0E - 6$  m/s) with negligible differences. This demonstrates the accurate performance of the PID controller.

Table 5.7. CCFL definition sensitivity analysis (initial downflow of  $-0.01$  m/s).

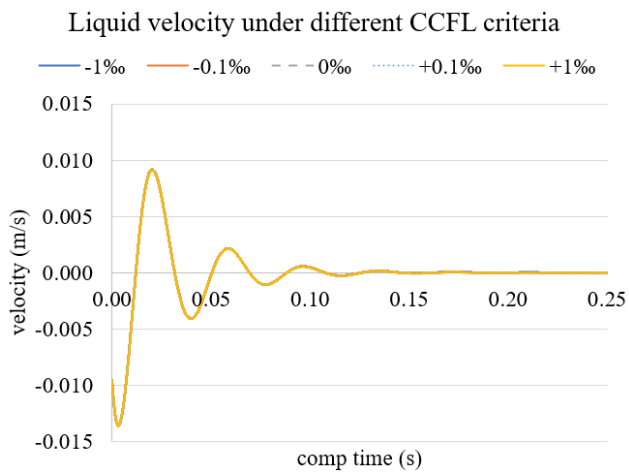
$\frac{u_t}{u_0}$	Desired liquid velocity (m/s)	Pressure gradient (Pa/m)	Liquid cross-sectional averaged velocity (m/s)	Steam volumetric averaged velocity (m/s)
-1‰	1.0E-5	5232.52	1.12E-05	0.46057
-0.1‰	1.0E-6	5232.44	2.16E-06	0.46055
0‰	0.0	5232.42	1.17E-06	0.46055
+0.1‰	-1.0E-5	5232.41	1.40E-07	0.46055
+1‰	-1.0E-6	5232.34	-8.83E-06	0.46052



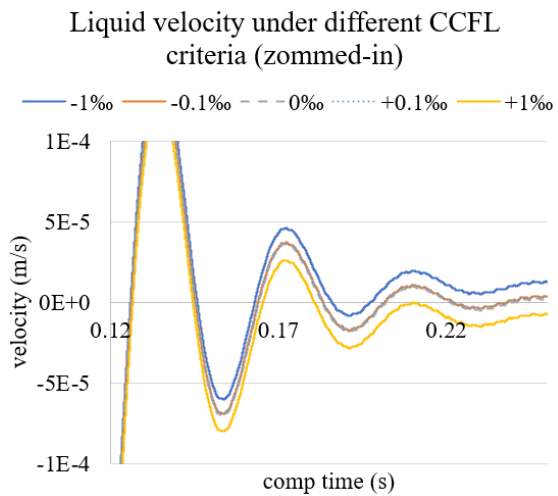
(a) Pressure gradient.



(b) Zoomed-in plot.



(c) Cross-sectional averaged liquid velocity.



(d) Zoomed-in plot.

Figure 5.17. PID controlled CCFL under different definition.

From Table 5.10, the pressure gradient and corresponding steam volumetric averaged velocity to achieve CCFL under different definitions are convergent with each other with a negligible relative error of  $\sim 0.01\%$ . While the 0 liquid velocity definition for CCFL is strict, loosening the definition to the range of  $-0.1\% \frac{u_t}{u_0}$  to  $0.1\% \frac{u_t}{u_0}$  has negligible effect on the determined pressure gradient. This observation is beneficial for experimental studies or CCFL simulations where exactly zero liquid velocity might not be achieved restricted by measurement or computational

methods. As long as the eventual liquid velocity is significantly smaller relative to the initial value, the change in CCFL condition is negligible.

Another observation in the study is that the obtained liquid velocity has a systematic difference with the desired liquid velocity and can be seen in Figure 5.22. The numerical error is small (averaged  $1.16E - 6 \text{ m/s}$ ) but it indeed exists. Although the simulation was run long enough to reach a quasi-steady state, the small fluctuation under PID control cannot be avoided due to the nature of the derivative component  $K_D(\int u dS^{(n)} - \int u dS^{(n-1)})$ . To quantify the numerical error, grid convergence study will be discussed in the next section.

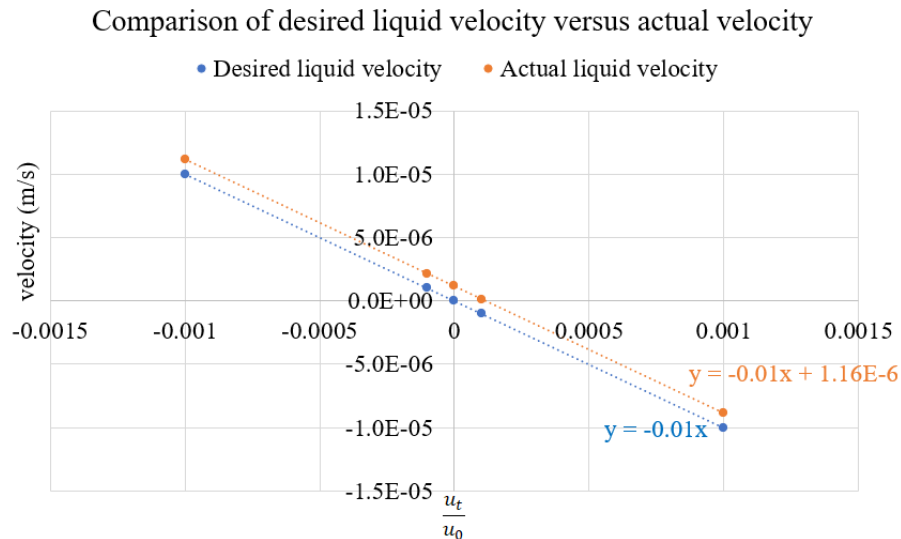


Figure 5.18. Desired terminal liquid velocity compared with actual simulation results.

### 5.2.2.5 Grid convergence study

Four different unstructured mesh configurations (tetrahedron elements in Figure 5.19) from the coarsest to the finest are designed for the grid convergence study to quantify the uncertainty of the spatial discretization and to investigate if it can explain the systematic error observed in Section 5.2.2.4. The four meshes were uniformly refined with a linear refinement ratio of  $r = 1.265$  and the mesh statistics are summarized in Table 5.8. Using 64 processing cores (1 node) on the local cluster Insight, it takes approximately 48 hours wall clock run time for the finest mesh to achieve

the quasi-steady state solution. The mesh study was performed to evaluate the evolution of the eventual pressure gradient at CCFL occurrence, which was averaged after a quasi-steady state was achieved for each mesh configuration (Table 5.8).

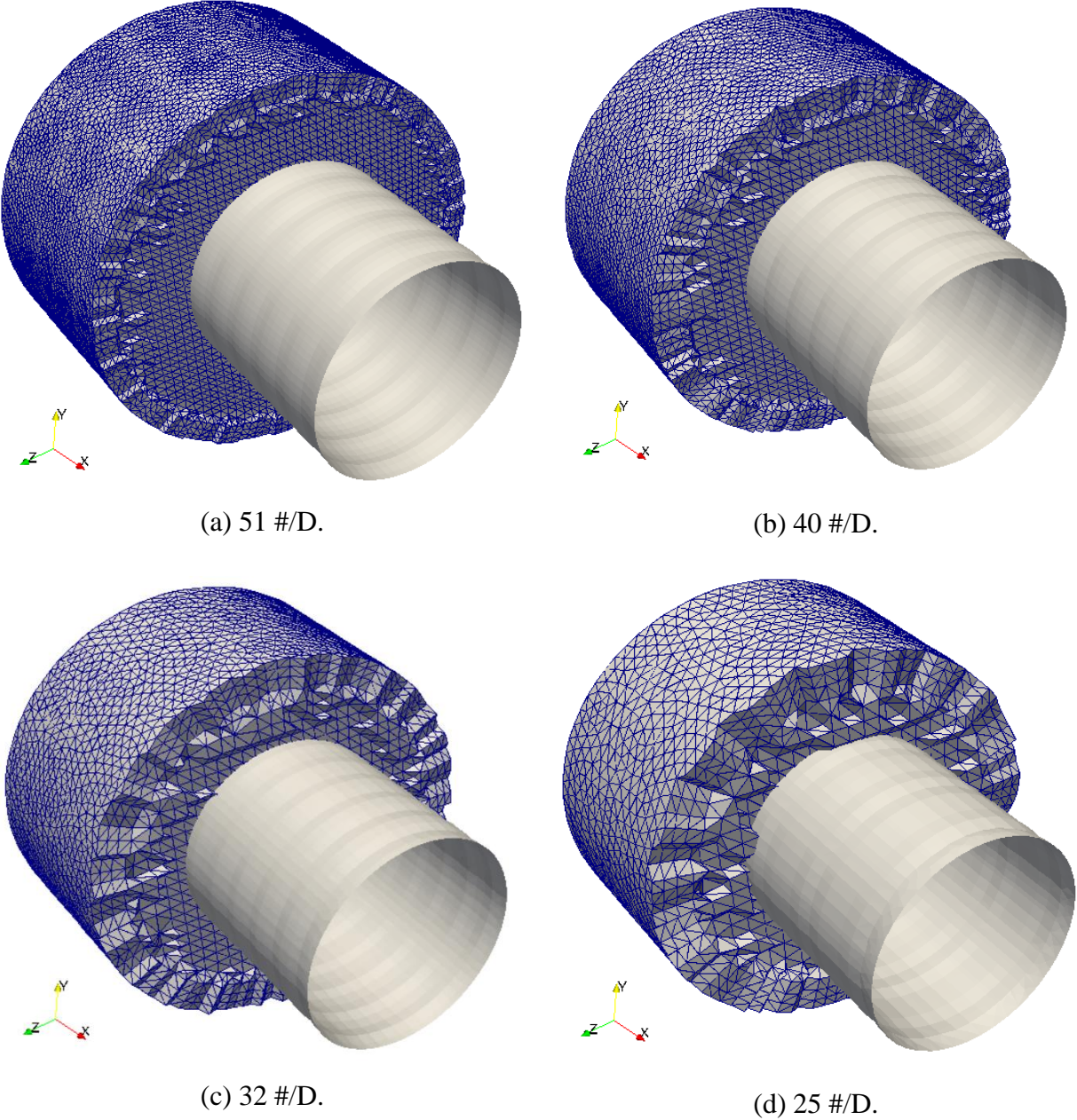


Figure 5.19. Mesh configurations with different elements across channel diameter (#/D).

Table 5.8. Mesh configuration statistics and the corresponding pressure gradients and coolant velocities at CCFL.

Case #	#/D	Mesh size	$\frac{dp}{dx}$ at CCFL (Pa/m)	Coolant velocity (m/s)
1	51	765,293	5245.53	2.85E-07
2	40	412,231	5235.76	7.44E-07
3	32	211,392	5223.2	2.69E-06
4	25	116,759	5159.95	3.45E-06

The mesh convergence is evaluated using standard grid convergence index (GCI) (Roache, 1998). *GCI* quantifies the percentage of the computed result away from the asymptotic numerical value and can be calculated by the results with different spatial discretizations. This was elaborated in Section 4.3.2 and computed by Eq. (42).

The GCI variation with different mesh resolutions is plotted in Figure 5.25. As the mesh is refined, GCI gradually decreases as finer meshes yield results closer to the asymptotic numerical value. If the mesh is further refined, GCI will eventually decrease to 0, but this is not practical due to the growing computation costs. Considering the GCI has already achieved  $1.51E-3$  in Figure 5.25, the current mesh is fine enough to approach the asymptotic numerical value. Therefore, the mesh in Case #2 (40 elements across the cylindrical diameter) is chosen to conduct all the production simulations. From Table 5.8, it also can be seen that the coolant velocity approaches zero as the mesh is refined. The deviation from zero is in a magnitude range of  $1E-7$  or  $1E-6$  m/s, which explains the systematic error in Section 5.2.2.4. The mesh in Section 5.2.2.4 uses the same mesh as in Case #2, only with a different initial velocity condition. The averaged velocity deviation from zero is  $1.16E-6$  m/s, which is very close to the  $7.44E-7$  m/s in Case #2.

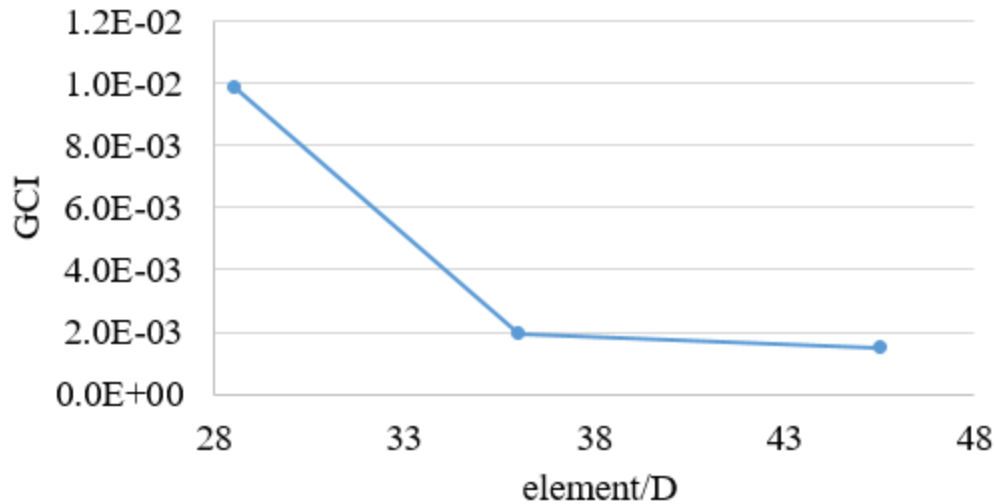


Figure 5.20. Grid convergence index vs. the mesh configuration.

### 5.2.3 CCFL studies under varying void fractions

In order to provide a high-resolution database for M-CFD and system-scale codes on CCFL, and to establish a model for evaluating the pressure gradient in debris bed channel, CCFL simulations under a series of void fractions are conducted in the debris channel. The computational domain is the cylindrical channel of  $D = 1\text{mm}$  and  $L = 1\text{mm}$  with an annular flow initialized. The working fluids are still the saturated water and steam under 3atm, and the simulation parameters are all from Table 5.4. The only parameter which is different among the 5 simulation cases is the void fraction varying from 60% to 20% as Table 5.9 shows. This range is selected based on the debris bed experimental measurements (Abe and Adachi, 1994). Since the annular flow is initialized by a steam volume in the center of the debris bed channel as Figure 5.14 (b) depicts, varying void fraction requires changing the steam column radius in the initialization as well. Among these 5 cases, Case #1 to #4 are conducted with PID pressure gradient controller to achieve CCFL conditions. The obtained pressure gradients under liquid flow rate of zero will be compared with experimental data. Then the pressure gradient correlation will be established with

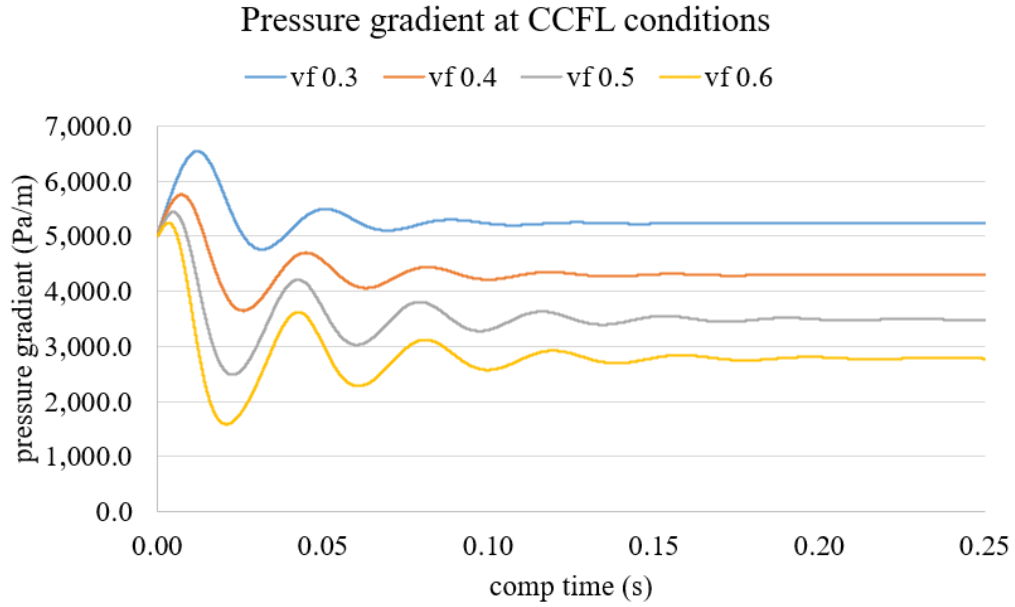
regards to the void fraction. At last, Case #5 will use the pressure gradient predicted from the correlation to verify the pressure gradient model.

Table 5.9. Void fraction and the corresponding gas column radius in the case study.

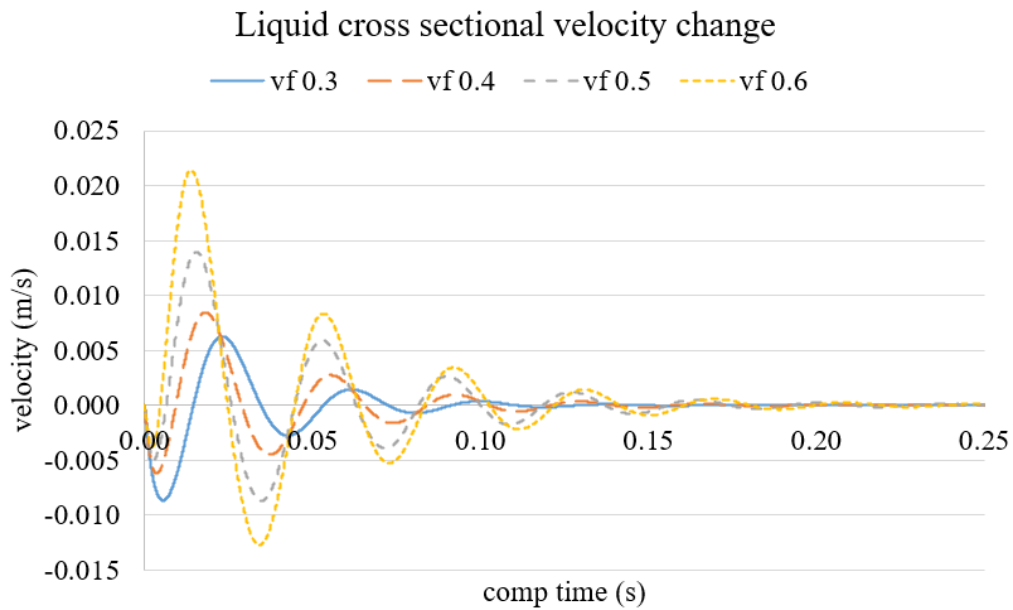
Case	1	2	3	4	5
Void fraction	60%	50%	40%	30%	20%
Steam column radius ( <i>mm</i> )	0.387	0.354	0.316	0.274	0.224

The simulation results are plotted in Figure 5.21 and the averaged values at quasi-steady state are summarized in Table 5.10. The flow regimes are all annular flows, with the evolution of velocity field shown in Appendix E.1, using 30% void fraction as an example. From Figure 5.21 (a) and Table 5.10, the pressure gradient to achieve CCFL conditions gradually reduces with void fraction. This is understandable as when more steam occupies the debris bed channel, less coolant can pass the channel, and less interfacial shear is needed to balance with the coolant gravity and wall shear to achieve CCFL. The phase averaged volumetric velocity is plotted in Figure 5.21 (c) with data obtained from bubble tracking algorithm which recognizes the steam column as a bubble (Fang, 2016). As the void fraction increases, the eventual steam flow rate shows an asymptotic trend. As the steam column size reduces, the gas phase velocity development is indeed restricted when CCFL condition is achieved. According to Figure 5.21 (b) and Table 5.10, with the void fraction increasing, the interface instability also grows stronger, thus the liquid velocity achieves steady state slower. However, the eventual cross sectional liquid velocity still reaches a magnitude of at most  $10^{-6}m/s$  which means CCFL is achieved with almost zero liquid flow rate.

Figure 5.21. Pressure gradient and velocities of liquid and gas phase to achieve CCFL conditions under varying void fractions.



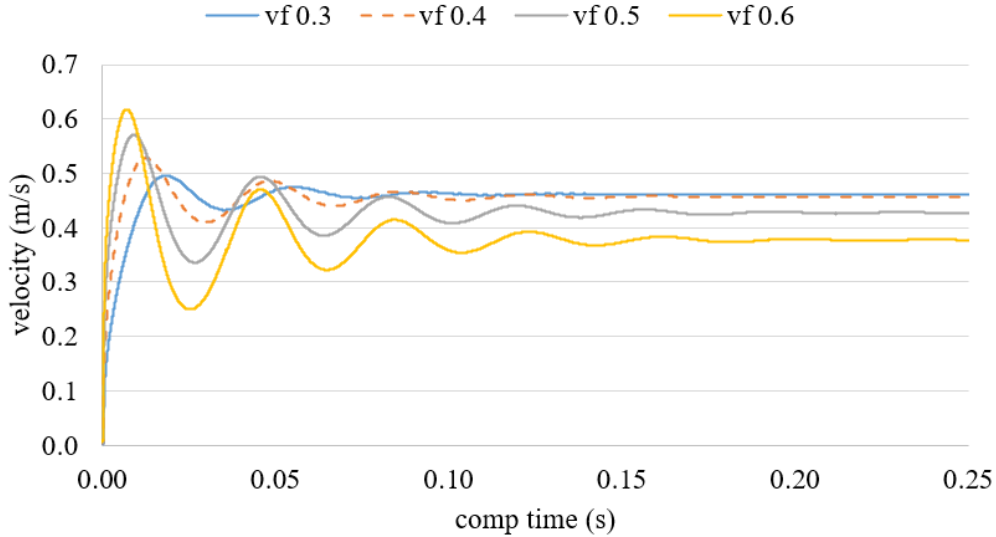
(a) Pressure gradient.



(b) Cross sectional liquid phase velocity.

Figure 5.21. (continued)

Steam volumetric velocity change



(c) Steam volumetric averaged velocity.

Table 5.10. Averaged variables in the quasi-steady state of each case.

Void fraction	Pressure gradient (Pa/m)	Liquid cross-sectional averaged velocity (m/s)	Steam volumetric averaged velocity (m/s)	Steam superficial velocity (m/s)
30%	5235.76	7.44E-07	4.61E-01	1.38E-01
40%	4299.29	4.80E-06	4.57E-01	1.83E-01
50%	3491.00	2.60E-07	4.27E-01	2.14E-01
60%	2785.52	-7.04E-06	3.77E-01	2.26E-01

#### 5.2.4 Comparison with CCFL experiments

The steam superficial velocity is computed based on void fraction and the steam volumetric averaged velocity in Table 5.10 is to compare with experimental data. There was no experiment conducted for debris bed channel and the comparison data of pressure gradient was obtained from the debris bed experiments using polydispersed particles (Rashid et al., 2012). Figure 5.22 compares the pressure gradient varied with steam superficial velocity obtained by PID control and

by the experimental CCFL data both under 3atm (Rashid et al., 2012). The uncertainty of simulation results is quantified by a composite error bar (Karniadakis, 1995), computed as a summation of spatial error, domain size error, and boundary condition error. The experimental study did not provide an uncertainty quantification; therefore, a 95% credibility interval is considered for an error estimation (Snedecor and Cochran, 1989). Since the experiments were conducted with a debris bed formed by stainless steel balls with diameters of 2 mm, 3 mm, and 6 mm, the debris bed channel can have various sizes (Figure 5.23). However, in the simulation the channel diameter is 1 mm, therefore the simulation results are expected to deviate from the experimental data. In Rashid’s experiments, it is observed that pressure gradients steeply decrease with steam superficial velocity under CCFL conditions, and a similar trend is observed for the simulation data from Table 5.10.

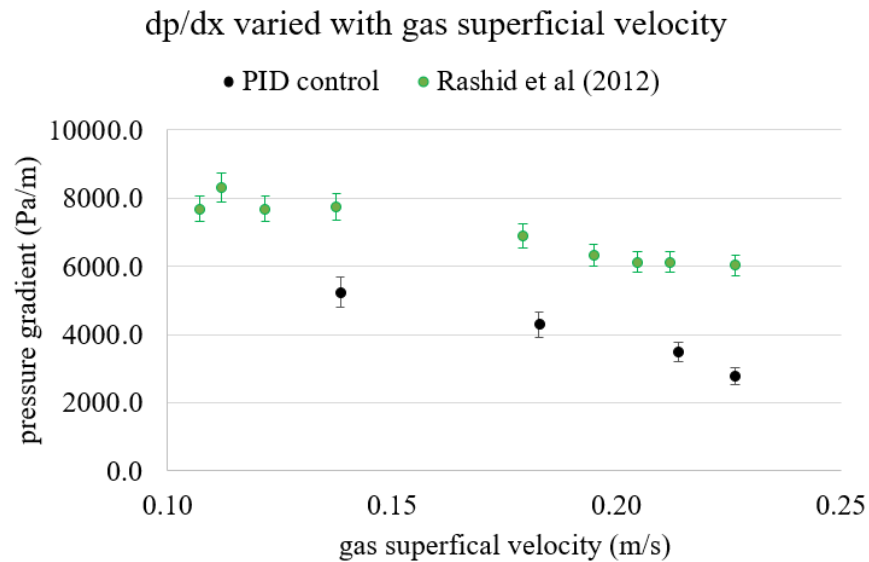


Figure 5.22. Pressure gradient obtained from PID control compared with experimental data (Rashid et al., 2012).

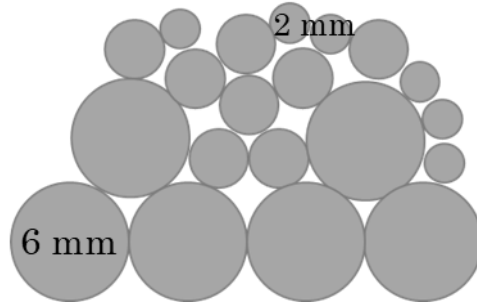
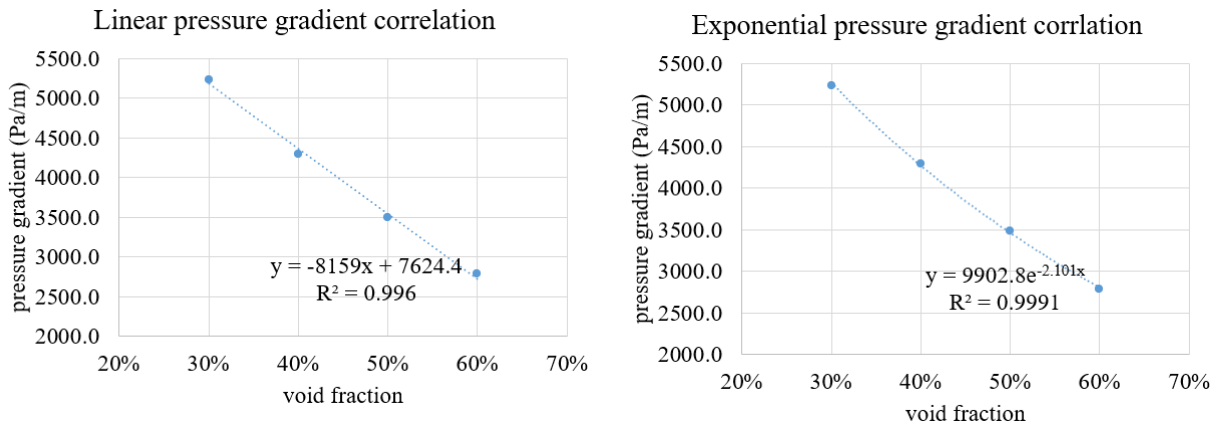


Figure 5.23. Illustration of possible channel configuration in the debris bed experiment (Rashid et al., 2012).

### 5.2.5 Pressure gradient model development

Quantitative analysis is provided for pressure gradients under varying void fractions to inform CCFL debris bed channel model development. If heat transfer is considered as if in real debris bed channels, the void fraction can be determined by the heat flux, channel surface area, and the latent heat. Therefore, with pressure gradient correlation established with regard to the void fraction, it can be converted to a correlation of heat flux and then used in engineering applications.

Figure 5.24 plots the pressure gradient varied with void fraction ( $\alpha$ ) with data from Table 5.10, and then the data points are fitted in linear and exponential trends separately.



(a) Linear.

(a) Exponential.

Figure 5.24. Pressure gradient correlations fitted in linear or exponential trends.

$$\text{Linear } \frac{dp}{dx} = -8159\alpha + 7624.4 \quad (47)$$

$$\text{Exponential } \frac{dp}{dx} = 9902.8 \exp(-2.101\alpha) \quad (48)$$

The exponential form has a better extrapolation performance than the linear form when  $\alpha \rightarrow 0$  and  $\alpha \rightarrow 100$ . If  $\alpha = 0$ , there is pure liquid in the debris bed channel, so pressure gradient only needs to balance with gravity to achieve CCFL. When  $\alpha = 0$ ,  $\frac{dp}{dx}$  obtained from the linear and exponential forms are  $7624.4 \text{ Pa/m}$  and  $9902.8 \text{ Pa/m}$  respectively, and the latter is much closer to  $\rho_l g = 9314.3 \text{ Pa/m}$ . If  $\alpha = 100\%$ , the channel is full of steam, so the pressure gradient just needs to balance with steam gravity and wall shear in order to drive steam move upward. Therefore,  $\frac{dp}{dx}$  should still be positive. However, in Eq. (47) when  $\alpha = 100\%$ ,  $\frac{dp}{dx} < 0$ , so it is not physically correct under such condition. In order to further compare the performance of the pressure gradient models,  $\frac{dp}{dx}$  under  $\alpha = 20\%$  is predicted and then used for simulations without PID control. According to Eq. (47),  $\frac{dp}{dx} = 5992.6 \frac{\text{Pa}}{\text{m}}$ ; according to Eq. (48),  $\frac{dp}{dx} = 6505.3 \text{ Pa/m}$ . The simulation conducted with  $5992.6 \text{ Pa/m}$  yields an eventual velocity magnitude around  $-6E - 2 \text{ m/s}$ , which is not strictly close to zero. The flow regime of this simulation also changes from the annular flow to a single bubble flow, which is depicted in Appendix E.2. The simulation conducted with  $6505.3 \text{ Pa/m}$  achieves an eventual velocity to be  $-5.41E - 3 \text{ m/s}$ , which is acceptable. Therefore, the exponential form is recommended to predict pressure gradient under a given void fraction. The correlation can be generally used as Eq. (49) which considers the extrapolation to  $\alpha \rightarrow 0$  and  $\alpha \rightarrow 100\%$  (Figure 5.25).

$$\frac{dp}{dx} = \rho_l g \cdot \exp(-2.0\alpha) \quad (49)$$

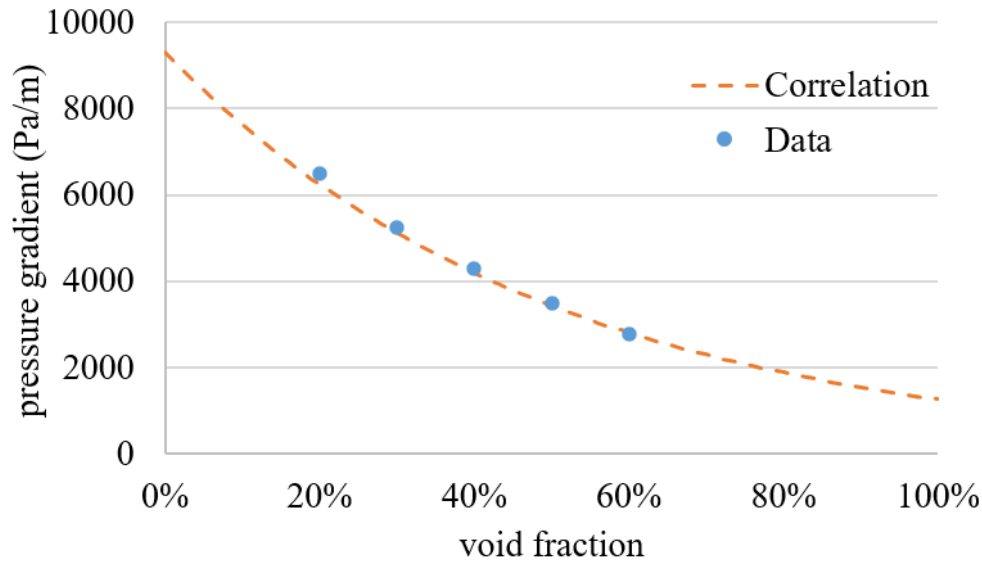


Figure 5.25. Pressure gradient correlations with regard to the void fraction.

As the debris bed experimental measurements show that the void fraction range is  $\alpha = 10\% \sim 60\%$  (Abe and Adachi, 1994), the presented correlation proposed by data from  $\alpha = 20\% \sim 60\%$  represents most of the debris channel conditions. The application range study in Section 5.4 is presented for demonstrating the accuracy of this correlation and to further explore the physics behind it as well.

### 5.2.6 Dimensionless number for pressure gradient under CCFL conditions

This section tries to build the connection between CCFL and bubble counter current flow studies. Interfacial shear in essence is a drag between liquid and gas phases, and CCFL is achieved when wall shear, interfacial shear, and gravity are balanced. Therefore, a dimensionless analysis is carried out to connect pressure gradient of CCFL with bubble drag force in Eq. (35). Table 5.11 summarizes the analogy terms between drag force and pressure gradient connection.

Table 5.11. Dimensional analysis of  $\frac{dp}{dx}$  with regarding to key parameters.

	$F_D \equiv -\frac{1}{2}C_D\rho_l A_b u_r^2$ (Eq. (35))	$\frac{dp}{dx} = SU(\rho_l - \rho_g)u_g^2/(\alpha D_{channel}) + C$
Inertia	$\rho_l$	$(\rho_l - \rho_g)/\alpha$
Momentum	$u_r^2$	$u_g^2$
Scale	$A_b$	$D_{channel}$

In Table 5.11,  $C$  is added to consider the wall shear and gravity effect. If  $C = 0$ , the dimensionless number which is equivalent to the drag coefficient  $C_D$  can be defined as

$$SU = \frac{\frac{dp}{dx} \alpha D_{channel}}{(\rho_l - \rho_g)u_g^2} \quad (50)$$

In this definition,  $D_{channel}$  is the diameter of the debris bed channel,  $(\rho_l - \rho_g)$  is the density difference between the liquid and the steam, and  $u_g$  is the steam volumetric velocity. Figure 5.26 shows the performance of this dimensionless study by plotting  $\frac{dp}{dx}$  and  $(\rho_l - \rho_g)u_g^2/(\alpha D_{channel})$  using data from Table 5.10. With the definition in Eq. (50), the trendline does not cross the origin to include the gravity and wall shear into consideration and  $SU$  is the slope of the trendline. The fitted linear trendline with  $R^2$  is almost equal to 1 which indicates that for each data set between  $\frac{dp}{dx}$  and  $(\rho_l - \rho_g)u_g^2/(\alpha D_{channel})$ , the ratio is a constant value, roughly 0.0056. Therefore, the proposed dimensionless number,  $SU$ , is consistently 0.0056 even under different void fractions and steam velocities. For application of  $SU$  number defined in Eq. (50), if it is computed to be lower than 0.0056, the flow regime in the debris bed channel is still counter current flow with liquid draining down. If  $SU$  is higher than 0.0056, it indicates that CCFL has already happened.

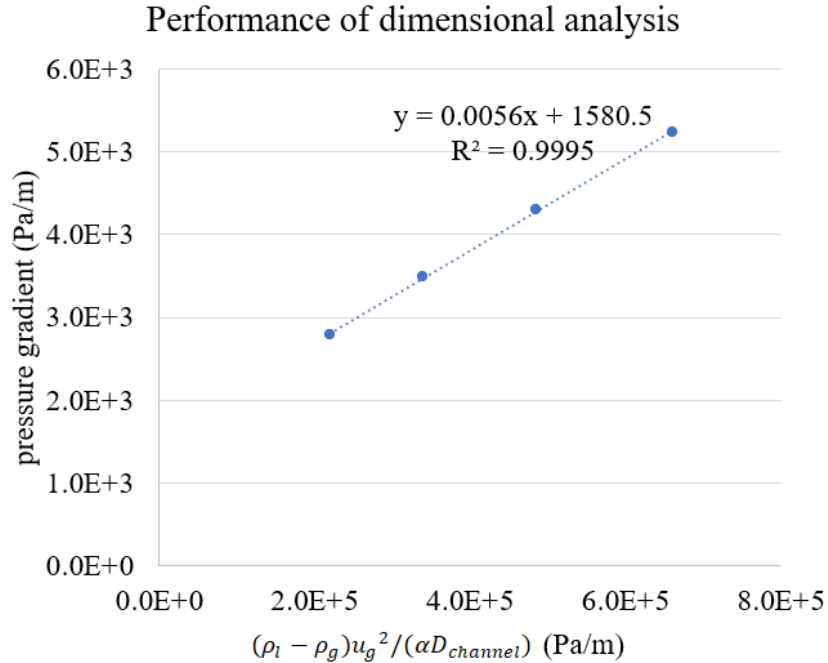


Figure 5.26. Performance of the dimensionless analysis where  $SU$  is the slope for the trendline. The trendline does not cross the origin because it includes the gravity and wall shear into consideration.

### 5.3 CCFL studies of complex debris bed channel under PID control

In order to investigate more realistic flow phenomena and to study the physics behind the debris bed CCFL behavior, cylindrical channels with added obstacles are used as imitation geometries of the actual debris bed. This section presents the simulation results of two such complex channels, with spherical obstacle sizes equal to 20% and 40% of the cylindrical channel diameter, respectively. The domain design is inspired by Lipinski's treatment that the debris bed is a porous media formed by single-sized spheres (Lipinski, 1984). The obstacle arrangements for small and big spherical obstacles are different for each scenario. For the channel with small obstacles, they are aligned on the wall inside the flow path. For the large obstacles' channel, the obstruction partially blocks the center of the flow channel. The effect of added obstacles on the occurrence of CCFL will be investigated and the PID control capability is also demonstrated given

the more complex flow conditions. The parameters used in this section are all duplicated from Table 5.4.

### 5.3.1 Debris bed channel with small obstacles

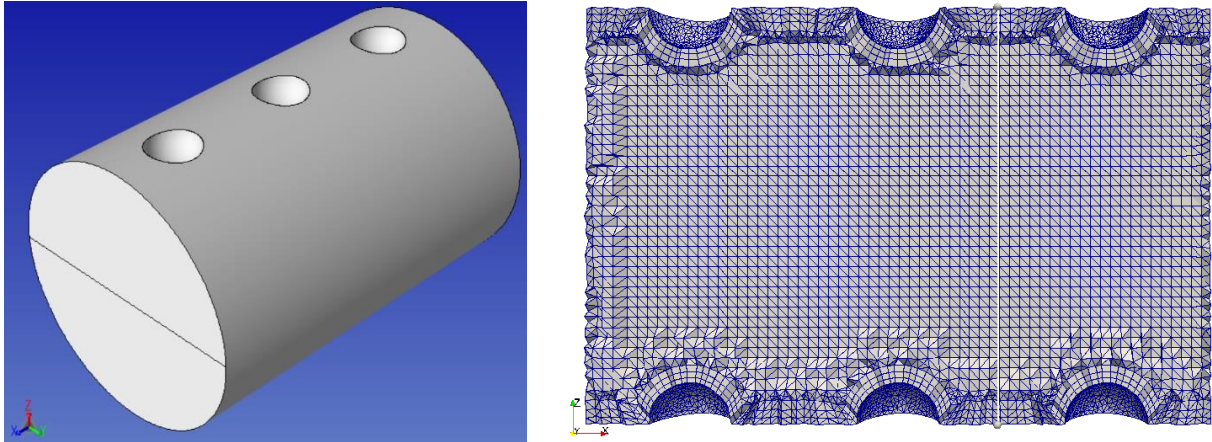
The cylindrical channel with small obstacles is designed by adding 6 hemispherical obstacles on the wall inside the flow path. The obstacles are aligned along the  $x - O - z$  plane as shown in Figure 5.27 (a) and their diameters are all 20% of the cylindrical channel diameter. The hydraulic diameter of the channel with small obstacles is kept constant at 1 *mm* to compare with the debris bed channels in Section 5.2. Since the channel cross-section with added obstacles are neither uniform nor circular, the hydraulic diameter is determined by Eq. (51) (White, 2003).

$$D_h = 4V/S \quad (51)$$

In this definition,  $D_h$  is the hydraulic diameter for non-uniform and non-circular cross-sectional channels,  $V$  is the total fluid volume of the channel, and  $S$  is the total wetted surface area. This definition is different than the traditional definition of the hydraulic diameter,  $D_h = 4A/P$ , where “ $A$ ” is the cross-sectional area of the flow and “ $P$ ” is the wetted perimeter of the cross-section. For uniform cross-sectional channels,  $4V/S$  can be reduced to  $4A/P$  (White, 2003).

The diameter of the cylinder in Figure 5.27 (a) is scaled to 1.0467 *mm*, which yields the  $D_h = 1\text{mm}$ . Therefore, the base mesh resolution, xyzts probe coordinates and the steam column radius are all scaled by a factor of 1.0467 accordingly, to be comparable with studies in Section 5.2. Figure 5.27 (b) shows the mesh configuration of 40 elements across the channel diameter with the number of elements being 0.725 million. Figure 5.27 (b) also depicts the location of xyzts probe plane with a white line, where the velocity integral information will be collected at each time step. Since the xyzts probes can only be assigned on tetrahedral mesh elements, the boundary layer mesh

elements along the cylindrical wall are all tetrahedralized. In contrast, the elements around the surface of obstacles are still prism boundary layer mesh.



(a) The geometry of debris bed channel with small obstacles.

(b) Mesh configuration with white line indicating the location of xyzts probes across the  $y - O - z$  plane.

Figure 5.27. Debris bed channel with small obstacles.

The additional obstacles are expected to affect the CCFL flow phenomenon considering the flow near the obstacles will produce local vortices. Such flow behavior will be investigated in the simulations. Moreover, the pressure gradient to achieve CCFL is studied under  $\alpha = 30\%$  to evaluate the predictive capability of the pressure gradient proposed in Section 5.2.5 when the channel is not a simple cylinder anymore. Moreover, the flow regime result from the additional obstacles will also be studied. In previous sections 5.2.3 and 5.2.5, the flow regime of  $\alpha = 20\%$  transitions from an annular flow to a single-bubble flow due to the low void fraction. In higher steam volume fractions ( $\alpha = 30\sim 50\%$ ) the annular flow is maintained. For comparison purposes, the same initial condition of annular flows will be applied in this channel with small obstacles and  $\alpha = 20\%$  and  $30\%$  are simulated as representative case studies.

### 5.3.1.1 Void fraction $\alpha = 30\%$

The annular flow initialization is depicted in Figure 5.28 with  $\alpha = 30\%$ . Figure 5.29 shows how pressure gradient and velocity integral on the  $xyzts$  probe plane changes. Although there is a small fluctuation in the quasi-steady state, the annular flow regime is maintained even after CCFL is achieved (Figure 5.30). The entire process of interface evolution is illustrated in Appendix F.1 where the two-phase velocity field also barely changes after  $t = 9.815E - 2s$ . In Figure 5.30 (a), the last time step of the simulation is shown. Here the steam column travels upwards (+ $x$  direction) without any lateral movement; the coolant region has re-circulations near the 6 obstacles. In Figure 5.30 (b), the velocity field is not laminar on the  $x - O - y$  plane. Based on the plotted velocity vector arrows in Figure 5.30 (b), which points in the  $-z$  and  $+z$  directions, secondary flow forms in the liquid film near the obstacles. Note that the secondary flow is not present in the simple cylindrical debris bed in Figure 5.30 (c).

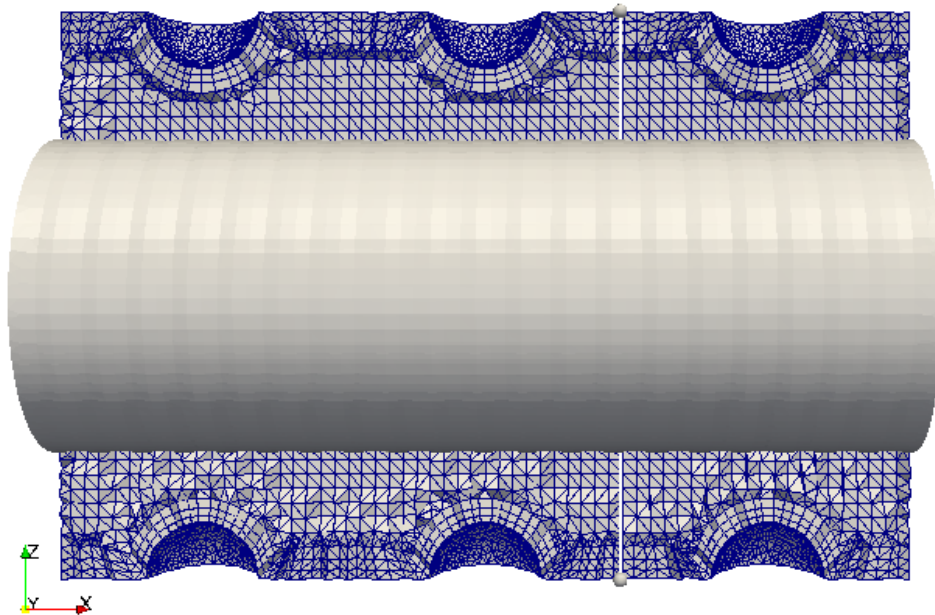


Figure 5.28. Two phase debris bed channel with small obstacles and  $\alpha = 30\%$ .

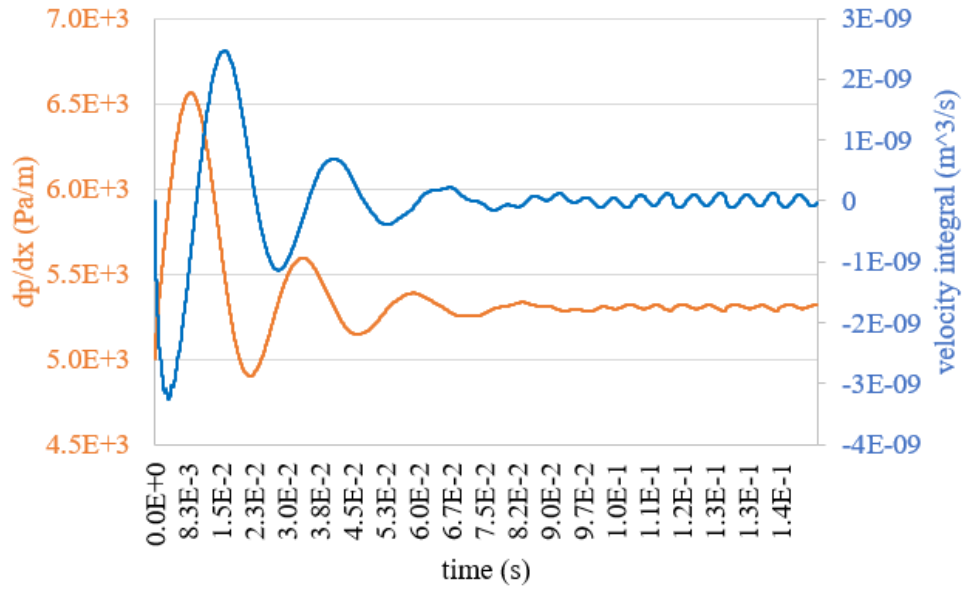
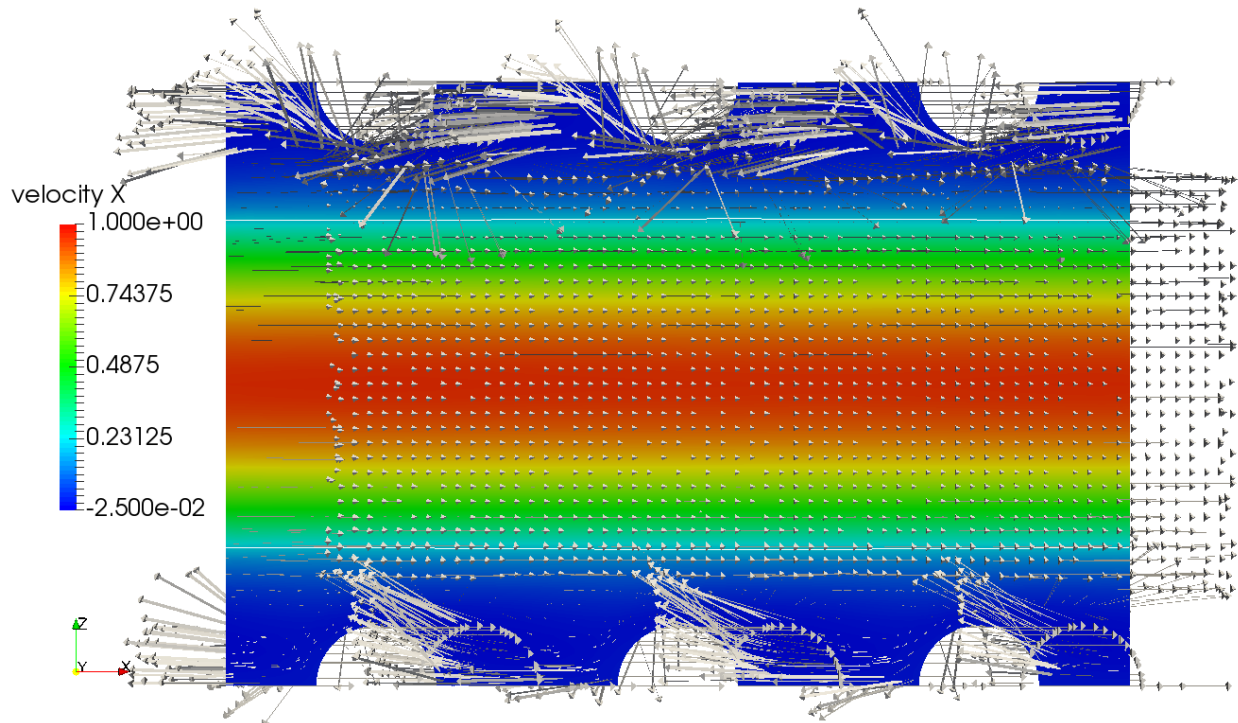


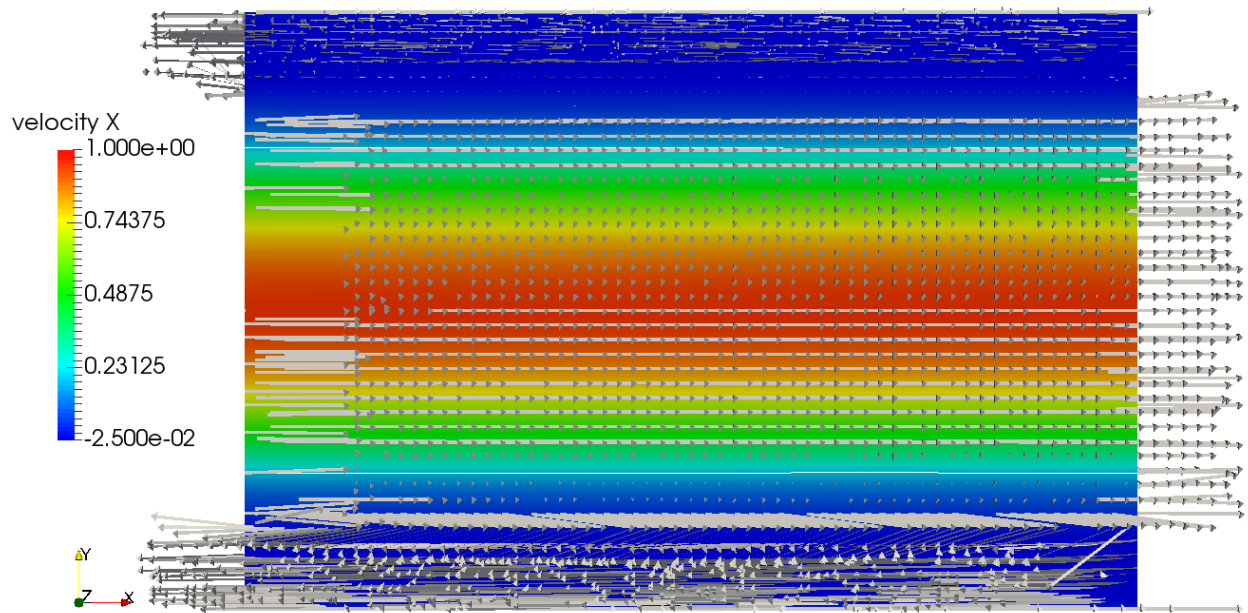
Figure 5.29. PID control on debris bed channel with small obstacles ( $\alpha = 30\%$ ).

Figure 5.30. Two-phase velocity vector fields under CCFL at the same time.

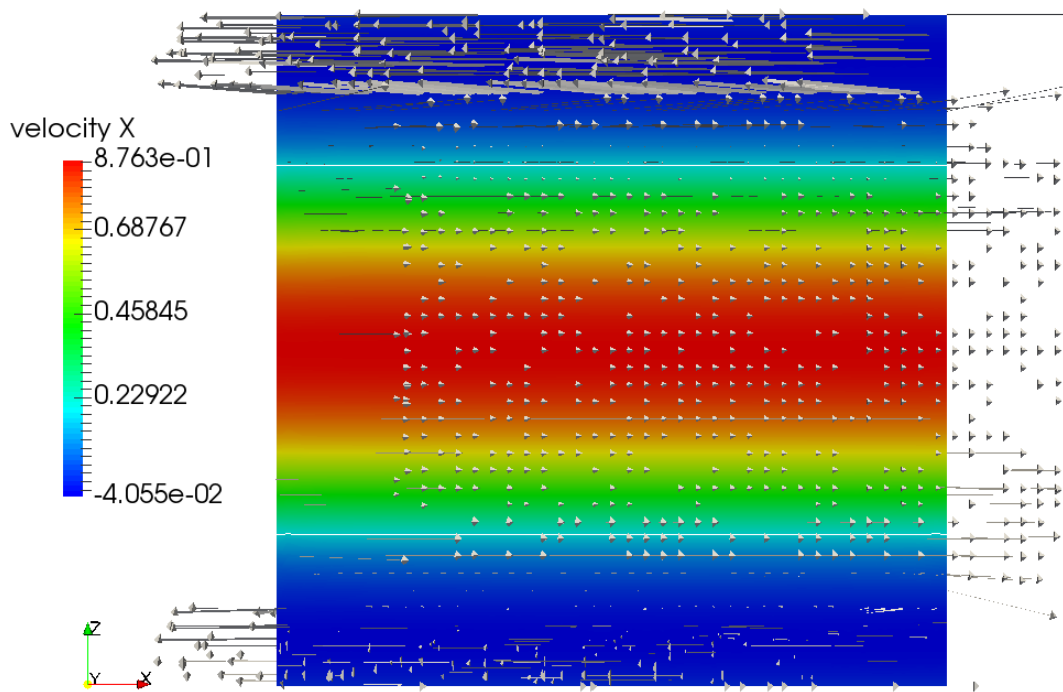


(a)  $x - O - z$  plane of debris channel with small obstacles ( $t = 1.307E - 1s$ ).

Figure 5.30. (continued)



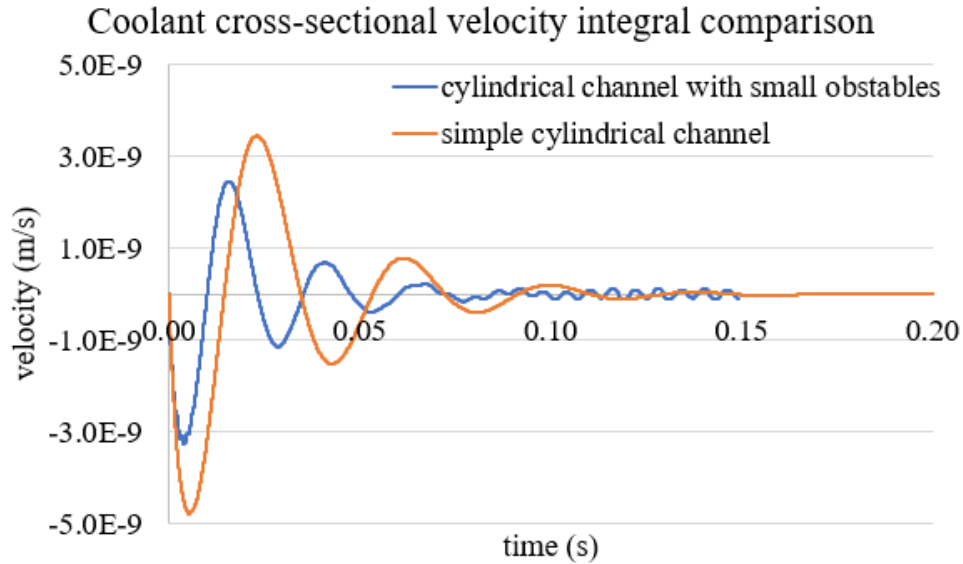
(b)  $x - O - y$  plane of debris channel with small obstacles ( $t = 1.307E - 1s$ ).



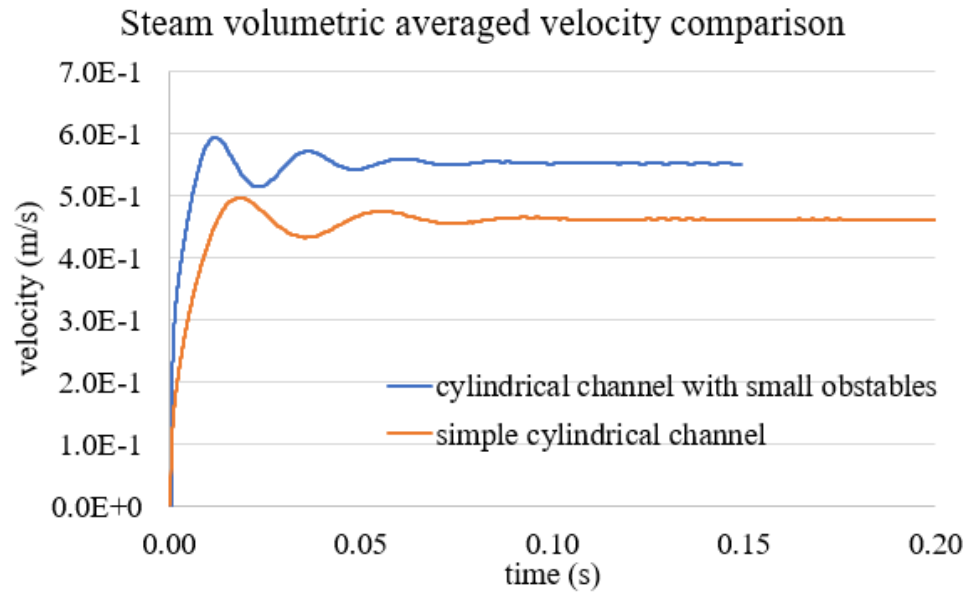
(c) Cylindrical debris bed channel ( $t = 1.307E - 1s$ ).

The eventual overall coolant flow field has very low velocity and the net effect is a zero velocity (Figure 5.29). With such quasi-steady state achieved, the time averaged pressure gradient is computed to be  $5304.10 Pa/m$  from Figure 5.29, which is only 5.9% higher than the prediction pressure gradient model (Eq. (49) in Section 5.2.5, when  $\alpha = 30\%$ ,  $\frac{dp}{dx} = 5009.56 Pa/m$ ). Even with obstacles added into the channel, the pressure gradient to yield CCFL can still be estimated by the proposed model with an acceptable uncertainty.

The time averaged pressure gradient at quasi-steady state is also 1.31% higher than the pressure gradient to yield CCFL in the simple cylindrical channel ( $5235.76 Pa/m$ ). It indicates that with the existence of obstacles the re-circulation affects the force balance in the coolant film, which ultimately changes the critical condition to achieve CCFL. As mentioned previously, the condition for CCFL to occur is the balance among wall shear, interfacial shear, and gravity in the liquid film region. Comparing the debris bed channels with and without obstacles, the gravity force does not change as the liquid densities are identical. However, the interfacial shear of small obstacles channel increases because the averaged coolant velocity is still zero (Figure 5.31 (a)) while the averaged steam velocity is 19.7% higher (Figure 5.31 (b)). Therefore, the overall wall shear reduces to compensate for the increased interfacial shear in order to achieve balance at CCFL. This conclusion is supported by the velocity vector distributions in Figure 5.30. When there are no obstacles, all liquid regions in the vicinity of the wall travels downwards (Figure 5.30 (c)). However, with the existence of the obstacles, the re-circulation near the wall yields a different distribution of liquid movement. A significant portion of liquid moves upward rather than downward, especially the coolant near the obstacle surfaces (Figure 5.30 (a) and (b)), which yields a much lower wall shear.



(a) Coolant velocity.



(b) Steam velocity.

Figure 5.31. Velocity comparison between two debris bed channels.

From a physical perspective, the existence of obstacles is actually more beneficial in preventing core melt-through in real debris bed condition. On one hand, although the steam velocity has increased by 19.7%, the pressure gradient to yield CCFL is 1.31% higher (rather than significantly lower), which indicates that achieving an overall zero velocity coolant is much more difficult with the existence of obstacles. On the other hand, the re-circulation near the debris

channel wall helps the heat exchange and cools down the high temperature walls. The existence of the obstacle also forms secondary flow around channel wall without obstacle. The flow spanwise continues even after CCFL is achieved (zero streamwise velocity) and can still remove heat, further reducing the risk of heat deterioration.

From a numerical perspective, the existence of obstacles influences PID control performance too. The drawback is a more obvious fluctuation in the quasi-steady state (Figure 5.31) since the liquid flow is not laminar anymore, which also indicates more challenges for CCFL simulations in even more complex geometries. The benefit comes from re-circulation however, is that the velocity distribution in the liquid region tends to generate a lower magnitude of the net liquid velocity. This results in the PID control to achieve CCFL requiring less time in the debris bed channel with small obstacles.

### **5.3.1.2 Void fraction $\alpha = 20\%$**

The annular flow initialization is depicted in Figure 5.32 with  $\alpha = 20\%$ . In Section 5.2.5, the flow regime of  $\alpha = 20\%$  in simple cylindrical channel transitions from an annular flow to a single-bubble flow due to low void fraction, which is illustrated in Appendix E.2. Similarly, the flow regime in the channel with small obstacles also transitions from an annular flow to a single-bubble flow, with the interface evolution shown in Appendix F.2. From Figure 5.33, the formed steam bubble is moving upward, with some inner circulations. Meanwhile, the coolant in the bulk region moves downward and forms a wake in the rear side of the bubble. Even though there are still local circulations around the corners of each small obstacle, the deformability factor of the formed single bubble is 0.94 which is very close to the deformability factor of the steam bubble in the cylindrical channel (0.97). This proves that under the same void fraction and hydraulic diameter, the flow

regime is not affected even with the existence of small obstacles or the resultant re-circulations near the channel wall.

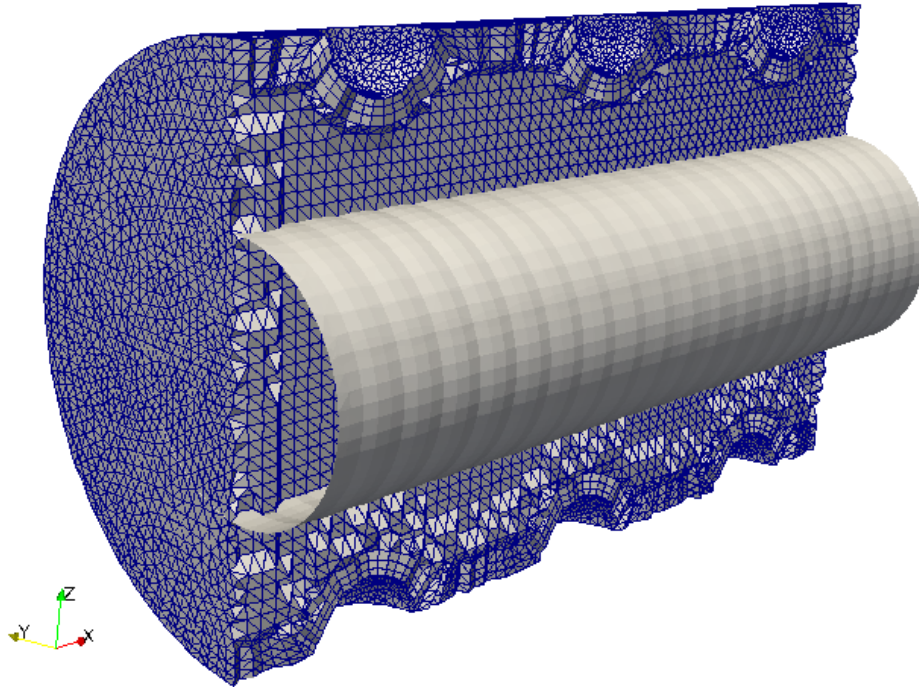


Figure 5.32. Two phase debris bed channel with small obstacles and  $\alpha = 20\%$ .

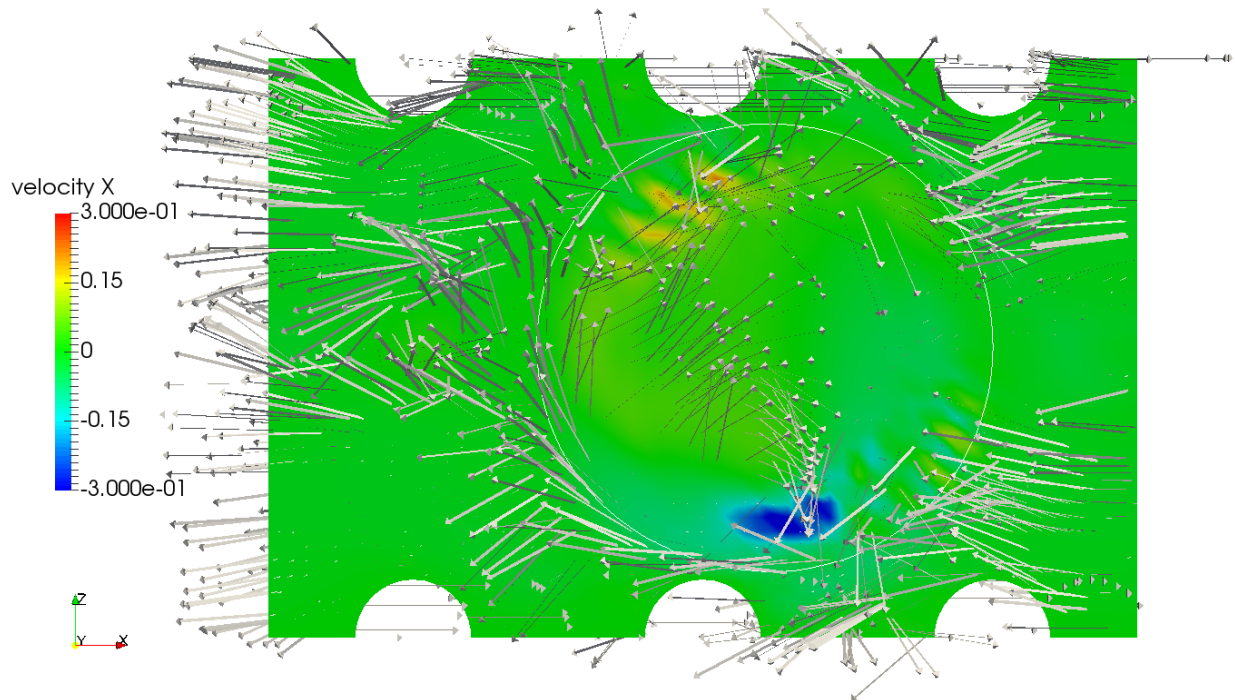
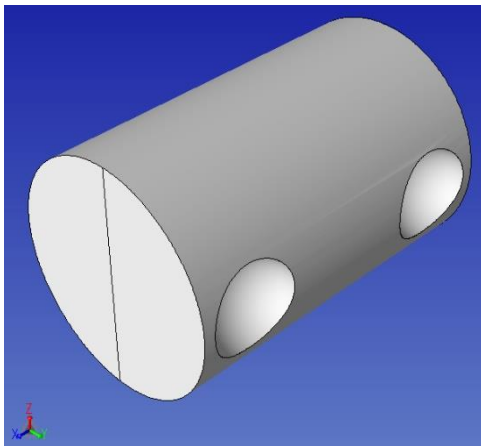


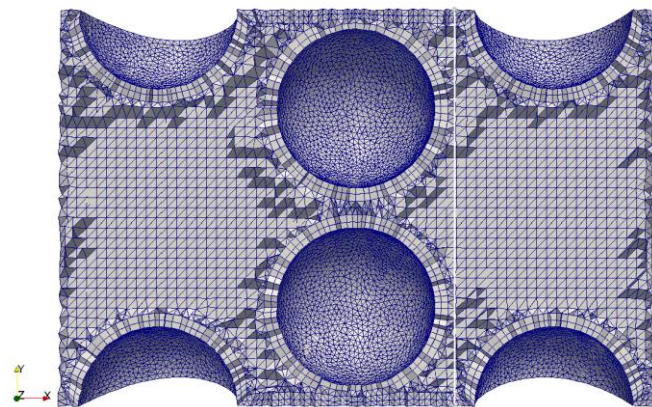
Figure 5.33. Velocity field distribution at  $t = 9.436E - 3s$  (gravity direction:  $-x$ ).

### 5.3.2 Debris bed channel with large obstacles

The cylindrical channel with large obstacles is designed by adding 4 hemispherical obstacles on the wall and 2 in the center of the channel. The obstacles are aligned along the  $x - O - y$  plane as shown in Figure 5.34 (a) and their diameters are all 40% of the cylindrical channel diameter. The diameter of the cylinder in Figure 5.34 (a) is scaled to  $1.4576 \text{ mm}$  which yields a  $D_h = 1 \text{ mm}$ . Therefore, the base mesh resolution, xyzts probe coordinates, and the steam column radius are all scaled with a factor of 1.4576 accordingly, to be comparable with studies in Section 5.2. Figure 5.34 (b) shows the mesh configuration also with 40 elements across the channel diameter and the location of xyzts probe plane. There are 894,709 mesh elements in total, among which the boundary layer elements along the cylindrical wall are also tetrahedralized for xyzts probes to collect velocity integral information. The elements around the surface of the obstacles are still prism boundary layer mesh, which can potentially be used for local interface contact angle control. In the presented studies, the contact angle control algorithm is not activated, therefore the contact angle between the interface and the obstacle walls is mainly dependent on the surface tension.



(a) The geometry of debris bed channel with large obstacles.



(b) Mesh configuration with white line indicating the location of xyzts probes across the  $y - O - z$  plane.

Figure 5.34. Debris bed channel with large obstacles.

Due to the complicated shape of this debris bed geometry, a single-phase simulation (0 steam volume fraction) is first carried out to show the flow distribution around the obstacles and to verify the predictive capability of the pressure gradient model proposed in Section 5.2.5. This verification is done at  $\alpha = 0$ . Afterwards, the two-phase simulation will be conducted to demonstrate the robustness of the PID controller and to investigate the two-phase dynamics when CCFL is achieved in this complicated debris channel.

### 5.3.2.1 Upflow phenomenon of zero steam volume fraction

A single phase simulation with  $\frac{dp}{dx} = 1.01\rho_l g = 9228.7 \text{ Pa/m}$  is conducted using the coolant as the working fluid and the material properties duplicated from Table 5.4. Since the pressure gradient is slightly higher than the coolant density, an upward flow is formed. The cross-sectional averaged velocity at the xyzts probe plane is plotted in Figure 5.35 with steady state achieved after the 4000<sup>th</sup> time step or  $t = 1.69\text{s}$ .

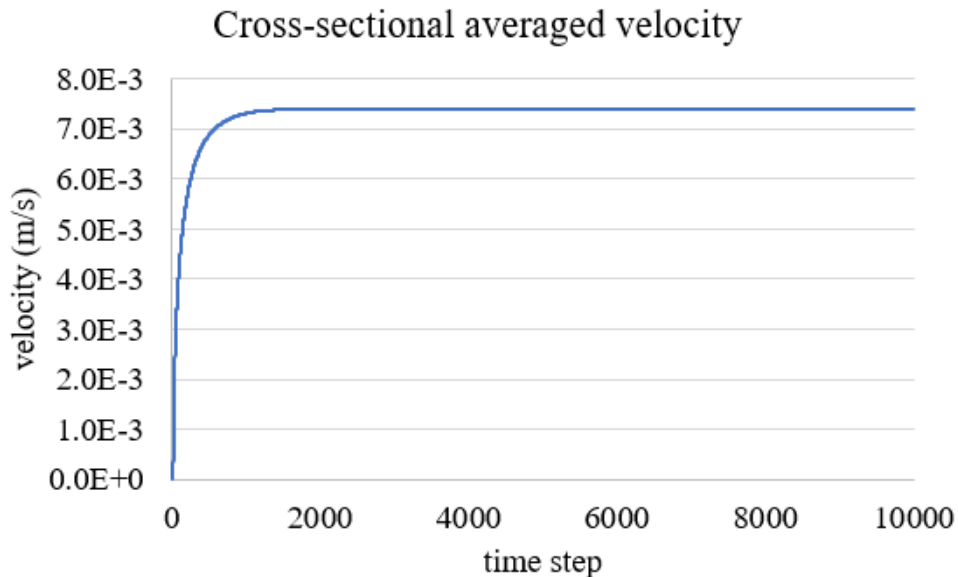
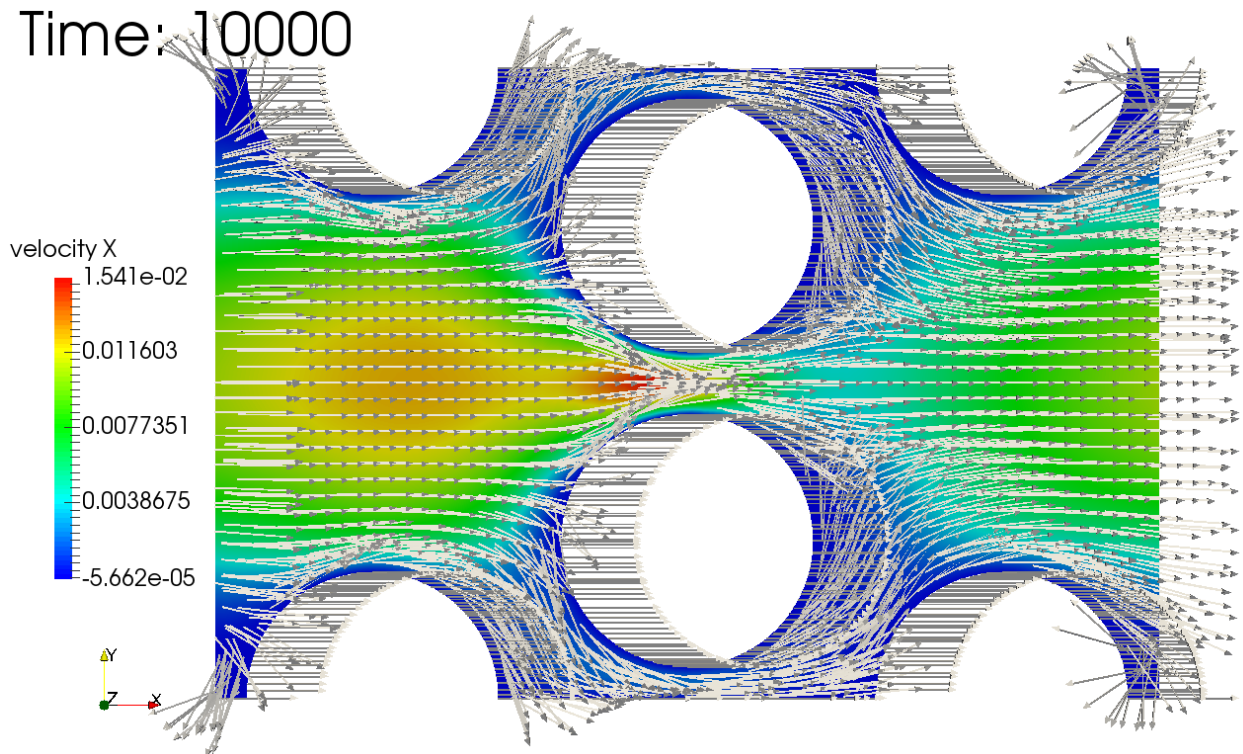


Figure 5.35. Velocity change in single-phase simulation under  $\frac{dp}{dx} = 1.01\rho_l g$ . The corresponding computation time at 10000<sup>th</sup> time step is  $t = 4.057\text{s}$ .

The velocity distribution after the flow is stabilized is shown in Figure 5.36 across 3 planes. On the  $x - O - y$  plane, two wakes are formed on the upper side ( $+x$  side) of the two middle obstacles. It is clear that re-circulation forms around the corners between the obstacle wall and the channel wall. In contrast, on the  $x - O - z$  plane where there are no obstacles, the flow is entirely upward without re-circulation. The maximum flow velocity is near the two middle obstacles, while the flow is relatively slow in the vicinity of the obstacle surfaces, especially on the lower side ( $-x$  side).

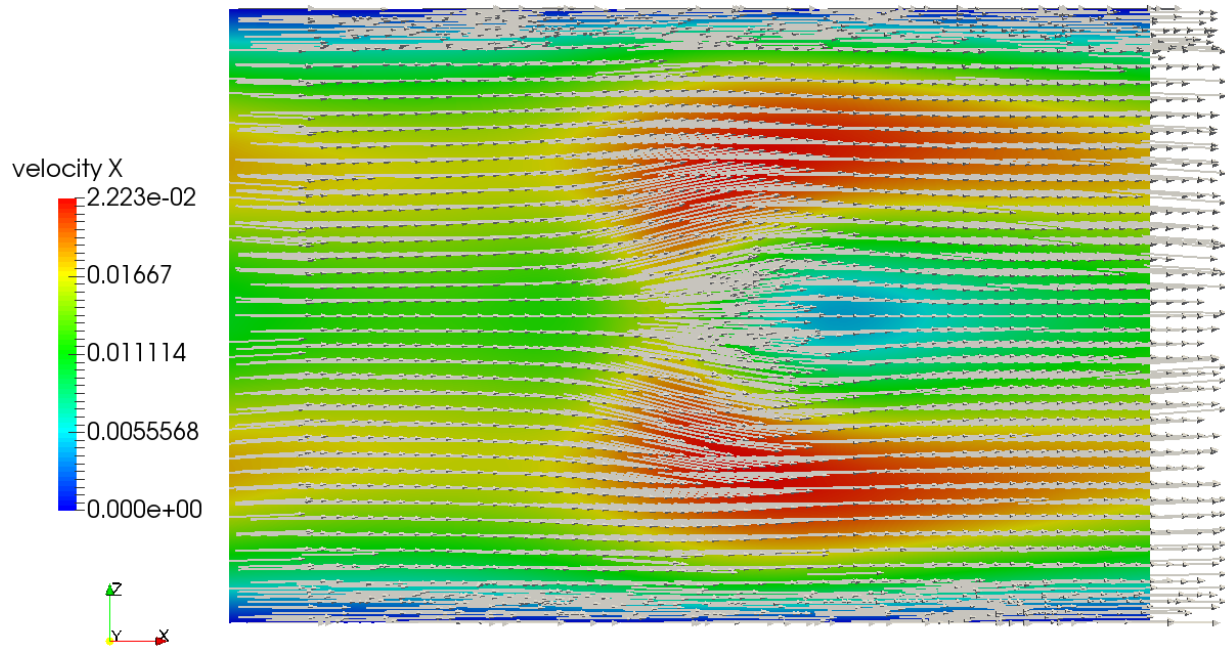
Figure 5.36. Single-phase flow in the debris bed channel with large obstacles.



(a)  $x - O - y$  plane.

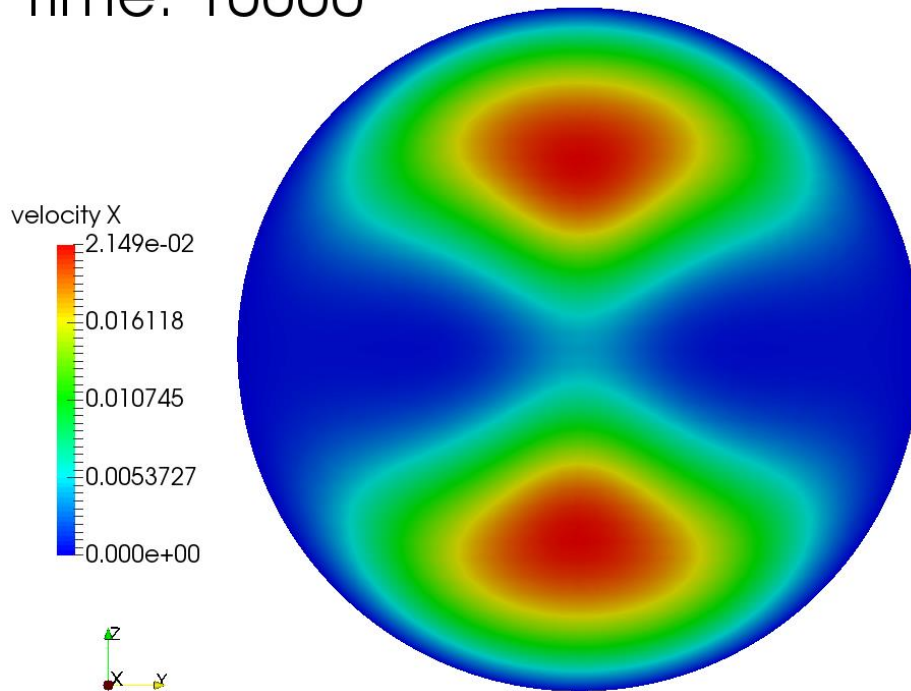
Figure 5.36. (continued)

Time: 10000



(b)  $x - 0 - z$  plane.

Time: 10000



(c) The  $y - z$  plane where xyzts probes locate at ( $x = 0.3625mm$ ).

The time-averaged steady state coolant velocity is  $7.4E - 3 \text{ m/s}$  (Figure 5.35), which corresponds to a Reynolds number of  $Re = 33.66$ . With the coolant and steam properties from Table 5.4, this Reynolds number also corresponds to a single-phase steam flow with a velocity of  $2.69 \text{ m/s}$ , which is much higher than the typical steam velocity at CCFL (Figure 5.21 (c)). Therefore, the flow distribution in Figure 5.36 also represents a post-CCFL scenario where the domain is filled with pure steam moving upwards. If heat transfer is considered, the middle obstacles tend to be cooled down with the fastest flow around them (Figure 5.36 (b)). The obstacles on the upper side (+ $x$  side) can also be cooled down since the flow in the vicinity is also moving fast (Figure 5.36 (b), (c)). However, the obstacles on the lower side ( $-x$  side) may face an overheated risk due to the low flow speed of the surrounding fluid (Figure 5.36 (a), (b)).

### 5.3.2.2 CCFL at zero steam volume fraction

According to the proposed pressure gradient model in Section 5.2.5, when  $\alpha = 0$  there is pure liquid in the debris bed channel, therefore the pressure gradient only needs to balance with gravity to achieve CCFL. This section will verify this prediction by continuing the single phase simulation from the above Section 5.3.2.1, while only changing the pressure gradient to be equal to the gravity force ( $\frac{dp}{dx} = \rho_l g = 9137.3 \text{ Pa/m}$ ). The cross-sectional averaged velocity collected by the xyzts probe plane is plotted in Figure 5.37 with a steady state achieved after 10,349<sup>th</sup> time step or  $t = 10.88\text{s}$ . From the zoomed-in plot in Figure 5.37 (b), the maximum velocity magnitude at the steady state is less than  $1E - 9 \text{ m/s}$  which indicates that the predicted pressure gradient from the proposed model in Section 5.2.5 is still effective even for very complex debris bed channels.

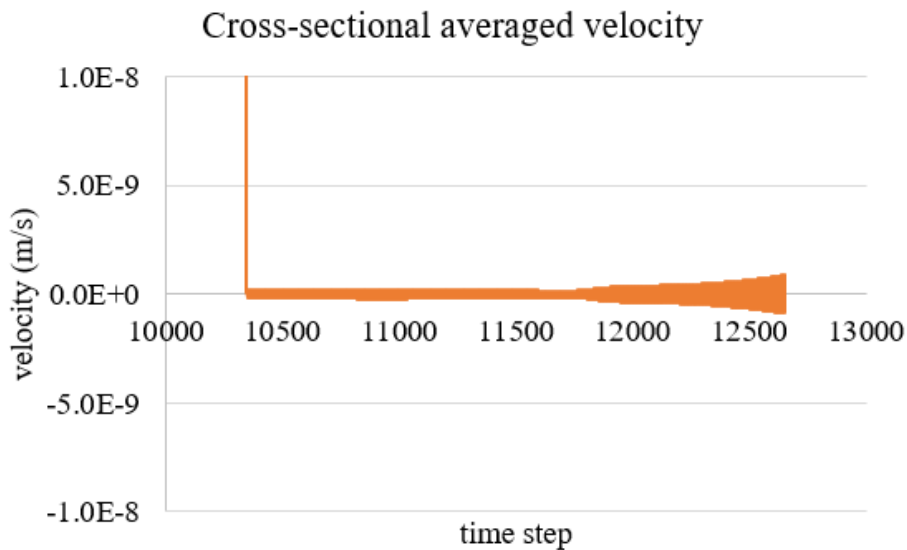
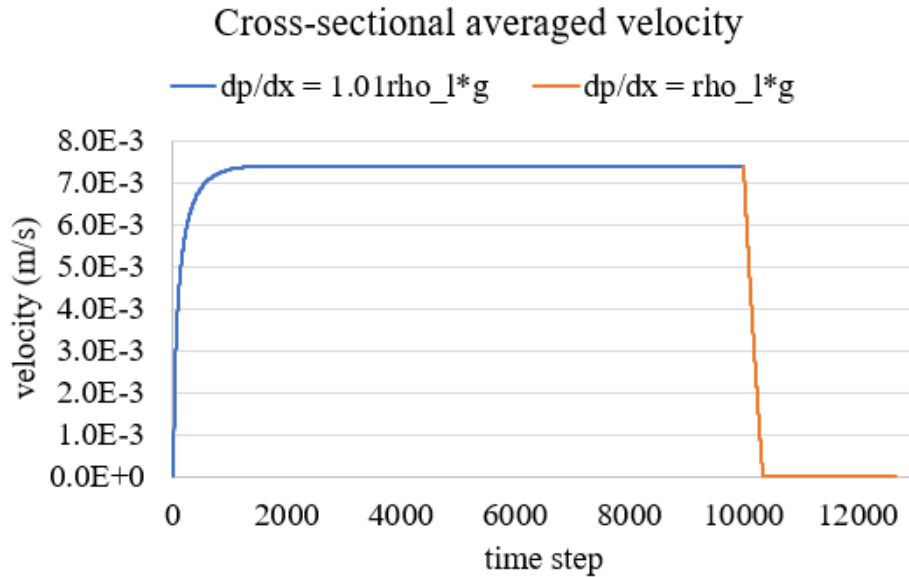
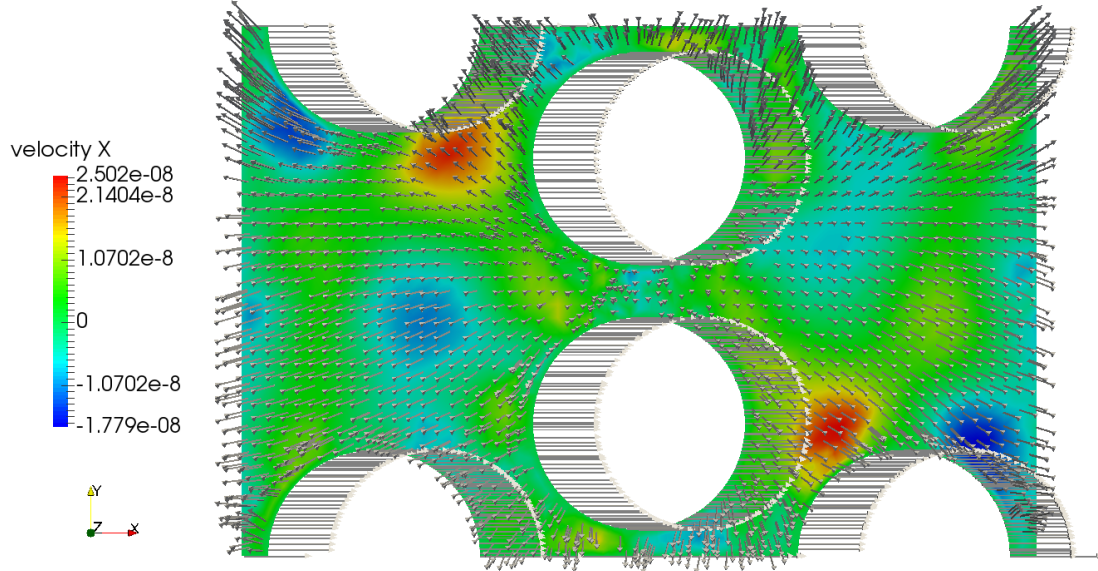


Figure 5.37. Velocity change with pressure gradient. A steady state is achieved with  $\frac{dp}{dx} = \rho_l g$  after 10349<sup>th</sup> time step or  $t = 10.88s$ .

The velocity distribution at steady state is plotted in Figure 5.38 where the liquid nearly does not move in the streamwise direction anymore, with a maximum  $x$  velocity of only  $1.281E - 7$   $m/s$ . The velocity vector field indicates dominant secondary flows where the coolant flows spanwise and around the obstacles, and the velocity distributions across the  $x - O - y$  and  $x - O - z$  planes are almost rotationally symmetric. If heat transfer is considered, although the net

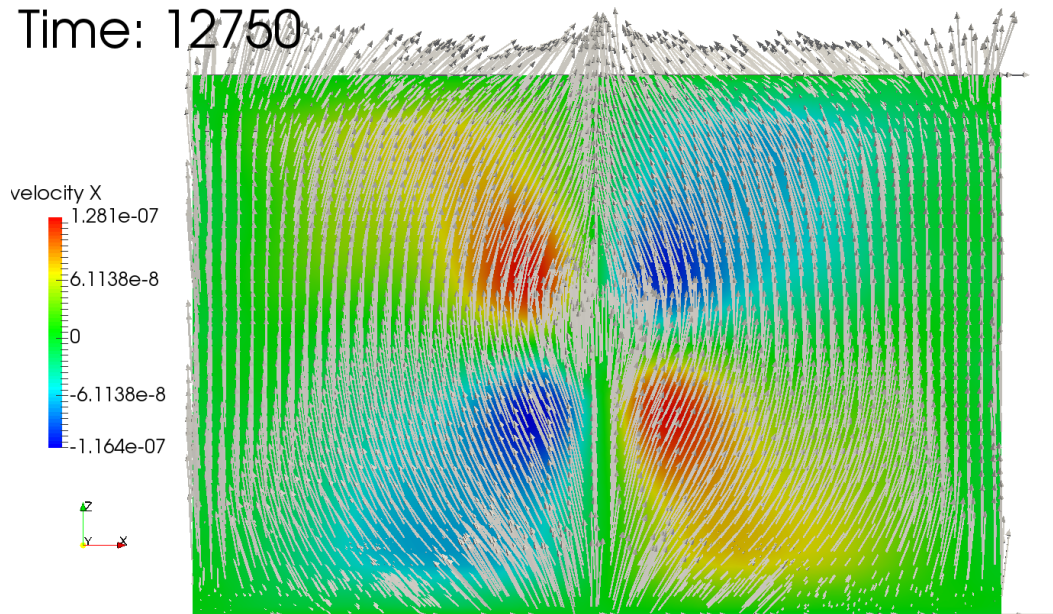
effect of the coolant flow is stagnant, the debris bed should be cooled evenly by the lateral and spanwise secondary flows. The chance of local high temperature is small therefore the risk of melt through is negligible under current condition.

Time: 12750



(a)  $x - O - y$  plane.

Time: 12750



(b)  $x - O - z$  plane.

Figure 5.38. Net zero liquid velocity in debris bed channel with large obstacles.

### 5.3.2.3 CCFL of steam volume fraction of 30%

The proposed pressure gradient model in Section 5.2.5 was verified by simulations of  $\alpha = 20\%$  in the cylindrical debris bed channel,  $\alpha = 30\%$  in the small obstacle debris bed channel, and  $\alpha = 0$  in the large obstacle debris bed channel. An additional large obstacle debris bed study is carried out under  $\alpha = 30\%$  to demonstrate the different flow dynamics in such complicated channel, and the robustness of the PID pressure gradient controller.

Figure 5.39 shows the initial condition of the two-phase distribution in the channel, with the interface across the middle two obstacles. The interface evolution during the simulation until achieving a quasi-state is depicted in Appendix G, and the last time step is also shown in Figure 5.40. Although the 30% steam volume fractions was also used in the simple cylindrical and the small obstacle debris bed channels, the flow regime with large obstacles is very different. The annular flow cannot be maintained and a steam bubble is formed around the middle obstacles and then deform into a thick steam film until reaching a quasi-steady state.

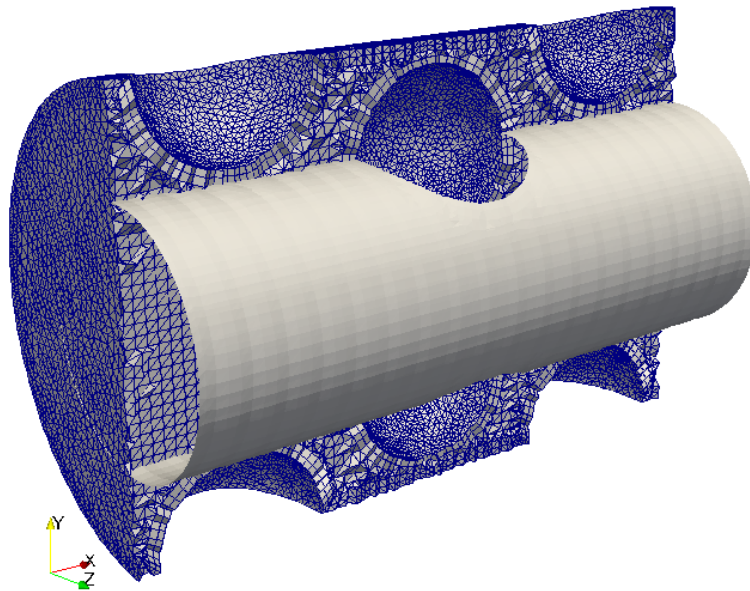


Figure 5.39. Interface initialization in the channel with a steam volume fraction of 30%.

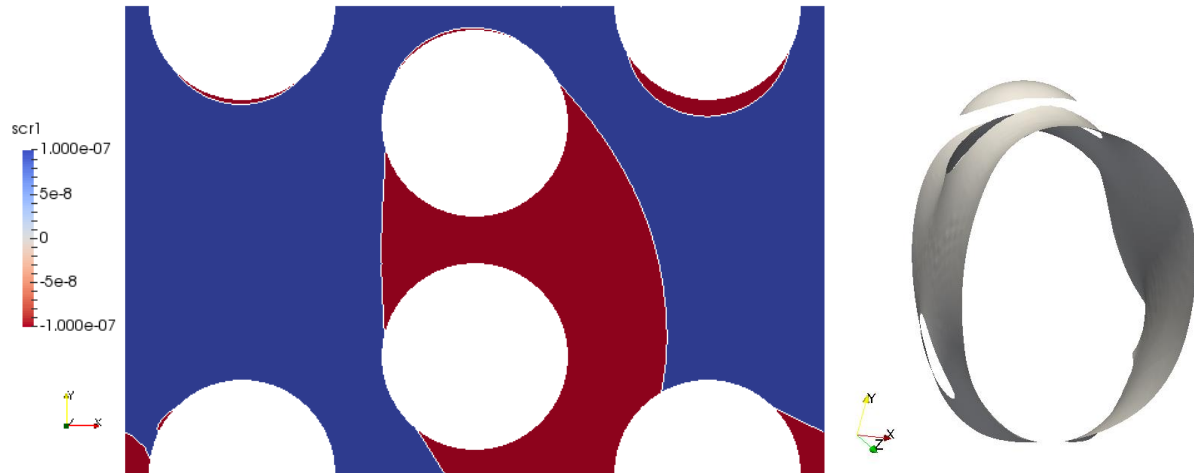


Figure 5.40. The phase distribution (red: steam; blue: coolant) and the 3D interface of formed steam film around the middle two obstacles.

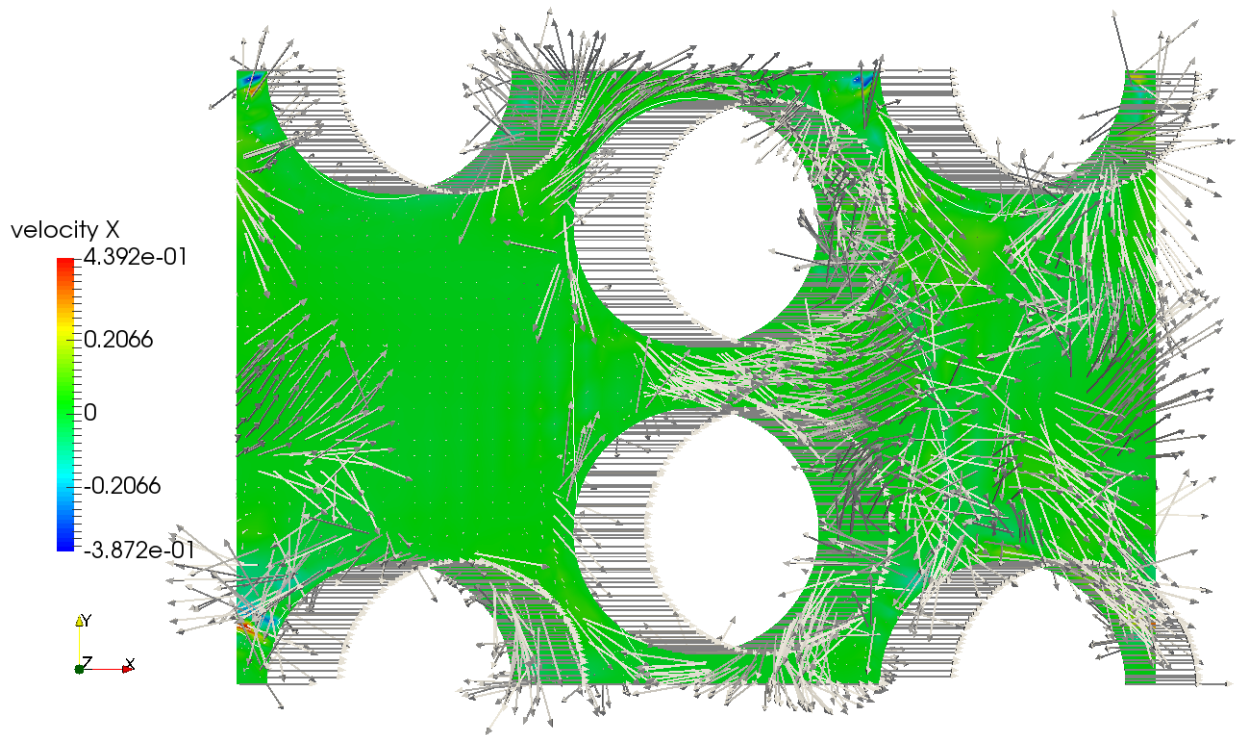
The bubble formation process is understandable due to the scale of the problem and the low phase velocities. First, the cylindrical channel is only  $1.4576 \text{ mm}$  in diameter, and with the existence of the large obstacles, the flow path can be smaller than  $0.87 \text{ mm}$ . Secondly, unlike the annular flow in simple cylindrical and the small obstacle debris bed channels where volumetric averaged steam velocity is around  $0.5 \text{ m/s}$ , the steam velocity in this channel with large obstacles is quite low (Figure 5.41). The velocity scale in Figure 5.41 is actually similar to Appendix E.2. and Appendix F.2 in cylindrical and small obstacle debris bed channels respectively, where annular flow transits to a single bubble under  $\alpha = 20\%$ . Under such low velocity, gas phase tends to form a bubble to minimize the surface area, in order to minimize the potential energy. Therefore, when obstacles disturb the steam flow, the surface tension pulls the interface to form a bubble shape.

Besides this thick film, thin films are also observed on the top of the middle obstacle, and around the obstacles along the channel walls (Figure 5.40). The velocity distribution under CCFL is also depicted in Figure 5.41. Similar to the single-phase simulation in Section 5.3.2.1, the obstacles on the lower side ( $-x$  side) also has the lowest flow speed in the coolant region. In contrast to the single-phase simulations, the entire flow field is moving extremely slowly except

in the re-circulation regions around the obstacles. This is because the obstacles significantly impede flow and the thick steam film blocks the coolant flow path. If heat transfer is considered, for the debris bed channel with large obstacles, the slowly moving steam film and almost stagnant coolant are very likely to cause heat transfer deterioration, especially for the middle two obstacles which are surrounded by the thick steam film.

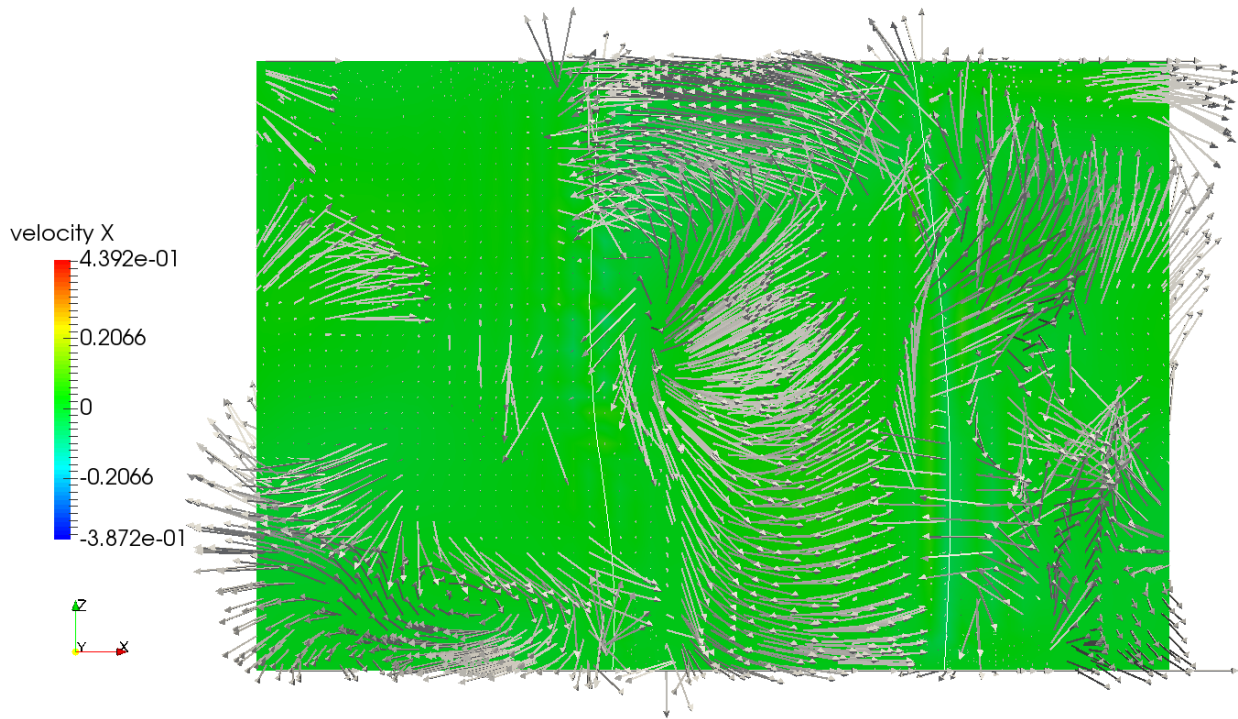
It is worth mentioning that since the contact angle algorithm is not available for this simulation, the interface distribution along the solid wall may not reflect the true physics. However, as long as the flow region is not in the vicinity of the contact line, the two-phase dynamics such as velocity and phase distributions are still reliable. Therefore, this simulation can still inform us on the riskier regions where heat transfer deterioration can occur in the debris bed channel.

Figure 5.41. Velocity distribution under CCFL in the debris bed channel when large obstacles exist.



(a)  $x - O - y$  plane

Figure 5.41. (continued)



(b)  $x - O - z$  plane.

Even in such complicated geometry, the PID controller is still capable at controlling the flow rate. Figure 5.42 shows the velocity and pressure gradient change with time under PID control. Due to the complicated geometry and complex two-phase flow dynamics, the control curves are not as smooth as the ones obtained in the simulation with simpler geometries. The eventual velocity integral is averaged to be  $9.73E - 10 \text{ m}^3/\text{s}$  which is adequate to refer the flow phenomenon as CCFL. The eventual averaged pressure gradient is  $9582.96 \text{ Pa/m}$  which is almost two times higher than the predicted value from the pressure gradient model (Eq. (49) in Section 5.2.5, when  $\alpha = 30\%$ ,  $\frac{dp}{dx} = 5009.56 \text{ Pa/m}$ ). This high pressure gradient is likely caused by the wall friction. Unlike the velocity profile in the liquid film of the annular flow regime where wall shear points to the upper direction, the wall shear in such complicated channel actually impedes the coolant flow considerably. At such low velocity (correspondingly low Reynolds number), the friction factor is very high. Also, the wall surface area with the existence of large obstacles increases significantly.

Therefore, a very high pressure gradient is needed to yield a net zero streamwise coolant velocity. In order to incorporate this factor into the pressure gradient model, a porosity term can be added into the correlation. This term is elaborated in Section 5.4.4.

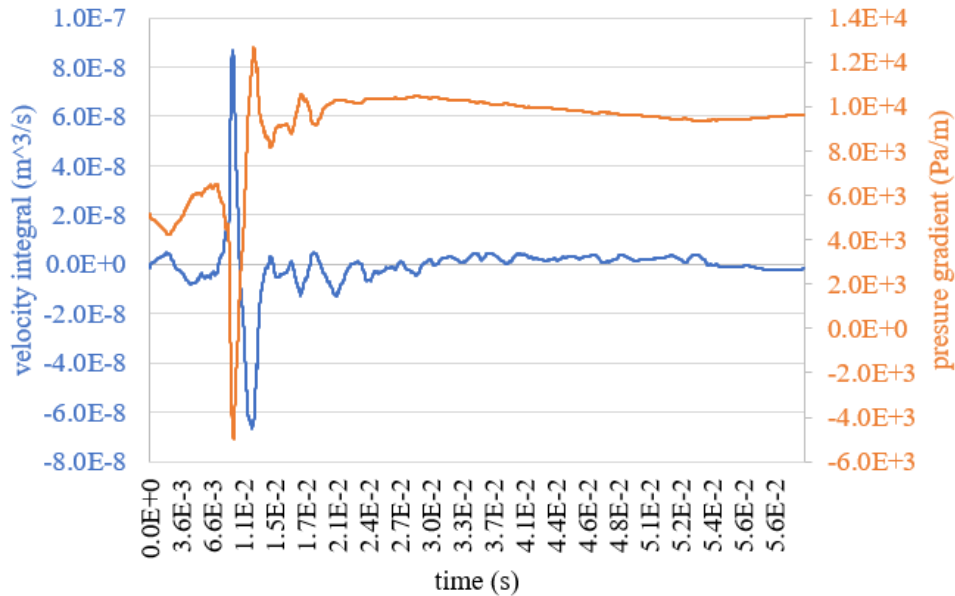


Figure 5.42. PID control on debris bed channel with large obstacles ( $\alpha = 30\%$ ).

### 5.3.3 Effect of PID control on fluid dynamics in complex debris bed channels

For the cylindrical debris bed channel, it is demonstrated in Section 3.3.2 that with and without PID, the two-phase fluid dynamics captured are almost identical at CCFL occurrence. In addition, the effect of more complex geometry on PID control on fluid dynamics is further investigated.

#### 5.3.3.1 Debris bed channel with small obstacles

The debris bed channel with small obstacles is first demonstrated using the same setup and steam volume fraction as Section 5.3.1.1. Since the pressure gradient averaged at the quasi-steady state from Figure 5.29 is  $5304.10 \text{ Pa/m}$ , this value is selected to drive the flow without PID control. The result is plotted in Figure 5.43 and velocity integral changes are compared with and without PID control. The quasi-steady state velocity integral is averaged to be  $4.71E - 12 \text{ m}^3/\text{s}$ , which indicates the CCFL occurrence. Similar to the cylindrical debris bed channel results (Figure

3.17), CCFL in the channel with small obstacles is achieved much earlier under PID control than when driven by the constant pressure gradient. When PID control is not activated, the two-phase flow takes a long time to develop until the force balance is achieved in the liquid film. Moreover, compared with cylindrical debris channel velocity results in Figure 3.17 (a), the maximum downflow velocity magnitude ratio when small obstacles exist ( $-6.78E - 9 : -3.25E - 9 \approx 2.1$ ) is much smaller than the cylindrical channel ( $-3.65E - 2 : -3.02E - 3 \approx 12.1$ ). The reduction on downflow velocity ratio should come from the re-circulations near the small obstacles (Figure 5.44), which prevents formation of laminar downflow in the debris bed channel. Numerically speaking, although re-circulations helps speed up the process to achieve CCFL, it also generates oscillation of the velocity integral even after a quasi-steady state is achieved.

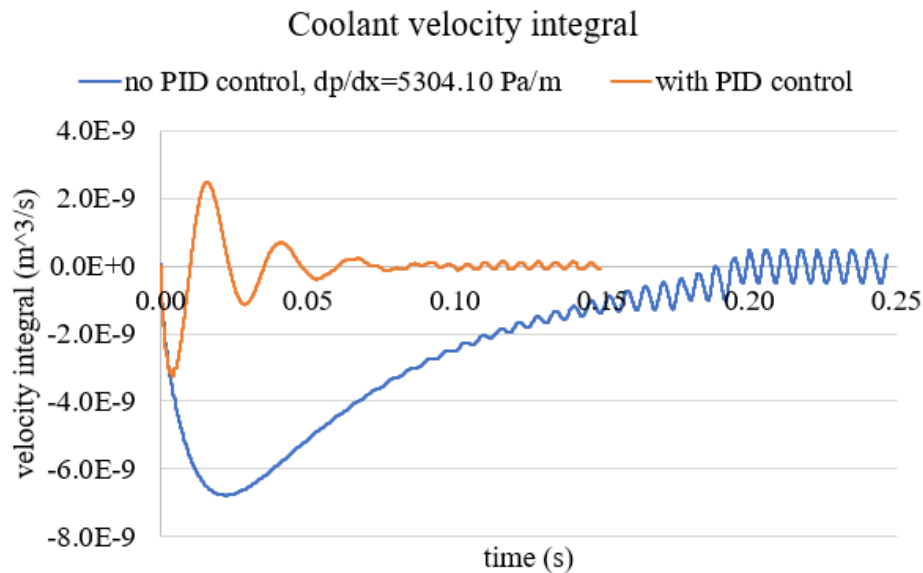
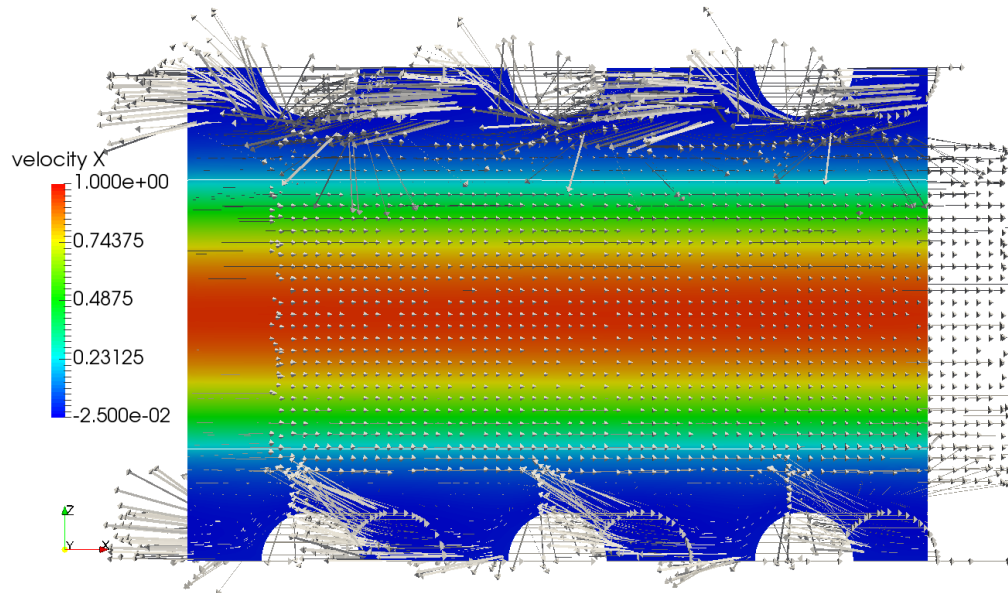


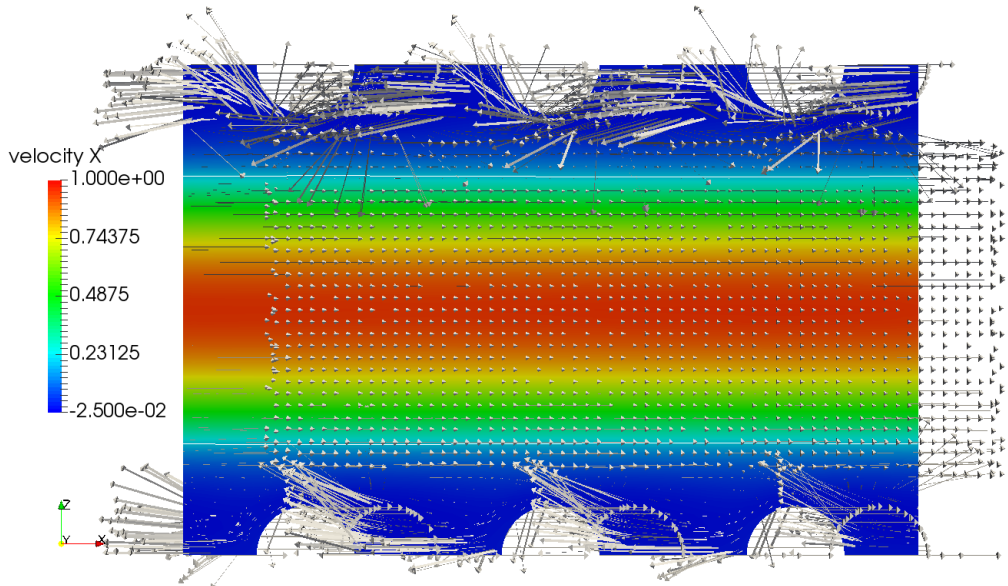
Figure 5.43. Comparison of coolant velocity integral changes where PID control is deactivated (flow driven by a constant pressure gradient) and activated (flow driven by PID controller) for debris bed channel with small obstacles.

The two-phase velocity distribution are still quite similar with or without PID control (Figure 5.44). From Figure 5.44 (a) and (b), the steam columns both show a laminar profile with or without PID control, and the velocity distributions are quite similar under the same color bar. Although

there are subtle differences of the velocity vector distribution in the coolant region, the recirculation behaviors are also quite similar. From this study, the PID controller is proved not to change the physics of the two-phase fluid dynamics even with small obstacles in the debris bed channel.



(a) With PID control ( $t = 1.307E - 1s$ ).



(b) Without PID control ( $t = 2.341E - 1s$ ).

Figure 5.44. Comparison of phase and velocity distributions at CCFL in small obstacle debris bed channel with or without PID control.  $-x$  indicates the gravity direction.

### 5.3.3.2 Debris bed channel with large obstacles

The debris bed channel with large obstacles is also demonstrated to prove that the PID controller does not change under two-phase fluid dynamics. The setup and steam volume fraction are the same as in Section 5.3.2.3, but with PID control deactivated. A constant pressure gradient is used to drive the flow,  $9582.96 \text{ Pa/m}$ , the eventual averaged pressure gradient from Figure 5.42. The result is plotted in Figure 5.45 compared with PID controlled velocity integral change. The quasi-steady state velocity integral driven by constant pressure gradient is  $1.70E - 9 \text{ m}^3/\text{s}$ , which is very close to the value obtained from PID control ( $9.73E - 10 \text{ m}^3/\text{s}$ ). Therefore, the PID control approach does not noticeably change the eventual coolant velocity at CCFL. However, due to the complexity of the obstacle distribution, this velocity integral deviates the most from zero compared with other simpler geometries. Such deviation is difficult to avoid considering the influence from the secondary flow produced by the obstacles. Another difference compared with cylindrical and small obstacle debris bed channel results is the time to achieve CCFL. Unlike plots in Figure 3.17 and Figure 5.43, in the channel with large obstacles CCFL driven by the constant pressure gradient is achieved at similar time as under PID control. The major reason is that for two-phase flow development among the large obstacles, no coolant film exists like the annular flow regime in cylindrical and small obstacle channels. Therefore, no time is needed for the velocity field in the film to develop until reaching a force balance. Also, the steam bubble blocking the flow path mitigates the coolant velocity change no matter with or without PID control, therefore the flows develop at similar paces.

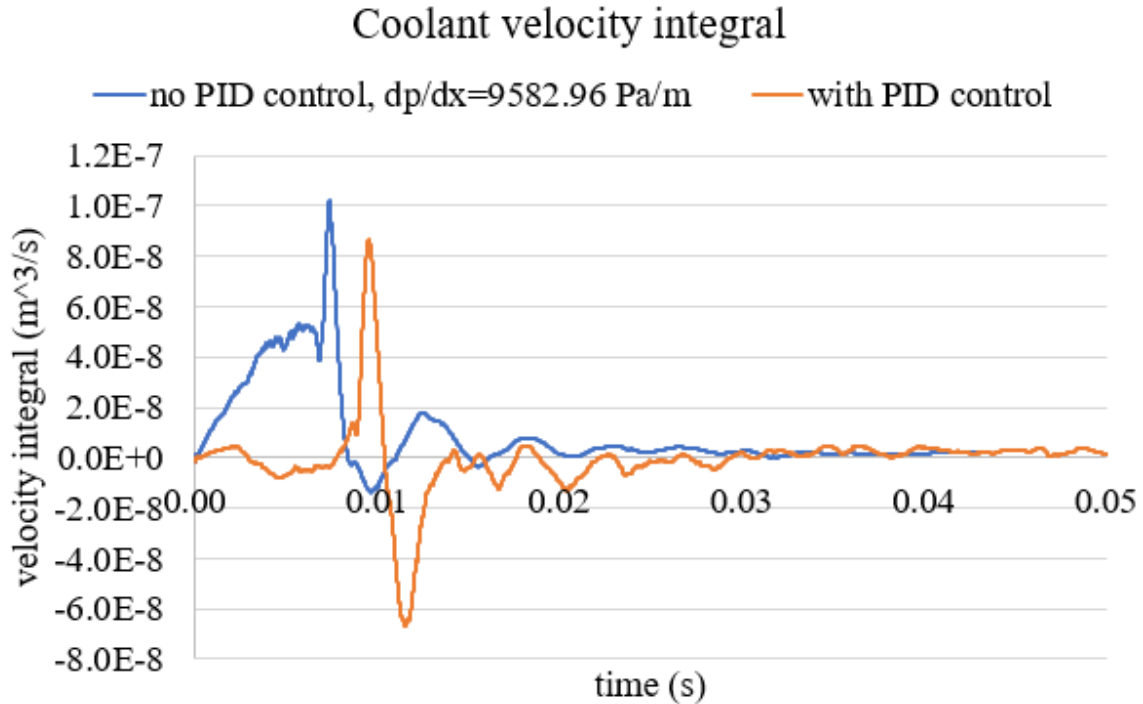
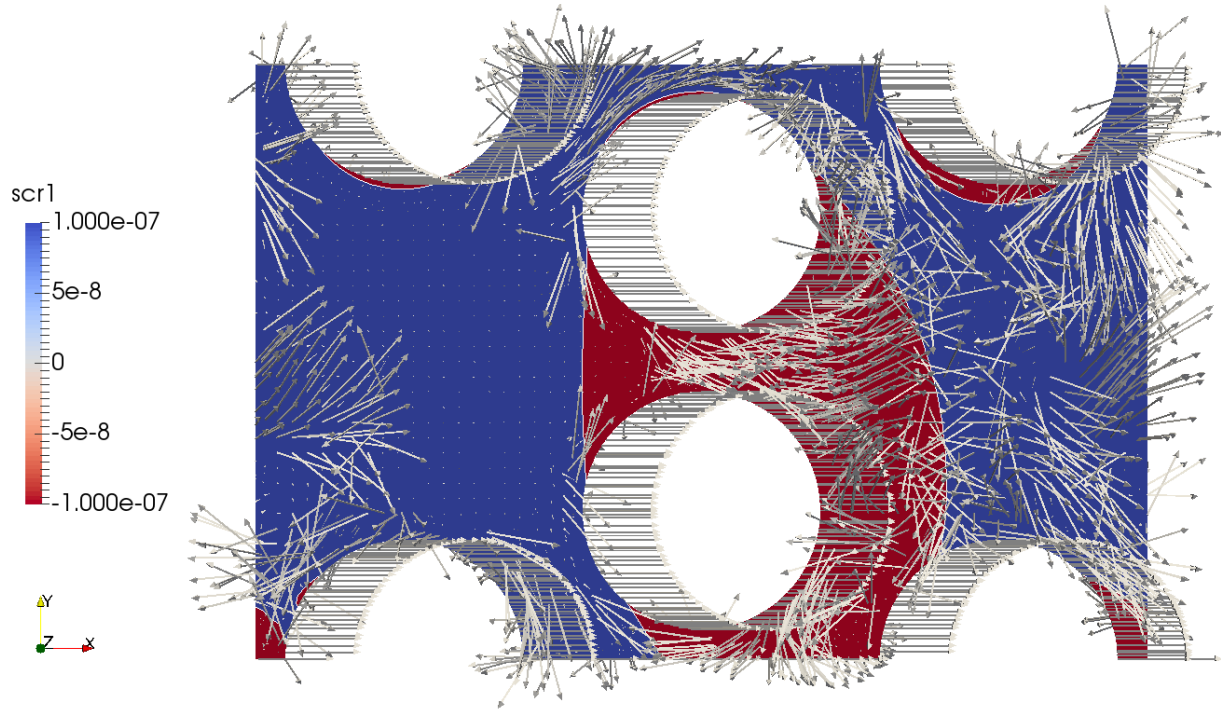
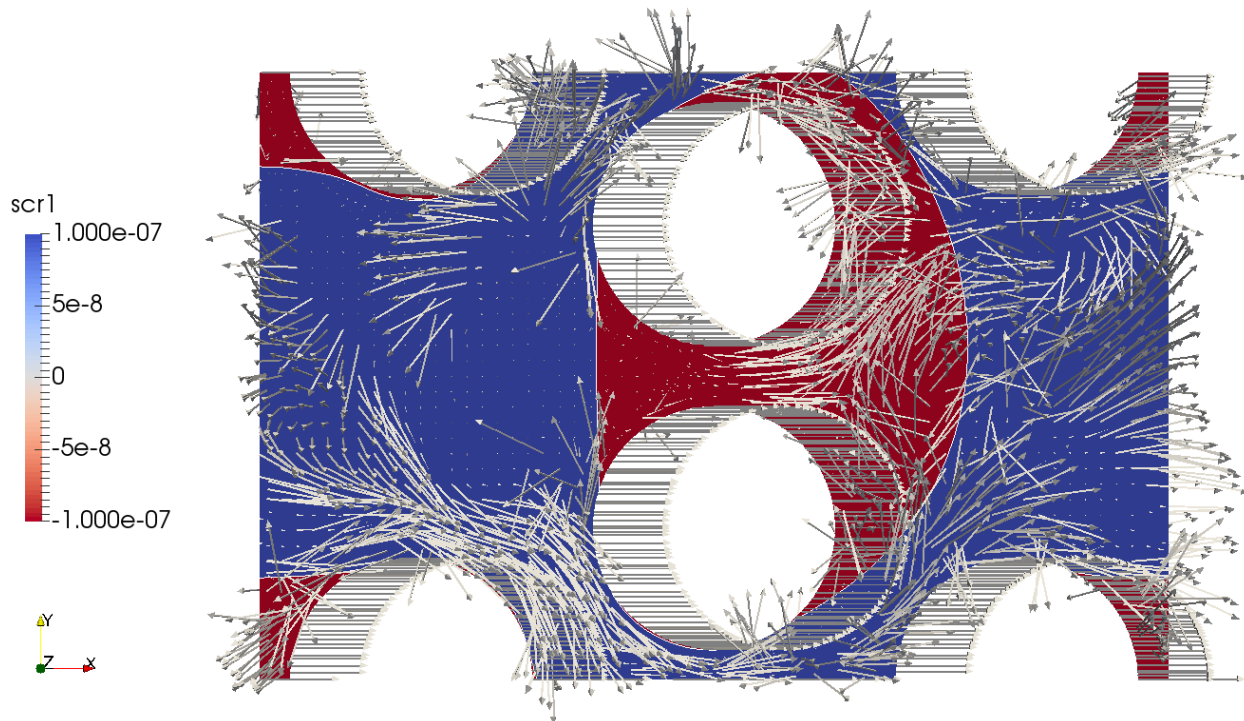


Figure 5.45. Comparison of coolant velocity integral changes where PID control is deactivated (flow driven by a constant pressure gradient) and activated (flow driven by PID controller) for debris bed channel with large obstacles.

The two-phase velocity distributions are depicted in Figure 5.46, which shows a strong similarity between the results obtained with and without PID control. The steam around the middle two obstacles both block the flow path, and steam films form on all the surrounding obstacles. Although the orientations of the middle bubble-shape steams in Figure 5.46 (a) and (b) are different, they are mirrored results and essentially represent the same flow distribution. Since the streamwise direction is  $+x$ , statistically, the wide portion of the steam can either show up in  $-y$  (Figure 5.46 (a)) or  $+y$  (Figure 5.46 (b)) side. From this study, the PID controller is proved to maintain the physics of the two-phase fluid dynamics even with large obstacles in the debris bed channel, and the related phase distribution can be properly captured with PID control approach even in such complicated geometries.



(a) With PID control  $t = 3.494E - 2$  s.



(b) Without PID control  $t = 4.35E - 2$  s.

Figure 5.46. Comparison of phase and velocity distributions at CCFL in large obstacle debris bed channel with or without PID control.  $-x$  indicates the gravity direction.

## 5.4 Application range and parametric studies

This section aims to shed more lights onto the debris bed CCFL physics, especially focusing on the application range of proposed models. The pressure gradient model (Eq. (49) in Section 5.2.5) implies that for annular flow in the debris bed channel, the pressure gradient at CCFL occurrence is solely dependent on the liquid density and the void fraction. However, it is necessary to demonstrate that other material parameters not included in the model have negligible effects on the annular debris bed CCFL condition. It is also important to incorporate the effect of geometry into the model for channels with large obstacles. In this section, effects of liquid density, steam density, surface tension, and channel porosity on CCFL are specifically studied. With a series of parametric studies, the predictive capability of the model will be confirmed, and the application range of the proposed correlation will be concluded. Besides the investigation of the pressure gradient model, the dimensionless  $SU$  number (Eq. (50) in Section 5.2.6) will be further investigated as well. In parametric studies  $SU$  number will be computed, and its application will be clarified in the end of this section.

### 5.4.1 Liquid density

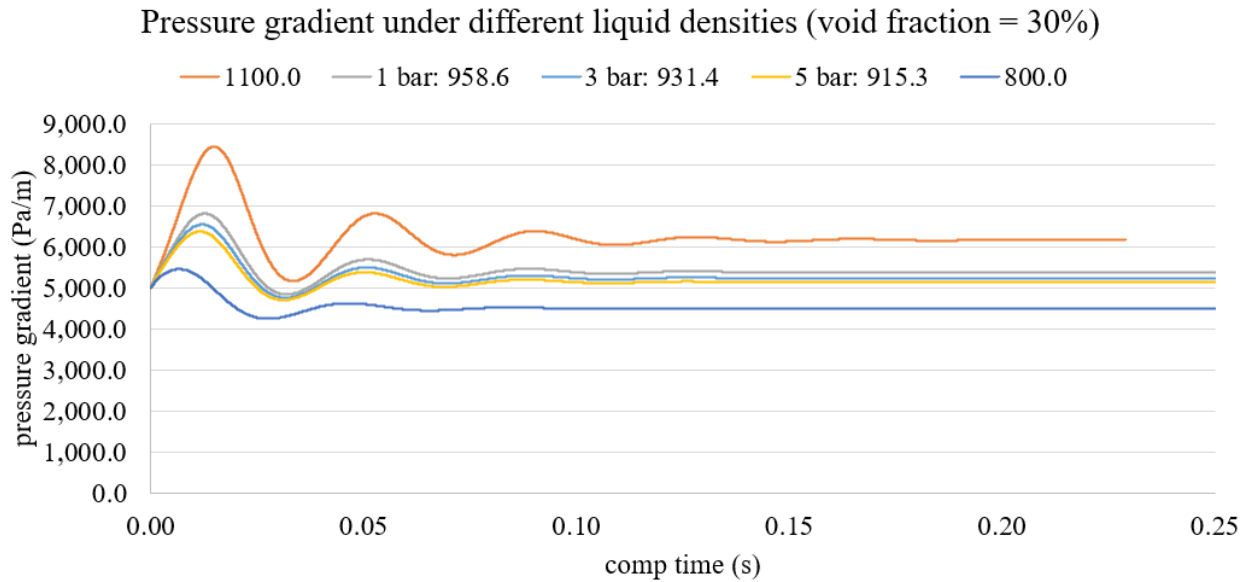
A series of liquid density values are used to conduct CCFL simulations at 30% steam volume fraction to demonstrate the predictive capability of the proposed pressure gradient model, Eq. (49). During the debris bed formation, the system pressure inside the reactor vessel is expected to be in the range of 1 to 5 bar, therefore the liquid densities at saturation conditions corresponding to 1, 3, and 5 bar system pressures are selected. Another two liquid density values outside of the 1-5 bar range are also added to expand the potential application range of the proposed correlation. The liquid density values are summarized in Table 5.12 and other relevant simulation parameters duplicated from Table 5.4. Note that in order to have only one variable change in the parametric

study, the steam density is kept at 3 bar when the liquid densities vary. Figure 5.47 depicts how the PID controller brings the two-phase annular flow with different liquid densities to CCFL, where the eventual liquid velocities all stabilize around zero. This demonstrates that the corresponding pressure gradient indeed depends on the liquid density.

Table 5.12. Liquid density values in the parametric study.

Condition	A heavy liquid	1 bar	3 bar	5 bar	> 5 bar
Density ( $kg/m^3$ )	1100.0	958.632	931.430	915.290	800.0

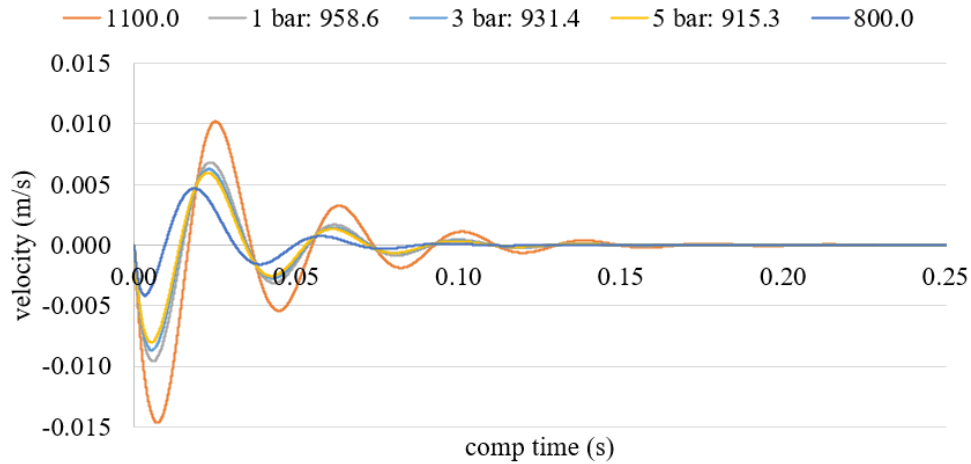
Figure 5.47. PID controlled CCFL in liquid density parametric study.



(a) Pressure gradient change with time under PID control.

Figure 5.47. (continued)

Liquid cross sectional averaged velocity under different  $\rho_l$   
(void fraction = 30%)



(b) Liquid velocity change with time under PID control.

Table 5.13 compares the predicted pressure gradients by the correlation Eq. (49) and the steady-state averaged pressure gradients from Figure 5.47. It is obvious that the predicted values match well with the simulation results with a relative difference around  $-4\%$ , which suggests the consistent accuracy of the proposed pressure gradient model for different density liquids. The physics behind is still the force balance when CCFL occurs specifically interaction among wall shear, interfacial shear, and gravity force inside the liquid film. According to the proposed definition that CCFL occurs only when the liquid averaged velocity is zero, the wall shear at the vicinity of the liquid is very small. There, the interfacial shear will be mainly determined by the gravity force, which is solely dependent on liquid density.

Table 5.13. Pressure gradient model predictive capability when liquid density changes.

Density ( $kg/m^3$ )	$\frac{dp}{dx}$ predicted by correlation	$\frac{dp}{dx}$ obtained from simulation	Relative difference
1100.0	5916.19	6164.62	-4.03%
958.632	5155.86	5383.67	-4.23%
931.430	5009.56	5235.76	-4.32%
915.290	4922.75	5142.67	-4.28%
800.0	4302.68	4502.32	-4.43%

The averaged liquid and steam velocities at steady state are computed and summarized in Table 5.14. The resulting conclusion is that when the liquid density decreases, the steam velocity decreases as well due to buoyancy effect. Since the five simulations all have void fractions equal to 30%, the steam volumes enclosed by the liquid are all the same, therefore the buoyancy force ( $\rho_l g V_{steam}$ ) only depends on the liquid density here. With an increase in system pressure, liquid density reduces (due to raising saturation temperature) and the buoyancy effect is lower, therefore steam travels slowly in the debris bed channel, which yields a smaller interfacial shear when liquid velocities are all approaching zero. Ultimately, this results in a smaller pressure gradient needed for CCFL to occur.

The pressure gradient for a single debris bed channel in the actual debris bed depends on the natural circulation and boiling intensity. The natural circulation effect is more dominant when there are multiple debris bed channels connected with each other and the channel sizes are different. Under the same channel size and excluding the natural circulation effect, if the boiling intensity is high, CCFL is expected as it tends to occur with high steam void fraction (also reflected by pressure gradient model Eq. (49)). On the other hand, high boiling intensity corresponds to

local high temperature, where nearby liquid density is correspondingly lower. According to the analysis above on buoyancy effect, lower liquid density makes CCFL even easier to happen. Occurrence of CCFL will in return deteriorate this process. Therefore, it is important to identify local high temperature spots in the debris bed due to both the intensive steam generation and buoyancy effect on CCFL, possibly through advanced debris bed full-core simulations.

Table 5.14. Liquid and steam velocities and the corresponding parameter with  $\frac{dp}{dx}$  unit.

Density ( $kg/m^3$ )	Liquid cross-sectional averaged velocity ( $m/s$ )	Steam volumetric averaged velocity ( $m/s$ )	$(\rho_l - \rho_g)u_g^2 / (\alpha D_{channel})$ ( $Pa/m$ )
1100.0	1.56E-06	5.44E-01	1.09E+06
958.632	3.54E-07	4.74E-01	7.17E+05
931.430	7.44E-07	4.61E-01	6.60E+05
915.290	6.09E-07	4.52E-01	6.24E+05
800.0	1.18E-07	3.95E-01	4.15E+05

Table 5.14 also has the column of  $(\rho_l - \rho_g)u_g^2 / (\alpha D_{channel})$  computed for dimensionless analysis of  $SU$  number. Figure 5.48 shows the performance of this dimensionless study by plotting  $\frac{dp}{dx}$  and  $(\rho_l - \rho_g)u_g^2 / (\alpha D_{channel})$  using data from Table 5.13 and Table 5.14. With the definition in Eq. (50),  $SU$  is the slope of the trendline, which is a constant value of 0.0024 for different liquid densities. For application, under any other conditions where liquid density changes, if the obtained  $SU$  is lower than 0.0024, the flow regime in the debris bed channel is still counter current flow with liquid draining down. If  $SU$  is higher than 0.0024, it indicates that CCFL has already occurred.

Compared with the dimensionless analysis in Section 5.2.6 where  $SU = 0.0056$  under varying void fractions, this dimensionless number changes under different condition. However, the dimensionless performance is still satisfactory. The fitted linear trendline with  $R^2$  is very close to 1 which indicates that for each data set between  $\frac{dp}{dx}$  and  $(\rho_l - \rho_g)u_g^2 / (\alpha D_{channel})$  the ratio is a constant value. The value change of  $SU$  is very similar to drag coefficient which changes with Reynolds number and the application of  $SU$  is further clarified in Section 5.4.5.

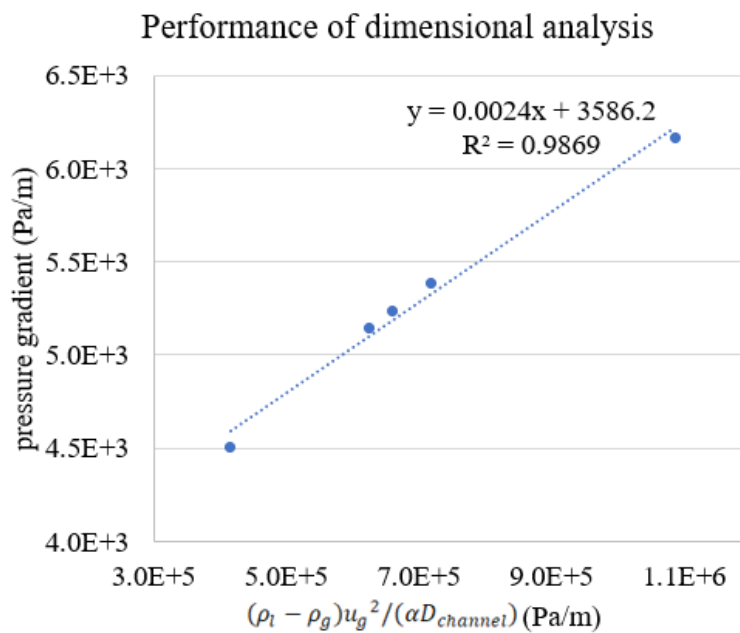


Figure 5.48. Performance of the dimensional analysis when liquid density varies.

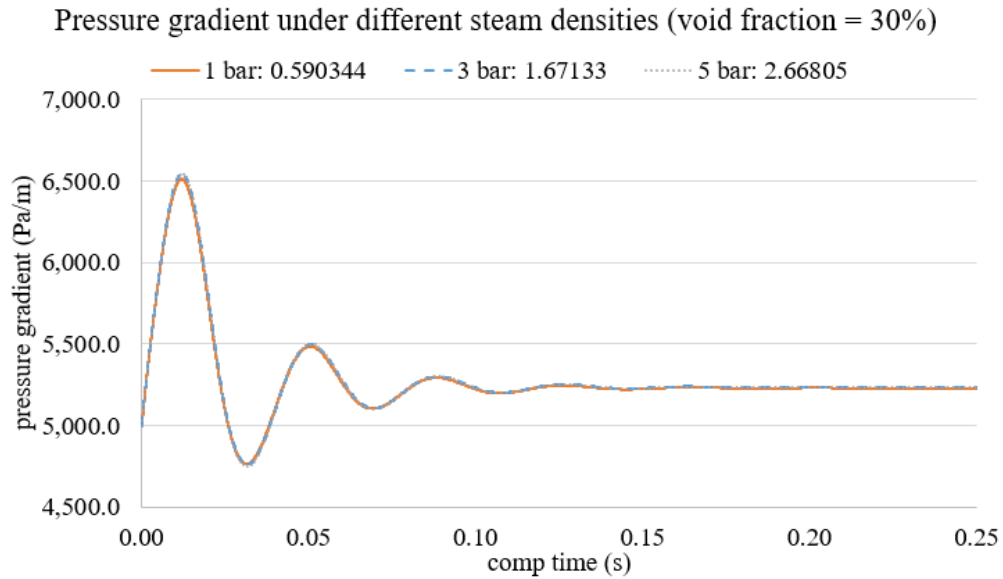
### 5.4.2 Steam density

Three steam densities at 1, 3, and 5 bar system pressures are used to conduct CCFL simulations at 30% steam volume fraction to demonstrate that the proposed pressure gradient model (Eq. (49)) is irrelevant to the steam density. The steam density values are summarized in Table 5.15 and other relevant simulation parameters are duplicated from Table 5.4. Note that in order to have only one variable change in the parametric study, the liquid density is kept at 3 bar when the steam densities

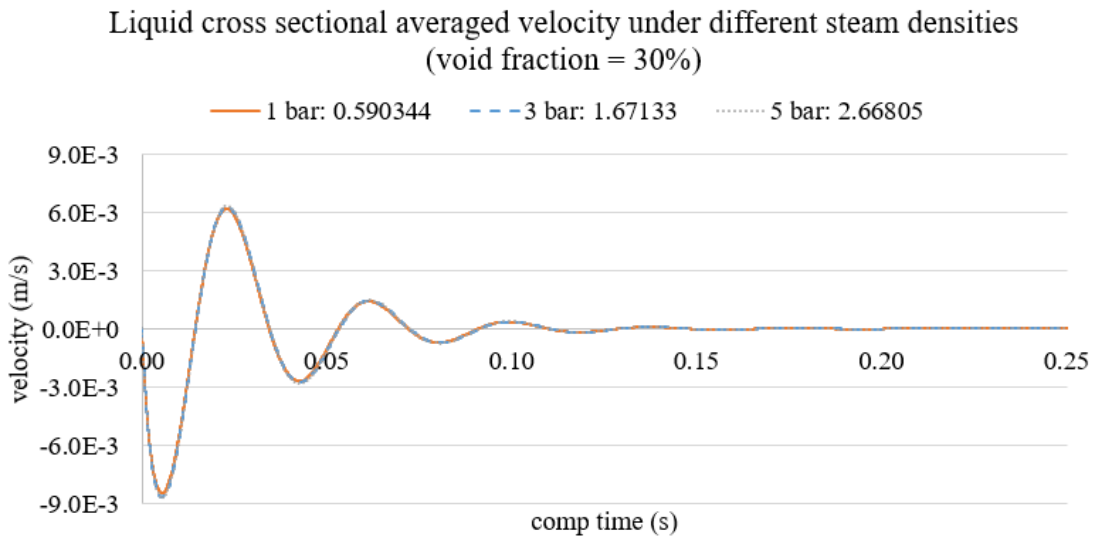
vary. Figure 5.49 depicts how the PID controller brings the two-phase annular flow with different steam densities to CCFL, where the eventual liquid velocities all stabilize around zero.

Table 5.15. Steam density values in the parametric study.

System pressure	1 bar	3 bar	5 bar
Density ( $kg/m^3$ )	0.590344	1.67133	2.66805



(a) Pressure gradient.



(b) Coolant velocity.

Figure 5.49. PID controlled CCFL in steam density parametric study

Table 5.16 lists the steady-state averaged pressure gradients and coolant velocities from Figure 5.49. The relative difference among the pressure gradients under different steam densities is less than 0.1% therefore it is quantitatively proved that the pressure gradient at CCFL indeed does not depend on the steam density, which suggests the consistent accuracy of the proposed pressure gradient model for different fluids.

The steam terminal velocities are listed in Table 5.16 and are quite close to each other. This is because the buoyancy force is equal to the weight of the replaced liquid ( $\rho_l g V_{steam}$ ) so steam density does not make a difference. When the steam volume fraction remains the same, buoyancy effect is only dependent on the liquid density, therefore the terminal steam velocity does not change even when the steam density varies.

With the obtained steam velocities, the  $(\rho_l - \rho_g)u_g^2/(\alpha D_{channel})$  term is also computed. The values are all approximately  $6.6E5 Pa/m$  with very subtle differences. Also, since  $\frac{dp}{dx}$  are very close among the three cases, the dimensionless performance is inherently valid when steam velocity changes.

Table 5.16. Pressure gradient model predictive capability when steam density changes.

System pressure (bar)	Density ( $kg/m^3$ )	$\frac{dp}{dx}$ (Pa/m)	Liquid cross-sectional averaged velocity (m/s)	Steam volumetric averaged velocity (m/s)
1	0.590344	5230.23	7.63E-07	0.4608
3	1.67133	5235.76	7.44E-07	0.4615
5	2.66805	5234.64	8.39E-07	0.4603

### 5.4.3 Surface tension

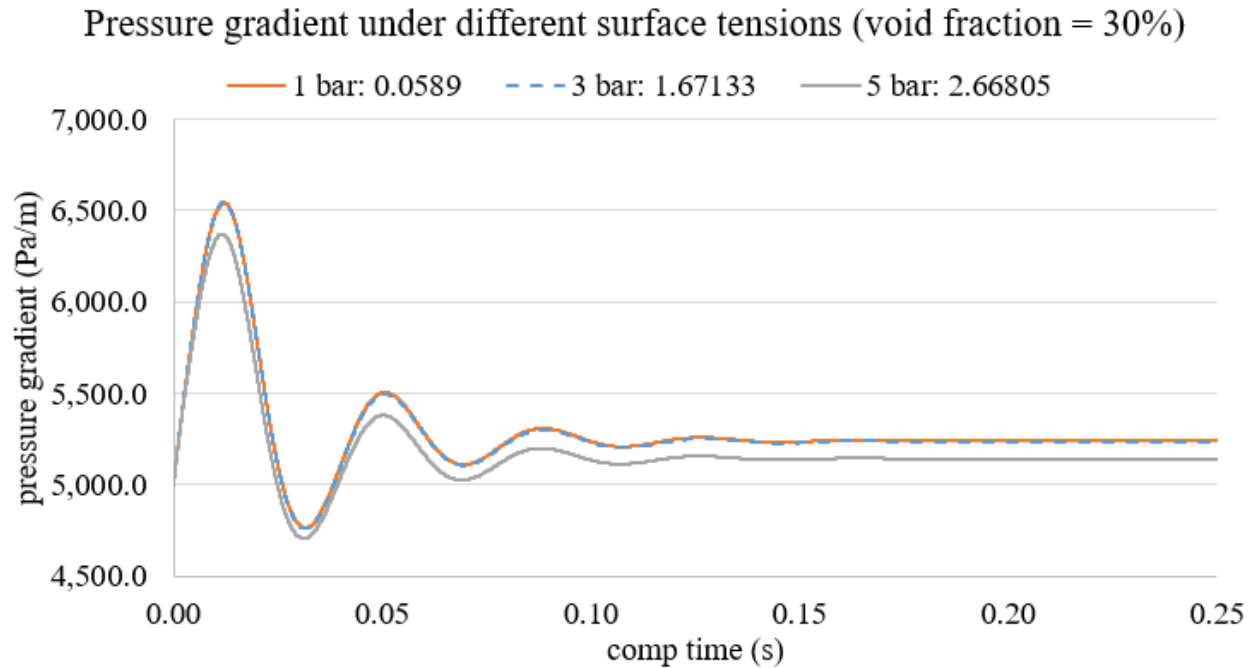
Three surface tensions are used to conduct CCFL simulations also at 30% steam volume fraction to demonstrate their effects on the proposed pressure gradient model (Eq. (49)). The

surface tension values are determined by the saturated temperatures at 1, 3, and 5 bar system pressures respectively (Table 5.17) and other relevant simulation parameters are duplicated from Table 5.4. Note that in order to have only one variable change in the parametric study, the liquid and steam densities are kept at 3 bar when the surface tension varies. Figure 5.50 depicts how the PID controller brings the two-phase annular flow with different steam densities to CCFL, where the eventual liquid velocities all stabilize around zero.

Table 5.17. Surface tension values in the parametric study.

System pressure	1 bar	3 bar	5 bar
Surface tension ( $N/m$ )	0.0589	0.0516	0.0482

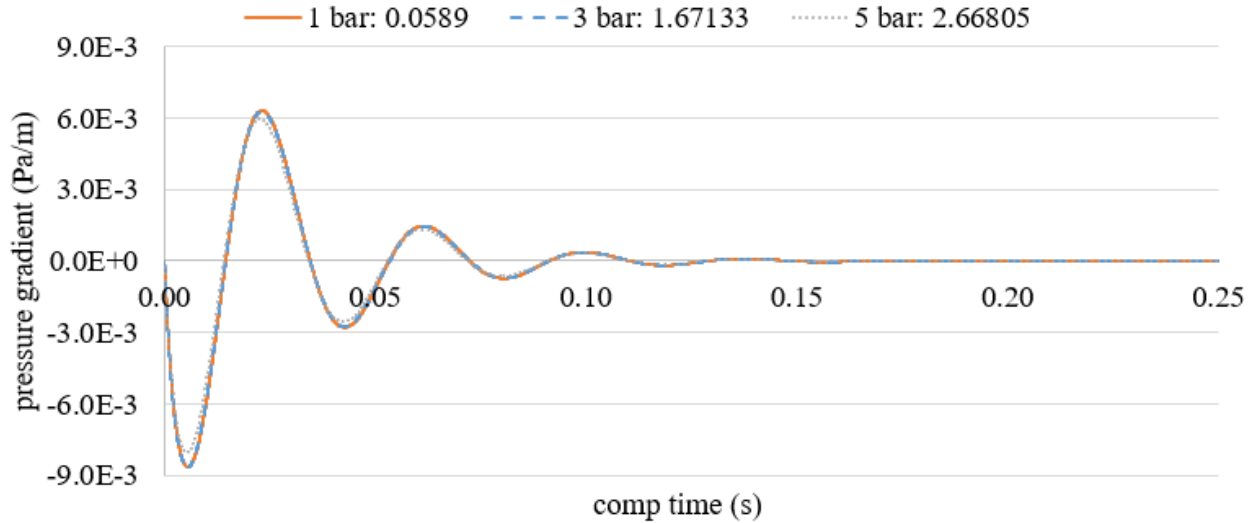
Figure 5.50. PID controlled CCFL in surface tension parametric study.



(a) Pressure gradient.

Figure 5.50. (continued)

Liquid cross sectional averaged velocity under different surface tensions  
(void fraction = 30%)



(b) Coolant velocity.

Table 5.18 compares the predicted pressure gradients by the correlation Eq. (49) and the steady-state averaged pressure gradients from Figure 5.50. It is obvious that the predicted values match well with the simulation results with a maximum relative difference of  $-4\%$ . Even though the lower surface tension results in a relatively lower pressure gradient at CCFL, it is still predictable by the proposed model. This study suggests the surface tension has negligible effect on the proposed pressure gradient model in the system pressure range of 1-5 bar.

Table 5.18. Pressure gradient model predictive capability when surface tension changes.

System pressure (bar)	Surface tension ( $N/m$ )	$\frac{dp}{dx}$ predicted by correlation ( $Pa/m$ )	$\frac{dp}{dx}$ obtained from simulation ( $Pa/m$ )	Relative difference
1	0.0589	5241.82	5009.56	-4.43%
3	0.0516	5235.76	5009.56	-4.32%
5	0.0482	5142.67	5009.56	-2.59%

The physics behind the independence of surface tension is that the flow regime can be maintained. Two-phase velocity distributions under the three surface tensions are compared in Figure 5.51. While surface tension values range from conditions corresponding to 1 - 5 bar range, the annular flow regime is still maintained. As the steam velocity does not change significantly (Table 5.19) and the void fraction is the same, the flow regimes are the same when surface tension changes. In addition, for such annular flow, among the 3 forces in liquid film, gravity, wall shear, and interfacial shear are all independent on the surface tension. Therefore, the force balance in the liquid film keeps consistent even if surface tension changes.

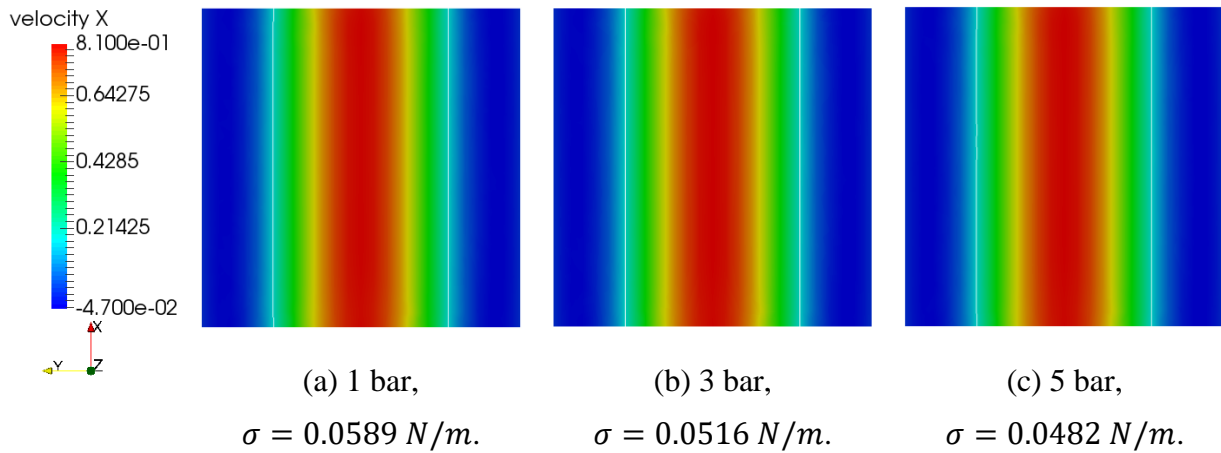


Figure 5.51. Two-phase velocity distributions in surface tension parametric study.

Table 5.19. Liquid and steam velocities at CCFL.

System pressure (bar)	Surface tension ( $N/m$ )	Liquid cross-sectional averaged velocity ( $m/s$ )	Steam volumetric averaged velocity ( $m/s$ )
1	0.0589	8.17E-07	0.4589
3	0.0516	7.44E-07	0.4615
5	0.0482	6.09E-07	0.4525

#### 5.4.4 Channel porosity

This section incorporates the effect of geometry into the proposed pressure gradient model, Eq. (49), by studying the results from channels with different porosities ( $\epsilon$ ). The porosity is defined as the volume of voids over the total volume. For the geometries used in debris bed CCFL studies in Section 5.2 and 5.3, the porosity can be computed as:

$$\epsilon = \frac{V_{fluid}}{\pi D^2 L / 4} \quad (52)$$

Here,  $V_{fluid}$  is the actual volume to hold the two-phase flow in the debris bed channel, and  $\pi D^2 L / 4$  is the cylinder volume if no obstacle exists. In this term,  $D$  is the diameter and  $L$  is the channel length in the streamwise direction. For the three geometries used in debris bed CCFL studies, their porosities are computed in Table 5.20.

Table 5.20. Porosity computation for three debris bed channels.

Geometry	Section	$D$ (mm)	$L$ (mm)	$\pi D^2 L / 4$ (mm <sup>3</sup> )	$V_{fluid}$ (mm <sup>3</sup> )	Porosity $\epsilon$
Simple cylinder	5.2	1.0	1.0	0.7854	0.7854	100.0%
With small obstacles	5.3.1	1.0467	1.5700	1.3509	1.3371	99%
With large obstacles	5.3.2	1.4576	2.1864	3.6485	3.2491	89%

Table 5.20 shows that from the simple cylindrical debris bed channel to the channel with small obstacles and then to the channel of large obstacles, the porosity gradually decreases as the obstacle volume increase. The pressure gradient model, Eq. (49), is proposed based on cylindrical channel and  $\epsilon = 100\%$ , but this model is also accurate enough for CCFL prediction in channel with small obstacles (Section 5.3.1.1) because the porosity (99%) is very close to 100%. However, Eq. (49) failed in predicting CCFL in debris bed channel with large obstacles since the porosity (89%) is

far below 100%. Therefore, a porosity term can be added into the pressure gradient correlation to better predict CCFL occurrence, and Eq. (49) can be updated to Eq. (53).

$$\frac{dp}{dx} = \rho_l g \cdot \exp(-2.0\alpha) \cdot f(\epsilon) \quad (53)$$

Here,  $f(\epsilon) = 1$  if  $\alpha = 0$  since for 0 steam volume fraction,  $\frac{dp}{dx}$  only needs to balance with  $\rho_l g$  to achieve a zero liquid velocity. This conclusion is also supported by the debris bed channel with large obstacles under 0 steam volume fraction (Section 5.3.2.2). A more general expression for  $f(\epsilon)$  can be investigated in the future with more geometries to be involved. The PID pressure gradient controller can also facilitate this investigation process with its efficiency, robustness, and accuracy in predicting CCFL occurrence. Table 5.21 summarizes the results in Section 5.2 and 5.3 for three geometries involved. The corresponding  $\frac{dp}{dx}$  and steam superficial velocities are compared in Figure 5.52 with data obtained from the debris bed experiments (Rashid et al., 2012).

Table 5.21. Summarization of CCFL results from different debris bed channels.

Debris bed channel	Steam volume fraction	$\frac{dp}{dx}$ (Pa/m)	Steam volumetric averaged velocity (m/s)	Superficial velocity (m/s)
Simple cylinder	30%	5235.76	4.61E-01	1.38E-01
	40%	4299.29	4.57E-01	1.83E-01
	50%	3491.00	4.27E-01	2.14E-01
	60%	2785.52	3.77E-01	2.26E-01
With small obstacles	30%	5304.10	5.52E-01	1.66E-01
With large obstacles	30%	9582.96	9.20E-04	1.24E-03

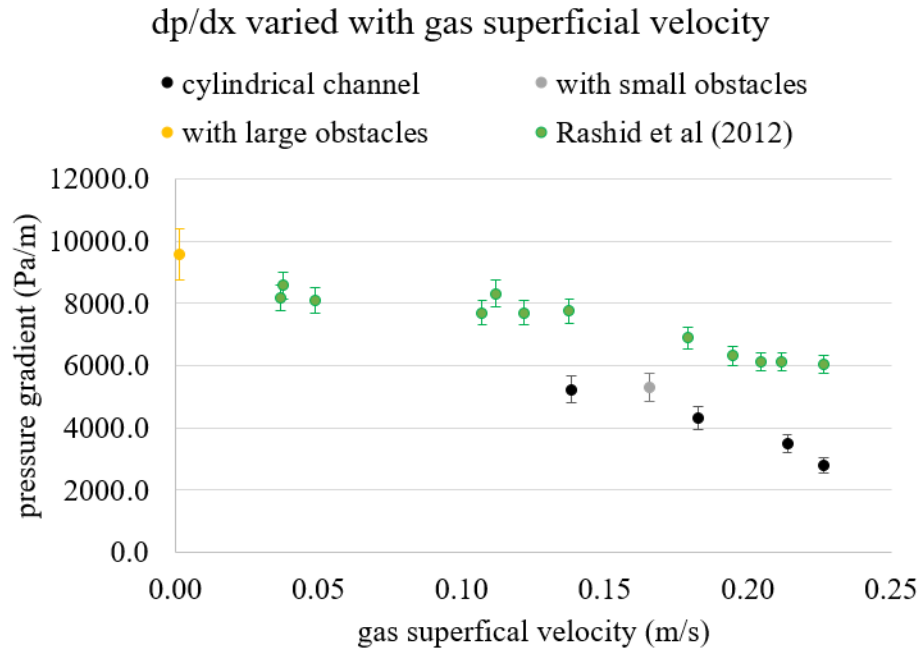


Figure 5.52. Pressure gradient obtained from PID control in three different debris bed channels, compared with experimental data (Rashid et al., 2012).

In Figure 5.52, it is obvious that when the obstacles are added, the simulation results are closer to the experimental data. The debris bed channel with small obstacles (grey symbols) is closer to the experimental data (green symbols) than the simple cylindrical channel (black symbols). Even the pressure gradients to achieve CCFL under  $\alpha = 30\%$  are very close in these two geometries (Table 5.21). Therefore, although the cylindrical geometry and the annular flow configuration is a validated approximation for the debris bed channel flow (Abe, 1995; Abe and Sudo, 2006), it is significant to imitate the simulation geometry to the real world debris bed channel to increase the accuracy of the numerical results. Moreover, the results from debris bed channel with large obstacles (yellow symbols) and small obstacles as well as cylindrical channels (grey and black symbols) distribute on the upper and lower sides of the experimental data. It is very possible that with a proper domain design matching the experimental debris bed geometry, the simulation data can overlap with the experimental results. In another perspective, the simulation results from PID control are also trustworthy enough to predict CCFL occurrence.

#### 5.4.5 Application of proposed models

The proposed pressure gradient model (Eq. (53)) can be used to evaluate the primary pressure loss along the debris bed under CCFL condition given the height of the bed. Parametric studies already proved its good predictability under the system pressure 1-5 bar, which reflects typical environment of the debris bed. With the expression of porosity term finalized in the future, the pressure gradient model can be incorporated in full debris bed analysis (sub-system level). Therefore, temperature and other conditions corresponding to CCFL with primary pressure drop obtained from this model.

Although the form of pressure gradient model Eq. (53) is different with the classical CCFL correlations (the Wallis correlation in Eq. (1)-(5)), they are not conflicting. The essence of the Wallis correlation is that for all liquid and vapor conditions at CCFL occurrences, data sets ( $J_l^{*0.5}$ ,  $J_g^{*0.5}$ ) all align on a straight line. With the CCFL definition in this dissertation, liquid has a zero velocity and the steam is still moving upward, therefore  $J_l^* = 0$  and  $J_g^* > 0$  respectively. Therefore, all the data sets ( $J_l^{*0.5}$ ,  $J_g^{*0.5}$ ) in the presented studies also align on one straight line which is overlapping with  $J_g^{*0.5}$  axis. Therefore, the obtained data sets and the correspondingly proposed models inheritably satisfy Wallis correlation.

As for the dimensionless number  $SU$  in Eq. (50), it can be applied for CCFL estimation in realistic conditions. There are five parameters in the  $SU$  definition ( $\rho_l$ ,  $\rho_g$ ,  $D_{channel}$ ,  $\alpha$ , and  $u_g$ ), and their estimations are discussed in below.

(1) Densities of working fluids  $\rho_l$  and  $\rho_g$ .

Densities of working fluids are usually easily accessible, especially for light water condition where water and steam properties have been documented very well. The density effects under potential system pressure of the debris bed (1-5 bar) was also studied in Section 5.4.1 and 5.4.2.

(2) Channel hydraulic diameter  $D_{channel}$ .

The channel hydraulic diameters can be estimated based on existing debris experimental studies, for example, from the photos taken for the formed debris bed (Karbojian et al., 2009). The  $1mm$  used in the presented studies is one of the potential values.

(3) Void fraction  $\alpha$ .

The void fraction can be estimated by empirical correlations proposed for small channels. For instance, Cioncolini and Thome proposed a very elegant void fraction correlation which only depended on vapor quality  $x$ , and the density ratio between gas and liquid  $\frac{\rho_g}{\rho_l}$  (Cioncolini and Thome, 2012).

$$\alpha = \frac{hx^n}{1 + (h-1)x^n}, 0 < x < 1, 10^{-3} < \frac{\rho_g}{\rho_l} < 1 \quad (54)$$

$$h = -2.129 + 3.129 \left( \frac{\rho_g}{\rho_l} \right)^{-0.2186} \quad (55)$$

$$n = 0.3487 + 0.6513 \left( \frac{\rho_g}{\rho_l} \right)^{0.5150} \quad (56)$$

This void fraction correlation was proposed based on 2673 experimental data points including water-steam working fluids under  $0.11 \sim 207 MPa$  system pressure, and in both circular and non-circular channels, which can be used for any small channel with a diameter of  $1.0 \sim 45.5mm$ . The application ranges of this correlation satisfy most of the debris bed channel conditions.

(4) Steam velocity  $u_g$ .

Decay heat can be computed by the empirical correlation determined by fission product half-lives, which just needs the reactor operation power before shutdown and the time of the reactor shutdown based on (Glasstone and Sesonske, 2012). The computed decay heat can be converted to the steam superficial velocity  $j_g$  with latent heat and channel size. The vapor quality  $x$  can also

be estimated by the decay heat and the latent heat, and then used for computing void fraction  $\alpha$  by Eq. (54). In the end, steam velocity  $u_g$  can be simply calculated as  $j_g/\alpha$ . In this estimation process, uncertainties do exist, especially for vapor quality  $x$ , but we can still estimate it in order to apply pressure gradient model and  $SU$  number in debris bed CCFL study. We also hope that relevant experiments can be conducted in the future to validate the proposed models.

The essence of applying  $SU$  number in debris bed CCFL study is that no matter which variable changes, as long as two data points of  $(\frac{(\rho_l-\rho_g)u_g^2}{\alpha D_{channel}}, \frac{dp}{dx})$  can be obtained, then  $SU$  can be estimated as the slope of straight line going through those two data points. Any other data points on this line corresponds to CCFL occurrence. The ideology here is very similar to the Wallis correlation in Eq. (1)-(5). In the application stage of  $SU$  number, no matter with DNS, multiphase CFD, or Reynolds-averaged Navier–Stokes (RaNS) simulations, only two data points are needed to extrapolate over other CCFL conditions, saving computational cost and time.

It is worth mentioning that although extrapolation of  $\alpha = 0$  (pure liquid) and  $\alpha = 100\%$  (pure steam) makes physical sense for the pressure gradient correlation in Eq. (53), such extrapolation does not apply in  $SU$  definition. If  $\alpha = 0$ ,  $\frac{(\rho_l-\rho_g)u_g^2}{\alpha D_{channel}} \rightarrow \infty$ ; if  $\alpha = 100\%$ , then including  $\rho_l$  in  $SU$  does not have physical significance. Therefore,  $SU$  number can be used as long as liquid and steam phases both exist.

## 5.5 Chapter summary

CCFL in nuclear reactor debris bed geometries is studied in this chapter. First, counter current flow driven by gravity and steam generation rate are presented. The steam rates are manually increased to explore the occurrence of CCFL. This study demonstrates the level-set method capability on solving CCFL in debris bed. It also reveals that the manual adaptation of steam rate

is a costly process and the simulation result may not accurately satisfy the CCFL criterion (zero liquid velocity). Therefore, PID control is needed to facilitate this process and obtain more accurate two-phase dynamics at CCFL occurrence.

With the PID pressure gradient controller to adjust liquid velocity, 3D high resolution simulations are conducted on debris bed CCFL using interface capturing method. CCFL in cylindrical debris bed channel is first investigated. The pressure gradients and steam superficial velocities under varying void fractions are obtained at CCFL occurrence. CCFL in debris channel with small and large obstacles are studied to demonstrate the PID pressure gradient control capability under very complex geometry and flow conditions. With the existences of the obstacles, re-circulation forms at each corner in the geometry, so the velocity distribution in the coolant tends to generate a lower magnitude of the net liquid velocity. This results in CCFL to be achieved in less time compared with simpler channels. The numerical data obtained from those three debris bed channels are qualitatively comparable with the experimental data. Therefore, two models are developed for the debris bed CCFL studies based on those simulation results. One is the pressure gradient correlation with regards to coolant density, void fraction, and the channel porosity, which can predict the pressure gradient of debris bed channel at CCFL occurrence. Its predictive capability is demonstrated by a series of parametric studies, and the pressure gradient at CCFL is proved to be independent of the steam density and the surface tension. The other model is developed based on the connection between the debris CCFL and single bubble. A dimensionless number  $SU$  is proposed to be equivalent to the bubble drag coefficient, where the application of  $SU$  can save significant computational cost when studying CCFL affected by any parameter.

Counter current flow is a complex two-phase phenomenon, which contains complicated flow characteristics such as interfacial shear and topology. Counter current flow in this dissertation is studied based on two topics; CCFL in the debris bed and the PID-controlled single bubble studies. Specially, the controlled bubble simulations, are fundamental for studying more complex CCFL flow characteristics in the debris bed channel.

CCFL in nuclear reactor debris bed is studied to shed lights in cooling debris bed during severe accidents. To predict the CCFL occurrence more efficiently, a PID pressure gradient controller was developed. By integrating control theory into the interface capturing approach in PHASTA code, CCFL mechanism in debris bed was comprehensively investigated with high resolution two-phase simulations. With the validated and verified unit problems through controlled bubble studies, and the verification and robustness tests of the PID control, the trustworthiness of PID controlled CCFL simulations is built.

Among the 3 objectives listed in Section 1.4, the presented research addressed nearly all of them. To tackle Objective 1, PID bubble controller is verified and validated in more broad studies, including wall-affected transverse forces and complex bubble topology evolutions. The capability and precision of the PID bubble controllers are assessed in revealing complex topology change, which is foundational for CCFL studies. The mesh studies of single bubbles provide reference on spatial discretization for more complex CCFL simulations as well. A new gravity control capability is added into the PID bubble controller. The control on gravity provides reference for the development of PID pressure gradient controller. To address Objective 2, counter current flow in nuclear debris bed driven by gravity and steam generation rate are presented as the smallest scale in studying nuclear reactor CCFL. The steam rates are manually increased to explore the

occurrence of CCFL. This study demonstrates the level-set method capability on solving CCFL in debris bed. To address Objective 3, a PID controller was developed to obtain the pressure gradient associated with CCFL. Here, achieving CCFL is commonly defined as when the average liquid velocity is zero under any upward flow condition or geometry. Section 5.2 fulfills Objective 3 by successfully developing a PID pressure gradient controller. Eventually, 3D high resolution simulations on CCFL using interface capturing method can be successfully carried out under PID control. Three debris bed channels with different porosities were selected to study two-phase mechanism at CCFL and the corresponding bed coolability. Based on those debris bed simulations, a pressure gradient correlation and a dimensionless number are then proposed to predict CCFL occurrence. The developed PID pressure gradient controller was also demonstrated to be efficient, accurate, and robust under complex geometry and flow conditions.

Future development of this research scope can use one or of the following directions.

### **6.1 Improvement on developed correlation and dimensionless number**

There are certain limitations of parameters used in developing the correlation of pressure gradient in Eq. (53) and the dimensionless number in Eq. (50), especially the channel size. In all the debris bed simulations across the entire 4.5, the hydraulic diameter is  $1mm$ . Given the complex geometry of the real debris bed,  $1mm$  is one of the potential channel sizes, and other diameters can be studied in the future. The current pressure gradient model does not include the channel diameter; therefore a wider channel size range can further demonstrate the performance of the developed models. As a contrast, the dimensionless number  $SU$  has the channel diameter in its definition, but simulations with wider channel size range can also evaluate the extrapolation behavior of  $SU$ .

Another parameter which is significant to finalize the correlation is the channel porosity. Three porosities were involved in 4.5, corresponding to the cylindrical channel, the channel with small obstacles, and with large obstacles, respectively. There are lots of other parameters which can change the porosity, such as channel size, obstacle shape and size, and obstacle distribution. Those parameters can be further investigated to develop the expression of  $f(\epsilon)$  term in Eq. (53) and to finalize the pressure gradient correlation.

## **6.2 PID pressure gradient control in more complex scenarios**

All of the debris bed CCFL simulations are conducted in a single channel. However, the multiple channel effect on CCFL can be studied in the future with adequate computational resource. Moreover, all the initial condition of the two-phase distribution is annular flow. Although a steady state can be achieved for all the involved simulations, it will be an interesting topic to study the initial interface topology effect on the CCFL condition. In addition, with contact angle model and other sub-grid capabilities added to the PID controlled CCFL simulations, more physics about debris bed two-phase dynamics can be revealed.

Aside from CCFL occurrence in the reactor debris bed (micro scale), it can also occur in mini-channels and nuclear reactor subchannels. In regard to mini-channels, inclined cylindrical channel could be used for studying both gravity and pressure gradient effects on CCFL. The flow characteristics under different inclined angles can also be a scaled study for the pressurizer surge line where the flow channel can be decomposed into a group of inclined cylindrical segments. There are also experimental results from pressurizer surge line which can be used for validation.

As for the nuclear subchannels, the geometry is very different from the cylindrical domain, thus the interface topology evolutions should be interesting, which reveals the wettability on the clad surface. This study is beneficial for severe accident analysis in nuclear reactors. Furthermore,

nuclear subchannels with spacer grids is an additional but interesting challenge, where the local disturbance caused by grids can be analyzed for CCFL.

Apart from the change in geometry, the velocity range will be completely different in nuclear subchannels or pressurizer surge lines. It will be worthwhile to investigate if models developed for debris bed channel can be extrapolated to high velocity conditions. To produce good quality data under such conditions, the spatial discretization can be challenging and an advanced super-computer may be required as well.

### 6.3 Improved PID pressure gradient controller for complex geometry

In current debris bed studies, the channel is simplified into a cylinder with obstacles, but a debris bed channel formed by the accumulation of spheres is more realistic (Figure 6.1). If using the PID pressure gradient controller in such condition, as the channel cross-sectional area changes, the velocity surface integral needs to be replaced by the velocity volumetric integral for a more robust control performance. This change will increase the computational cost, but it is a requirement for studying CCFL in irregular geometry flow channels.

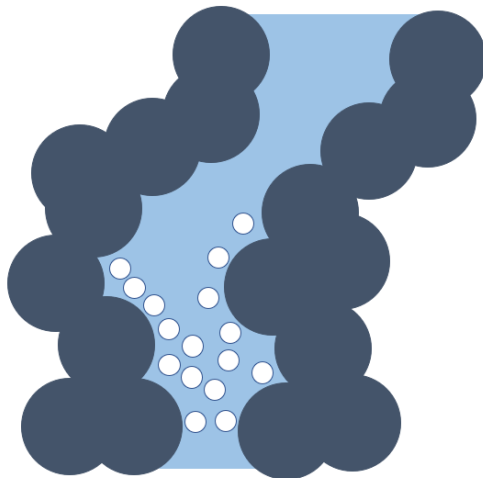


Figure 6.1. Illustration of debris bed flow channel with steam generated in the heated channel. The channel geometry is more realistic than the simplified cylindrical channel, but it still needs the debris to be simplified into overlapping spheres.

With adequate computational resources, two-phase studies can be conducted on the flow in debris bed with even more realistic flow channel geometries designed based on debris bed photos. Specifically, of interest is CCFL under multiple conditions, especially with interaction effect among multiple flow channels. Furthermore, with world-leading supercomputers, simulations on whole reactor debris bed can be considered, potentially involving hundreds of fully resolved channels at flow conditions of interest. Desirable information on the flow conditions are dimensionless number, channel geometry and porosity, pressure gradient, steam rate at CCFL, and liquid-steam flow regime.

#### **6.4 Potential coupling of PID theory with boiling**

The PID control methodology can also be expanded for boiling scenarios. Instead of using pressure gradient to automatically generate the CCFL occurrence, the heat flux ( $q''$ ) on the channel wall can be used. In such a scenario, the periodical boundary condition is removed and the flow field will be initialized with single phase coolant. The PID- $q''$  controller can automatically adjust the heat flux to heat the coolant and generate the steam, until the steam rate is high enough that the coolant is no longer contacting the heated surface. This PID- $q''$  controller needs to be robustly coupled with boiling and condensation models in PHASTA.

In the future, with more mature integration of control theory, the control objective is not limited to CCFL and can be applied to any problem of interest. As long as the objective is defined and controlled by the PID, the required conditions to meet the objective (such as pressure gradient) can be calculated, possibly opening up a new chapter in reactor thermal hydraulic analysis.

## REFERENCES

- Abe, Y., 1995. Applicability of annular flow model to counter-current flow in debris beds. *J Nucl Sci Technol* 32, 763-772.
- Abe, Y., Adachi, H., 1994. Flow characteristics of counter-current flow in debris bed. International Topical Meeting on Nuclear Thermal Hydraulics, Operations and Safety, Taipei, Taiwan (China), 1994.
- Abe, Y., Sudo, Y., 2006. Experimental measurement of frictional law under CCFL in porous debris. *Nucl. Eng. Des.* 236, 2075-2083.
- Ahmed, Z., Bindra, H., Eckels, S., 2019. Scaling Analysis on the Coolability of Fuel Rods and Debris Bed with Seawater. 18th International Topical Meeting on Nuclear Reactor Thermal Hydraulics (NURETH-18).
- Al Issa, S., Macian, R., 2011. A review of CCFL phenomenon. *Ann. Nucl. Energy* 38, 1795-1819.
- Antal, S., Lahey, R., Flaherty, J., 1991. Analysis of phase distribution in fully developed laminar bubbly two-phase flow. *Int. J. Multiphase Flow* 17, 635-652.
- Azam, M.S., Niu, F., Wang, D., Zhuo, W., 2018. Experimental and CFD analysis of the effects of debris deposition across the fuel assemblies. *Nucl. Eng. Des.* 332, 238-251.
- Bankoff, S., Lee, S., 1983. A comparison of flooding models for air-water and steam-water flow, in *Anonymous Advances in Two-Phase Flow and Heat Transfer*. Springer, pp. 745-780.
- Behafarid, F., Jansen, K., Podowski, M., 2015. A study on large bubble motion and liquid film in vertical pipes and inclined narrow channels. *Int. J. Multiphase Flow* 75, 288-299.
- Bhaga, D., Weber, M.E., 1981. Bubbles in viscous liquids: shapes, wakes and velocities. *J. Fluid Mech.* 105, 61-85.
- Bolotnov, I.A., 2013. Influence of Bubbles on the Turbulence Anisotropy. *ASME J. Fluids Eng.* 135, 051301.
- Brackbill, J.U., Kothe, D.B., Zemach, C., 1992. A continuum method for modeling surface tension. *Journal of computational physics* 100, 335-354.
- Chakravarty, A., Datta, P., Ghosh, K., Sen, S., Mukhopadhyay, A., 2019. Coolability of heat-generating porous debris beds in severe accident situations, in *Anonymous Two-Phase Flow for Automotive and Power Generation Sectors*. Springer, pp. 305-336.

Cioncolini, A., Thome, J.R., 2012. Void fraction prediction in annular two-phase flow. *Int. J. Multiphase Flow* 43, 72-84.

Deendarlianto, T.H., Lucas, D., Vallée, C., 2010. Numerical simulation of air-water counter-current two-phase flow in a model of the hot-leg of a pressurized water reactor (PWR). *Proceedings of the 7th International Conference on Multiphase Flow (ICMF'10)*.

Dueñas, A.M., 2019. Investigation of Drag Coefficient and Virtual Mass Coefficient on Rising Ellipsoidal Bubbles.

Dukler, A., Smith, L., 1977. Two phase interactions in counter-current flow: studies of the flooding mechanism. Annual report, November 1975--October 1977.

Dutt, N., Singh, A.R., Sahoo, P.K., 2020. CFD analysis of suspended debris during postulated severe core damage accident of PHWR. *Nucl. Eng. Des.* 357, 110390.

Ervin, E., Tryggvason, G., 1997. The rise of bubbles in a vertical shear flow. *Journal of Fluids Engineering* 119, 443-449.

Fan, Y., Bolotnov, I., 2020. Gravity Controller Capability for Single-Bubble Interface-Resolved Simulations. *ANS Winter Meeting 2020 Transactions*.

Fan, Y., Fang, J., Bolotnov, I., 2021. Complex bubble deformation and break-up dynamics studies using interface capturing approach. *Experimental and Computational Multiphase Flow* 3, 139-151.

Fan, Y., Feng, J., Bolotnov, I., 2018. Investigation of Wall Effect on Deformable Bubble Using Interface Tracking Method. *ANS Annual Meeting 2018 Transactions*.

Fang, J., 2016. Development of Advanced Analysis Toolkit for Turbulent Bubbly Flow Simulations.

Fang, J., Rasquin, M., Bolotnov, I.A., 2017. Interface tracking simulations of bubbly flows in PWR relevant geometries. *Nucl. Eng. Des.* 312, 205-213.

Feng, J., Bolotnov, I.A., 2017a. Effect of the wall presence on the bubble interfacial forces in a shear flow field. *Int. J. Multiphase Flow* 99, 73-85.

Feng, J., Bolotnov, I.A., 2017b. Evaluation of Bubble-Induced Turbulence Using Direct Numerical Simulation. *Int. J. Multiphase Flow* 93, 92-107.

Feng, J., Bolotnov, I.A., 2017c. Interfacial force study on a single bubble in laminar and turbulent flows. *Nucl. Eng. Des.* 313, 345-360.

Feng, J., Bolotnov, I.A., 2016. Evaluation of bubble-induced turbulence using direct numerical simulation. *International Topical Meeting on Advances in Thermal Hydraulics 2016*.

Feng, J., Bolotnov, I.A., 2015. Interfacial forces evaluation on a single bubble in shear flows using interface tracking approach. Transactions of the American Nuclear Society.

Fichot, F., Duval, F., Tregoures, N., Béchaud, C., Quintard, M., 2006. The impact of thermal non-equilibrium and large-scale 2D/3D effects on debris bed reflooding and coolability. Nucl. Eng. Des. 236, 2144-2163.

Franken, D., Ahmed, Z., Eckels, S., Eckels, S., Bindra, H., 2019. Impact of dissolved salts on two-phase flow and boiling heat transfer in a natural circulation loop. Chemical Engineering Science 206, 463-470.

Fukano, T., Kariyasaki, A., 1993. Characteristics of gas-liquid two-phase flow in a capillary tube. Nucl. Eng. Des. 141, 59-68.

Gallego, M.G., 2004. Countercurrent flow limitations in horizontal stratified flows of air and water.

Glasstone, S., Sesonske, A., 2012. Nuclear Reactor Engineering: Reactor Systems Engineering. Springer Science & Business Media.

Gore, R., Crowe, C.T., 1989. Effect of particle size on modulating turbulent intensity. Int. J. Multiphase Flow 15, 279-285.

Govan, A., Hewitt, G., Richter, H., Scott, A., 1991. Flooding and churn flow in vertical pipes. Int. J. Multiphase Flow 17, 27-44.

Guillen, D.P., Cambareri, J., Abboud, A.W., Bolotnov, I.A., 2018. Numerical comparison of bubbling in a waste glass melter. Annals of Nuclear Energy 113, 380-392.

Hessheimer, M.F., Dameron, R.A., 2006. Containment Integrity Research at Sandia National Laboratories An Overview. NUREG/CR-6906 SAND2006-2274P.

Hewitt, G.F., Wallis, G.B., 1963. Flooding and associated phenomena in falling film flow in a tube.

Höhne, T., Lucas, D., Vierow, K., 2012. Gas-liquid countercurrent two-phase flow in a PWR hot leg: A comprehensive research review. Nucl. Eng. Des. 243, 214-233.

Hwang, B., Park, H.S., Jung, W.H., Lee, M., Kim, M.H., 2019. Numerical validation and investigation for the sedimentation of solid particles in liquid pool using the CFD-DEM coupling algorithm. Nucl. Eng. Des. 355, 110364.

Ishii, M., Paranjape, S., Kim, S., Sun, X., 2004. Interfacial structures and interfacial area transport in downward two-phase bubbly flow. Int. J. Multiphase Flow 30, 779-801.

Ishii, M., 1990. Two-fluid model for two-phase flow. Multiphase science and technology 5.

- Jansen, K.E., 1993. Unstructured grid large eddy simulations of wall bounded flows. Annual Research Briefs, Center for Turbulence Research, NASA Ames/Stanford University, 151.
- Jansen, K.E., 1999. A stabilized finite element method for computing turbulence. *Comput. Methods Appl. Mech. Eng.* 174, 299-317.
- Jansen, K.E., Rasquin, M., Brown, J., Smith, C., Shephard, M.S., Carothers, C., 2017. Extreme scale unstructured adaptive CFD for aerodynamic flow control.
- Jayanti, S., Tokarz, A., Hewitt, G., 1996. Theoretical investigation of the diameter effect on flooding in countercurrent flow. *Int. J. Multiphase Flow* 22, 307-324.
- Jeong, J.H., 2008. Counter-current flow limitation velocity measured in annular narrow gaps formed between large diameter concentric pipes. *Korean Journal of Chemical Engineering* 25, 209-216.
- Karbojian, A., Ma, W., Kudinov, P., Dinh, T., 2009. A scoping study of debris bed formation in the DEFOR test facility. *Nucl. Eng. Des.* 239, 1653-1659.
- Karniadakis, G.E., 1995. Toward a numerical error bar in CFD. *Journal of Fluids Engineering* 117.
- Kutateladze, S., 1972. Elements of the hydrodynamics of gas liquid systems. *Fluid Mech.-Soviet Res.* 1, 29.
- Legendre, D., Magnaudet, J., 1998. The lift force on a spherical bubble in a viscous linear shear flow. *J. Fluid Mech.* 368, 81-126.
- Li, C., Wang, K., Pellegrini, M., Erkan, N., Okamoto, K., 2021. Numerical Simulation and Validation of Debris Bed Self-Leveling Behavior with Mixed-Density Particles Using CFD-DEM Coupling Algorithm. *Nucl Technol*, 1-17.
- Li, M., Zeng, K., Wonnell, L., Bolotnov, I.A., 2019. Development of a New Contact Angle Control Algorithm for Level-Set Method. *Journal of Fluids Engineering* 141, 061301.
- Lipinski, R.J., 1984. A coolability model for postaccident nuclear reactor debris. *Nucl Technol* 65, 53-66.
- Lu, H., Lu, L., Luo, Y., Qi, R., 2016. Investigation on the dynamic characteristics of the counter-current flow for liquid desiccant dehumidification. *Energy* 101, 229-238.
- Ma, W., Dinh, T., 2010. The effects of debris bed's prototypical characteristics on corium coolability in a LWR severe accident. *Nucl. Eng. Des.* 240, 598-608.
- Maneri, C., 1970. The motion of plane bubbles in inclined ducts. Ph.P.Thesis, Polytechnic Institute of Brooklyn, New York.

- McComb, W.D., 1999. Dynamics and Relativity. Oxford University Press, Oxford (UK).
- Moujaes, S., Dougall, R., 1985. Two-phase upflow in rectangular channels. *Int. J. Multiphase Flow* 11, 503-513.
- Murase, M., Tomiyama, A., Lucas, D., Kinoshita, I., Utanohara, Y., Yanagi, C., 2012. Correlation for countercurrent flow limitation in a PWR hot leg. *J Nucl Sci Technol* 49, 398-407.
- Murase, M., Utanohara, Y., Kusunoki, T., Yamamoto, Y., Lucas, D., Tomiyama, A., 2017. Prediction of countercurrent flow limitation and its uncertainty in horizontal and slightly inclined pipes. *Nucl Technol* 197, 140-157.
- Nagrath, S., Jansen, K.E., Lahey, R.T., 2005. Computation of incompressible bubble dynamics with a stabilized finite element level set method. *Comput. Methods Appl. Mech. Eng.* 194, 4565-4587.
- Nagrath, S., Jansen, K., Lahey Jr, R.T., Akhatov, I., 2006. Hydrodynamic simulation of air bubble implosion using a level set approach. *Journal of Computational Physics* 215, 98-132.
- Park, J.H., Lee, M.E., Kim, E.H., Park, H.S., 2016. Influence of Spherical Particle Size Distribution on Pressure Gradients in Mixed Bed.
- Popinet, S., 2003. Gerris: a tree-based adaptive solver for the incompressible Euler equations in complex geometries. *Journal of Computational Physics* 190, 572-600.
- Prosperetti, A., Tryggvason, G., 2007. *Computational Methods for Multiphase Flow*. Cambridge university press.
- Rapolu, P., Son, S.Y., 2007. Capillarity effect on two-phase flow resistance in microchannels. 43025, 1039-1045 ASME International Mechanical Engineering Congress and Exposition.
- Rashid, M., Kulenovic, R., Laurien, E., 2012. Experimental results on the coolability of a debris bed with down comer configurations. *Nucl. Eng. Des.* 249, 104-110.
- Repetto, G., Chikhi, N., Fichot, F., 2013. Main outcomes on debris bed cooling from PRELUDE experiments. 6th European Review Meeting on Severe Accident Research (ERMSAR-2013), Avignon, France.
- Roache, P.J., 1998. *Verification and Validation in Computational Science and Engineering*. Hermosa.
- Rodriguez, J., Sahni, O., Lahey, R., Jansen, K., 2013. A parallel adaptive mesh method for the numerical simulation. *Computers and Fluids* 87, 115-131.

- Saini, N., 2020. High-Fidelity Interface Capturing Simulations of the Post-LOCA Dispersed Flow Film Boiling Regime in a Pressurized Water Reactor Sub-Channel. North Carolina State University.
- Salibindla, A.K., Masuk, A.U.M., Tan, S., Ni, R., 2020. Lift and drag coefficients of deformable bubbles in intense turbulence determined from bubble rise velocity. *J. Fluid Mech.* 894.
- Sharaf, D., Premlata, A., Tripathi, M.K., Karri, B., Sahu, K.C., 2017. Shapes and paths of an air bubble rising in quiescent liquids. *Phys. Fluids* 29, 122104.
- Shaver, D.R., Podowski, M.Z., 2015. Modeling of interfacial forces for bubbly flows in subcooled boiling conditions. *Transactions of the American Nuclear Society*.
- Shin, S., Chergui, J., Juric, D., Kahouadji, L., Matar, O.K., Craster, R.V., 2018. A hybrid interface tracking–level set technique for multiphase flow with soluble surfactant. *Journal of Computational Physics* 359, 409-435.
- Snedecor, G.W., Cochran, W.G., 1989. *Statistical Methods*, 8th Edition. Iowa State University Press, Ames, Iowa.
- Sugrue, R., Magolan, B., Lubchenko, N., Baglietto, E., 2017. Assessment of a simplified set of momentum closure relations for low volume fraction regimes in STAR-CCM and OpenFOAM. *Ann. Nucl. Energy* 110, 79-87.
- Sussman, M., Fatemi, E., Smereka, P., Osher, S., 1998. An improved level set method for incompressible two-phase flows. *Comput. Fluids* 27, 663-680.
- Sussman, M., Smereka, P., Osher, S., 1994. A level set approach for computing solutions to incompressible two-phase flow. *Journal of Computational physics* 114, 146-159.
- Sussman, M., Smith, K.M., Hussaini, M.Y., Ohta, M., Zhi-Wei, R., 2007. A sharp interface method for incompressible two-phase flows. *Journal of computational physics* 221, 469-505.
- Sussman, M., Fatemi, E., 1999. An efficient, interface-preserving level set re-distancing algorithm and its application to interfacial incompressible fluid flow. *Siam J. on Scientific Computing* 20, 1165-1191.
- Tekavčič, M., Končar, B., Kljenak, I., 2016. Simulation of flooding waves in vertical churn flow. *Nucl. Eng. Des.* 299, 214-224.
- Thomas, A.M., Fang, J., Feng, J., Bolotnov, I.A., 2015. Estimation of shear-induced lift force in laminar and turbulent flows. *Nucl Technol* 190, 274-291.
- Tomiya, A., Sou, A., Zun, I., Kanami, N., Sakaguchi, T., 1995. Effects of Eötvös number and dimensionless liquid volumetric flux on lateral motion of a bubble in a laminar duct flow. *Advances in multiphase flow* 1995, 3-15.

- Tomiyama, A., Kataoka, I., Zun, I., Sakaguchi, T., 1998. Drag coefficients of single bubbles under normal and micro gravity conditions. *JSME International Journal Series B Fluids and Thermal Engineering* 41, 472-479.
- Tomiyama, A., Tamai, H., Zun, I., Hosokawa, S., 2002. Transverse migration of single bubbles in simple shear flows. *Chemical Engineering Science* 57, 1849-1858.
- Tripathi, M.K., Sahu, K.C., Govindarajan, R., 2015. Dynamics of an initially spherical bubble rising in quiescent liquid. *Nature communications* 6.
- Utomo, M., Warsito, W., Sakai, T., Uchida, S., 2001. Analysis of distributions of gas and TiO<sub>2</sub> particles in slurry bubble column using ultrasonic computed tomography. *Chemical Engineering Science* 56, 6073-6079.
- Vierow, K., 2008. Countercurrent flow limitation experiments and modeling for improved reactor safety.
- Vijayan, M., Jayanti, S., Balakrishnan, A., 2001. Effect of tube diameter on flooding. *Int. J. Multiphase Flow* 27, 797-816.
- Wallis, G.B., 1969. *One-Dimensional Two-Phase Flow*. McGraw-Hill, New York.
- Wang K., S., Lee J., S., Jones C., O., Lahey T., R., 1987. 3-D turbulence structure and phase distribution measurements in bubbly two-phase flows. *Int. J. Multiphase Flow* 13, 327-343.
- Watanabe, T., Takata, T., Yamaguchi, A., 2017. Numerical study on modeling of liquid film flow under countercurrent flow limitation in volume of fluid method. *Nucl. Eng. Des.* 313, 447-457.
- Wesselingh, J., Bollen, A., 1999. Single particles, bubbles and drops. *Chem. Eng. Res. Design* 2, 89-96.
- White, F., 2003. *Fluid Mechanics*. McGraw-Hill, New York.
- Yamatake, A., Katayama, H., Yasuoka, K., Ishii, S., 2007. Water purification by atmospheric DC/pulsed plasmas inside bubbles in water. *Int.J.Plasma Environ.Sci.Technol* 1, 91-95.
- Zapke, A., Kröger, D., 1996. The influence of fluid properties and inlet geometry on flooding in vertical and inclined tubes. *Int. J. Multiphase Flow* 22, 461-472.
- Zimmer, M.D., Bolotnov, I.A., 2019. Slug-to-churn vertical two-phase flow regime transition study using an interface tracking approach. *Int. J. Multiphase Flow* 115, 196-206.
- Zimmer, M.D., 2020. *Vertical Two-Phase Flow Regime Transition Study using Interface Resolved Simulations*. North Carolina State University.

## APPENDICES

## A. Scripts of probe area computation

The original xyztsGen.f only computed the coordinates of each probe. The following script is an extended version adding the computation of the area around each probe.

```
! Create an array for radial locations

! Number of regions:
  Nar = 3

! Create an array for theta angles for all regions:
  do j = 1, Nar
    i_max(j) = int(real(nhom)/2.0**real(j-1))
    do i = 1, i_max(j)
      Angles(j,i) = real(i-1)/real(i_max(j))*2.0*pi
!      write(*,*) j, i, Angles(j,i)
    end do
  end do

! Radial locations: (ignore BL for now!)
! For uniform in R spacing and preserving total homogeneous directions
! we will need to have a geometric progression in terms of number of
! layers in each "angle" region

! First let's compute number of the radius coordinates
  Nrad = 0
! Number of layers for the dense near wall region (will be spaced as BL
! in the future):
  Nlayer1 = 4
  do j = 1, Nar
    Nregion(j) = Nlayer1*int(2.0**(j-1))
    Nrad = Nrad + Nregion(j)
  end do
!write(*,*) 'Nregion(Nar)', Nregion(Nar)
write(*,*) 'Nrad = ', Nrad

! Split and fill with coordinates:
  do j = 1, Nrad
!    Radii(j) = rmax*(1.0 - (real(j)-0.5)/real(Nrad))
    Radii(j) = rmax*cos((real(j)-0.5)/real(Nrad)*0.5*pi)
  end do
  Rrgt(1) = Radii(1)
  Rrlt(1) = Radii(Nregion(1))
  Rrgt(2) = Radii(Nregion(1)+1)
  Rrlt(2) = Radii(Nregion(1)+Nregion(2))
  Rrgt(3) = Radii(Nregion(1)+Nregion(2)+1)
  Rrlt(3) = Radii(Nrad)
  do j = 1,3
    write(*,*) 'Rrgt(j) =', Rrgt(j)
    write(*,*) 'Rrlt(j) =', Rrlt(j)
  enddo

! See if we can print out the final result:
! (check the sequence later)
```

```

Nrad = 0
SumArea = 0.0
do j = 1, Nar    ! Loop over the regions
  do k = 1, Nregion(j) ! Loop over the radial positions
    do i = 1, i_max(j) ! Loop over the tangential angles
      if (j.eq.1 .and. k.eq.1) then
        Area = ((rmax-Radii(Nrad+k))
&              + 0.5d0*(Radii(Nrad+k) - Radii(Nrad+k+1)))
&              *(2.0d0*pi/real(i_max(j)))*Radii(Nrad+k)
      elseif(j.eq.Nar .and. k.eq.Nregion(Nar)) then
        Area = pi* (2.0d0*Radii(Nrad+k)**2.0d0/real(i_max(j))
      else
        Area = 0.5d0*(Radii(Nrad+k-1)-Radii(Nrad+k+1))
&              *(2.0d0*pi/real(i_max(j)))*Radii(Nrad+k)
      endif

      write(13,369) axial, Radii(Nrad+k)*cos(Angles(j,i))
&                  , Radii(Nrad+k)*sin(Angles(j,i))
&                  , Area
&                  , Radii(Nrad+k)
369 format(E16.9,1X,E16.9,1X,E16.9,1X,E16.9,1X,E16.9)
      SumArea = SumArea + Area
    end do !i
  end do !k
  if (j.eq.1) ANar(1) = SumArea
  if (j.eq.2) ANar(2) = SumArea - ANar(1)
  if (j.eq.3) ANar(3) = SumArea - ANar(1) - ANar(2)

  Nrad = Nrad + Nregion(j)
end do !j
ErrorArea = (SumArea-pi*rmax**2.0d0)/(pi*rmax**2.0d0)
do j = 1,Nar
  if(j.eq.1) Rrmax = rmax
  if(j.eq.2.or.j.eq.3) Rrmax = 0.5d0*(Rrlt(j-1) + Rrgt(j))
  if(j.eq.1.or.j.eq.2) Rrmin = 0.5d0*(Rrlt(j) + Rrgt(j+1))
  if(j.eq.3) Rrmin = 0.0d0
  Aring = pi*(Rrmax**2.0d0-Rrmin**2.0d0)
  relE(j) = (ANar(j) - Aring)/Aring
enddo
end if !pipe option
write(*,*)'The error between computed and analytical area is',
& ErrorArea
write(*,*)'The error between comp. and ana. ring area is', relE
close(13)

```

## B. Scripts of subroutine *asigmr*

A record code of 7 is added in *asigmr.f* to specially collect velocity and level-set in-situ data for velocity integral computation. During the data collection process, *timeseries* will be called to collect those two values and store them in *varts* array.

```
subroutine ASIGMR (y,          ac,          banma,
```

```

&          x,          xmudmi,
&          shp,          shgl,          ien,
&          res,          qres,
&          xKebe,          xGoC,          rerr,
&          cfl,          icflhits,          elemvol_local,
&          xarray,          yarray,          zarray,
&          bubradius, bubradius2, coordtag, TPgrad, divq)
c
c-----
c
c This routine computes and assembles the data corresponding to the
c interior elements.
c
c Zdenek Johan, Winter 1991. (Fortran 90)
c-----
c
c      use stats
c      use rlssave ! Use the resolved Leonard stresses at the nodes.
c      use timedata ! time series
c      use turbsa ! access to d2wall and effvisc & x2wall, y2wall, z2wall
c
c      include "common.h"
c
c      dimension y(nshg,ndofl),          ac(nshg,ndofl),
&          x(numnp,nsd),
&          shp(nshl,ngauss),          shgl(nsd,nshl,ngauss),
&          ien(npro,nshl),
&          res(nshg,nflow),
&          qres(nshg,idflx),          cfl(nshg),
&          icflhits(nshg), TPgrad(nshg,6), divq(nshg,4)
c
c      dimension banma(nshg,1),          bml(npro,nshl,1)
c
c      dimension yl(npro,nshl,ndofl),          acl(npro,nshl,ndofl),
&          xl(npro,nenl,nsd),          dwl(npro,nenl),
&          rl(npro,nshl,nflow),
&          ql(npro,nshl,idflx),
&          evl(npro,nenl),
&          cfl1(npro,nshl),
&          xwl(npro,nenl), ywl(npro,nenl), zwl(npro,nenl),
&          TPgrad1(npro,nshl,6), divql(npro,nshl,4)
c
c      dimension xKebe(npro,9,nshl,nshl),
&          xGoC(npro,4,nshl,nshl)
c
c      dimension rls1(npro,nshl,6)
c
c      real*8 lStsVec(npro,nshl,nResDims)
c
c      dimension xmudmi(npro,ngauss)
c      dimension sgn(npro,nshl)
c
c      real*8 rerr1(npro,nshl,6), rerr(nshg,numerr)
c!... Matt Talley's Bubble Coalescence Control

```

```

real*8 xarray(ibksiz), yarray(ibksiz), zarray(ibksiz)
real*8 bubradius, bubradius2

integer coordtag(ibksiz)
c
c!.... gather the variables
c
c
c!.... get the matrix of mode signs for the hierarchic basis functions.
c
      if (ipord .gt. 1) then
        call getsgn(ien,sgn)
      endif

      call localy(y,      yl,      ien,      ndofl, 'gather ')
      call localy(ac,     acl,     ien,      ndofl, 'gather ')
      call localx(x,      xl,      ien,      nsd,   'gather ')
      call local (qres,   ql,      ien,      idflx, 'gather ')
      if (iRANS .eq. -2.or.((iDNS.gt.0).and.(abs(itwmod).eq.1))
&      .or. iBT.eq.1) then ! kay-epsilon & DNS slip-vel
        call localx (d2wall,  dwl,      ien,      1,      'gather ')
      endif

      if(wallrhodist .gt. 0.0d0)then
        call local(d2wall,  dwl,      ien,      1,      'gather ')
      endif

      if( (iLES.gt.10).and.(iLES.lt.20)) then ! bardina
        call local (rls, rls1,      ien,      6, 'gather ')
      else
        rls1 = zero
      endif

      if ((iDNS.gt.0).and.(itwmod.eq.-2)) then
        call local(effvisc, evl,      ien,      1,      'gather ')
      endif

c
c          write(*,*) 'iLES = ', iLES

      if ((iDNS.gt.0).and.(abs(itwmod).eq.1)) then
        call local(x2wall, xwl,      ien,      1,      'gather ')
        call local(y2wall, ywl,      ien,      1,      'gather ')
        call local(z2wall, zwl,      ien,      1,      'gather ')
      endif

c
c.... zero the matrices if they are being recalculated
c
      if (lhs. eq. 1) then
        xKebe = zero
        xGoC  = zero
      endif

c
!      Update the marker field.
IF(iBT .eq. 1) THEN

```

```

        call banmaUpdate(xl, yl, banma, ien, bml)
    ENDIF !iBT

c.... get the element residuals, LHS matrix, and preconditioner
c
    rl      = zero
    cfl1    = zero

    if(ierrcalc.eq.1) rerrl = zero

    call e3 (yl,      acl,      dwl,      shp,
&          shgl,    xl,        rl,
&          ql,      xKebe,    xGoC,    xmudmi,
&          sgn,     rerrl,    rls1,
&          cfl1,    evl,      xwl,     ywl,
&          zwl,     xarray,   yarray,  zarray,
&          elemvol_local, bml,
&          bubradius, bubradius2, coordtag)
c
c.... assemble the statistics residual
c
    if ( stsResFlg .eq. 1 ) then
        call e3StsRes ( xl, rl, lStsVec )
        call local( stsVec, lStsVec, ien, nResDims, 'scatter ' )
    else
c
c.... assemble the residual
c
        call local (res,      rl,      ien,      nflow, 'scatter ' )

        if ( ierrcalc .eq. 1 ) then
            call local (rerr, rerrl, ien, 6, 'scatter ' )
        endif
    endif
c
c.... sum the CFL value from IPs. These will be divided by the number of
c contributors in elmgmr to get average CFL value at node
c
    call localSum (cfl, cfl1, ien, icflhits, 1)
c
c.... end
c
    if (exts) then
        if ((iter.eq.1).and.(mod(lstep,freq).eq.0)) then
            if(recordcode .eq. 4)then
C Pay attention to numvar in xyzts. Here it is considered that
C numvar is 15
                call timeseries(yl,xl,ien,sgn,1,4)
C 5 is reserved for time, assigned in itrdrv
                call timeseries(yl(:, :, 5),xl,ien,sgn,6,6)
                call timeseries(ql(:, :, 11:19),xl,ien,sgn,7,15)
            elseif(recordcode .eq. 5)then
                call local(TPgrad, TPgradl, ien, 6, 'gather ' )
                call local(divq, divql, ien, 4, 'gather ' )
                call timeseries(yl,xl,ien,sgn,1,4)
                call timeseries(yl(:, :, 5),xl,ien,sgn,6,6)
                call timeseries(ql(:, :, 11:19),xl,ien,sgn,7,15)
            end
        end
    end

```

```

        call timeseries(TPgrad1,xl,ien,sgn,16,21)
        call timeseries(divql,xl,ien,sgn,22,25)
elseif(recordcode .eq. 1)then
    call timeseries(yl,xl,ien,sgn,1,4)
    call timeseries(yl(:, :, 4),xl,ien,sgn,5,5) !dummy call
elseif(recordcode .eq. 6)then
    call timeseries(yl,xl,ien,sgn,1,4)
    call timeseries(yl(:, :, 6),xl,ien,sgn,6,6)
elseif(recordcode .eq. 7)then !velocity integral
    call timeseries(yl,xl,ien,sgn,1,4)
    if (iLSet.eq.2) then !two phase
        call timeseries(yl(:, :, 6),xl,ien,sgn,6,6)
    else !single phase
        call timeseries(yl(:, :, 2),xl,ien,sgn,6,6)
    endif
else !original
    call timeseries(yl,xl,ien,sgn,1,4)
    call timeseries(ql(:, :, 10),xl,ien,sgn,5,5)
    call timeseries(ql(:, :, 11:19),xl,ien,sgn,6,14)
c    Two-phase flows averaging:
    if (numvar.ge.15) then
        call timeseries(yl(:, :, 6),xl,ien,sgn,15,15)
    endif
    if (numvar.eq.19) then
        call timeseries(ql(:, :, idflx-2:idflx),xl,ien,sgn,16
$,            ,18)
        endif
    endif
endif
endif
return
end

```

### C. Scripts of subroutine *timeseries* and *modify\_xyzts*

The  $x$ ,  $y$ ,  $z$  coordinates and probe area of each xyzts probe is read into an array *ptts*. The 2<sup>nd</sup> dimension of *ptts* was expanded from 3 to 4 to store the newly added probe area in the subroutine *timeseries*. During the initialization of the simulation, information of xyzts probes is read. Some probes are deleted if located outside mesh elements or at cell boundaries. No matter how well the domain is refined, it is hard to perfectly resolve the original geometry with discretized mesh elements. Therefore, depending on the mesh configuration, usually a small portion of the probes are deleted near the wall. Subroutine *modify\_xyzts* is then modified to make sure that the probe deletion are carried out by individual probe. Therefore, even if probes are deleted, the remaining probes still have the correct corresponding probe areas.

```
subroutine timeseries(ycl, xl, ien, sgn, n_0, n_1)

use timedata
include "common.h"

dimension shape(nshl), ycl(npro,nshl,9),
& ien(npro,nshl), xl(npro,nenl,nsd),
& sgn(npro,nshl)
real*8 al(npro,nenl,nsd),
& zi0(npro,nsd), detaij(npro), dzi0(npro,nsd),
& m11(npro), m12(npro), m13(npro), m21(npro), m22(npro),
& m23(npro), m31(npro), m32(npro), m33(npro),
& r1(npro), r2(npro), r3(npro), shgradl(nshl,nsd)

real*8 xts1, xts2, xts3
real*8, allocatable, dimension(:) :: soln
integer e, founde, n_0, n_1, ndiff

ndiff = n_1 - n_0 + 1

allocate(soln(ndiff))

if(size(varts) .eq. 0 .and. nproctspts .gt. 0) then
c -----
  allocate(varts(nproctspts,numvarc))
  if (iVeloIntg .eq. 0) then
    allocate(comptts(nproctspts,nsd))
  elseif (iVeloIntg .eq. 1) then
    allocate(comptts(nproctspts,nsd+1))
  endif
  allocate(comparptts(nproctspts,nsd))
  allocate(comstatptts(nproctspts,2))
```

```

i=1
do jj = 1,ntspts
  if(statptts(jj,2) .gt. 0)then
    comptts(i,:) = ptts(jj,:)
    comparptts(i,:) = parptts(jj,:)
    comstatptts(i,:) = statptts(jj,:)
    i = i + 1
  endif
enddo
write(*,*)nproctspts," probes found on ",myrank
-----
endif

do jj=1,nproctspts
  founde = 0
  if(comstatptts(jj,1) .gt. 0 .or. tssearch .eq. 0)then
    if(comstatptts(jj,1).eq.iblkt) then
      if(lcsyst.eq.2) then ! hex
        call shphex (ipord, comparptts(jj,:),shape(:),
&          shgradl(:,:))
      elseif(lcsyst.eq.1) then
        call shptet (ipord, comparptts(jj,:),shape(:),
&          shgradl(:,:))
      endif
      founde=comstatptts(jj,2)
    endif
    if(founde.ne.0) then
      soln(1:ndiff) = zero
      do i = 1,nenl
        soln(1:ndiff) = soln(1:ndiff)
&          +ycl(founde,i,1:ndiff)*shape(i)
      enddo
      do i = 1+nenl,nshl
        soln(1:ndiff) = soln(1:ndiff)
&          +ycl(founde,i,1:ndiff)*shape(i)*sgn(founde,i)
      enddo

      varts(jj,n_0:n_1) = soln(:)
C Write Coordinates
      if(n_1 .eq. numvar)then
        if (iVeloIntg .eq. 0) then
          varts(jj,numvar+1:numvar+3) = comptts(jj,1:3)
        elseif (iVeloIntg .eq. 1) then
          varts(jj,numvar+1:numvar+4) = comptts(jj,1:4)
        endif
      endif
    endif
  endif
enddo

deallocate(soln)

return
end

```

```

subroutine modify_xyzts

use timedata

include "common.h"
include "mpif.h"

integer, allocatable :: found(:)

integer, allocatable :: newstatptts(:, :)
real*8, allocatable :: newptts(:, :)
real*8, allocatable :: newparptts(:, :)
c   real*8, allocatable :: newvarts(:, :)

integer newntspts, itemp

allocate(found(ntspts))

call MPI_ALLREDUCE(statptts(:, 2), found, ntspts,
&   MPI_INTEGER, MPI_MAX, MPI_COMM_WORLD, ierr)

if(any(found .eq. 0))then
  newntspts = 0
  do i=1, ntspts
    if(found(i) .ne. 0)then
      newntspts = newntspts+1
    endif
  enddo

  allocate(newstatptts(newntspts, 2))
  if (iVeloIntg .eq. 0) then
    allocate(newptts(newntspts, nsd))
  elseif (iVeloIntg .eq. 1) then
    allocate(newptts(newntspts, nsd+1))
  endif
  allocate(newparptts(newntspts, nsd))
c   allocate(newvarts(newntspts, numvar))

  j=1
  do i=1, ntspts
    if(found(i) .ne. 0)then
      newstatptts(j, :) = statptts(i, :)
      newptts(j, :) = ptts(i, :)
      newparptts(j, :) = parptts(i, :)
c     newvarts(j, :) = varts(i, :)
      j=j+1
    endif
  enddo

  deallocate(statptts)
  deallocate(ptts)
  deallocate(parptts)
c   deallocate(varts)

```

```

allocate (statptts (newntspts, 2))

if      (iVeloIntg .eq. 0) then
  allocate (ptts (newntspts, nsd))
elseif (iVeloIntg .eq. 1) then
  allocate (ptts (newntspts, nsd+1))
endif

allocate (parptts (newntspts, nsd))
c      allocate (varts (newntspts, numvar))

statptts = newstatptts
ptts = newptts
parptts = newparptts
c      varts = newvarts

deallocate (newstatptts)
deallocate (newptts)
deallocate (newparptts)
c      deallocate (newvarts)

itemp = ntspts
ntspts = newntspts

if (myrank .eq. master) then
  write (*, *) "Extraneous Probes Deleted"
  write (*, *) "Old points: ", itemp, " new points: ", newntspts
  open (unit=2019, file="xyzts.dat", action="write",
    &      status="unknown")
  &      write (2019, " (2I8, 5X, 1E15.6, 2X, 3I8) ") ntspts, freq, tolpt,
  &      iterat, numvar, numrun
  do i=1, ntspts
    if      (iVeloIntg .eq. 0) then
      write (2019, " (3E20.8) ") (ptts (i, j), j=1, 3)
    elseif (iVeloIntg .eq. 1) then
      write (2019, " (4E20.8) ") (ptts (i, j), j=1, 4)
    endif
  enddo
  close (2019)
endif
endif

deallocate (found)

end

```

#### D. Scripts of PID pressure gradient control in *itrdrv.f*

The MPI process of velocity integral happens in *itrdrv.f* through *varts*. In *varts(i,j)* array, dimension *i* corresponds to each xyzts probe. Dimension *j* includes recorded or read data, in which *varts(i,2)* and *varts(i,6)* are  $u_i$  and  $\phi_i$  respectively; and *varts(i,7 – 10)* are the *x*, *y*, and *z* coordinates and  $S_i$  of each xyzts probe. In each processor, a summation loop is coded for  $varts(i,2) \cdot varts(i,10)$  if  $varts(i,6) > 0$ . Then MPI\_ALLREDUCE computes the desired velocity integral,  $\int u dS = \sum_{i=1}^N u_i S_i, \phi_i > 0$ , by adding the contribution from each processor.

This velocity integral computation can be carried out with or without PID pressure gradient control and the computed velocity integral will be output into file `PIDpresgradout.dat`. If PID pressure gradient control is activated (`idpdxPID .eq. 1`), the change of pressure gradient will be revealed in this output file as well.

```
if (iVeloIntg .eq. 1) then !compute velocity integral
  if (iLSet.eq.2) then !Two-phase
    veloIntg = 0.0
    do jj=1,nproctspts
      iprobe = (jj-1)*numvarc
      varts(jj,5) = delt(itseq)
      vartsbuffer(iprobe+1:iprobe+numvarc) = varts(jj,:)
      if(varts(jj,6).gt.0.0) then
        veloIntg = veloIntg + varts(jj,2)*varts(jj,10)
      endif
    enddo

    call MPI_ALLREDUCE (veloIntg, veloIntgSum, 1,
& MPI_DOUBLE_PRECISION,MPI_SUM, MPI_COMM_WORLD,ierr)

  elseif (iLSet.eq.0) then !Single-phase
    veloIntg = 0.0
    do jj=1,nproctspts
      iprobe = (jj-1)*numvarc
      varts(jj,5) = delt(itseq)
      vartsbuffer(iprobe+1:iprobe+numvarc) = varts(jj,:)
      veloIntg = veloIntg + varts(jj,2)*varts(jj,10)
    enddo

    call MPI_ALLREDUCE (veloIntg, veloIntgSum, 1,
& MPI_DOUBLE_PRECISION,MPI_SUM, MPI_COMM_WORLD,ierr)

  endif !(iLSet.eq.2)
```

```

else !original code
  do jj=1,nproctspts
    iprobe = (jj-1)*numvarc
    varts(jj,5) = delt(itseq)
    vartsbuffer(iprobe+1:iprobe+numvarc) = varts(jj,:)
  enddo
endif !(iVeloIntg .eq. 1)

call MPI_Gatherv(vartsbuffer,nproctspts*numvarc,
& MPI_DOUBLE_PRECISION, vartsout, nproberanks,
& idispranks,MPI_DOUBLE_PRECISION,0,
& nvartscomm,ierr)

if(MPI_COMM_NULL .ne. iwritecomm)then
  call MPI_FILE_WRITE_AT(vartsfile,
& offset,vartsout,
& iwritenum,
& MPI_DOUBLE_PRECISION,MPI_STATUS_IGNORE,ierr)

  offset = offset + iwriteinc
endif

tssearch = 0

if(myrank.eq.master)write(*,*)"Done with parallel IO"

!Joy pressure gradient controller
if (iVeloIntg .eq. 1 .and. idpdxPID.eq. 1) then
  if(bctlIter .gt. 0 .and. lstep.eq.(bctlIter+1)) then
    inquire(file='varts/PIDpresgrad.dat',exist=exts)
    if(exts) then
      open(unit=629,file='varts/PIDpresgrad.dat',status='old')
      read(629,*) dpdxI, dpdxdummy, datmat(1,7,1), vIntgdummy
      close(unit=629)
      if(myrank.eq.master) then
        write(*,*) "read dpdxI          = ", dpdxI
        write(*,*) "read dpdxdummy       = ", dpdxdummy
        write(*,*) "read datmat(1,7,1) = ", datmat(1,7,1)
        write(*,*) "read vIntgdummy        = ", vIntgdummy
      endif
    else
      if(myrank.eq.master)write(*,*)"No varts/PIDpresgrad.dat"
    endif
  endif

  dpdx = datmat(1,7,1)

  if (lstep .gt. 1) then
    dpdxI = (1.0-1.0/PIDrelax)*dpdxI + 1.0/PIDrelax*dpdxdummy
    dpdxdummy = dpdx
  else !if(lstep .eq. 1) then
    dpdxI = dpdx
    dpdxP = 0.0 !initial value for proportional
    dpdxD = 0.0 !initial value for derivative
    vIntgdummy = 0.0
  endif
endif

```



## E. Velocity field evolution of cylindrical debris bed channel

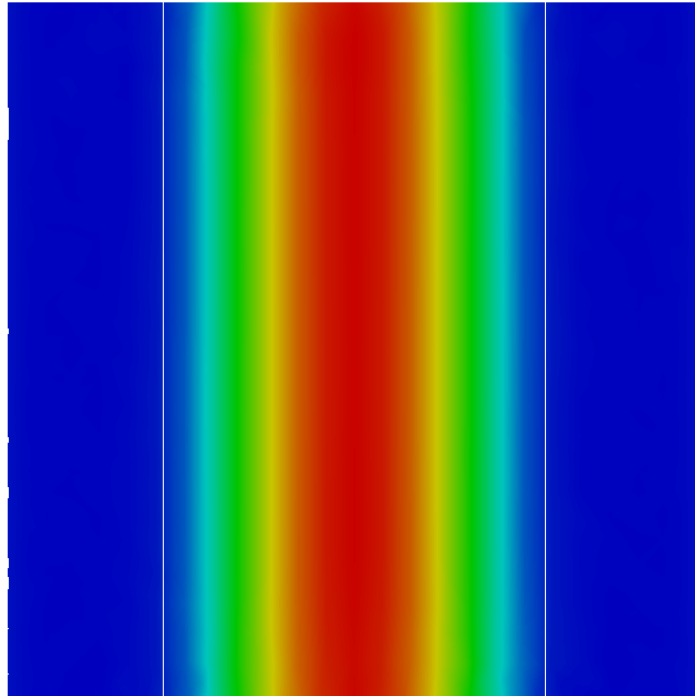
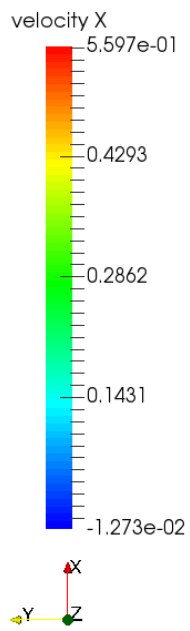
### 1. Annular flow ( $\alpha = 30\%$ )

This appendix shows the velocity field evolution in CCFL simulation with void fraction equal to 30%. Due to velocity fluctuation (Figure 5.21(b)), all the color bars represent the instantaneous velocity range at each time step. Table A.1 summarizes the maximum and minimum  $x$  velocity at each time step for the following images. The two-phase flow is very laminar both for center steam column and the liquid film, therefore the interface topology barely changes.

Table A.1 Maximum and minimum  $x$  velocity at each time step

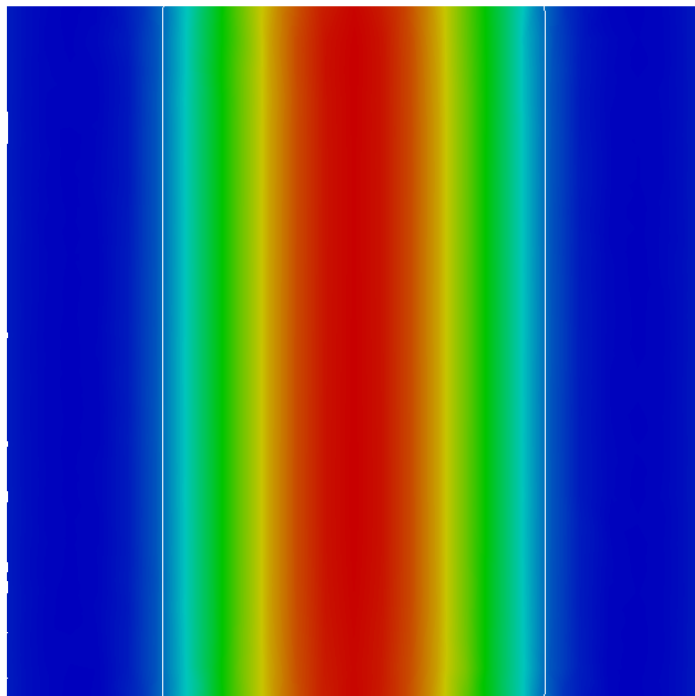
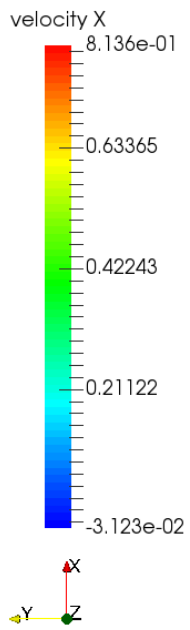
Time step	Time (s)	Maximum $x$ velocity (m/s)	Minimum $x$ velocity (m/s)
100	2.439E-03	5.597E-01	-1.273E-02
500	8.737E-03	8.136E-01	-3.123E-02
5000	6.841E-02	8.000E-01	-4.696E-02
20000	2.699E-01	8.114E-01	-4.747E-02

Time: 100



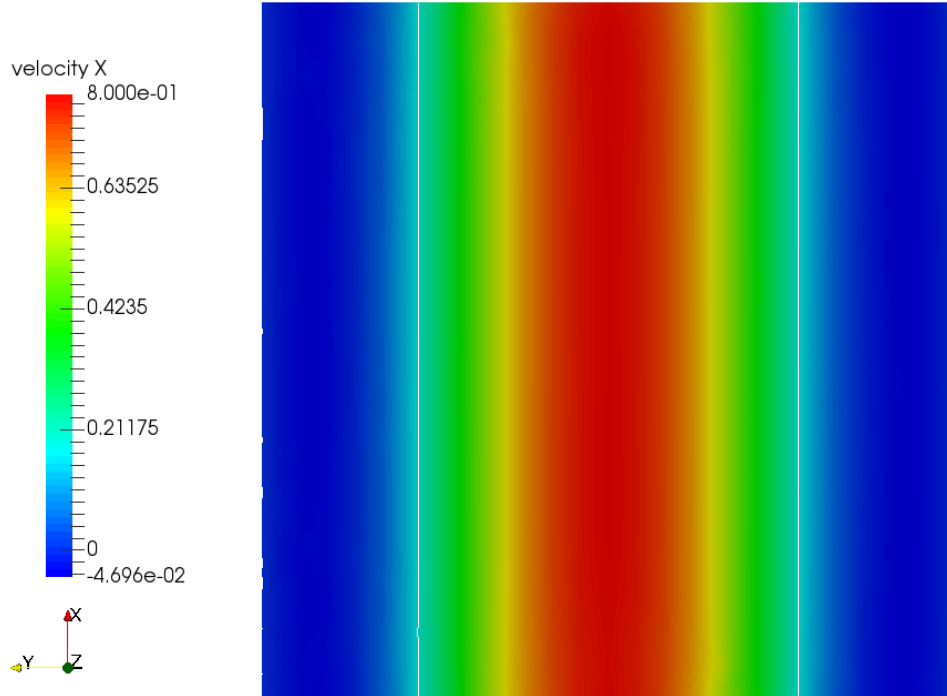
$t = 2.439E - 03 \text{ s}$

Time: 500



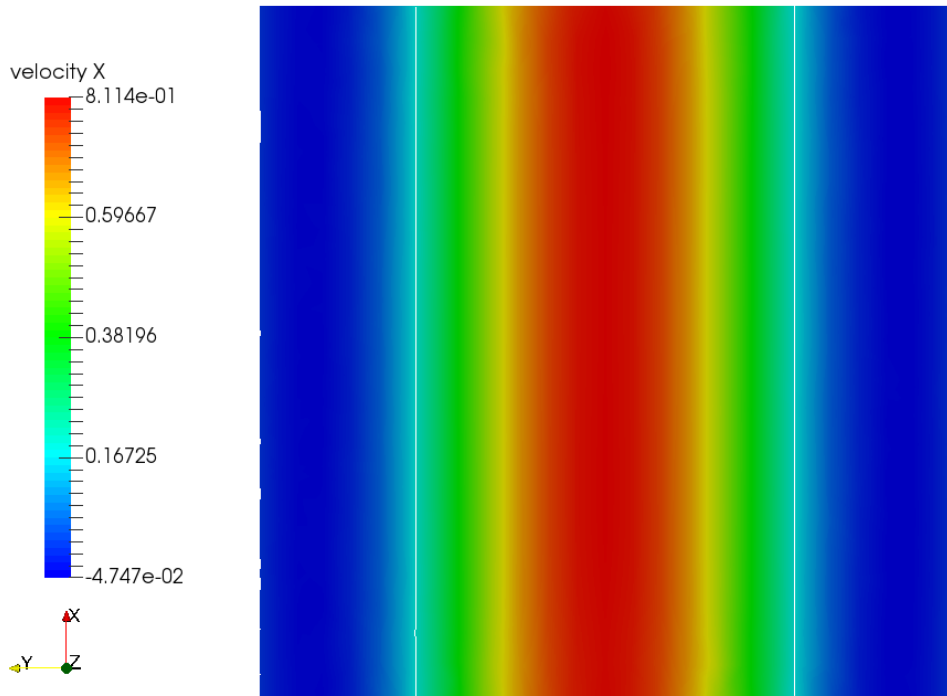
$t = 8.737E - 03 \text{ s}$

Time: 5000



$t = 6.841E - 02 \text{ s}$

Time: 20000



$t = 2.699E - 01 \text{ s}$

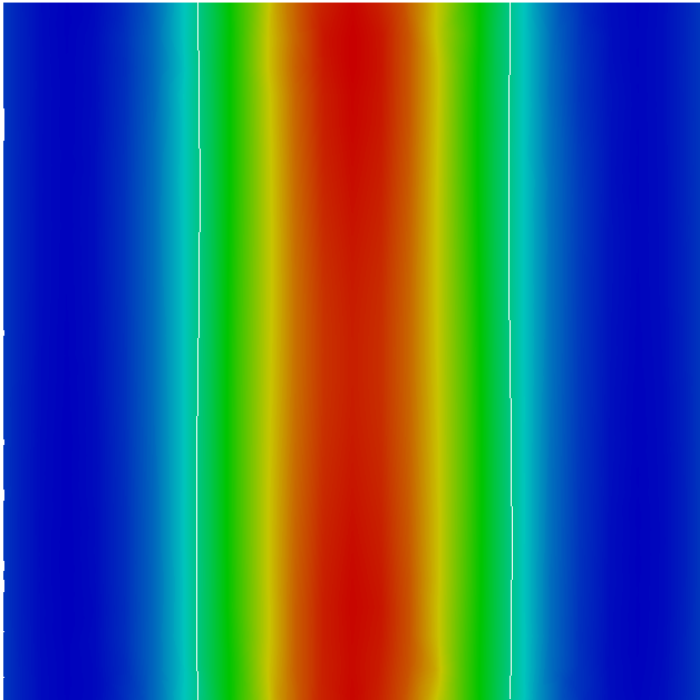
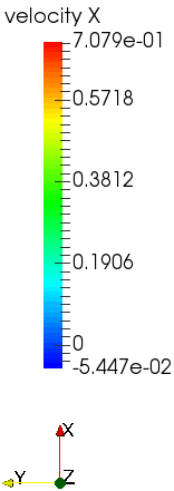
## 2. Velocity field evolution where annular flow changes to bubble flow ( $\alpha = 20\%$ ).

This appendix shows the velocity field evolution in the CCFL simulation with a void fraction of  $\alpha = 20\%$ . And  $\frac{dp}{dx}$  used in this simulation is predicted by the pressure gradient correlation with regard to void fraction developed using data from  $\alpha = 30\% \sim 60\%$ . Due to velocity fluctuation, all the color bars represent the instantaneous velocity range at each time step. Table A.2 summarizes the maximum and minimum velocity at each time step for the following images. The flow regime of this simulation changes from the annular flow to a single bubble flow due to the low void fraction.

Table A.2 Maximum and minimum  $x$  velocity at each time step

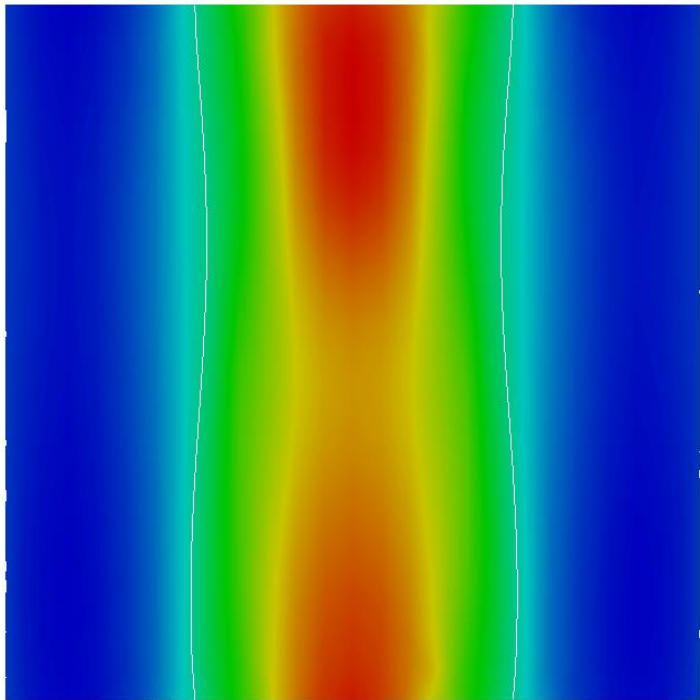
Time step	Time (s)	Maximum $x$ velocity (m/s)	Minimum $x$ velocity (m/s)
2500	4.611E-02	7.709E-01	-5.447E-02
3500	6.210E-02	7.702E-01	-5.843E-02
4000	7.023E-02	9.760E-01	-6.972E-02
4500	7.646E-02	1.253E+00	-6.721E-01
4750	8.234E-02	3.084E-01	-1.100E-01
15000	3.899E-01	3.040E-01	-1.907E-01

Time: 2500



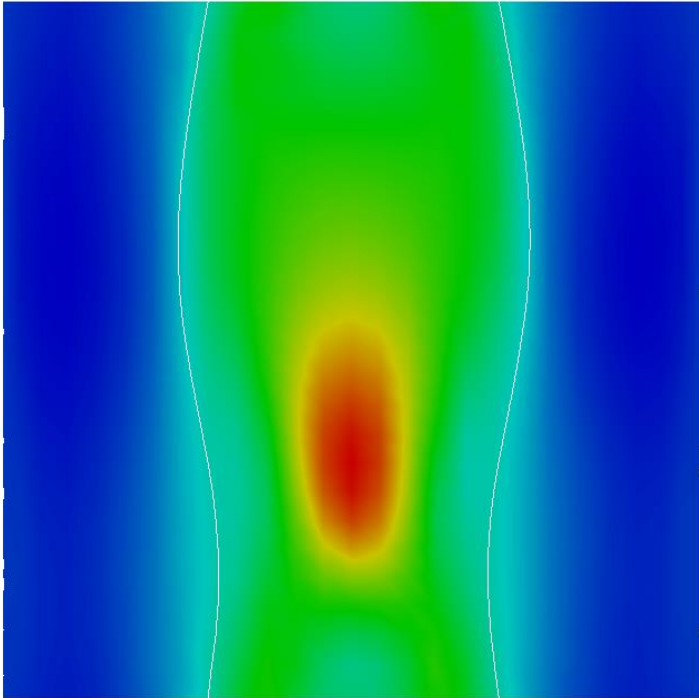
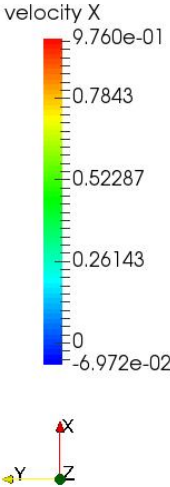
$t = 4.611E - 02 \text{ s}$

Time: 3500



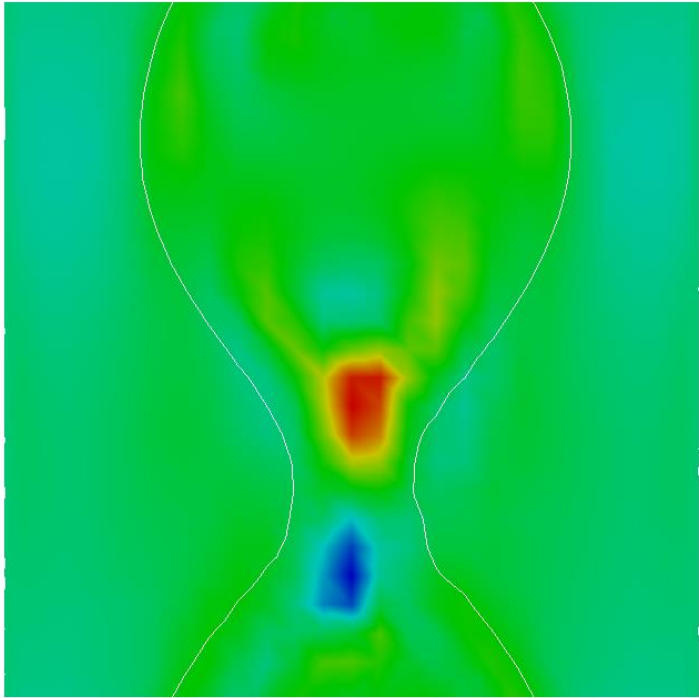
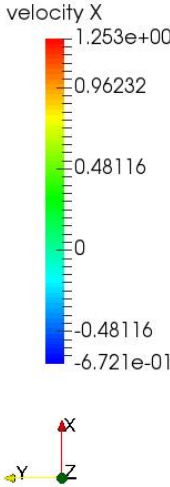
$t = 6.210E - 02 \text{ s}$

Time: 4000



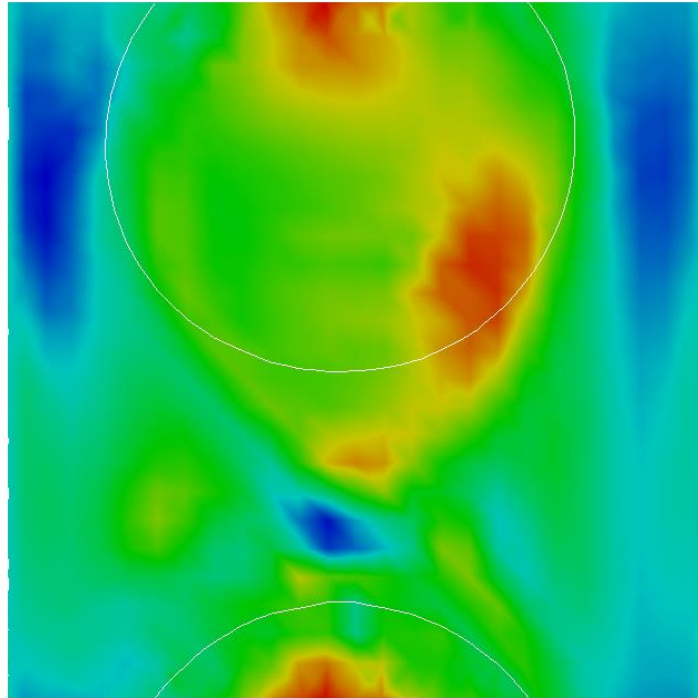
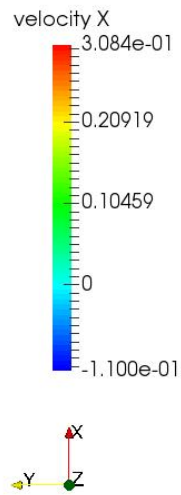
$t = 7.023E - 02 s$

Time: 4500



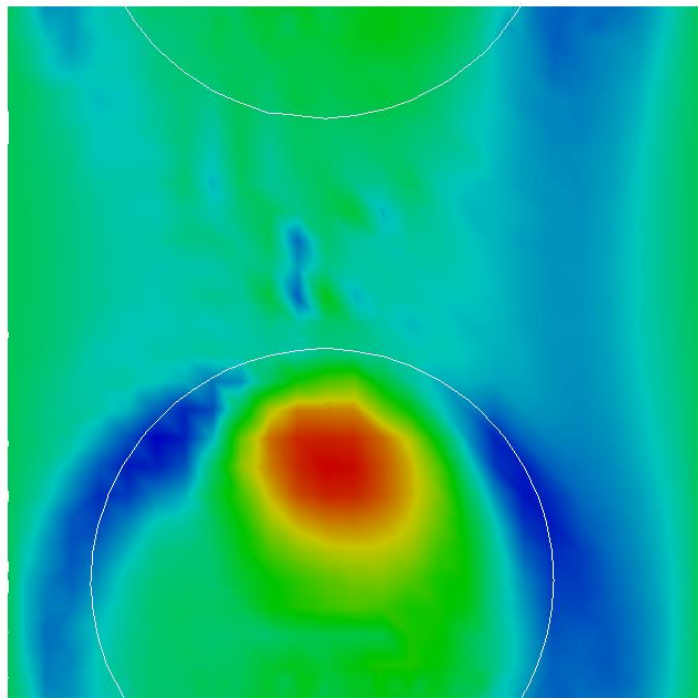
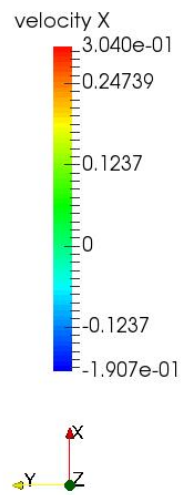
$t = 7.646E - 02 s$

Time: 4750



$t = 8.234E - 02$  s

Time: 15000

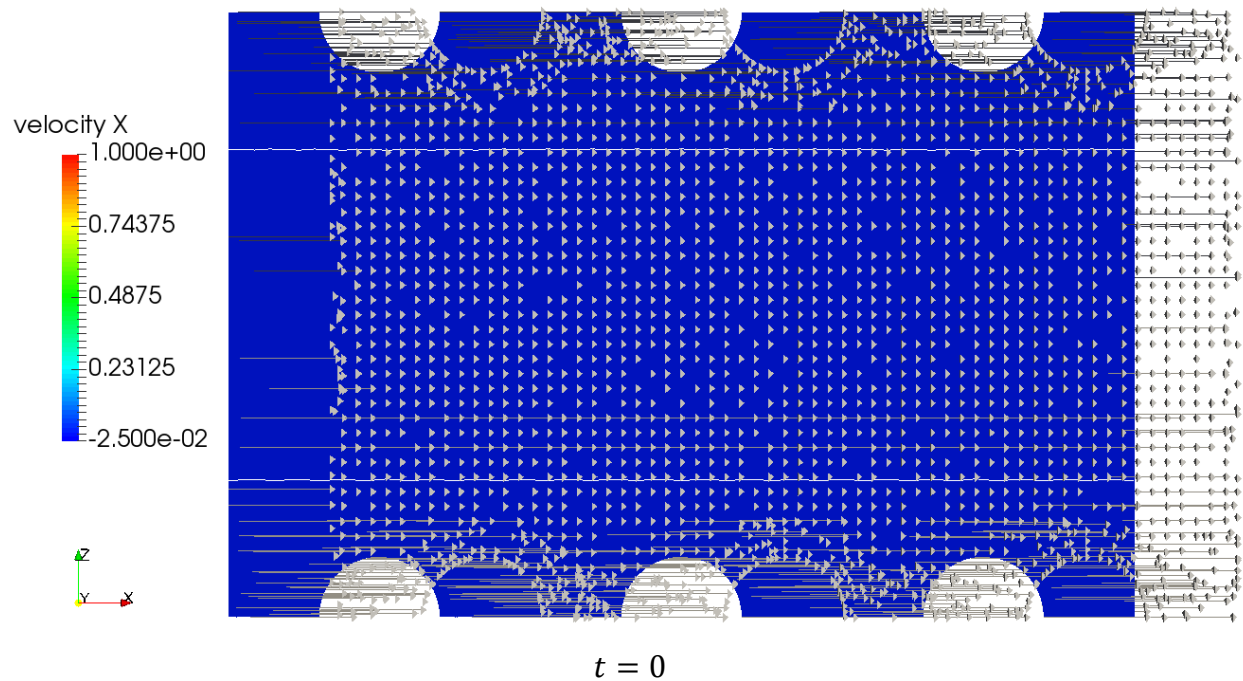


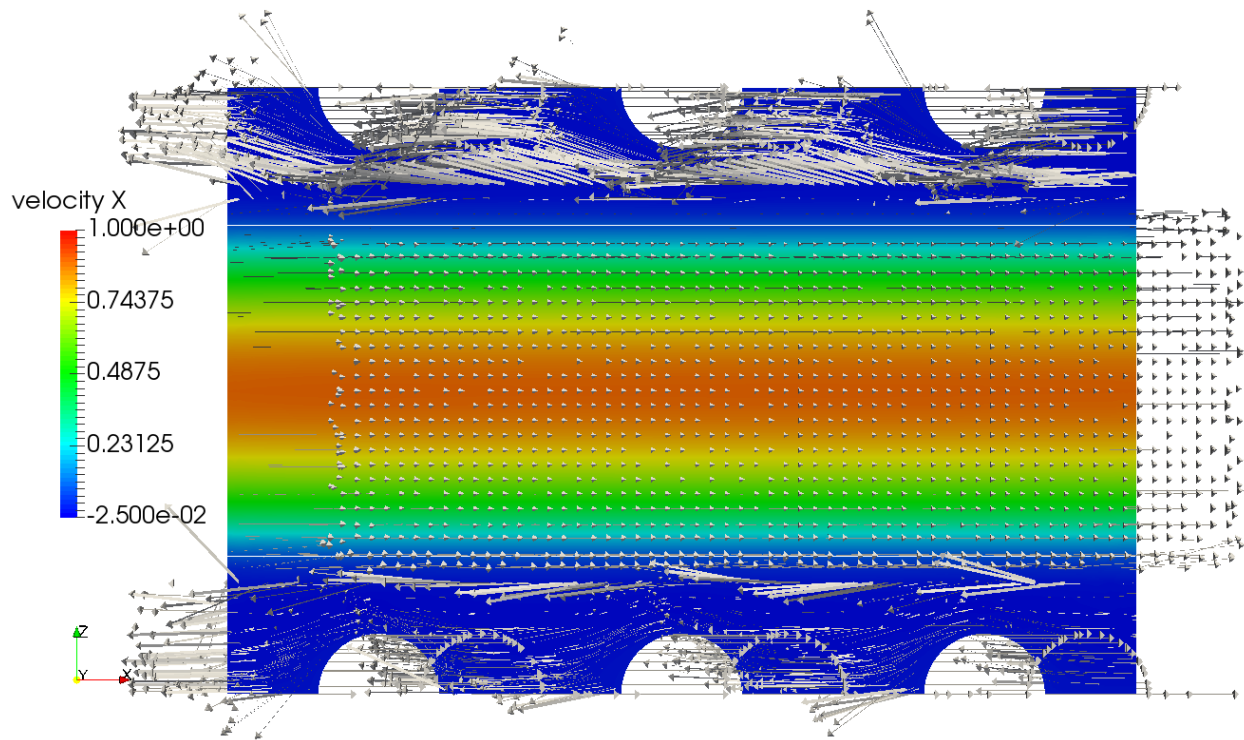
$t = 3.899E - 01$  s

## F. Velocity field of debris bed channel with small obstacles

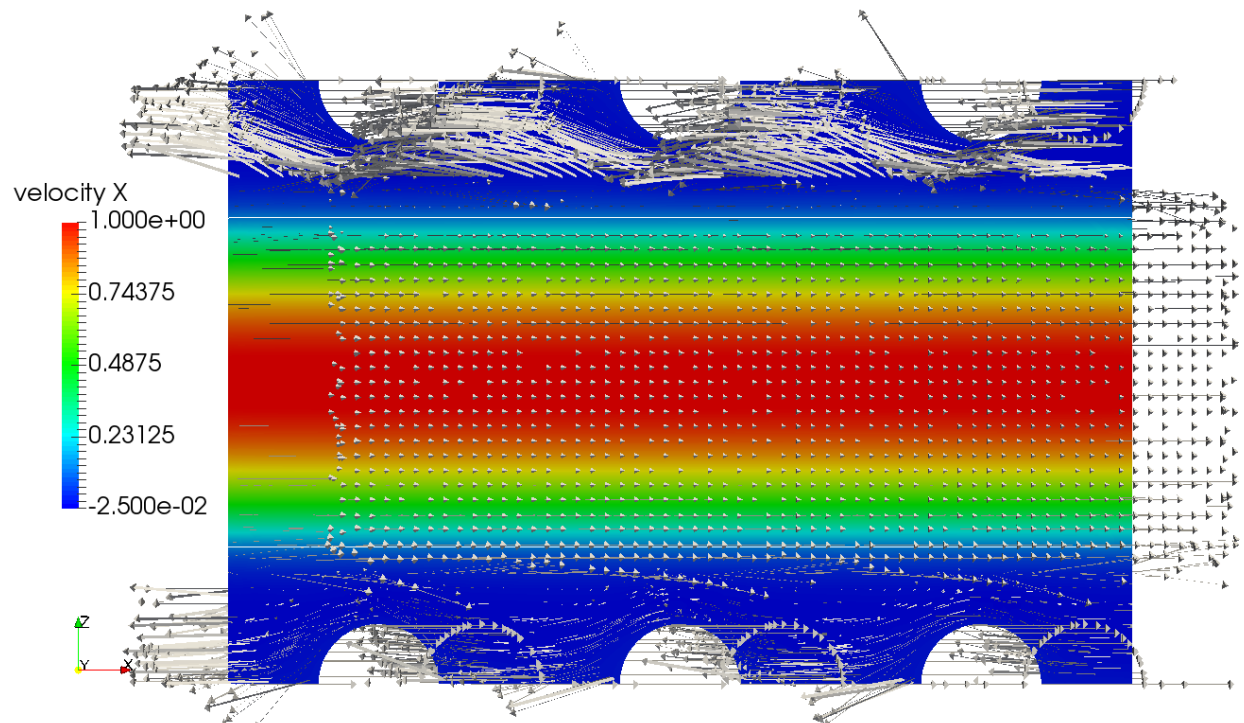
### 1. Annular flow ( $\alpha = 30\%$ )

This appendix shows the velocity field evolution of the debris bed channel with small obstacles until CCFL achieves with steam volume fraction equal to 30%. The flow regime is still annular flow and the white line indicates the interface. Due to page layout direction, all the figures in this appendix are rotated 90 degrees clockwise, with  $-x$  indicating the gravity direction.

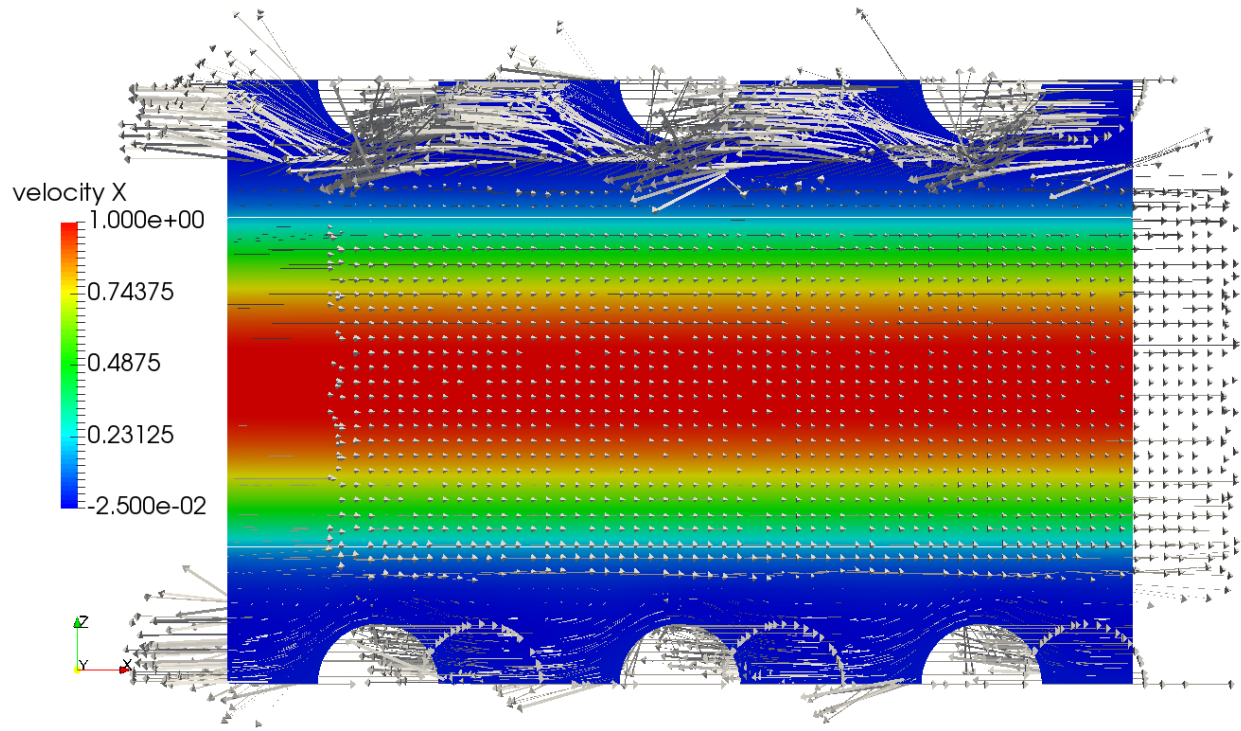




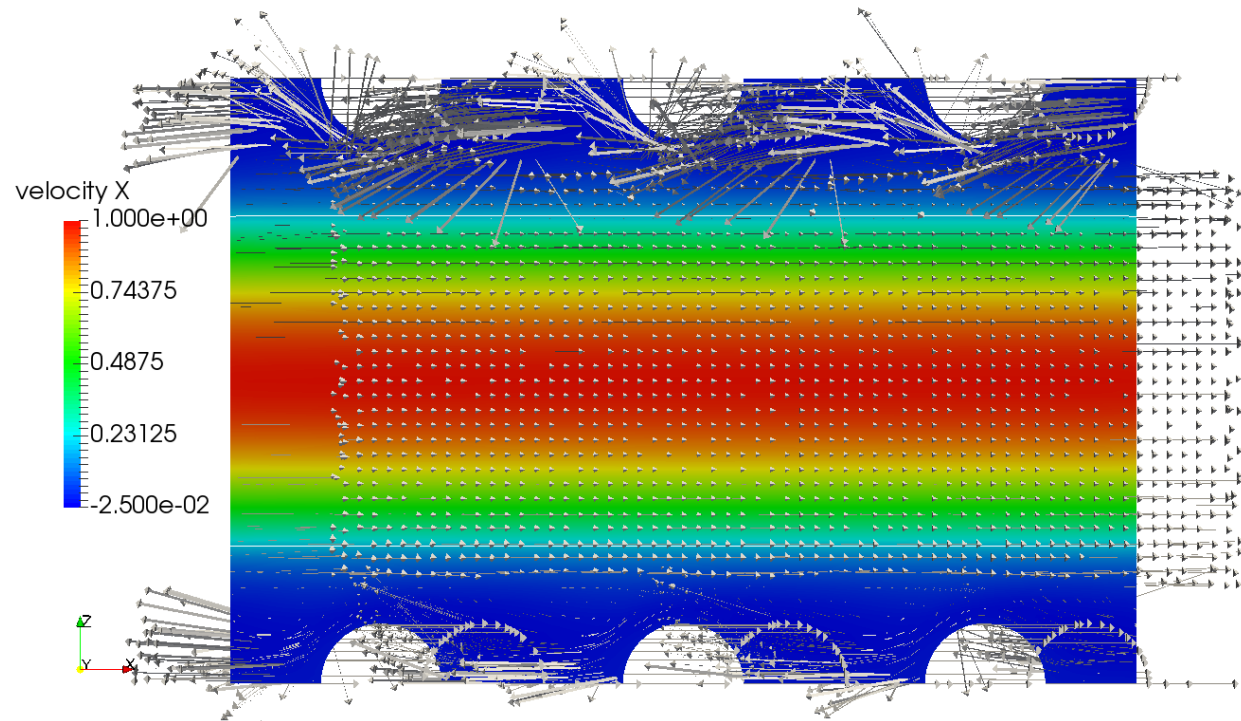
$t = 4.226E - 3 \text{ s}$



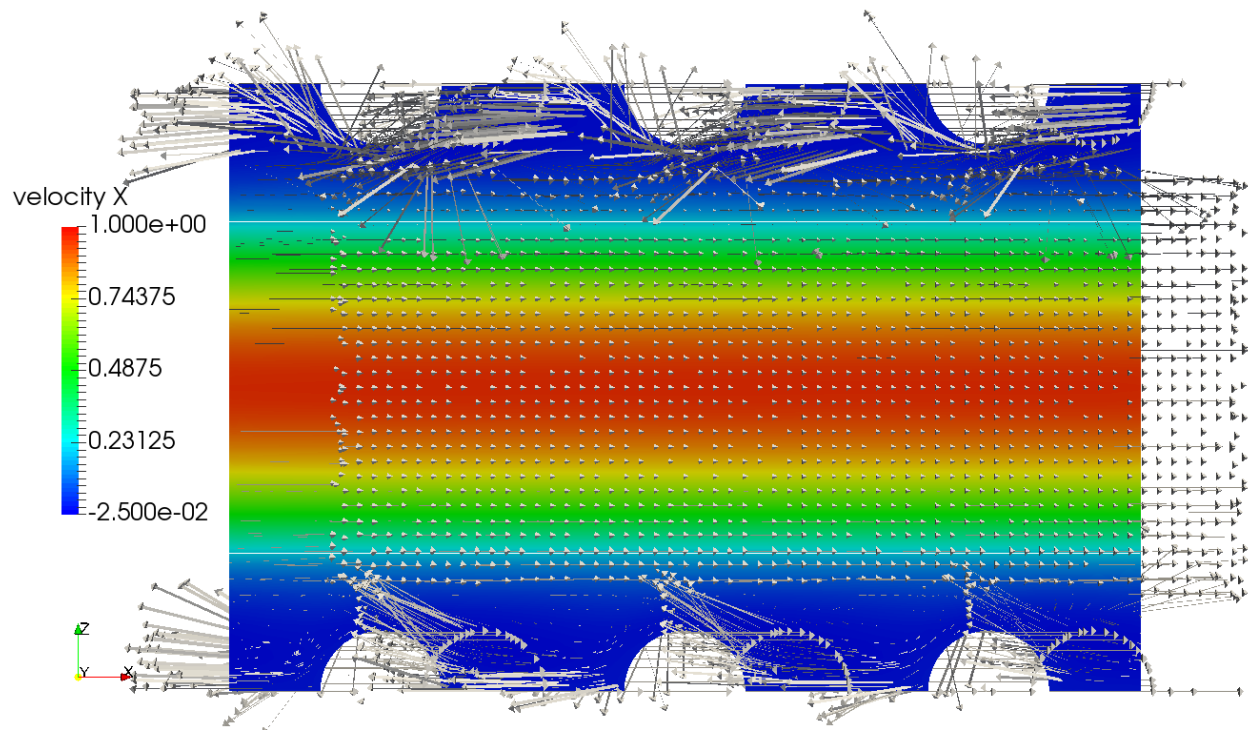
$t = 7.444E - 3 \text{ s}$



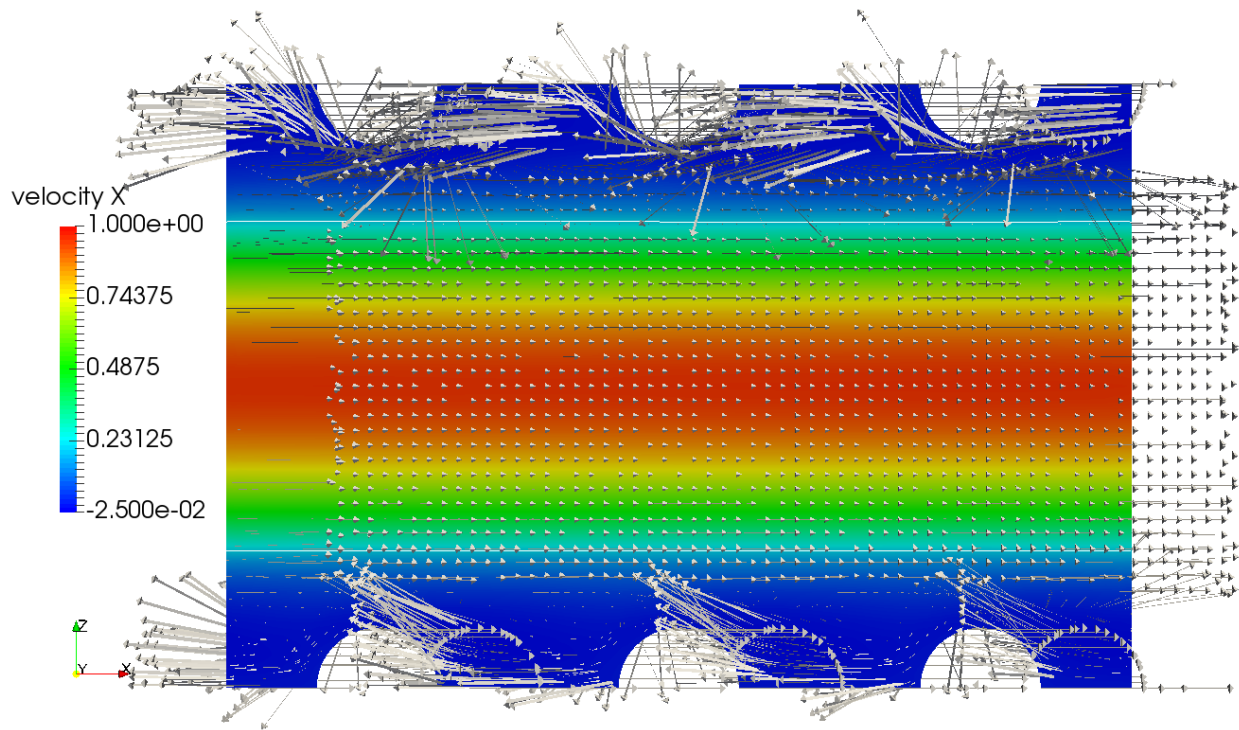
$t = 1.328E - 2s$



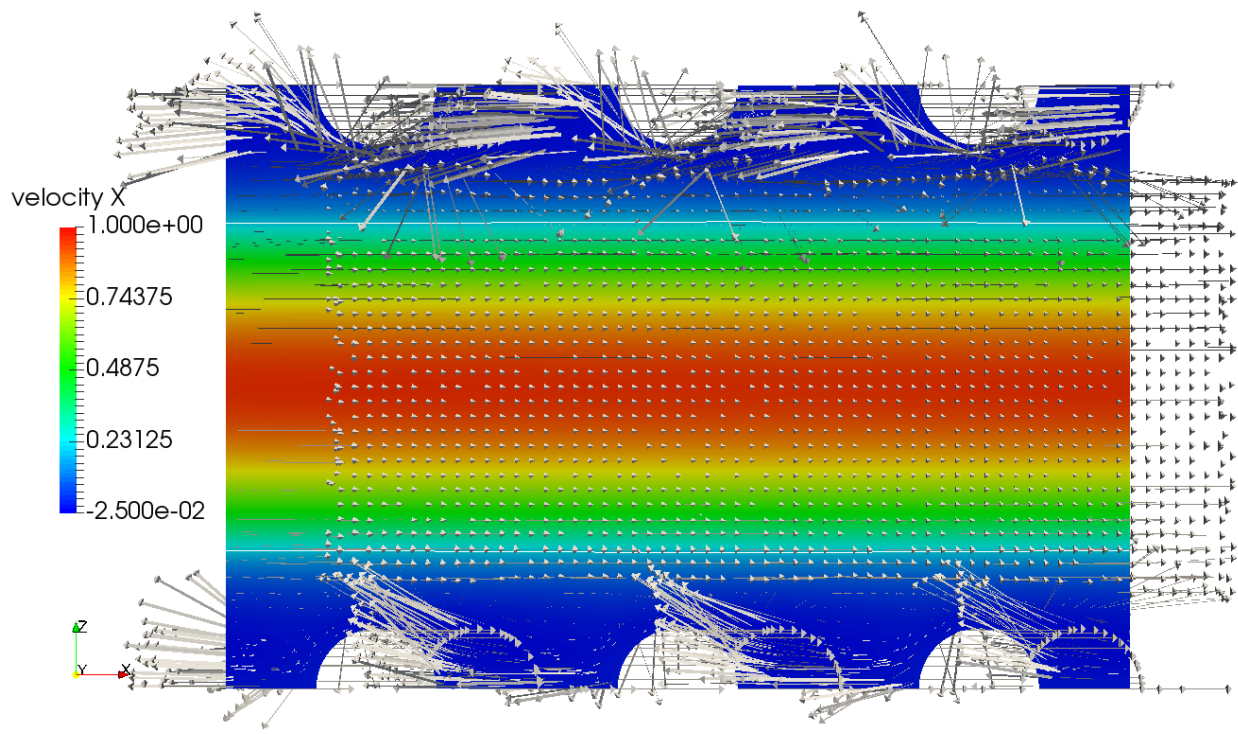
$t = 3.315E - 2s$



$t = 6.555E - 2s$



$t = 9.815E - 2s$



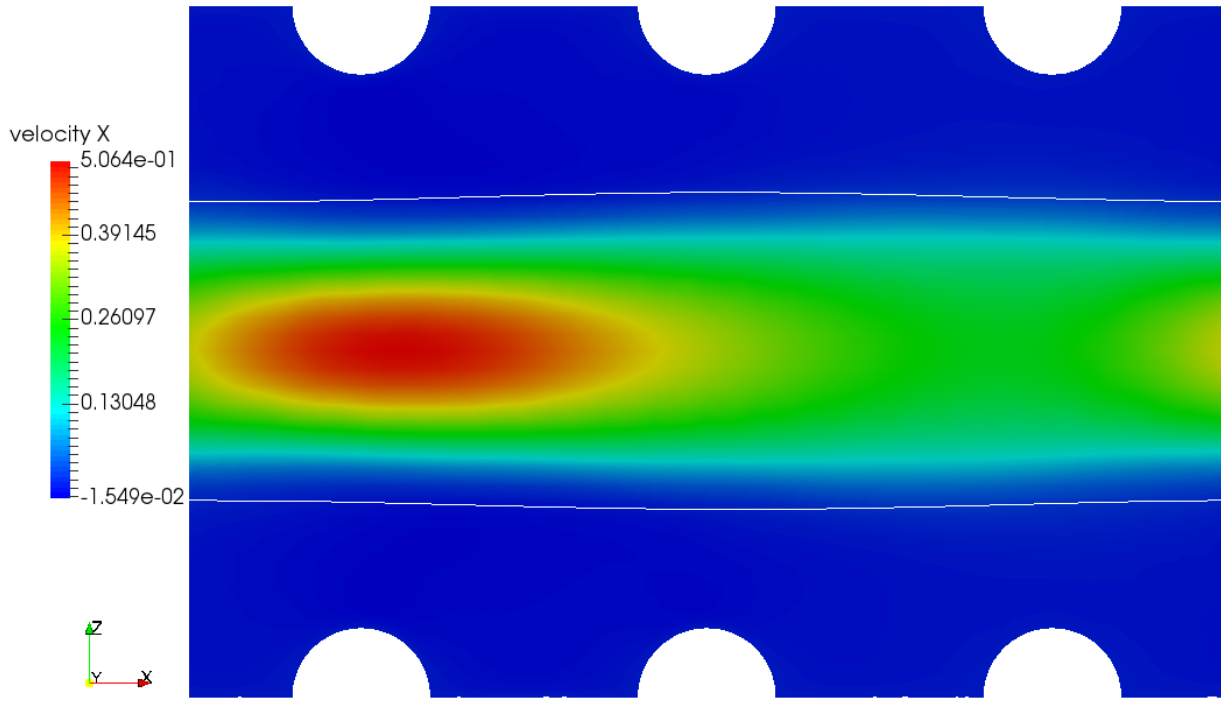
$t = 1.307E - 1s$

## 2. Velocity field of debris bed channel with small obstacles ( $\alpha = 20\%$ )

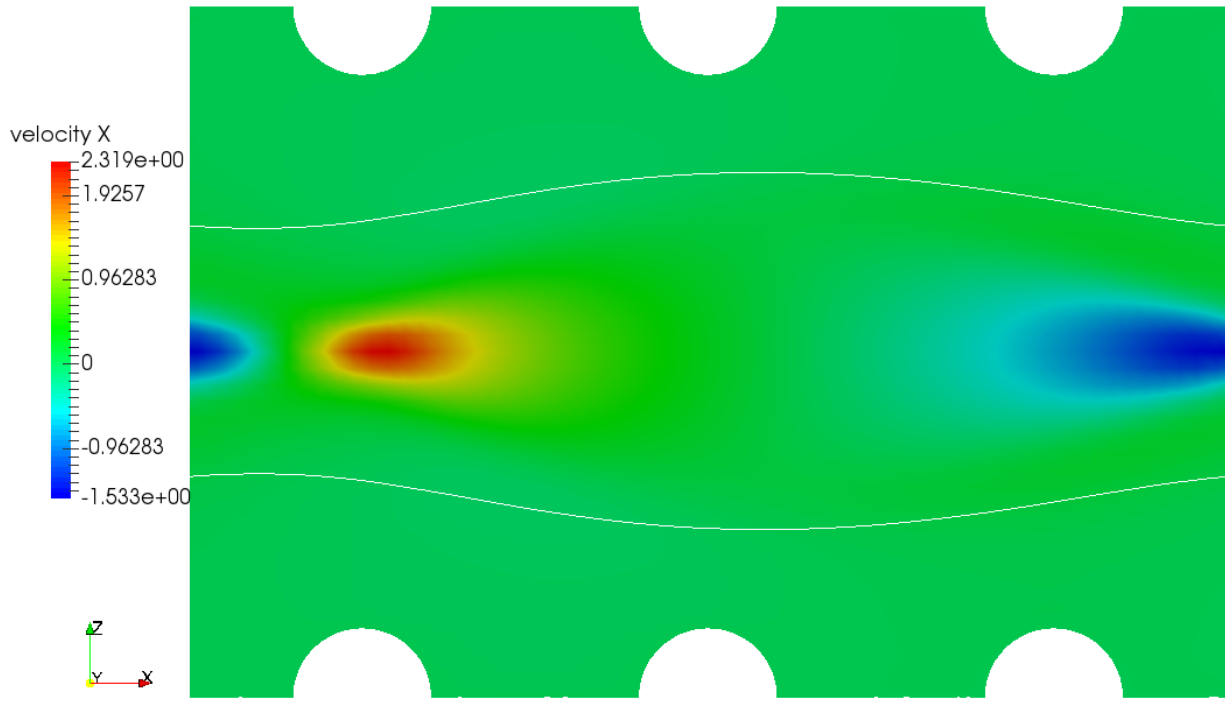
This appendix shows the velocity field evolution in the CCFL simulation with a void fraction of  $\alpha = 20\%$ . Due to velocity fluctuation, all the color bars represent the instantaneous velocity range at each time step. Table A.3 summarizes the maximum and minimum velocity at each time step for the following images. The flow regime of this simulation changes from the annular flow to a single bubble flow due to the low void fraction.

Table A.3 Maximum and minimum  $x$  velocity at each time step

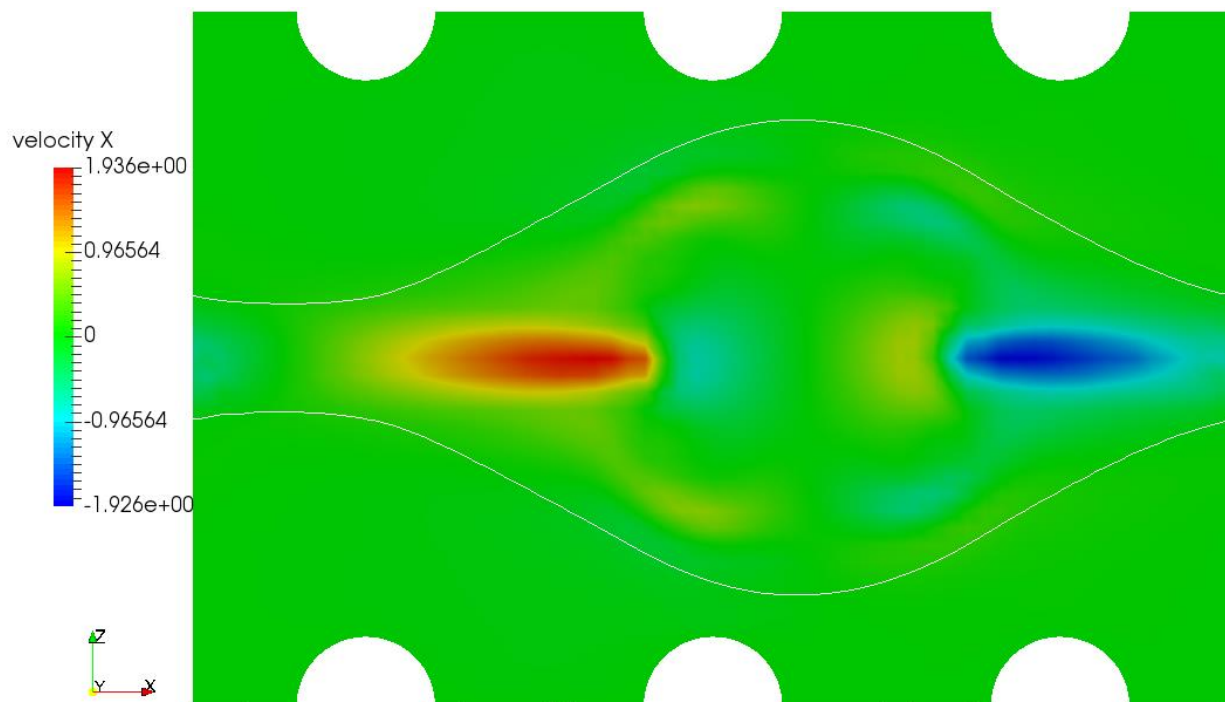
Time (s)	Maximum $x$ velocity (m/s)	Minimum $x$ velocity (m/s)
1.980E-3	5.064E-1	-1.549E-2
3.281E-3	2.319	-1.533
4.340E-3	1.936	-1.926
8.331E-3	8.649E-1	-5.655E-1
1.359E-2	7.066E-1	-6.444E-1



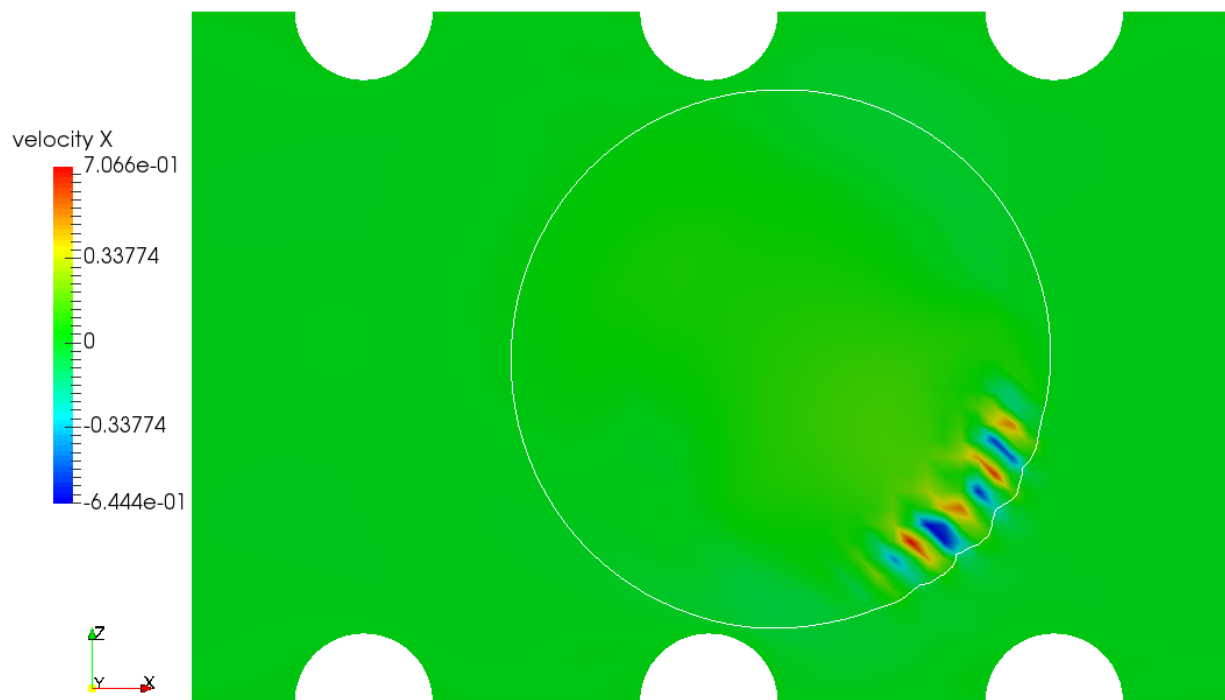
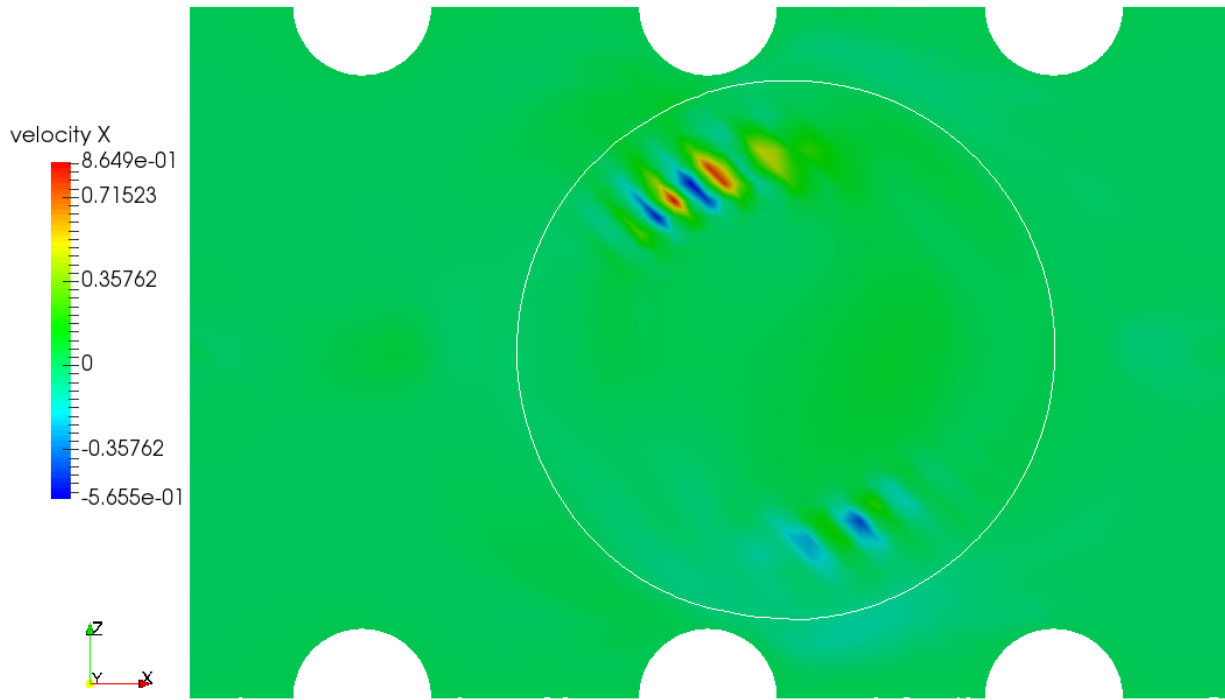
$t = 1.980E - 3 \text{ s}$



$t = 3.281E - 3 s$

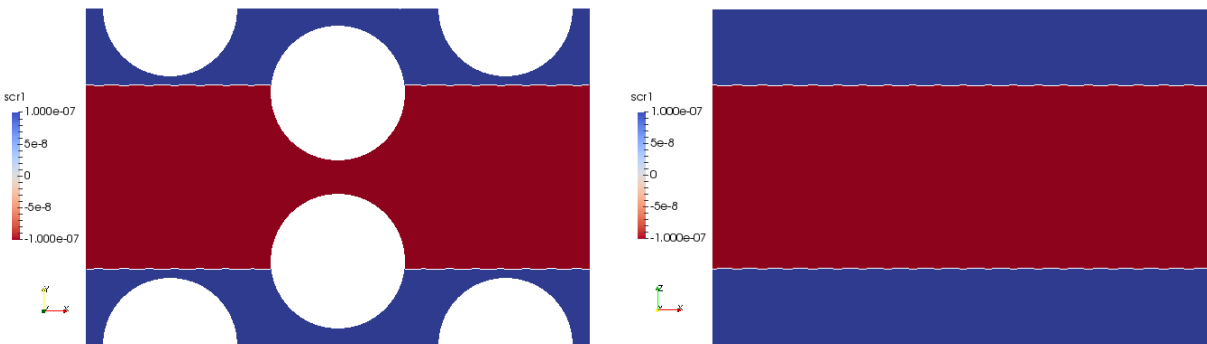


$t = 4.340E - 3 s$

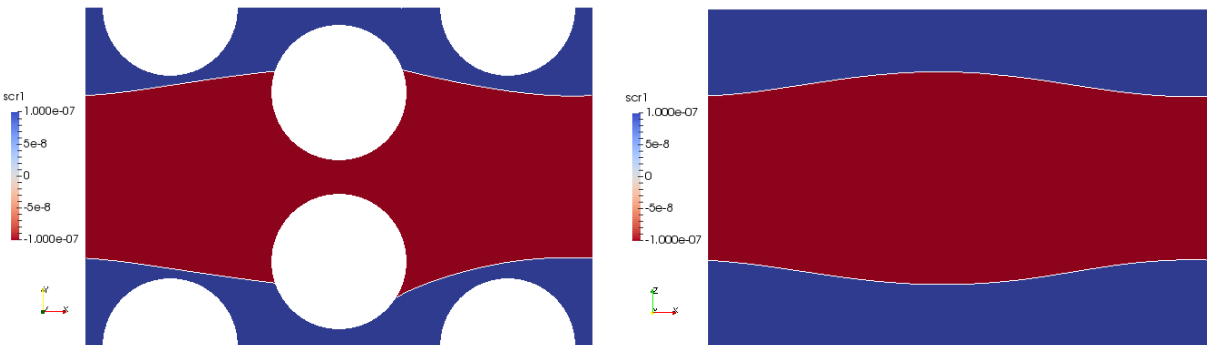


### G. Interface evolution of debris bed channel with large obstacles

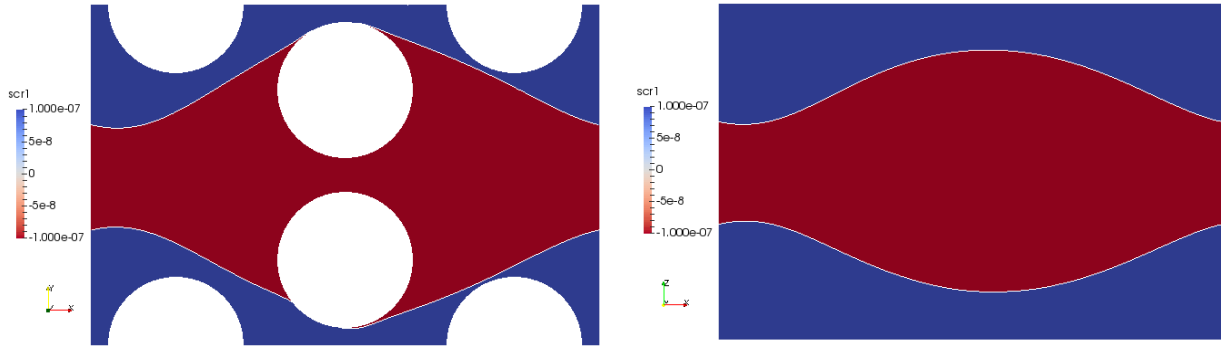
This appendix shows the liquid and steam two-phase evolution in the debris bed channel with large obstacles until CCFL achieves. The steam volume fraction is  $\alpha = 30\%$ . In the figures below, liquid is blue and steam is in red, with white line indicating the two-phase interface. The left figure is on  $x - O - y$  plane and the right figure shows  $x - O - z$  plane at the same time. Due to page layout, all the figures in this appendix are rotated 90 degrees clockwise, with  $-x$  indicating the gravity direction. Although the steam volume fraction is  $\alpha = 30\%$ , which was also used in the simple cylindrical channel and the small obstacle channel, the flow regime with large obstacles is very different. The annular flow cannot be maintained and a steam bubble will be formed around middle obstacles.



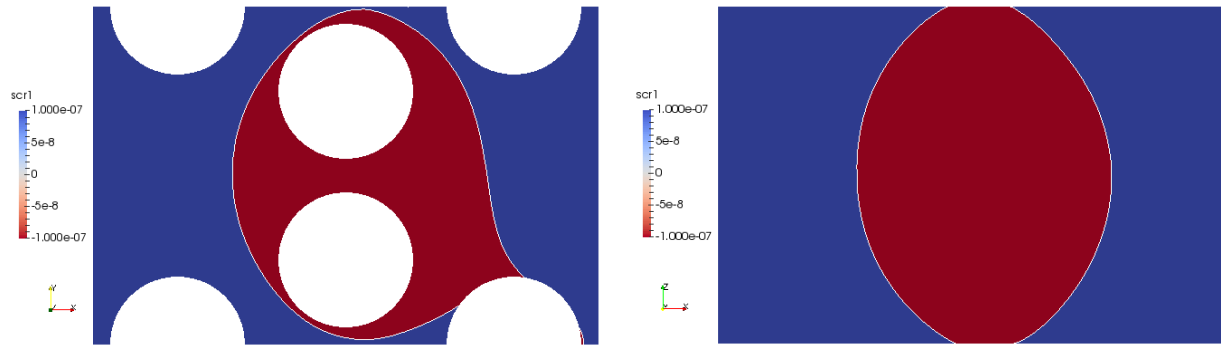
$t = 0$



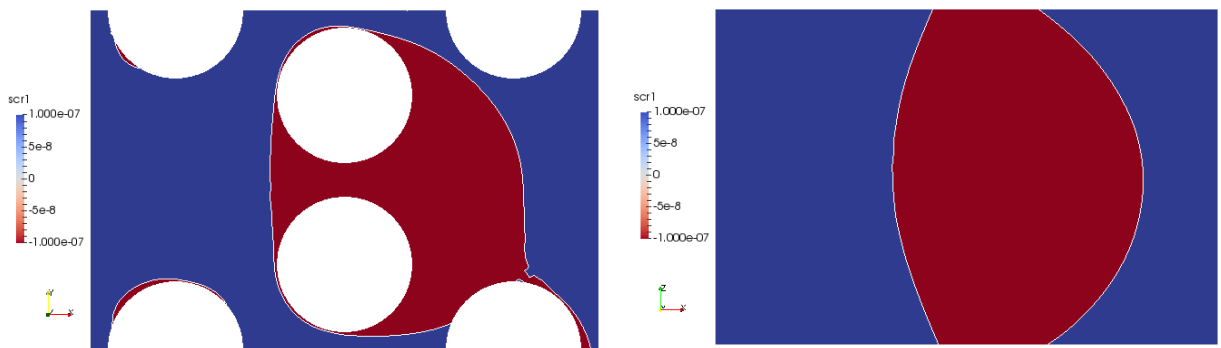
$t = 3.748E - 3 s$



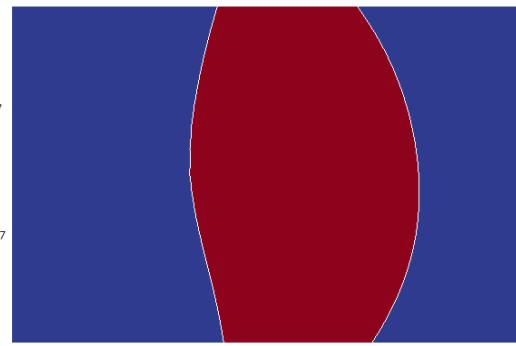
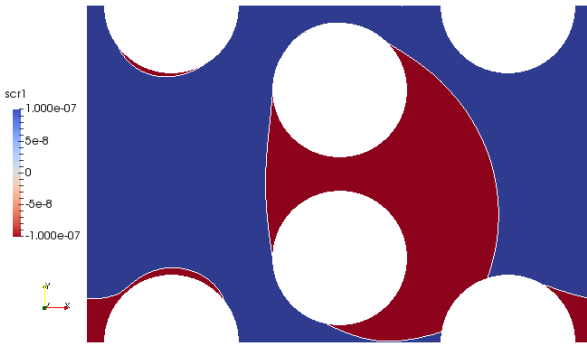
$t = 7.088E - 3 \text{ s}$



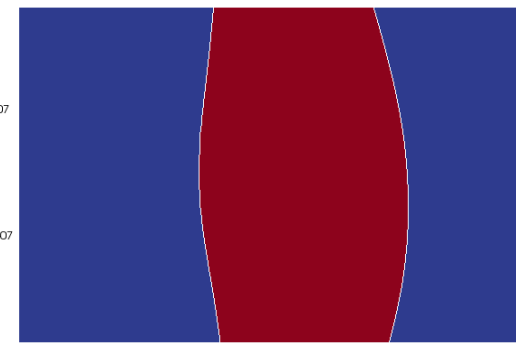
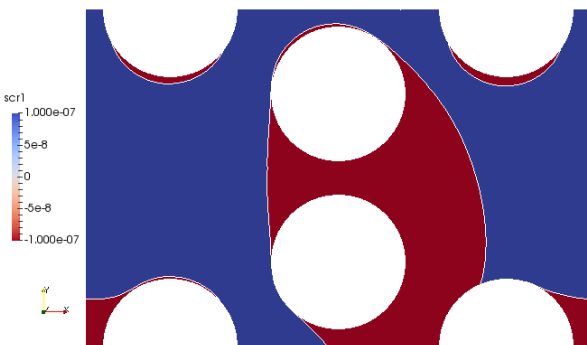
$t = 1.125E - 2 \text{ s}$



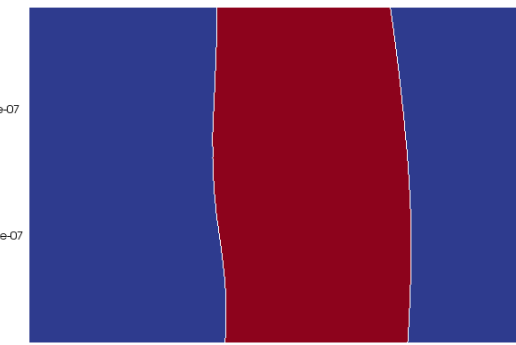
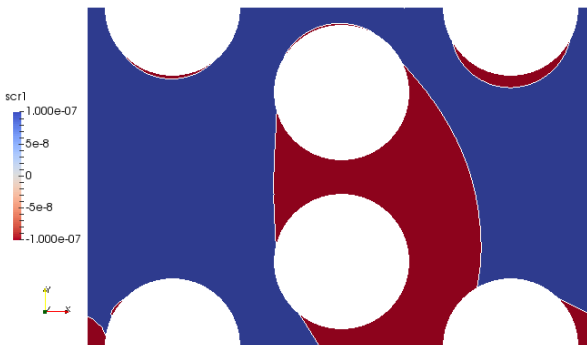
$t = 1.493E - 2 \text{ s}$



$t = 2.166E - 2 \text{ s}$



$t = 2.792E - 2 \text{ s}$



$t = 3.494E - 2 \text{ s}$